Title
Piezoceramic Sensors/Actuators with Interdigitated Electrode Patterns

Author
Pisani, David McIntyre

Publication Date
2014

University of California
Los Angeles

Piezoceramic Sensors/Actuators with Interdigitated Electrode Patterns

A dissertation submitted in partial satisfaction
of the requirements for the degree
Doctor of Philosophy in Mechanical and Aerospace Engineering

by

David McIntyre Pisani

2014

ABSTRACT OF THE DISSERTATION

Piezoceramic Sensors/Actuators with Interdigitated Electrode Patterns

by

David McIntyre Pisani

Doctor of Philosophy in Mechanical and Aerospace Engineering

University of California, Los Angeles, 2014

Professor Christopher S. Lynch, Chair

Monolithic piezoelectric ceramic devices are well understood and employed in a wide variety of structural actuation and sensing applications. Over the last twenty years piezoceramic fiber composites with interdigitated electrodes (IDE) have fallen into favor. These piezocomposite devices with IDE have been shown to be more conformal, durable and responsive than conventional monolithic devices. One of the more prevalent piezocomposite devices with IDE is the Macro Fiber Composite (MFC) developed at the NASA-Langley Research Center. The MFC shows superior free strain actuation performance, manufacturability and reliability over conventional devices.

While the MFC boasts some improved characteristics over conventional devices, the use of IDE also introduces added complexity. Simple in design, the IDE causes nonuniform electric fields, large electric field gradients and increased hysteresis in the device. Characterization and modeling efforts of the MFC beyond a linear approximation have been limited. The majority of published work relies on experimental quantification and a heavy reliance on linear finite element analysis. The MFC has significant time dependent effects, conduction issues, creep, and other nonlinear effects that have not been explored.

This study serves as an attempt to rectify some of the previously overlooked issues of nonlinearity in piezocomposite actuators with IDE. As a baseline of comparison, the capability of a MFC to serve as a strain sensing/actuating rosette was compared to single crystal PMN-

PT. It was found that increased hysteresis and creep caused the MFC to perform poorly by comparison. This spurred the process of seeking improved IDE designs. A twenty actuator study was performed using actuators with different electrode line widths and spacings. It was found that the hysteresis of an actuator with IDE could be reduced, but with the sacrifice of some of the free strain actuation. For accurate strain sensing/actuation, devices with large electrode line widths were found to show less hysteresis. For maximal free strain actuation, devices with small electrode line widths and large electrode spacing were found to have larger free strain actuation. The free strain frequency response was explored for the MFC, and custom devices were designed to mitigate some of the frequency dependence. The IDE devices were characterized using a dielectric finite element model and using a nonlinear ferroelectric finite element model. A phase field model was also developed to explore domain formation along electrode edges.

The dissertation of David McIntyre Pisani is approved.

Ertugrul Taciroglu

William S. Klug

Gregory P. Carman

Christopher S. Lynch, Committee Chair

University of California, Los Angeles

2014

Table of Contents

List of Figures

LIST OF TABLES

Vita

2006–2008	Library Information Technology Technician, Maintained information technology systems of all campus libraries, UCLA Library, Los Angeles, California.
2008	Pratt & Whitney Scholarship, UCLA
2009	B.S. (Mechanical Engineering), UCLA, Los Angeles, California.
2009–2014	Teaching Assistant, Mechanical Engineering and MSOL Departments, UCLA. Taught sections including Systems Architecture, Statics, Design of Aircraft Structures, Linear Elasticity, and Mechanics of Intelligent Materials.
2009–2014	Graduate Student Researcher, UCLA. Researched projects including, Piezoceramic Sensor/Actuator Rosettes, High-Rate Deformation Physics of Heterogenous Materials, Piezoceramic Manufacturing Techniques and Piezocomposites with Interdigitated Electrodes.
2011	M.S. (Mechanical Engineering), UCLA, Los Angeles, California.

Publications and Presentations

Gallagher J.A., Pisani, D.M., Smith-Stewart B., and Lynch, C.S., “Stress and electric field gradient contributions to dielectric loss in ferroelectrics with interdigitated electrodes” *Journal of Intelligent Material Systems and Structures* (ONLINE MAY 2014)

Cui, J., Hockel, J.L., Nordeen, P.K., Pisani, D.M., Carman, G.P., and Lynch, C.S., “Giant electric-field-induced magnetic anisotropy reorientation with patterned electrodes on a Ni thin film/ lead zirconate titanate heterostructure" *Journal of Applied Physics* **115** (JAN 2014)

Dong, W.D., Pisani, D.M., and Lynch, C.S., "A Finite Element Based Phase Field Model For Ferroelectric Domain Evolution" *Smart Materials and Structures* **21** (SEP 2012)

Zhao, P., Pisani, D., and Lynch, C.S., "Piezoelectric Strain Sensor/Actuator Rosettes," *Smart Materials and Structures* **20** (OCT 2011)

Pisani, D.M., Gallagher J.A., Smith-Stewart B., and Lynch, C.S., "Modeling and characterization of the effects of field gradients on the behavior of ferroelectrics with interdigitated electrodes," in [*ASME 2013 Conference on Smart Materials, Adaptive Structures and Intelligent Systems*], (SEP 2013)

Pisani, D. and Lynch, C., "3D Effects of Polarization Switching on Interdigitated Electroded Ferroelectrics," in [*Proceedings of the SPIE - The International Society for Optical Engineering*], 797802 (9 pp.)(2011). Behavior and Mechanics of Multifunctional Materials and Composites 2011, 7-9 March 2011, San Diego, CA, USA.

Dong, W., Pisani, D., and Lynch, C., "Discrete Phase Model of Domain Walls in Ferroelectric Crystals," in [*Proceedings of the SPIE - The International Society for Optical Engineering*], 797804 (10 pp.)(2011). Behavior and Mechanics of Multifunctional Materials and Composites 2011, 7-9 March 2011, San Diego, CA, USA.

CHAPTER 1

Introduction

1.1 Motivation

Active materials are a material class in which their mechanical properties can be controlled by external stimuli such as electric field, magnetic field, or temperature. There exists many useful active materials ranging from piezoelectric, shape-memory, magnetostrictive, and magnetorheological. Some of the most widely studied active materials are piezoelectric ceramics. In piezoceramics, the application of electric field creates a mechanical deformation in the crystal structure and vice versa. Their scope of application includes sonar, ultrasonic transducers, accelerometers, and high precision actuators [1, 2].

While piezoceramic devices are widely used, many have been packaged as monolithic wafers. The monolithic wafer device traditionally depended on d_{31} modes of sensing/actuation. The d_{31} mode of actuation is the deformation of the wafer perpendicular to the polarization axis in response to applied electric field parallel with the polarization axis. Conversely, the d_{31} mode of sensing is the generation of electric field along the polarization direction in response to deformations perpendicular to the polarization axis. This d_{31} effect is weaker than the d_{33} effect in which the material deformation / electric field generation along the polarization axis is in response to electric fields / deformations along the polarization axis.

In order to take advantage of the d_{33} mode of actuation in monolithic wafers, interdigitated electrode designs have been used. The interdigitated electrode (IDE) consists of two interlocking electrode combs. The IDE structure on a piezoceramic wafer can be seen in figure 1.1. With this device design, the electric field / polarization in the piezoceramic is directed along the plane of the wafer. In this configuration, d_{33} modes of sensing/actuation can be exploited.

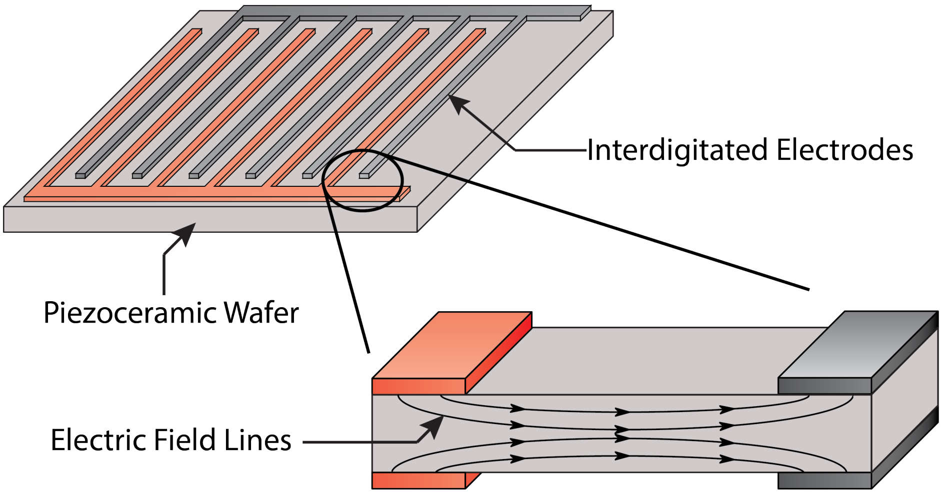

Figure 1.1: Interdigitated Electrodes on a Piezoceramic Wafer

While IDE are used in many types of sensors/actuators, a lot of simplifying assumptions have been made when characterizing them. Most research has assumed the IDE device to be linear piezoelectric. In this dissertation it will be shown that increased hysteresis, strain creep, and frequency dependency due to ferroelectric domain wall motion can dominate the sensor/actuator response. It was found that the IDE geometry can be tailored to partially mitigate some of these issues.

1.1.1 History of IDE on Piezoceramic Fiber Composites

One of the first uses of interdigitated electrodes on a piezoelectric substrate was by Cutchen in the development of flash goggles [3]. The flash goggles consisted of PLZT sandwiched between two cross polarizers. The PLZT wafer with interdigitated electrodes electrically controlled the plane of polarization of the light waves traveling through it. Thus, when the device was placed between crossed polarizers it could control transmitted light using applied voltage. The device was used for aircraft pilot goggles to mitigate flash blindness from a nuclear blast.

Piezoelectric fiber composites (PFC) were first introduced by Hagood and Bent in 1993

[4]. The piezoelectric fiber composite consisted of a built-up active structure of piezoelectric fibers embedded in an epoxy matrix sandwiched between etched interlaminar electrodes. The electric field was delivered from the interlaminar electrodes through thickness to the active sub-ply. While more robust, the PFC suffered from dielectric mismatch between the fibers and the epoxy matrix resulting in diminished electric field values in the fiber and poor actuation. Figure 1.2 shows a layout of the piezoelectric fiber composite structure.

While the initial designs of the piezoelectric fiber composite were more robust and conforming to curved surfaces than monolithic piezoelectric wafers, they only took advantage of d_{31} mode actuation in the plane of the piezocomposite. Hagood et al used the interdigitated electrode design to increase planar actuation in a monolithic wafer [5]. The electric field was transmitted along the plane of the wafer allowing for d_{33} mode actuation in the plane of the wafer. By combining the larger strain outputs of the interdigitated electrode design with the flexibility of the piezoelectric fiber composite, a more robust actuator was designed. This led to the design of active fiber composites.

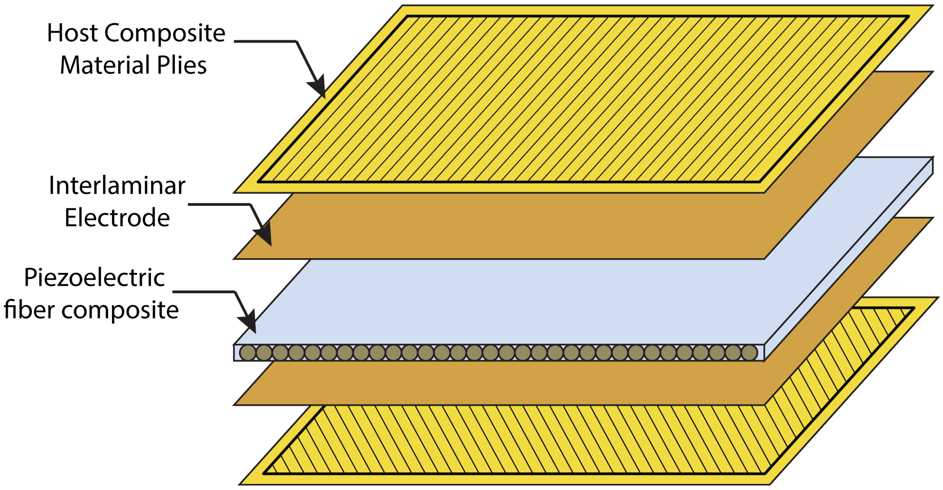

Figure 1.2: Piezoelectric Fiber Composite Structure

1.1.1.1 Active Fiber Composites

Bent et al combined the PFC design with interdigitated electrodes in 1997 [6]. The design was first coined Interdigitated Electrode Piezoelectric Fiber Composites (IDEPFC). The structure of the IDEPFC can be seen in figure 1.3. An immediate improvement of the

IDEPFC over the PFC was apparent with increased strain output while maintaining directional actuation, flexibility and durability. It was found that the effective piezoelectric tensor d_{33} increased from 30 pm/V to 150 pm/V. This corresponded to a free strain actuation of the IDEPFC five times greater than the PFC with uniform interlaminar electrodes.

In Bent's doctoral dissertation, a reference was made in describing IDEPFC as an active fiber composites or AFC [7]. The AFC, which is more well known today, is synonymous with the IDEPFC. In the dissertation, Bent advanced characterization techniques of AFC using a uniform field method and a finite element approach. The models were used to explore different design parameters of the AFC. Dielectric fillers with high dielectric permittivity were used in an attempt to alleviate the problems of the dielectric mismatch between the fibers and the epoxy matrix. It was found that adding high permittivity PZT particles to the epoxy matrix provided little improvement in actuator performance.

Manufacturing techniques were also explored by Bent. Key concepts from the manufacturing of graphite/epoxy composites were borrowed for the manufacturing techniques of AFC. This manufacturing process helped with electrode alignment and uniformity of fiber distributions in the epoxy matrix. Utilizing this technique resulted in an improvement in actuator reliability and repeatability of performance between actuators.

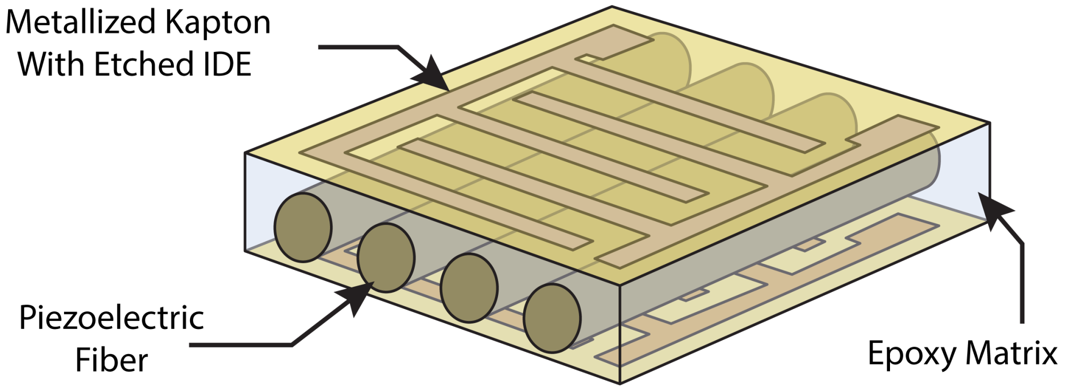

Figure 1.3: Interdigitated Electrode Piezoelectric Fiber Composite Structure

In a short period of time several modeling and experimental efforts had advanced the study of AFC to address some of their inherent problems. In 2000, Bent released a manuscript describing these recent advances [8]. It was found that AFC immediately impacted actuator strength and conformability, actuation performance and directional sensitivity. Also the use of the graphite/epoxy manufacturing techniques allowed for low complexity manufacturing in turn leading to lower cost.

While many improvements were made with AFC, they introduced some problems too. The piezoceramic fibers were difficult to handle during manufacture. Processing of piezoceramic fibers yielded varying fiber diameter impacting performance consistency. Also, poor contact area between the electrode and the fiber decreased actuator performance. Suggestions were made that the use of non-circular fibers could prevent some of these issues. By using square or ribbon fibers with rounded edges, the problems could be alleviated.

1.1.1.2 Macro Fiber Composites

Tasked to solve the AFC performance problems, Wilkie et al at the NASA-Langley Research Center developed the macro fiber composite actuator (MFC) [9]. The macro fiber composite's structure is shown in figure 1.4. The MFC consists of a sheet of rectangular piezoceramic fibers sandwiched between two interdigitated electrode patterns on polymide film and structural epoxy.

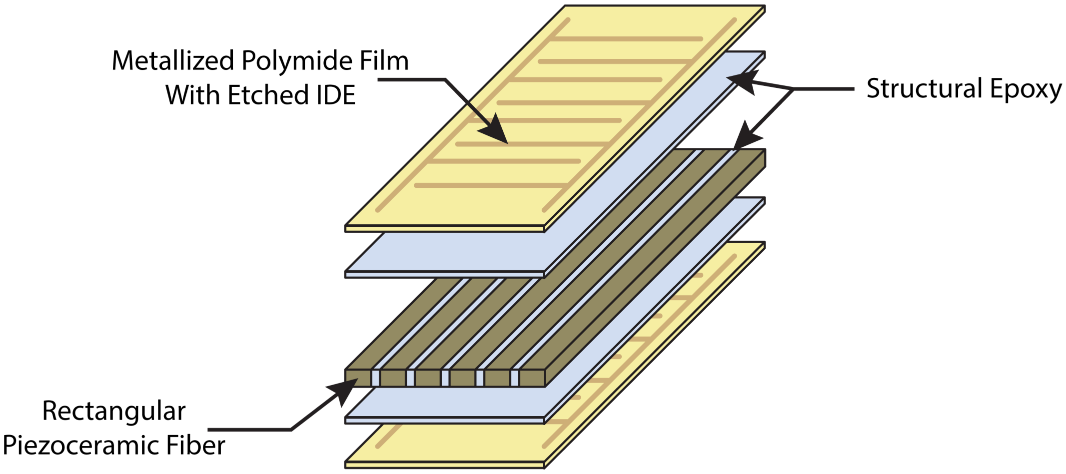

Figure 1.4: Macro Fiber Composite Structure

Constructing a square cross section fiber composite using individually handled fibers had previously been attempted by others, but the sharp corners of the fibers tended to sever the electrodes. The MFC design solved this by using a polymer carrier film during the manufacturing process. A piezoceramic wafer is placed on a polymer carrier film. A dicing saw is used to cut the wafer in place into fibers. With the wafer cut into fibers, the polymer carrier film allows for the handling of a whole sheet of fibers instead of individual ones. The preparation and assembly of the MFC can be found in the detailed instruction manual by High and Wilkie [10].

The MFC immediately solved some problems inherent in the AFC. The fiber sheet with a polymer carrier alleviated the need to handle individual fibers in the manufacturing process. This lowered device costs along with time to manufacture. The square fibers increased the contact area between the electrodes and the fibers. This mitigated some dielectric mismatch problems and allowed for more electric field to reach the fibers for increased actuation performance. Also, the precision dicing and manufacturing allowed for more consistent device performance from actuator to actuator.

Experimental characterizations of the MFC were performed by Williams. Williams et al measured the four independent linear elastic orthotropic engineering constants of the MFC under short circuit electrical conditions [11]. Three sets of tensile experiments were performed. The first set measured the stress/strain behavior along the fiber's longitudinal axis. The second set measured the stress/strain behavior transverse to the fiber's longitudinal axis. And, the third set measured in-plane shear stress/strain components. The engineering constants were then used to characterize nonlinear stress/strain behavior using plastic deformation models.

Williams et al set out to measure the thermoelastic properties of the MFC [12]. Considering the MFC is a symmetric cross-ply laminate, it was determined that only two distinct coefficients of thermal expansion (parallel and transverse to the fibers longitudinal axis) were needed. The temperature dependent behavior of the MFC was then determined by finding the individual layer material properties and combining them with a classical lamination model. Continuing on evaluating temperature effects, Williams et al investigated cure kinetics when manufacturing MFC [13]. While the MFC was being produced with consistent properties the cure time was time consuming. Thus, a cure kinetics model was developed to produce time/temperature profiles that result in a fully cured actuator in the shortest amount of time.

1.1.2 Computational Modeling of Piezocomposites

The finite element method (FEM) has been used to model linear piezoelectrics and subsequently to model the non-linearity and hysteresis that occur in ferroelectrics. Allik and Hughes introduced linear piezoelectric finite elements in 1970 [14]. Their model used a scalar electric potential with tetrahedral elements. Piezoelectric elements are now available in commercial codes with numerous plate, shell, beam, and volumetric elements [15]. Non-linearity associated with polarization reorientation in ferroelectric materials in a finite element code tends to only be found in specialized codes used by researchers in this area. Hom implemented a quadratic electrostrictive constitutive law with no hysteresis [16] and addressed field concentration effects at electrode edges in multilayer actuators. Chen developed a code with triangular elements that called a micromechanics based subroutine to obtain ferroelectric/ferroelastic switching behavior and used this code to simulate the effects of crack tip field concentrations in ferroelectrics [17]. Fang and Soh used FEA with a ferroelectric material model to address effects of defects in ferroelectrics [18]. Kamlah implemented a phenomenological model to account for ferroelectric hysteresis [19]. Landis addressed an instability that can occur when using the method of Allik and Hughes with a ferroelectric/ferroelastic material model by introducing a vector potential function for the electric displacement as a nodal degree of freedom [20].

Multiaxial ferroelectric/ferroelastic constitutive laws are required for finite element calculations. These material models fall into two categories: phenomenological and micromechanical. The phenomenological internal state variable based laws are computationally faster but have many adjustable parameters and can be difficult to calibrate. The micromechanical based laws are based on volume averaging a model of the microscale material behavior (the underlying mechanism responsible for non-linearity and hysteresis). A mechanics based phenomenological model was introduced by Chen in 1980 [21]. This model represented the electrical properties using dipoles. The dipole behavior was partitioned into instantaneous and transient responses. Lynch introduced a phenomenological model based on an energy function with polarization and strain as state variables [22]. This model was used to describe uniaxial loading with 180° and 90° switching. A fully multiaxial phenomenological constitutive law was introduced in 1999 by Kamlah and Tsakmakis [23]. Kamlah implemented their 3D model within a finite element code [19]. Landis introduced a 3D phenomenological model by using Helmholtz free energy with switching surfaces and a flow rule [20, 24]. Several other models have been developed using plasticity as a basis for ferroelectric switching. Ferroelectric analogues to kinematic hardening, plastic yielding, and radial return mapping have been modeled [25–28].

Micromechanical models express the macroscale material behavior as a volume average of the microscale behavior. Hwang et al introduced a micromechanical hysteresis model composed of a set of randomly oriented grains [29]. The remnant polarization, remnant strain, and constitutive tensors were determined from the volume average behavior of the grains. Ferroelectric and ferroelastic evolution of the remnant strain and remnant polarization were governed by a work/energy criterion. This early micromechanical model has undergone multiple refinements such as the introduction of single crystal behavior, saturation, and phase transformations [30–32]. The early micromechanical models lacked interaction between grains. Inclusion models were introduced to simulate the interactions between grains [33, 34]. Huber combined micromechanics with plasticity analogues and used an incremental switching model to simulate the evolution of different domain volume fractions within a grain [35, 36]. Kamlah introduced a finite element method with a micromechanical model that used a single grain in an element with a multidomain switching model [37]. More recent micromechanical models have been formulated using constrained domain switching, free charge screening, and coupled finite elements [38, 39].

While phenomenological and micromechanical models with ferroelectric/ferroelastic polarization reorientation have been implemented in finite element methods, few simulations have addressed the effect of IDE on the polarization process and the resulting properties. Bent and Hagood modeled piezofiber composites using representative volume elements with a uniform field approximation [6]. Azzouz et al used enhanced three-noded Mindlin plate elements [40]. The plate elements were sandwiched with piezoelectric and structural layers forming a MFC. Extending Bents approach to MFCs, Deraemaeker et al used representative volume elements to model both d_{33} and d_{31} composites [41].

1.1.3 Applications

The flexibility, low cost, anisotropic actuation, and high strain output of piezocomposite actuators have led to several publications tailored to application of the devices. A large focus has been on aerospace and naval device applications. The applications have ranged from twin tail aeroelastic buffet alleviation [42], helicopter rotorblade harmonic control [43], to torpedo silencing [44].

A helicopter suffers from premature wear and failure in the rotating assemblies due to excessive vibration levels. Blade chord profile variances, component mass differences, and variable aerodynamic loads all contribute to increased vibration and a decrease in performance and stability. Active rotor control using piezoelectric actuators can modify the vibratory loads and partially mitigate these problems. A method to achieve this is with an active twist rotor blade (ATR). The ATR blade uses piezocomposite actuators embedded in the blade structure.

Several simulations and experiments have been performed using ATR blades. Wilkie et al performed an aeroelastic analysis on an ATR blade in one-g hovering flight conditions, and found interdigitated electrode actuators could twist the blade up to 1° [45]. The ATR blade system was tested with active fiber composite (AFC) [46] actuators using a 1/6th scaled CH-47D rotor blade [47]. A model four blade rotor system was designed and significant load reductions were found while only using 1% of the available operating power [43, 48]. Booth and Wilbur showed that not only was vibration reduction of the rotor components possible, rotor noise could be also be reduced [49]. An advanced active twist rotor (AATR) blade was designed that utilized single crystal MFC resulting in lower input voltage and higher blade twist [50].

Piezocomposites and MFC have been use extensively for actuation of aerostructures. Park and Kim analyzed single crystal MFC for use in active twist helicopter rotors [51]. Mudupu used two MFC in a piezoelectric bimorph configuration to control the fin of a projectile [52]. Paradies and Ciresa computationally analyzed and tested surface mounted MFC on a wing with integrated roll control [53]. Bilgen utilized MFC to actively control airfoil camber in flight [54] and roll control in a swept wing aircraft [55].

Piezocomposites with IDE have also been used as sensor/actuator rosettes [56]. Due to the anisotropic properties of IDE piezocomposites, a rosette can be oriented to enable resolving two principle strain components and the corresponding principle directions. This concept enables not only directional sensing, important for structural health monitoring, it also enables directional actuation, important for structural vibration and acoustic control [57–59].

The in-plane anisotropy of ferroelectric with IDE enables their use as directional sensor/actuators. Piezorosettes have been used as lamb wave detectors to locate a wave source. Kawiecki and Jesse first used monolithic piezoelectric plates to sense damage on an aluminum plate [57]. Matt and di Scalea used MFC as piezorosettes [58]. Salamone et al induced high velocity impact and used piezoelectric rosettes for damage detection [59]. Zhao et al [56] used anisotropic single crystals to develop a piezoelectric rosette.

1.2 Contributions

The following describes the contributions of this dissertation in advancing the technology of piezocomposite actuators.

- An expression was developed to relate longitudinal and transverse strains in a substrate to the charge output of a MFC. A strain rosette equation for piezoelectric materials was developed and applied to the MFC charge output model. This allowed for the relation to the charge output of a MFC rosette to strains in a substrate.
- A method was developed to polarize small electrode line width piezocomposites. The

method resulted in the discovery of an actuator with 3657 $\mu\epsilon$ longitudinal free strain output.

- A ferroelectric finite element method was developed using a micromechanical model. The ferroelectric FEA was used to investigate the polarization process of MFC and improve prediction of MFC behavior.

- A study on electrode line width sizes discovered that larger electrode line widths produce less hysteresis and creep than smaller electrode line width devices. It was also discovered that by shrinking electrode line widths, the inherent material property of the MFC can change from that of a “soft” ferroelectric to be like that of a “hard” ferroelectric.

- A free strain frequency response analysis of MFC was performed from 0.1 Hz to 15 Hz. It was discovered that electrically driving a commercially available MFC from 0.1 Hz to 15 Hz degrades the piezoelectric coefficient by over 30%. A custom electrode geometry piezocomposite was developed to mitigate this degradation.

- A finite element phase field model with a Landau-Devonshire multi-well potential material subroutine was created. The model could prove useful for use in predicting domain evolution along an electrode edge to mitigate fatigue and failure.

1.3 Dissertation Overview

The following describes each chapter and serves as a overview of the dissertation.

Chapter 2: The equations for a $0^\circ, 45^\circ, 90^\circ$ rosette were developed using the conditions of coupling between the in-plane strain of the crystal and a substrate, and zero out-of-plane stress on the crystal (plane stress conditions in the crystals). The crystals were bonded to a substrate aluminum plate that was instrumented with strain gages next to the crystals. The plate was subjected to bending about different axes and the resulting electric displacement change of the crystals was monitored. The strain components calculated using the change of electric displacement were compared with the strain components measured using strain gages. This sensor/actuator rosette approach was demonstrated to enable both sensing principal strain components and actuating principal strains in an electronically controllable direction.

Chapter 3: Electrode line widths were found to play a key role in the poling process and time dependent behavior of an interdigitated electrode piezocomposite actuator. When the electrode line widths were smaller than the substrates thickness, the device typically had poor performance due to Gauss's law limiting polarization. It was found that when a high DC voltage was applied to an actuator with small relative electrode line widths, the net polarization increased and the strain output increased over time. In some cases an hour of applied DC voltage was required to saturate the strain in the actuator. Subsequent actuation under normal operating procedures / time scales was able to sustain the improved performance. It was found that the free strain actuation of a small electrode line width actuator increased from 500 $\mu\epsilon$ to 3657 $\mu\epsilon$ using this procedure.

Interdigitated electrodes on piezocomposites produce nonuniform electric fields and stress concentrations in the vicinity of the electrode causing nonlinearities. This complicates defining the electric field. A methodology of using a dielectric finite element analysis was used to find an average electric field at the midplane between two electrodes when comparing actuators. A meshing methodology was also developed to automatically generate meshes with a higher concentration of elements along an electrode edge to account for high electric field gradients.

Chapter 4: A commercial macro fiber composite actuator was explored for use as a shape memory piezoelectric actuator. It was found that it was suitable, but several custom piezocomposite actuators were also explored. As the electrode line widths decreased in the actuator, the material behavior changed from a "soft" ferroelectric to be like a "hard" ferroelectric. This changed the behavior of the actuator when used as a shape memory piezocomposite immensely. For small line widths, the piezocomposite actuator was able to provide power off set and hold capability across a larger range of strains than the commercially available MFC.

A ferroelectric finite element code was developed to improve on linear piezoelectric models used when characterizing piezocomposites with IDE. The ferroelectric model was used to explain polarization switching within the actuator when running a unipolar electric field. The increased domain wall motion due to polarization switching leading to increased hysteresis was explored.

Chapter 5: A commercial MFC was used to test its free strain frequency response from 0.1 to 15 Hz. A methodology to find the piezoelectric coefficients of the MFC as a function of frequency was employed. It was found that the piezoelectric coefficients of the MFC were dependent on frequencies in this range. Increasing the actuation frequency to 15 Hz caused the low field d_{33} coefficient to be 51% of the reported value. A custom made interdigitated electrode actuator was manufactured with larger relative electrode line widths than the commercial MFC. It was found that the custom actuator was able to mitigate the decay of the piezoelectric coefficient. The decay of the piezoelectric coefficients was fit to a exponential decay model.

Chapter 6: Two different ferroelectric ceramic material compositions were synthesized using a mixed oxide method. The compositions synthesized were phase transforming 55/33/12 PLSnZT and quadratic electrostrictive 9.5/65/35 PLZT. The material compositions were packaged in a standard size commercial MFC configuration with the same electrode geometries. The free strain actuation of each of the actuators was explored and compared to a commercial MFC.

Chapter 7: Finite element based phase field modeling was applied using a finite element framework with a Landau-Devonshire type multi-well potential as a material subroutine to model domain evolution in ferroelectrics. In this approach, the domain wall width is controlled by a balance between mechanical, structure, electrostatic, and local gradient contributions to the free energy density. The effect of this energy balance on the resulting domain wall width of 90° and 180° tetragonal domain walls was discussed as an example of its use. The domain evolution phase field model could potentially be used to explore the domain patterns along an electrode edge in an attempt to mitigate electric field concentrations.

CHAPTER 2

Piezocomposite Actuator Applications

2.1 Piezoelectric Strain Rosettes

Strain rosettes are commonly used to measure strain components on a surface when the principal directions are not known. Three longitudinal strain measurements are made in three different directions and the orthogonal transformation equations are used to determine the two principal strain components and their orientation relative to the rosette orientation. Typical strain rosettes have gages at angles of $0\,^{\circ}, 45\,^{\circ}, 90\,^{\circ}$ and at $0\,^{\circ}, 60\,^{\circ}, 120\,^{\circ}$.

Piezoelectric materials are used as both sensors and actuators. If the piezoelectric materials are in the form of thin plates that can be bonded to a surface and the plates have anisotropic properties in-plane, they can be used as a piezoelectric rosette [57–60]. The converse piezoelectric effect can be used to actuate desired principal strain components through application of appropriate voltage signals to the three piezoelectric elements.

There are several ways to achieve in-plane piezoelectric anisotropy. This can be accomplished using interdigitated electrodes to produce an electric field in-plane of a piezoelectric plate to produce d_{33} coupling along the electric field direction, and $d_{31}\backslash d_{32}$ coupling orthogonal to the field. Combining interdigitated electrodes with macro fiber composite technology in which the piezoelectric plate is sliced into rectangular fibers, the strain component transverse to the fibers is decoupled furthering in-plane anisotropy [11, 46, 58–63]. Preliminary work with macro fiber composites has shown that hysteresis inherent in the sensor design leads to large inaccuracies when using these composites for strain sensing, but if this can be tolerated in exchange for their ability to actuate principal strains in electronically controllable directions, they can be used as sensor/actuator rosettes.

Previous work with $[011]_c$ cut and poled PZN-4.5%PT [64,65] and with PMN-xPT [66,67] with x ranging from 28 to 32% has demonstrated that these materials display highly linear material behavior as long as the material is operated in a regime where field driven phase transformations do not take place. It is important to not reverse bias the crystals, because the crystals are easily depolarized with a negative electric field. Although the linear piezoelectric properties are temperature dependent, the thermal changes in properties can be compensated in sensor/actuator applications. The following sections describe the single crystal material and the anisotropic constitutive behavior of the $[011]_c$ cut, the development of the equations for the single crystal strain rosette, and a set of experiments designed to demonstrate the technique and assess its accuracy and precision.

2.1.1 Modeling Scheme

PZN-xPT and PMN-xPT and more recently developed ternary compounds of PIN-PMN-PT single crystals have a perovskite type crystal structure. The compositions of interest undergo a phase transformation from cubic to rhombohedral as they are cooled through the Curie temperature. The rhombohedral, tetragonal, and orthorhombic phases in PZN-PT,PMN-PT and PIN-PMN-PT single crystals can coexist in certain ranges of temperature and composition [68–80].

Prior work has shown that the properties of different crystal cuts of the rhombohedral compositions can be determined using crystal variant models based on volume averaging. The rhombohedral crystal can be polarized toward one of eight corners of the unit cell. A crystal can therefore have different volume fractions of eight possible crystal variants. If plates are cut in a given orientation, the plate can be poled in a way that results in controlled volume fractions of the different variants. For example, the crystal cut and poled in the $[001]_c$ direction shown in figure 2.1a will have roughly equal volume fractions of four variants and a tetragonal symmetry ($4mm$), the crystal cut and poled in the $[011]_c$ direction shown in figure 2.1b will have roughly equal volume fractions of the two crystal variants and an orthorhombic symmetry ($mm2$), and the crystal cut and poled in the $[111]_c$ orientation shown in figure 2.1c will have a single variant present (single domain single crystal) and rhombohedral symmetry ($3m$). Determining the properties of the crystals with different volume fractions of crystal variants is discussed in several articles [81–85].

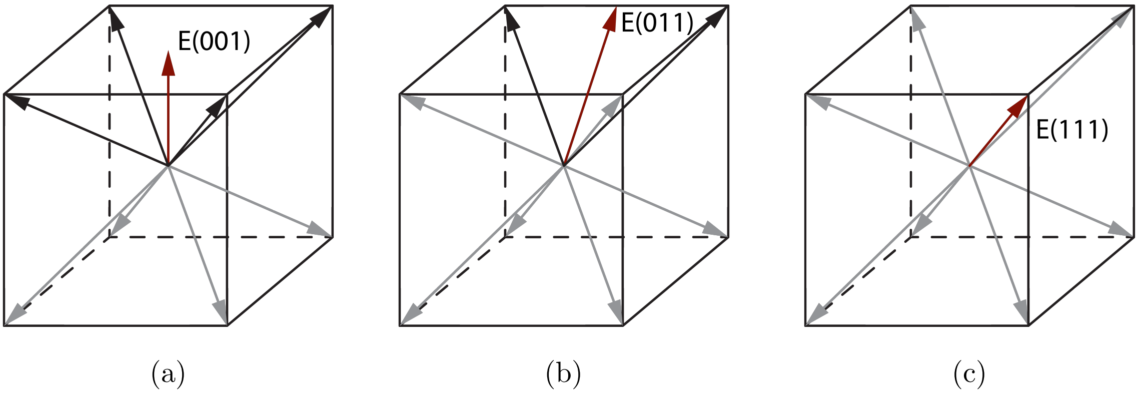

Figure 2.1: Rhombohedral crystal variants. a) Four variants with electric field E in $[001]_c$ direction; b) Two variants with E in $[011]_c$ direction; c) Single variant with E in $[111]_c$ direction.

It has been shown that $[001]_c$ oriented and $[011]_c$ oriented rhombohedral PZN-PT and PMN-PT single crystals have larger piezoelectric coefficients, are highly linear, and have lower loss than $[111]_c$ oriented crystals [81, 86, 87]. The $[001]_c$ cut and poled crystals provide high longitudinal piezoelectric coefficients d_{33}, while $[011]_c$ cut and poled crystals provide high transverse piezoelectric coefficients d_{31} and d_{32} [64, 65, 83, 84].

The $[011]_c$ cut single crystals have orthorhombic symmetry and thus the piezoelectric coefficients d_{31} and d_{32} are not equal. In the local coordinates shown in figure 2.2a, the x_3 direction is parallel to the orientation of remnant polarization. Figure 2.2b shows the orientation on a $[011]_c$ cut and poled single crystal plate.

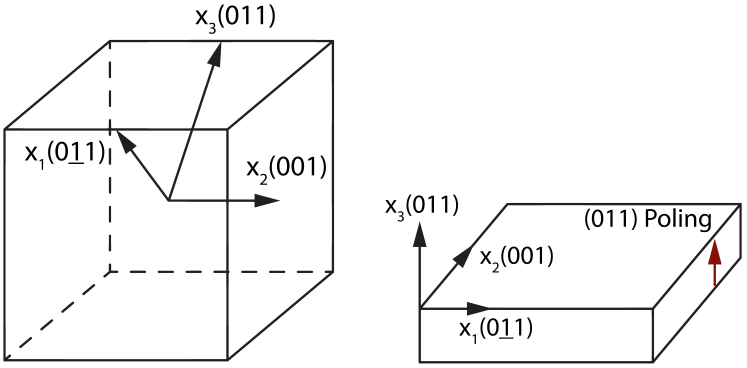

(a) (b)

Figure 2.2: a) Coordinate system used to describe $[011]_c$ cut and poled single crystal. b) A $[011]_c$ and poled crystal plate.

The development for the rosette equations requires the definition of crystal properties in a crystal coordinate system relative to strain components in a rosette coordinate system. Using Voigt notation, the orthorhombic symmetry $[011]_c$ poled crystal cut has five nonzero coefficients of the piezoelectric tensor $e_{31}, e_{32}, e_{33}, e_{15}$ and e_{24} in a local coordinate system aligned with each crystal as shown in figure 2.2b. The coefficients are written in matrix form as equation 2.1.

$$\boldsymbol{e}^{011} = \begin{bmatrix} 0 & 0 & 0 & 0 & e_{15} & 0 \\ 0 & 0 & 0 & e_{24} & 0 & 0 \\ e_{31} & e_{32} & e_{33} & 0 & 0 & 0 \end{bmatrix} \tag{2.1}$$

The single crystal piezoelectric rosette layout is shown in figure 2.3. Three single crystals are assigned rosette angles of $0^\circ, 45^\circ$ and 90°. The piezoelectric properties of each crystal are expressed in local coordinates (x_1^0, x_2^0, x_3^0), $(x_1^{45}, x_2^{45}, x_3^{45})$ and $(x_1^{90}, x_2^{90}, x_3^{90})$. Electric displacement that is produced when each crystal is deformed by straining the substrate material is given by D_3^0, D_3^{45} and D_3^{90}.

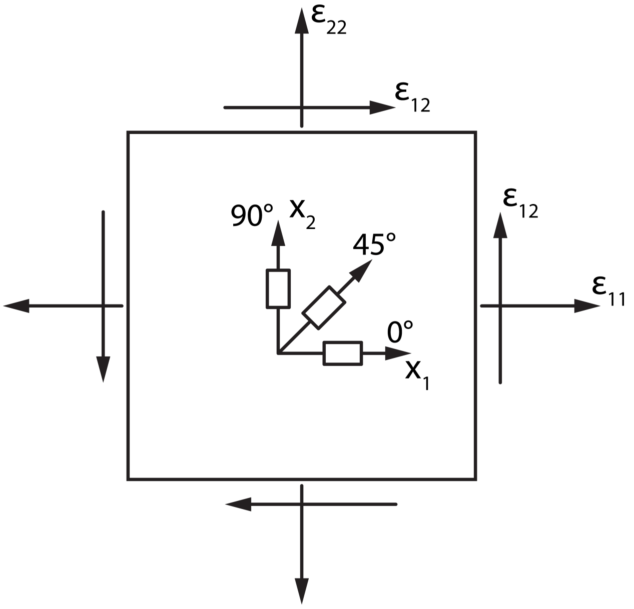

Figure 2.3: Schematic of rosette with piezoelectric elements at $0\,^\circ, 45\,^\circ$ and $90\,^\circ$ angles.

A derivation of the rosette equations is provided in Appendix A using the conditions of continuous in-plane displacement components from the substrate to the crystals and a traction free boundary on the crystal surface giving zero normal stress and shear components ouf of plane.

The resulting piezoelectric rosette equations are given by equation 2.2. The piezoelectric coefficients e_{ijk} from the Appendix A are written in Voigt notation. For example, $e_{311} = e_{31}, e_{322} = e_{32}$ and $e_{333} = e_{33}$

$$\boldsymbol{D} = \boldsymbol{M}\boldsymbol{\varepsilon} + \left(\kappa_{33}^{\varepsilon} + \frac{e_{33}^{2}}{C_{33}^{E}}\right)\boldsymbol{E} \tag{2.2}$$

where,

$$\boldsymbol{D} = \begin{Bmatrix} D_3^0 \\ D_3^{45} \\ D_3^{90} \end{Bmatrix} \qquad \boldsymbol{\varepsilon} = \begin{Bmatrix} \varepsilon_{11} \\ \varepsilon_{12} \\ \varepsilon_{22} \end{Bmatrix} \qquad \boldsymbol{E} = \begin{Bmatrix} E_3^0 \\ E_3^{45} \\ E_3^{90} \end{Bmatrix},$$

and

$$\boldsymbol{M} = \begin{bmatrix} e_{32} - e_{33}\dfrac{C_{32}^{E}}{C_{33}^{E}} & 0 & e_{31} - e_{33}\dfrac{C_{31}^{E}}{C_{33}^{E}} \\ \dfrac{1}{2}\left(e_{31} + e_{32} - \left(\dfrac{C_{32}^{E} + C_{31}^{E}}{C_{33}^{E}}\right) e_{33}\right) & e_{32} - e_{31} - \left(\dfrac{C_{31}^{E} - C_{32}^{E}}{C_{33}^{E}}\right) e_{33} & e_{31} + e_{32} - \left(\dfrac{C_{32}^{E} + C_{31}^{E}}{C_{33}^{E}}\right) e_{33} \\ e_{31} - e_{33}\dfrac{C_{31}^{E}}{C_{33}^{E}} & 0 & e_{32} - e_{33}\dfrac{C_{32}^{E}}{C_{33}^{E}} \end{bmatrix}.$$

This is solved for the strain component of the substrate in equation 2.3

$$\boldsymbol{\varepsilon} = \boldsymbol{M}^{-1}\boldsymbol{D} - \left(\kappa_{33}^{\varepsilon} + \frac{e_{33}^{2}}{C_{33}^{E}}\right)\boldsymbol{M}^{-1}\boldsymbol{E} \tag{2.3}$$

The rosette can be used as a sensor or an actuator. As a sensor, the applied electric field $\boldsymbol{E}$ is zero and the electric displacement change is measured. By measuring the electric displacement of each element $\boldsymbol{D}$, the strains in the substrate are obtained. As an actuator, an electric field is applied to each element of the rosette and principal directions of induced strain can be controlled.

2.1.2 Experimental Results

Several $4\text{mm} \times 6\text{mm} \times 0.2\text{mm}$ plates of $[011]_c$ oriented and poled PMN-0.29PT single crystal plates were provided by Ceracomp. The orientation and dimension of the crystals are shown in figure 2.4a. Figure 2.4b shows the sketch of the experimental setup. Three crystals aligned at $0^\circ, 45^\circ$ and 90° were mounted on an aluminum plate using resin epoxy. A modified Sawyer-Tower circuit shown in figure 2.4 was used to measure the electric displacement from the piezoelectric crystals. By measuring the voltage on the sensing capacitor, the electric displacement D of each piezoelectric element was obtained using the equation $D = CV/A$. Where C is the sensing capacitor's capacitance, V is the voltage on the capacitor, A is the area of the piezoelectric element's electrode. Three strain gages were mounted near the crystal plates aligned at $0^\circ, 45^\circ$ and 90°. While bending the plate along the direction of angle θ, three independent electric displacement measurements were obtained. The output of the strain gages connected to a Wheatstone bridge circuits were recorded.

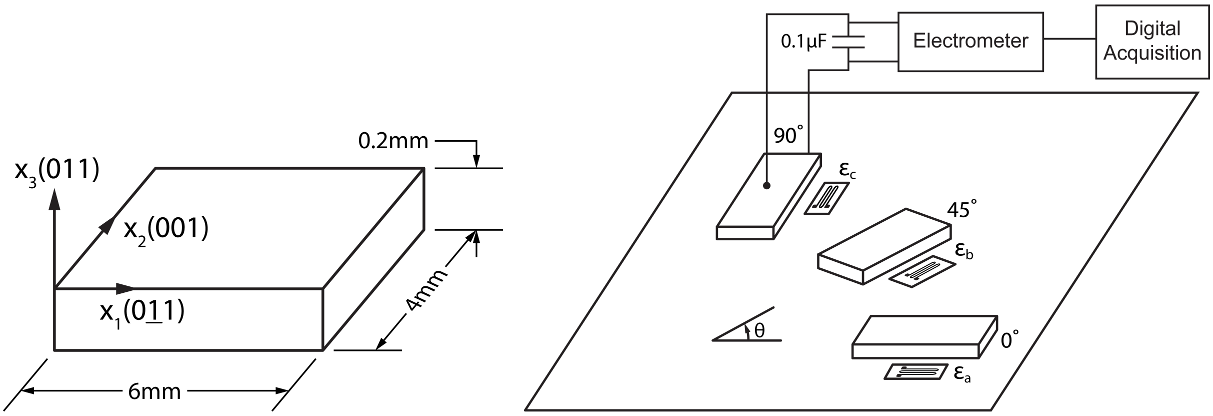

(a) (b)

Figure 2.4: Rosette experimental setup. a) Dimension and orientation of $[011]_c$ oriented and poled PMN-0.29PT single crystal, b) Sketch of the experimental setup

The three obtained strains from the strain gages with $0^\circ, 45^\circ$, and 90° orientations are defined as ε_a, ε_b and ε_c as shown in figure 2.4b. The strain transformation equations are given by,

$$\begin{Bmatrix} \varepsilon_a \\ \varepsilon_b \\ \varepsilon_c \end{Bmatrix} = \boldsymbol{T} \begin{Bmatrix} \varepsilon_{11} \\ 2\varepsilon_{12} \\ \varepsilon_{22} \end{Bmatrix}, \tag{2.4}$$

where,

$$\boldsymbol{T} = \begin{bmatrix} \sin^2\theta & \sin\theta\cos\theta & \cos^2\theta \\ \sin^2\left(\theta+\frac{\pi}{4}\right) & \sin\left(\theta+\frac{\pi}{4}\right)\cos\left(\theta+\frac{\pi}{4}\right) & \cos^2\left(\theta+\frac{\pi}{4}\right) \\ \sin^2\left(\theta+\frac{\pi}{2}\right) & \sin\left(\theta+\frac{\pi}{2}\right)\cos\left(\theta+\frac{\pi}{2}\right) & \cos^2\left(\theta+\frac{\pi}{2}\right) \end{bmatrix}.$$

Taking the inverse, the principal strains in the substrate can be found as,

$$\begin{Bmatrix} \varepsilon_{11} \\ 2\varepsilon_{12} \\ \varepsilon_{22} \end{Bmatrix} = \boldsymbol{T}^{-1} \begin{Bmatrix} \varepsilon_{a} \\ \varepsilon_{b} \\ \varepsilon_{c} \end{Bmatrix}. \tag{2.5}$$

Liu and Lynch [64, 65] conducted experiments to obtain elastic, dielectric and piezoelectric coefficients of PZN-4.5%PT single crystals. Zhang [88] carried out the measurements on $[011]_c$ cut PMN-0.29PT single crystals. Wang [89] measured a complete set of elastic, dielectric, and piezoelectric constants of $[011]_c$ cut PMN-0.29PT single crystals. The data for the PMN-0.29PT crystals are shown in table 2.1.

Constants	$[011]_c$ cut PMN-0.29PT
Piezoelectric constants	$e_{31} = 14.66\mathrm{C/m^2}$
	$e_{32} = -9.53\mathrm{C/m^2}$
	$e_{33} = 5.70\mathrm{C/m^2}$
Elastic constants	$C_{31} = 13.03 \times 10^{1}0\mathrm{N/m^2}$
	$C_{32} = 11.30 \times 10^{1}0\mathrm{N/m^2}$
	$C_{31} = 13.90 \times 10^{1}0\mathrm{N/m^2}$

Table 2.1: Properties of PMN-0.29PT

The parameters in table 2.1 were used with equation 2.3. As a strain sensor, the electric field E is near zero in the piezoelectric elements, thus equation 2.3 can be simplified to,

$$\boldsymbol{\varepsilon} = \boldsymbol{M}^{-1}\boldsymbol{D}.$$

With this simplified expression, the in-plane strain components ε_{11}, ε_{22} and ε_{12} are calculated.

2.1.3 Results, Comparison, and Discussion

An aluminum plate was first bent about an angle $\theta = 0^\circ$ as shown in figure 2.4b. The strain component ε_a obtained from the strain gage at 0° was close to zero and the strain component ε_b at 45 ° was about half of the value of the strain component ε_c at 90 °. In this case, the principal strain components align with the strain gages. Figure 2.5 shows the comparison of the piezoelectric rosette with the strain gage rosette. The plot represents a slight nonlinearity at very low strains, possibly due to the circuit at low signal levels. A linear trend line was fit using linear least squares. The trend line has a slope of 1.0935, for perfect agreement the slope should be unity. The error was calculated using the relative error's average deviation from the mean,

$$\frac{1}{N}\sum_{j=1}^{N}\left|\frac{\varepsilon_j^{\text{PMN-PT}}-\varepsilon_j^{\text{Gage}}}{\varepsilon_j^{\text{Gage}}}\right|, \tag{2.6}$$

where N is the number of data points collected, $\varepsilon_j^{\text{PMN-PT}}$ is the jth strain data point for the PMN-PT elements, and $\varepsilon_j^{\text{Gage}}$ is the jth strain data point for the strain gages. The average relative error was found to be 6.21%.

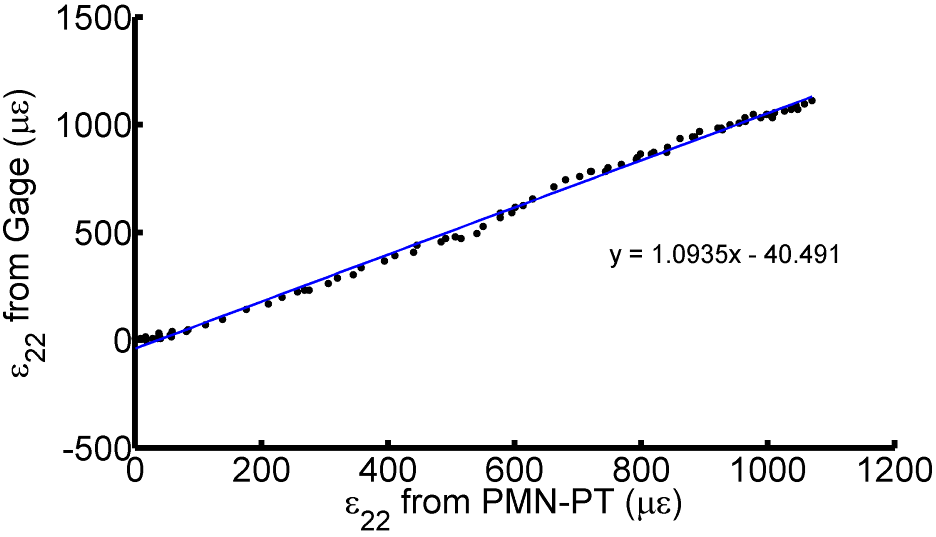

Figure 2.5: Comparison of Strain Gage / Piezoelectric Rosettes at $\theta = 0\,°$ Bending.

For a second case, an aluminum plate was bent about an angle $\theta = 90\,°$. The results are similar to those of the case for $\theta = 0\,°$. The strain component ε_c at 90 ° was almost zero and the strain component ε_b at 45 ° was about half of the value of strain ε_a at 0 °. Figure 2.6 shows the comparison of the two measurements of strain ε_{11}. A linear trend line was fit, and the slope was found to be 1.0075. The calculated average relative error is 14.74%.

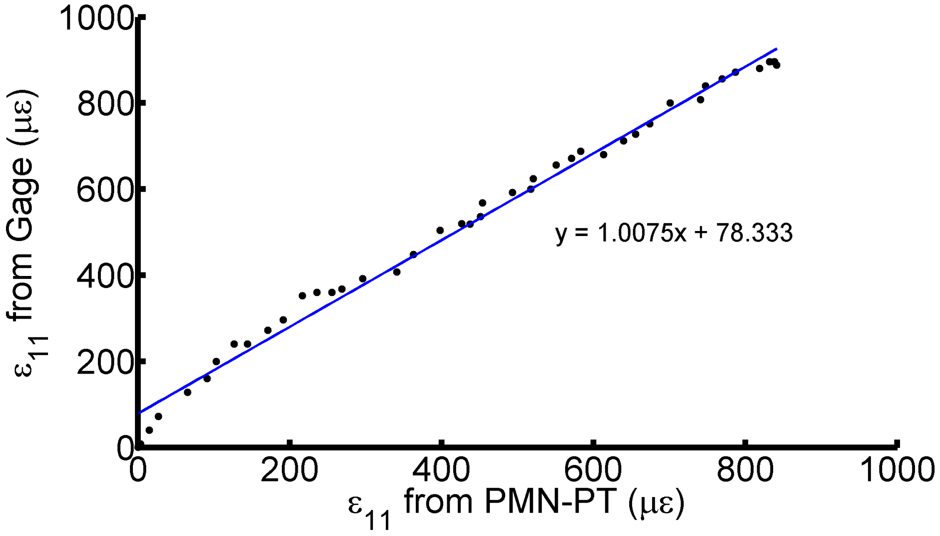

Figure 2.6: Comparison of Strain Gage / Piezoelectric Rosettes at $\theta = 90°$ Bending.

A third bending case involved off axis bending about an angle $\theta = 30°$. The in-plane strains ε_{11}, ε_{22} and ε_{12} were obtained using equations 2.3 and 2.5. Figure 2.7 shows the comparison between the strain gage and the PMN-PT strain measurements. Figure 2.7a and b present normal strain ε_{11} and ε_{22} measurements. The plots are fitted with linear trend lines and their slopes are 0.9791 and 1.0213 respectively. The mean relative error from the PMN-0.29PT single crystals are 14.86% and 6.92% respectively. Also calculated was the average relative error for the shear strain component ε_{12}. For that case, the trend line had a slope of 1.0515 and the average relative error was 9.32%.

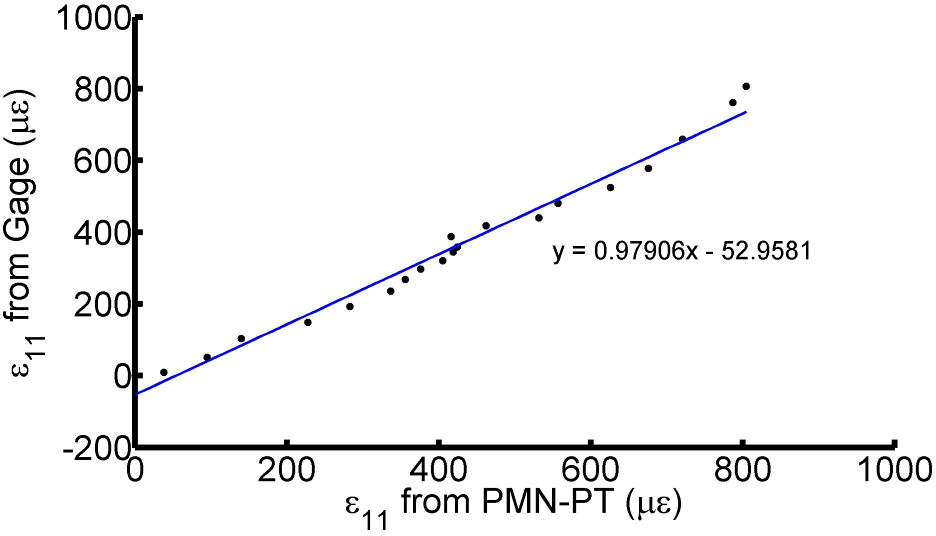

(a)

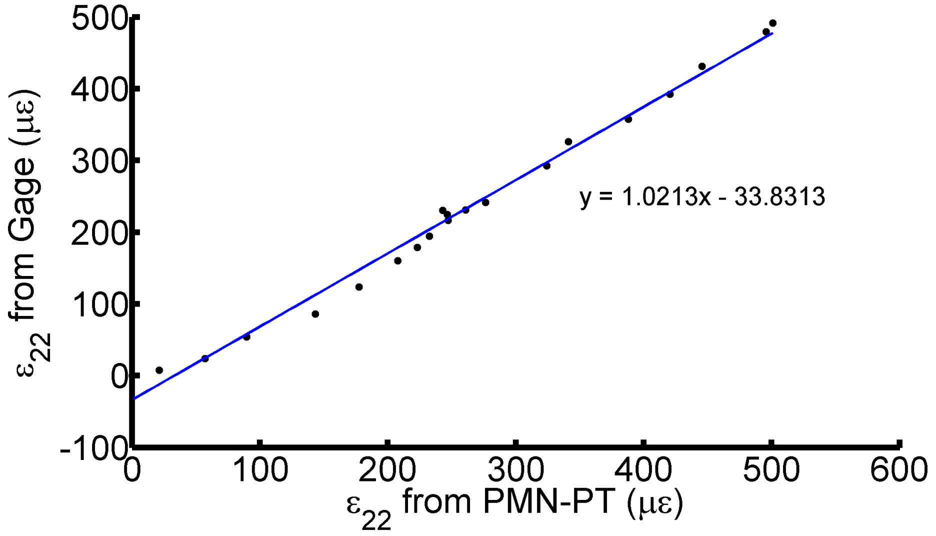

(b)

Figure 2.7: Comparison of strain gage / piezoelectric rosettes for off axis bending. a) Strain component ε_{11} comparison. b) Strain component ε_{22} comparison.

In the three cases, the results from $[011]_c$ oriented PMN-0.29PT single crystals match the results from strain gages aligned at 0 °, 45 °, and 90 ° angles. The worst case scenario showed average relative errors of 14.74%, but in the best case an average relative error of 6.21% was obtained. While the relative errors are large, more can be done to calibrate the PMN-PT rosettes. The absolute error between the strain gages and the PMN-PT rosette was fairly uniform. This caused very large errors when the strain was small, but when strains were large the relative error drops off. By measuring the three independent electric displacements from the piezoelectric rosettes, the in-plane strains were able to be found.

2.2 Macro Fiber Composites as Sensors/Actuators

The use of piezoelectric strain rosettes was explored for single crystal piezoceramics in section 2.1. The in-plane strain components were obtained by utilizing the anisotropic properties of the crystal and the direct piezoelectric effect. IDE piezocomposite actuators have the same anisotropic properties of the single crystal PMN-PT tested. In this section, the use of the MFC in a piezoelectric strain rosette is explored.

2.2.1 Introduction

This work develops the technology that enables exploiting the properties of piezoelectric materials to develop compact and inherently directional dynamic sensing and actuation devices. Such devices will provide the means to determine the principle components of vibration induced strain on a structure, as well as to actuate with essentially arbitrarily controllable components of strain. Simultaneous sensing of orthogonal strain components as well as controlled actuation of these components provides information not only as to magnitude, but also propagation direction for structural vibrations. Kawiecki [57] first demonstrated a piezoelectric rosette using PZT bars mounted on a plate. Matt et al [58] recently demonstrated that this approach is suitable for sensing Lamb waves and the ability to use this information for acoustic source location. The conceptual device is termed a piezoelectric rosette, in analogy with the more traditional strain gage rosette. The motivation for this line of investigation includes applications in structural health monitoring and active noise and vibration control.

The use of piezoelectric materials for structural health monitoring and active vibration control is reasonably well developed, yet continues to receive research attention due to the importance of monitoring our aging infrastructure and controlling noise and vibration. In these applications, the piezoelectric element is often a ceramic plate poled through the thickness. This results in transverse isotropic symmetry about the poling axis with $d_{31} = d_{32}$. In this mode, when laminated to a structure subjected to bending, the Poisson's ratio effect can cause much of the signal to be canceled since the portion of the signal produced by the negative transverse strain cancels part of the positive signal generated by the longitudinal strain. This can be improved upon by manipulating the piezoelectric symmetry in the sensor. Several techniques are available to do this.

Interdigitated electrode configurations [4] have been used to produce a poling axis along the plate as shown in figure 2.8. This rotates the symmetry axis of the piezoelectric tensor to an in-plane orientation, enabling use of the larger d_{33} coefficient. It also greatly enhances the coupling for bending applications when only a single bending mode and direction are present, because d_{33} couples to the stretching and d_{31} to the Poisson's ratio lateral contraction. If the plate is rotated 90 degrees relative to the bending axis, the sensitivity is greatly reduced since now d_{33} couples to the Poisson's ratio induced strain. Also, the smaller d_{32} coefficient with opposite sign couples to the longitudinal strain, canceling most of the signal. This is an example of the ability to design the material symmetry to enable sensing of different strain components.

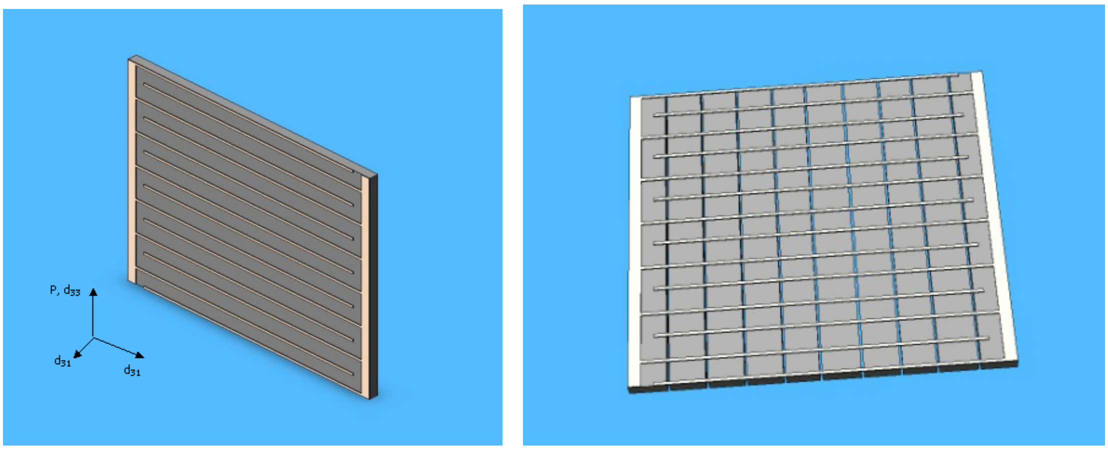

(a) (b)

Figure 2.8: A poled piezoelectric ceramic displays transverse isotropic symmetry about the poling axis x_3. (a) With interdigitated electrodes the symmetry axis lies in-plane, and (b) a fiber composite with a compliant fill material decouples the strain component perpendicular to the fibers and breaks the effective transverse isotropic symmetry of the sensor/actuator.

The development of sensor/actuator piezoelectric rosettes requires the design of piezoelectric elements with anisotropic in-plane piezoelectric coefficients. This can be accomplished through a combination of controlling the polarization direction, through selection of crystal cut (e.g. [001] vs. [011]PMN-28PT single crystals) [64,83,84,90], through uniaxial stretching of PVDF films, and mechanically through design of composite microstructures [91–96].

2.2.2 Approach

The goal of this work is to characterize the longitudinal and transverse strain sensitivity of the MFCs and to determine the degree of shear strain sensitivity.

Equation 2.7 gives the isothermal strain-polarization form of the linear piezoelectric constitutive laws,

$$\begin{aligned} \varepsilon_{ij} &= s^E_{ijkl}\sigma_{kl} + d_{mij}E_m \\ D_m &= d_{mkl}\sigma_{kl} + \kappa^{\sigma}_{mn}E_n, \end{aligned} \tag{2.7}$$

where the components of the various vectors and tensors are ε_{ij}-strain, s^E_{ijkl}-compliance at constant electric field, σ_{kl}-stress, d_{mkl}-piezoelectric, E_m-electric field, D_m-electric displacement, and κ^{σ}_{mn} dielectric permittivity at constant stress. When a coordinate system is aligned with symmetry axes of the piezoelectric tensor, relations between various components can be determined and other components can be shown to be zero. MFC are typically described in terms of effective coefficients. Matt et al [58] solved equations 2.7 to obtain expressions that relate charge to voltage and strain. This is a reasonable first approximation, but one has to make the assumption that the fiber is in a state of either plane stress or uniaxial stress and that it is uniformly poled. In this work the plane stress assumption is made, but no assumption is made regarding the coupling between the fiber and the plate in the transverse direction. Rather, an expression is developed for the charge in terms of the normal stress(which is zero), the longitudinal strain of the substrate, the transverse strain of the substrate, and the voltage.

The necessary equation is arrived at as follows. The internal energy density U is a function of strain, electric displacement, and entropy; from which a set of piezoelectric constitutive equations can be developed with these quantities as independent variables. If constitutive laws are needed with temperature as an independent variable, one subtracts the terms Ts from U. This Legendre transformation leads to a new energy function and a new constitutive law. To interchange stress and strain as the independent variables, one subtracts $\sigma_{ij}\varepsilon_{ij}$. To obtain an equation for the composite MFC at constant temperature we introduce a partial Legendre transformation and subtract only $\sigma_{33}\varepsilon_{33}$, i.e. $U - Ts - \sigma_{33}\varepsilon_{33}$. This leads to a constitutive law in terms of the two in-plane strains and the out of plane stress (which is zero since there is no traction on the out of plane free surface). This results in a constitutive law of the form given in equation 2.8,

$$Q = C_{311}\varepsilon_{11} + C_{3333}\varepsilon_{33} + k_{33}V, \tag{2.8}$$

where C_{111}, C_{333}, and k_{33} are effective coefficients for the composite. Note that the area and the spacing between electrodes are folded into the coefficients. This makes the coefficients dependent on the specific geometry (electrode area, spacing between interdigitated electrodes, fiber thickness, fiber width, spacing between fibers, and polymer packaging thickness).

A 200 nF capacitor was placed in parallel with the approximately 1nF MFC to make the voltage contribution to the charge negligible in equation 2.8. The strain components used in equation 2.8 are the average strain of the substrate transverse and parallel to the MFC fibers, not the strain in the fibers themselves. Determining the strain in the fibers is a complex mechanics problem that involves shear lag in the transverse direction and at the PZT fiber ends.

Figure 2.9 shows the configuration used for characterizing the MFC. The MFC was bonded to a circular 6061 aluminum plate using Loctite E120 HP Epoxy. The center of the active area was aligned with the center of the circular plate. The disc was vacuum bagged while the epoxy cured. Three strain gages were placed parallel to the MFC's longitudinal axis (fiber direction). Vishay Micro-Measurements 062LT series tee-rosettes were used to measure the strain along the MFC's longitudinal and transverse axes. Strain gages were connected to Wheatstone bridge based Vishay 2120A signal conditioning modules. Dimensions are given in table 2.2.

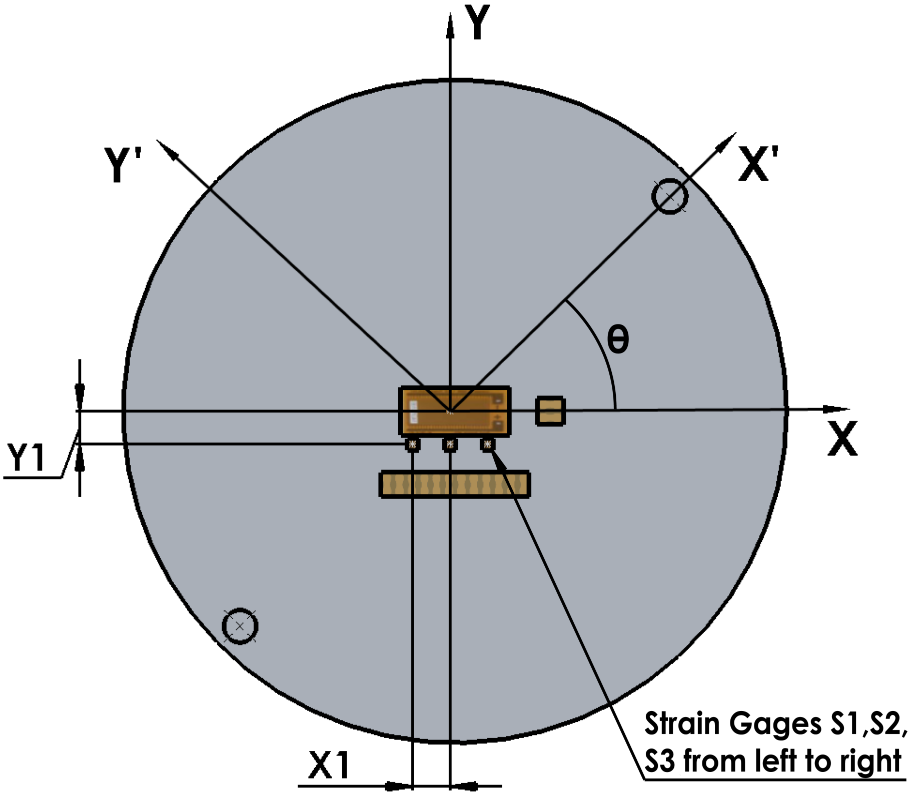

Figure 2.9: Schematic of MFC and strain gage arrangement on the aluminum plate

Voltage output from the MFC was measured across the 200nF capacitor using a Keithley 6512 electrometer. The input impedance of the electrometer is approximately 10^{14} ohms. This effectively enables the reading of charge without draining it. The electrometer and strain gage amplifier were connected to a National Instruments 2110 ADC module. All the data were recorded using LabVIEW Signal Express.

Application	Dimension	Value
Aluminum Plate	Y1	15 mm
	X1	17 mm
Test Setup	D1	280 mm
	D2	305 mm
	D3	200 mm
	D4	30 mm
	t	1 mm
MFC*	d_{33}	460 pC/N
	Y3	30.34 GPa
	Y1	15.86 GPa

Table 2.2: Dimensions and Published MFC Properties

The disc was loaded in four point bending using the arrangement shown in figure 2.10. The coordinate system that indicates the disc's orientation is noted in figure 2.9. Axis X corresponds to the longitudinal axis of the MFC and Y its transverse axis, X' and Y' correspond to the loading orientation. The disc was centered on the inner span. Force was applied to the outer span points labeled D_1. The disc was rotated in 15 degree increments and the loading repeated.

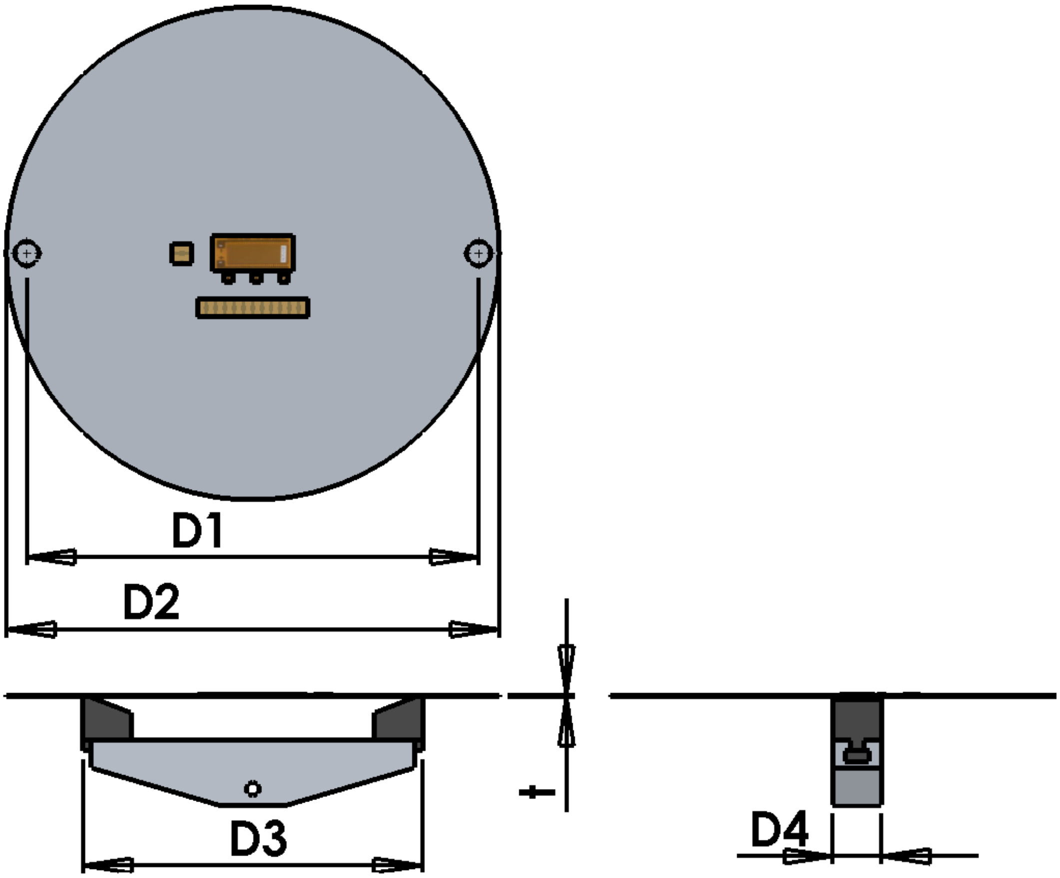

Figure 2.10: Schematic of experimental arrangement used to bend the plate.

2.2.3 Results

In each case gages 1 and 3 (outer gages) gave the same response and gage 2 (center gage) was different. This is due to the inhomogeneity of the plate bending. The curvature increased from the center of the plate to the inner spans of the loading apparatus. Output from gages 1 and 2 are presented in the following figures and used in the discussion.

Figure 2.11 shows the results of the longitudinal and transverse strain measurements vs. time with loading at 0 degrees through 90 degrees. At 0 degrees, the circular plate arrangement initially follows a beam theory type bending wherein the transverse strain differs from the longitudinal strain by Poisson's ratio. As the loading increases, the plate undergoes a transition from a potato chip shape to a bell shape. This appears as an inversion of the transverse strain from negative to positive values. The effect reverses upon unloading.

The longitudinal and transverse strain are the same for gage 1 (outer) when the loading is at 45 degrees, but the stiffening effect of the PZT fibers is apparent on gage 2 (center). The potato chip effect is not symmetric. It is affected by the reinforcing behavior of the MFC on the Al plate in the fiber direction as is apparent when 0 and 90 degree loading are compared. The difference between S1T and S2T at 90 degrees was sufficiently large that the system was set back up, additional calibrations were run, and the tests repeated multiple times with the same results. The strain gages were also checked under a microscope for any signs of delamination. This difference does not appear to be an experimental error or a bad strain gage. It appears to be the result of the reinforcing effect of the MFC.

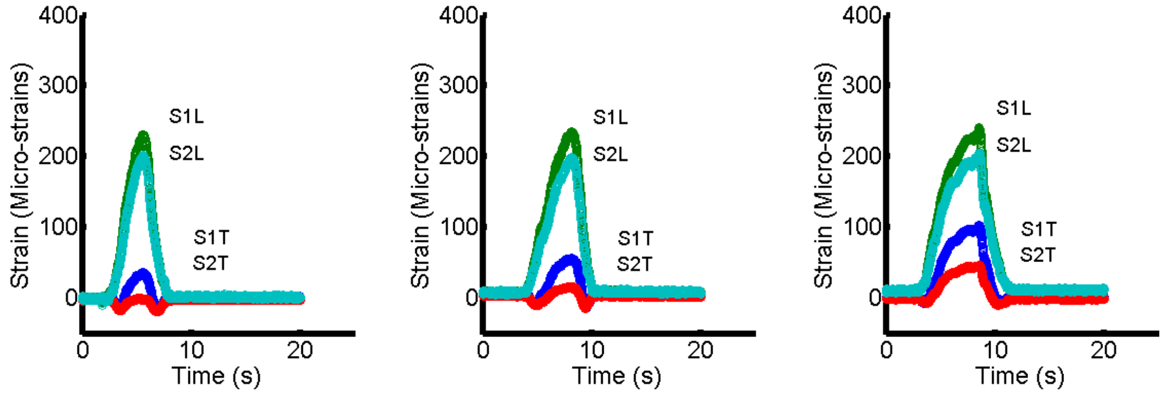

(a) 0° (b) 15° (c) 30°

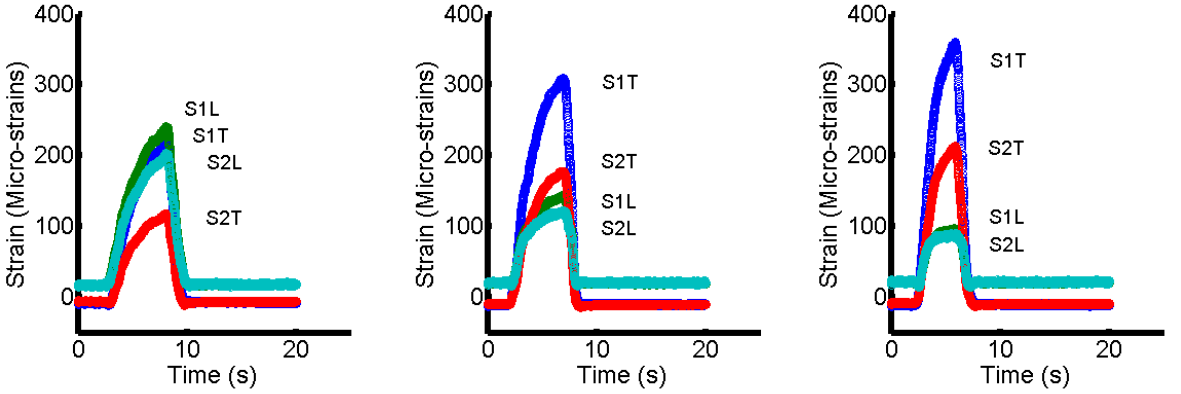

(d) 45° (e) 60° (f) 90°

Figure 2.11: Longitudinal and transverse strain vs. time with the loading at 0 through 90 degrees relative to the fiber direction.

The asymmetry of the plate bending induced by the addition of the PZT fibers is also apparent when the transverse strain is plotted as a function of longitudinal strain in figure 2.12. Differences between the gages at the edge (S1) and at the center (S2) of the MFC are readily apparent. The applied force was not the same for each loading, so no additional information can be obtained from the maximum strain values.

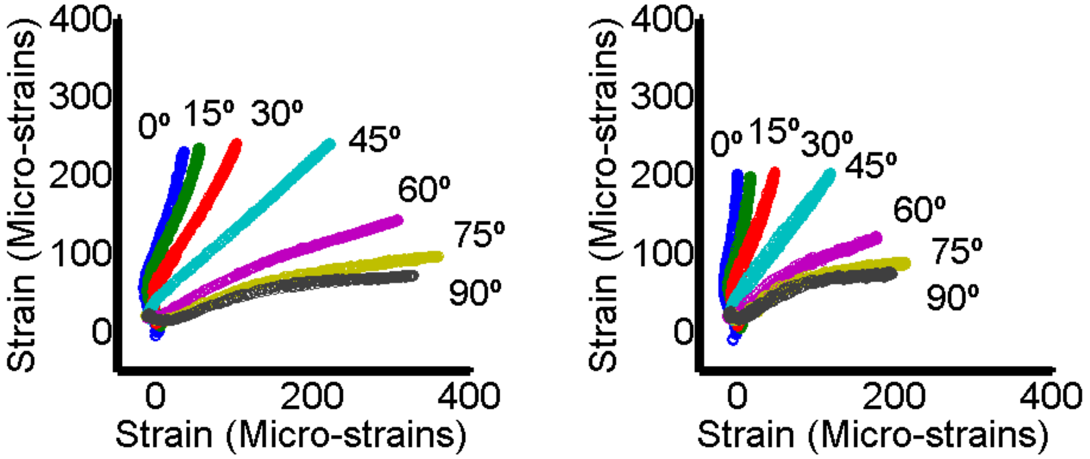

(a) (b)

Figure 2.12: Longitudinal vs. Transverse Strain for Gages 1 (Outer) and 2 (Center)

Figure 2.13 shows the charge produced on the MFC as a function of strain. Significant hysteresis is evident when the longitudinal strain exceeds 150 $\mu\varepsilon$.

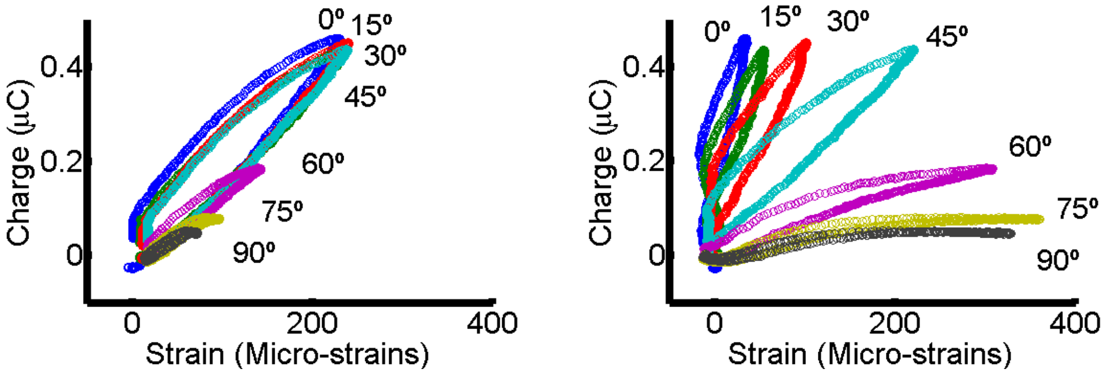

(a) S1 Longitudinal (b) S1 Transverse

Figure 2.13: Charge output versus (a) longitudinal strain and (b) transverse strain

2.2.4 Analysis

In the linear regime, the strain sensitivity of the MFC is governed by equation 2.8. The approach taken is to identify the coefficients through the entire range using a least squares fit to obtain an average response. Note that a very different response would be obtained if only the measurements below 150 $\mu\varepsilon$ were used. Equation 2.9 relates the charge output of the MFC at each angle to the measured strain at that angle.

$$\begin{bmatrix} \varepsilon_{11}^{0} & \varepsilon_{33}^{0} \\ \varepsilon_{11}^{15} & \varepsilon_{33}^{15} \\ \varepsilon_{11}^{30} & \varepsilon_{33}^{30} \\ \varepsilon_{11}^{45} & \varepsilon_{33}^{45} \\ \varepsilon_{11}^{60} & \varepsilon_{33}^{60} \\ \varepsilon_{11}^{75} & \varepsilon_{33}^{75} \\ \varepsilon_{11}^{90} & \varepsilon_{33}^{90} \end{bmatrix} \begin{Bmatrix} C_{311}^{\text{eff}} \\ C_{333}^{\text{eff}} \end{Bmatrix} = \begin{Bmatrix} Q_3^{0} \\ Q_3^{15} \\ Q_3^{30} \\ Q_3^{45} \\ Q_3^{60} \\ Q_3^{75} \\ Q_3^{90} \end{Bmatrix} \tag{2.9}$$

To find the strain sensitivity factors, a least squares solution method was employed. The least square method was setup as follows; A unique solution $C_n \in \mathbb{R}$ which minimizes $\|\boldsymbol{\varepsilon C} - \boldsymbol{Q}\|$ is found by equation 2.10,

$$\boldsymbol{C} = \left(\boldsymbol{\varepsilon}^T \boldsymbol{\varepsilon}\right)^{-1} \boldsymbol{\varepsilon}^T \boldsymbol{Q}, \tag{2.10}$$

where each of the strain and charge measurements include the full 2000 digitally collected data points associated with the measurements.

The resulting effective strain sensitivities were determined to be,

$$C_{311}^{\text{eff}} = -0.00049$$
$$C_{333}^{\text{eff}} = 0.00265,$$

each in microcoulombs per microstrain.

These effective coefficients were then used to predict the charge output based on the experimental strain. The results are shown in figure 2.14, a comparison plot of the experimental charge and predicted charge output. Each spike corresponds to an experiment at a different angle. The first spike corresponds to 0 degrees and the last 90 degrees. The time doesn't correspond to the whole experiment, but can be used to find the relative time for each individual experiment at different angles.

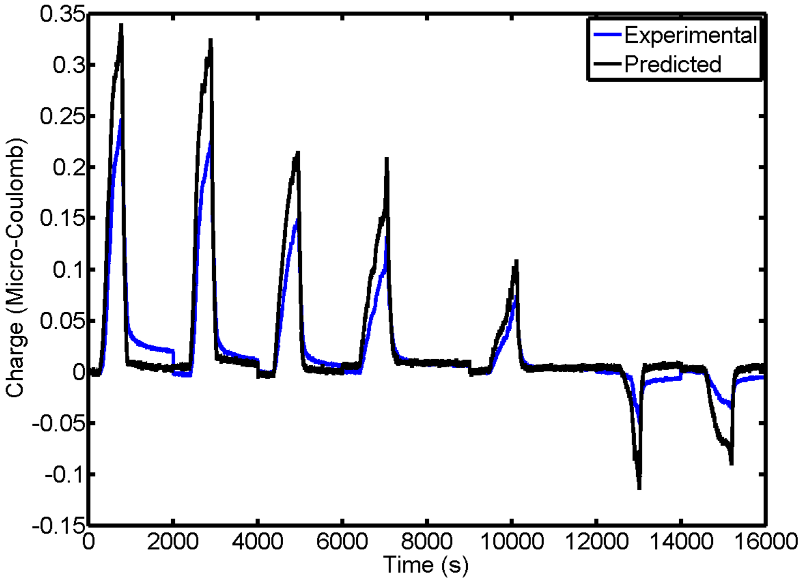

(a) Experiment

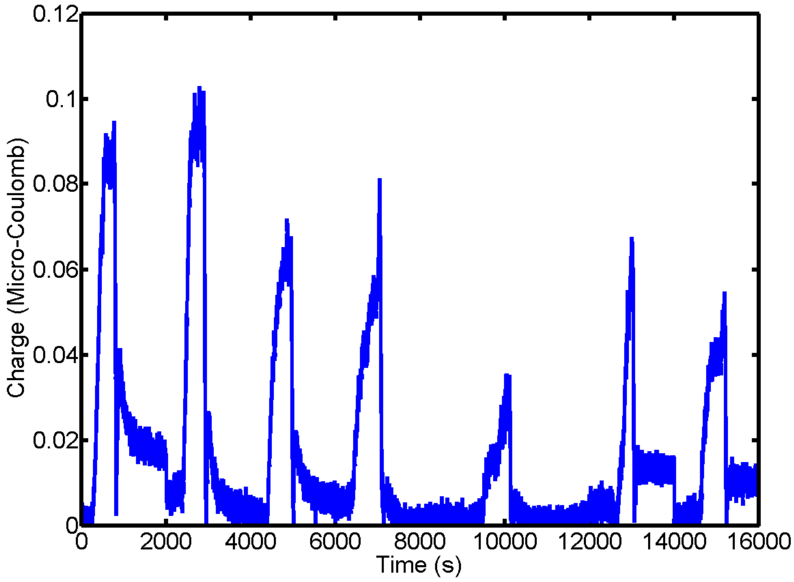

(b) Predicted

Figure 2.14: Measured MFC charge output (a) charge comparison and (b) absolute charge error

Hysteresis is definitely a problem if this type of sensor is to be used as a strain sensor. Referring back to figure 2.14, the hysteresis when loaded to 200 $\mu\varepsilon$ is considerably larger than would be expected from a uniformly poled PZT specimen. The MFC specimen also had some charge creep after the loading was finished which affected the predictions. Further analysis in chapter 4 gives insight into the source of this hysteresis and charge creep.

The results of this preliminary study have given insight into some of the parameters that will be important to producing a MFC rosette. This includes the effect of the MFC locally adding stiffness to a plate or shell, the contribution of transverse strain to the MFC output, the various geometric factors that contribute to the MFC output, and the significantly larger amount of hysteresis produced in the MFC arrangement relative to a homogeneously loaded parallel plate PZT specimen. The increased hysteresis is a significant trade off for the increased strain that can be achieved using the interdigitated electrode arrangement to place the polarization direction in-plane.

In their current configuration, MFCs have been optimized for the production of strain and force when a voltage is applied. It appears that some improvement can be made for sensor applications. Work in chapters 4 and 5 include manufacturing MFC so that predictions of optimized patterns can be tested, thus improving the devices.

CHAPTER 3

Polarization of Piezoceramics with IDE

The motivation of this chapter was the development of a self-latching shape memory piezocomposite actuator [97]. By improving actuator performance, the self-latching piezocomposite can be used to create more efficient morphing aerodynamic control surfaces with power-off set-and-hold capabilities. Piezocomposite actuators can be implemented into homogeneous composite control and trim tab surfaces along with variable camber airfoils [98]. Supplementing the controllable surfaces with the self-latching actuator, deflections can be adjusted in-flight and maintained without constant applied electrical power.

While there have been many analytical and computational studies of MFC, few have addressed the effects of time dependent creep behavior inherent in the device. Schröck et al analyzed the control of a flexible beam using MFC patches accounting for hysteresis and creep [99,100]. To exemplify the need for models to account for time dependent behavior in MFC, a set of plates with 20 different IDE geometries was fabricated, poled and characterized. The results led to the discovery that, as anticipated from Gausss law, specimens with very thin electrode line widths relative to plate thickness did not produce good electric displacement vs. electric field or strain vs. electric field hysteresis loops. It also led to the unexpected result that this issue with the poling process could be overcome by taking advantage of the time dependence of the material behavior. The following work addresses the effect of reducing the electrode line width of IDE on the performance of piezoelectric plates.

3.1 Experimental Arrangement

3.1.1 Materials and Specimen Preparation

The actuator material was PZT-5A plate. The desired electrode pattern was etched from copper clad polyimide film. Unlike traditional MFCs where the piezoelectric material is diced into fibers, the IDE experiments performed in this work were on monolithic plate. The dimensions of the actuators were 85 mm × 25 mm × 0.6 mm. The laminated actuators were produced by Smart Material Corp.

The dimensions and coordinate directions used to describe the electrode geometric parameters are shown in figure 3.1. The three different geometric parameters considered were electrode spacing L, electrode line width L_2, and plate height H. Table 3.1 lists the geometric parameters used. While 20 custom actuators were fabricated and tested, only three distinct custom actuators will be discussed in this chapter. The full set of 20 custom actuators will be discussed in chapter 4. The first two actuators investigated were used to compare the effect of the DC bias field on actuator performance. They were designed such that the relative electrode line width L_2/H would vary while the relative electrode gap $(L - L_2)/H$ would remain constant. Figure 3.2 shows an optical micrograph of the electrode pattern of these two actuators. The third actuator examined was found to have superior free strain actuation performance of over 3500 $\mu\epsilon$. This actuator was compared against a commercially available macro fiber composite actuator, model M8528-P1.

The actuators were instrumented with longitudinal (x_3) and transverse (x_1) oriented strain gages (tee rosettes). The longitudinal gages were chosen such that they spanned six electrode spacings. Two gages were mounted on the top and two on the bottom of the actuator to monitor the bending and extension of the specimen. The strain gages were powered by a Wheatstone bridge strain gage amplifier and recorded using a digital acquisition system. The actuators were electrically driven with a 10 kV amplifier. Both applied voltage and strain were recorded.

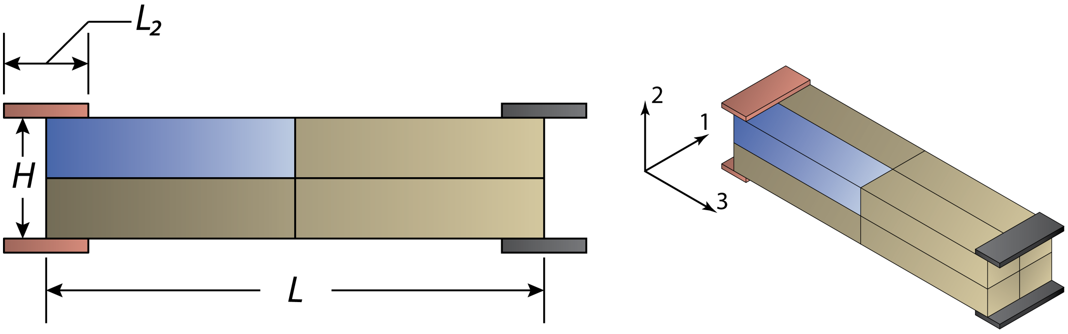

Figure 3.1: Layout of an interdigitated electrode on a ferroelectric substrate

Table 3.1: Actuator Geometry Values for Polarization Study

Actuator	L_2(mm)	L(mm)	H(mm)	L_2/H	$(L - L_2)/H$
1	0.48	1.06	0.60	0.80	0.96
2	0.12	0.68	0.60	0.20	0.93
3	0.11	1.29	0.60	0.18	1.97
MFC	0.09	0.45	0.23	0.40	1.60

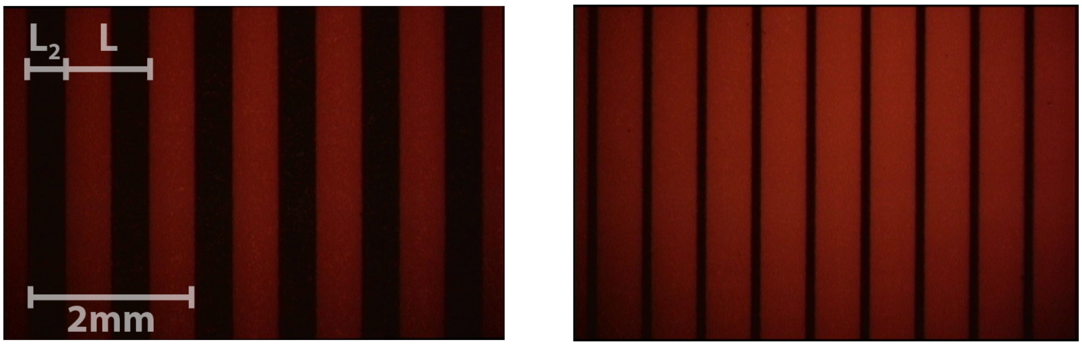

(a)

(b)

Figure 3.2: Micrograph image of electrode geometries (a) Actuator 1 ($L_2/H = 0.8$) and (b) Actuator 2 ($L_2/H = 0.2$). Darker areas indicate electrode lines, while lighter areas indicate areas only covered by polyimide film.

3.1.2 Experimental Procedure

Actuators 1 and 2 each started in an unpoled state. A unipolar sinusoidal nominal electric field of 5 MV/m at 0.1 Hz was applied to each specimen. The nominal electric field

$E^{\mathrm{Nom}} \equiv V/\left(L - L_2\right)$ is defined as the applied voltage V divided by the gap distance between electrodes $L - L_2$.

After the initial polarization cycle, a DC voltage was held on both actuators. The DC voltage was chosen such that a nominal electric field of 5 MV/m was achieved. The strain of each actuator was observed to creep. The voltage was held until the creep process stopped. A DC voltage of reverse polarity was held on both actuators until the strain again saturated. The actuators were again subjected to a unipolar sinusoidal nominal electric field of 5 MV/m at 0.1 Hz and the strain responses were compared.

A dielectric study was run on each actuator geometry to determine the average electric field at the midsection of the fiber/plate between two adjacent electrodes. This electric field is denoted as a midplane electric field E^{Mid}. Actuators 1 and 2 were subjected to a unipolar sinusoidal midplane electric field of 3.5 MV/m at 0.1 Hz and the strain responses were compared.

The DC voltage polarization process was applied to actuator 3 and a commercial MFC. Actuator 3 was subjected to a unipolar sinusoidal midplane electric field from -1.0 MV/m to 3.0 MV/m. The MFC was subjected to a unipolar sinusoidal midplane electric field from -1.4 MV/m to 4.0 MV/m. The MFC and actuator 3 were then compared.

3.2 Experimental Results and Discussion

The results of the initial unipolar polarization cycle for actuators 1 and 2 are shown in figure 3.3. Figure 3.3a shows the longitudinal strain for both actuators during the unipolar polarization cycle. Actuator 1 with the larger electrode line widths had a peak longitudinal strain of 2039 $\mu\epsilon$ and a remnant longitudinal strain of 1321 $\mu\epsilon$. Actuator 2 with the smaller electrode line widths had a peak longitudinal strain of 536 $\mu\epsilon$ and a remnant longitudinal strain of 363 $\mu\epsilon$. Figure 3.3b shows the transverse strain for both actuators during the unipolar polarization cycle. Actuator 1 had a peak transverse strain of -1950 $\mu\epsilon$ and a remnant transverse strain of -1356 $\mu\epsilon$. Actuator 2 had a peak transverse strain of -550 $\mu\epsilon$ and a remnant transverse strain of -400 $\mu\epsilon$.

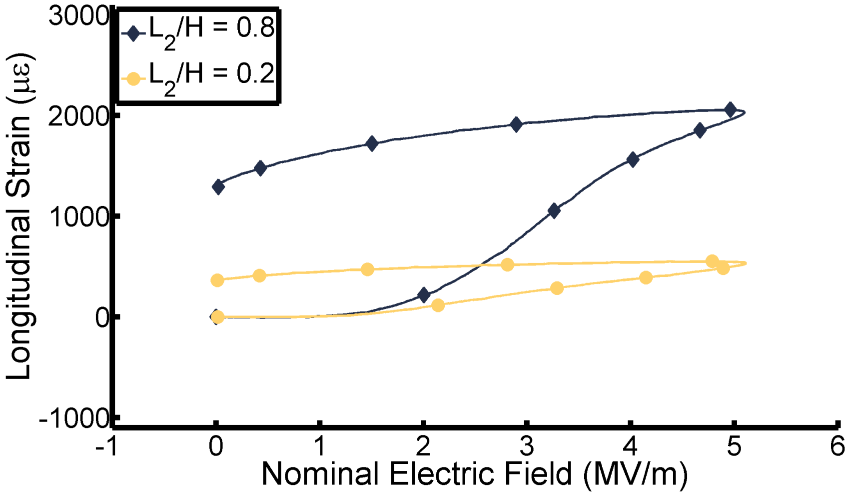

(a)

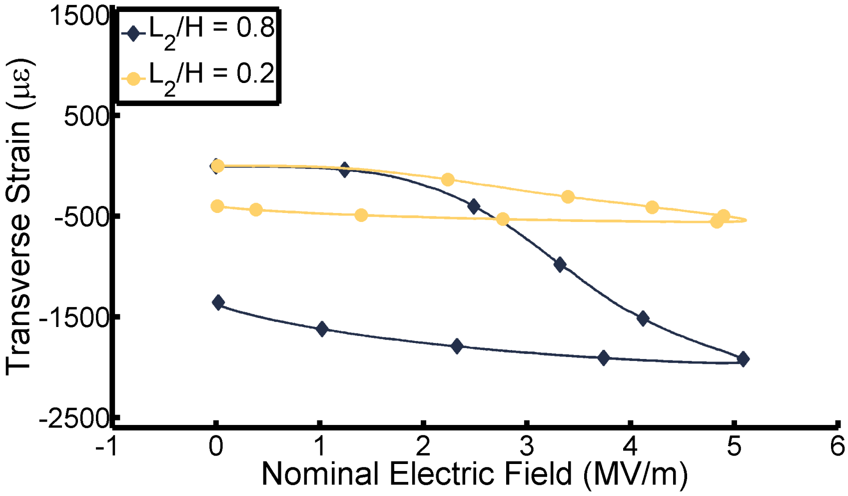

(b)

Figure 3.3: Initial Polarization cycle of actuators 1 and 2 for (a) longitudinal strain and (b) transverse strain.

While both specimens were run to the same nominal electric field, the explanation for the smaller strain of actuator 2 can be explained with Gauss's Law. Consider Gauss's Law integrated over two different volumes for the IDE geometry: the first surrounds the electrode but extends just below the electrode as shown in Figure 3.4a; the second surrounds the electrode and extends out to the midsection of the fiber/plate between two electrodes as shown in Figure 3.4b. In each case the free charge on the electrode is equal to the area integral of the normal component of electric displacement, or

$$Q = \int_{\Gamma_1} \boldsymbol{D}_1 \cdot d\boldsymbol{A} = \int_{\Gamma_2} \boldsymbol{D}_2 \cdot d\boldsymbol{A}, \tag{3.1}$$

where Γ is the boundary, $\boldsymbol{D}$ is electric displacement and Q is the total free charge. Assuming a uniform electric displacement $\boldsymbol{D}_1$ and $\boldsymbol{D}_2$, equation 3.1 can be rewritten in terms of its magnitudes as

$$Q \approx \|\boldsymbol{D}_1\| \, A_1 = \|\boldsymbol{D}_2\| \, A_2, \tag{3.2}$$

where A is the area encompassing the respective electric displacements. Relating the encompassing areas to geometric parameters, equation 3.2 can be rearranged such that,

$$\|\boldsymbol{D}_2\| = \|\boldsymbol{D}_1\| \, \frac{L_2}{H}. \tag{3.3}$$

The maximum electric displacement $\boldsymbol{D}$ is limited to the saturation polarization of the ferroelectric material. For $L_2/H < 1$, the maximum electric displacement in the fiber $\boldsymbol{D}_2$ is thus limited proportionally to L_2/H. Actuator 2 with an L_2/H ratio of 0.2 could not be fully polarized and by equation 3.3 was limited to 20% of the saturation value. Similarly, actuator 1 should have only reached 80% saturation. These ratios are similar to the observed strain ratios and applying them to figure 3.3 causes the strains to coalesce.

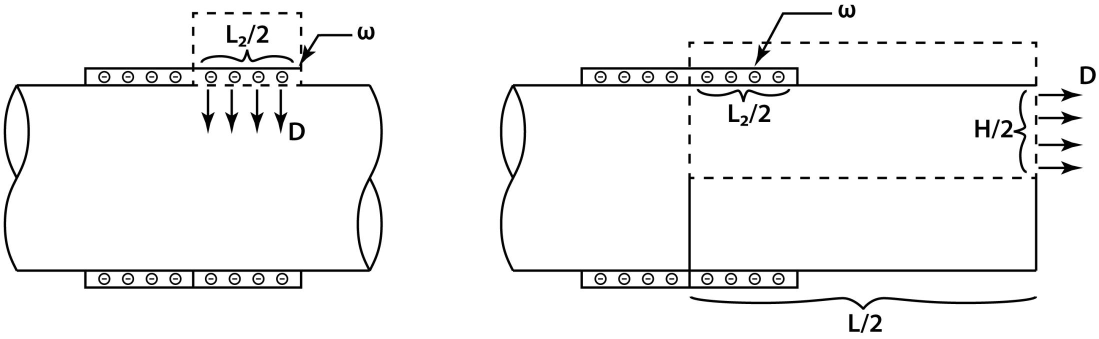

(a) (b)

Figure 3.4: Gauss' law applied to the same material under the the same boundary conditions to demonstrate limitations of substrate polarization. The integration contours are shown for (a) the electric displacement just under the electrode and (b) the electric displacement in the middle of the plate between two electrodes.

The results of the DC polarization after the unipolar polarization cycle is shown in figure 3.5. The actuators were quickly ramped to a negative nominal electric field of 5 MV/m. The nominal electric field was held steady until the strain saturated. Actuator 1 only took 5 seconds to saturate its strain and thus only actuator 2 is discussed regarding the DC polarization process. The saturation process took 40 minutes for actuator 2, and it produced a saturation strain of 2366 $\mu\epsilon$. The DC polarization experiment was repeated with a positive nominal electric field. The actuator took only 25 minutes to saturate and achieved a similar saturation strain of 2465 $\mu\epsilon$.

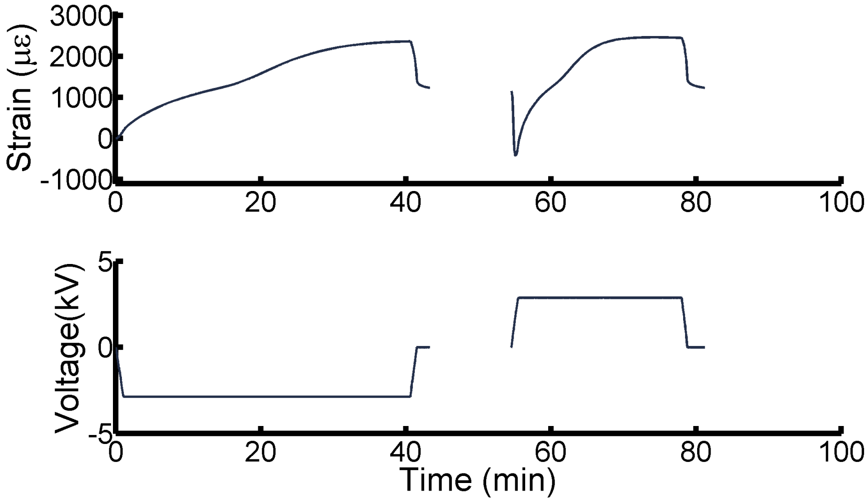

Figure 3.5: DC Polarization after initial unipolar polarization cycle for $L_2/H = 0.2$ actuator. Strain indicated is longitudinal strain.

Again unipolar cycling was applied to the actuators. The result of a unipolar electric field cycle in the same direction as the actuator's polarization direction is shown in figure 3.6. The strains used for actuators 1 and 2 for the rest of the manuscript are about a reference strain state after the material was fully polarized. Figure 3.6a shows the longitudinal strain for actuators 1 and 2. At a nominal electric field of 5 MV/m actuator 2 achieved a peak longitudinal strain of 1129 $\mu\epsilon$. Upon removal of the field, the actuator initially held a remnant longitudinal strain of 275.5 $\mu\epsilon$. Over the course of 90 seconds, the actuator's strain diminished back to 0 $\mu\epsilon$ in a creep like process. This contrasts with actuator number 1 which over the course of only 20 seconds had longitudinal strain creep of 166 $\mu\epsilon$ when the electric field was removed. A similar process was noted in the transverse strains shown in figure 3.6b.

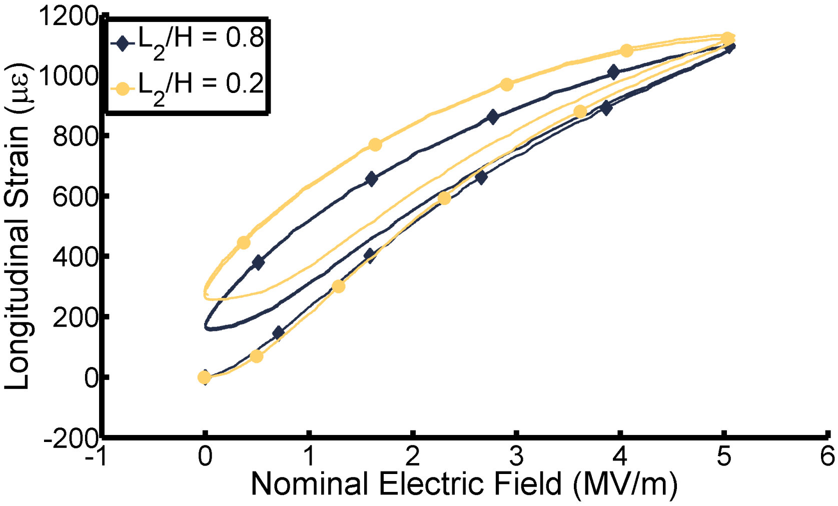

(a)

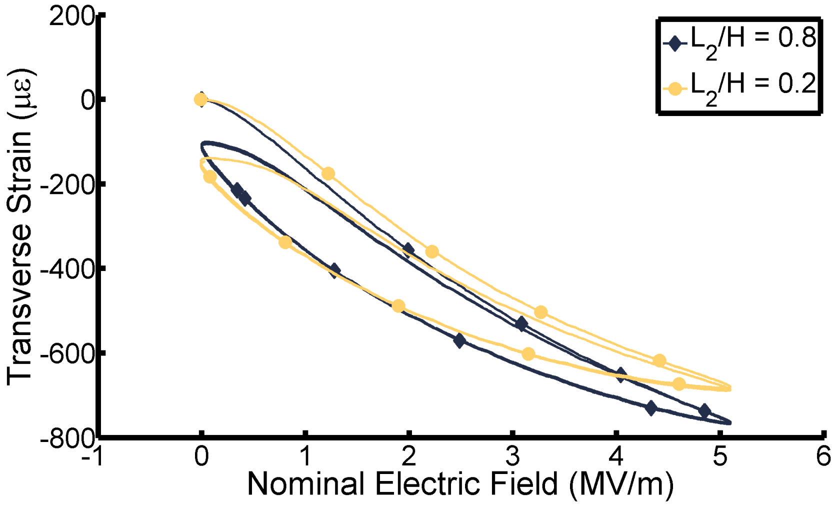

(b)

Figure 3.6: A comparison of actuators 1 and 2 with unipolar sinusoidal nominal electric field of 5 MV/m at 0.1 Hz applied after DC polarization for (a) longitudinal strain and (b) transverse strain. Electric field was applied in same direction as actuator polarization.

With the atypical DC polarization response of actuator 2, a unipolar electric field cycle was ran against the polarization direction of actuators 1 and 2. The results are shown in figure 3.7. The response of actuator 1 is shown in figure 3.7a. Upon the first cycle the actuator exhibits butterfly loop behavior in which the strain initially dips negative, but once the coercive field is reached the polarization reorients and the strain jumps positive. Further cycling exhibits a unipolar response similar to figure 3.6. The response of actuator 2 is shown in figure 3.7b. During the first cycle, the actuator achieved peak strain of -1733 $\mu\epsilon$. This strain magnitude is 53% greater than the case in which the electric field and polarizations were positively aligned. The actuator resisted polarization reorientation and no jump in strain was observed. Continued cycling causes the peak strain to ratchet until eventually the polarization fully switches and the strain responds similarly to that of figure 3.6.

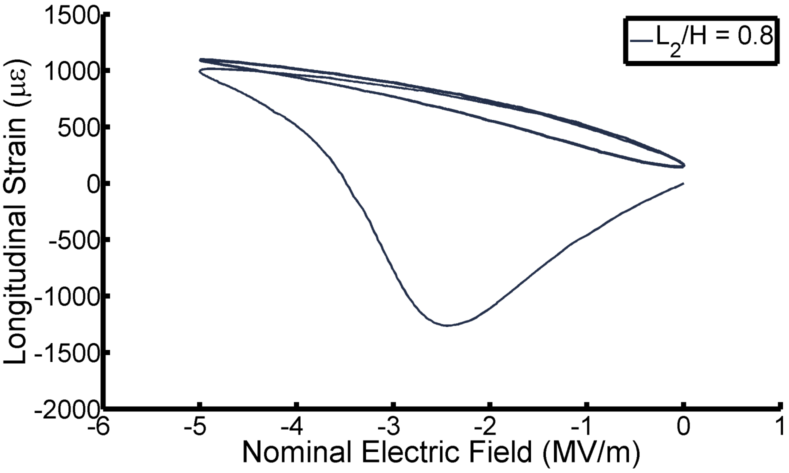

(a)

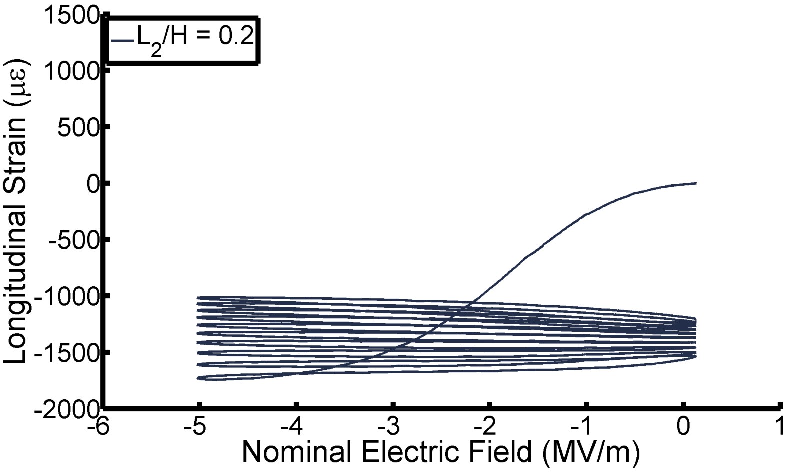

(b)

Figure 3.7: A unipolar sinusoidal nominal electric field of 5 MV/m at 0.1 Hz applied to actuator after DC polarization for (a) actuator 1 and (b) actuator 2. Electric field was applied opposite to actuator polarization.

3.3 Computational Model

A nominal electric field was used in comparison plots shown in figures 3.3 and 3.6. The actual electric field varies in amplitude and direction within the actuator, and as seen electrode geometry has significant affect on actuator response. In some cases the nominal electric field may not be a good estimate of the electric field in the piezoelectric plate/fiber.

Far enough away from the electrode edges in the x_3 direction, the electric field is nearly uniform in the x_3 direction. Actuators with a large electrode gap to electrode line width ratio $(L - L_2)/L_2$ will have a high percentage of a uniform electric field in the x_3 direction. The electric field magnitude in this region does not necessarily equal to the nominal electric field defined above. An electric field was obtained from a dielectric finite element analysis and denoted the midplane electric field. An attempt was made to identify whether the midplane electric field was needed when comparing actuator responses, or if a nominal electric field suffices.

3.3.1 Dielectric Model

The equations describing an electrostatic dielectric material follow directly from Maxwell's equations. Under quasi-static conditions, Maxwell's equations reduce to,

$$\begin{aligned} \nabla \times \boldsymbol{E} &= \boldsymbol{0}, \\ \nabla \cdot \boldsymbol{D} &= \rho. \end{aligned} \tag{3.4}$$

According to equation 3.4, the electric field is irrotational and is conservative. A conservative field can be represented with a scalar potential, ϕ, such that,

$$\boldsymbol{E} = -\nabla \phi. \tag{3.5}$$

The relations between the electric field $\boldsymbol{E}$ and electric displacement $\boldsymbol{D}$ in the linear regime, can be represented as,

$$\boldsymbol{D} = \boldsymbol{\kappa} \boldsymbol{E}, \tag{3.6}$$

where $\boldsymbol{\kappa}$ is a symmetric 2nd order permittivity tensor.

The validity of the field equations 3.4 are only for ordinary points in space in which their properties vary continuously. For any surface which separates two regions, a sharp change in $\boldsymbol{\kappa}$ occurs leading to discontinuities in the field vectors. Using the integral form of Gauss's law, the change in the normal component of $\boldsymbol{D}$ between two mediums (1) and (2) are,

$$(\boldsymbol{D}_2 - \boldsymbol{D}_1) \cdot \boldsymbol{n} = \omega, \tag{3.7}$$

where the subscripts represent the respective medium, $\boldsymbol{n}$ is the unit normal drawn from medium (1) to (2), and ω is a surface charge density.

With the electrostatic field vectors defined for ordinary points in space and across boundaries, the strong form boundary-value problem for dielectric materials is as follows:

$$\begin{cases} \nabla \cdot \boldsymbol{D} = \rho & \text{in } \Omega \\ \boldsymbol{E} = -\nabla \phi & \text{in } \Omega \\ \boldsymbol{D} = \boldsymbol{\kappa} \boldsymbol{E} & \text{in } \Omega \\ \phi = \bar{\phi} & \text{on } \Gamma_\phi \\ -\boldsymbol{D} \cdot \boldsymbol{n} = \omega & \text{on } \Gamma_\omega \end{cases}, \tag{3.8}$$

where $\bar{\phi}$ is a defined scalar potential, Γ_ϕ is the boundary in which ϕ is defined, Γ_ω is the boundary in which ω is defined and Ω is the problem domain.

Multiplying the first relation in equation 3.8 with a weighting function w and integrating by parts yields the weak formulation of the problem,

$$\int_\Omega -\nabla w \cdot \boldsymbol{D} \, d\Omega = \int_\Omega w\rho \, d\Omega + \int_{\Gamma_\omega} w\omega \, d\Gamma. \tag{3.9}$$

Replacing the weighting function by a virtual potential $\delta\phi$ and using the relations in equations 3.8 reformulates the weak form in a virtual work framework,

$$\int_\Omega \boldsymbol{D} \cdot \delta \boldsymbol{E} \, d\Omega = \int_\Omega \rho \delta\phi \, d\Omega + \int_{\Gamma_\omega} \omega \delta\phi \, d\Gamma. \tag{3.10}$$

3.3.2 Finite Element Formulation

Introducing the finite element approximation, the unknown scalar potential ϕ can be approximated by,

$$\phi \approx \hat{\phi} = N_a \tilde{\phi}^a, \tag{3.11}$$

where $\hat{\square}$ denotes an approximation of a function, N_a is a shape function for a specific elements node a, and $\tilde{\square}^a$ denotes a functions nodal value for an element's node a. In equation 3.11 and all following, the shape function with its nodal value counterpart $N_a\tilde{\square}^a$ denotes a summation across all the nodes of the element,

$$N_a\tilde{\square}^a = \sum_a N_a\tilde{\square}^a. \tag{3.12}$$

The remainder of the finite element formulation will be denoted in indicial notation. Einstein summation convention and comma differentiation are used. Similar to the scalar potential formulation, the electric field approximation can be written as,

$$\boldsymbol{E} \approx \hat{\boldsymbol{E}} = -N_{a,i}\tilde{\phi}^a. \tag{3.13}$$

Integrating over an elements domain Ω^e and applying the approximations of equations 3.11 and 3.13, the weak form can be approximated over an element as,

$$\delta\tilde{\phi}^a \left(\int_{\Omega^e} \kappa_{ij} N_{a,i} N_{b,j} d\Omega \tilde{\phi}^b - \int_{\Gamma_\omega^e} \omega N_a d\Gamma \right) = 0. \tag{3.14}$$

Noting that $\delta\tilde{\phi}^a$ is arbitrary, equation 3.14 can be represented as the compact equilibrium equations,

$$K^{ab}\tilde{\phi}^b = F^a, \tag{3.15}$$

where K^{ab} is a stiffness matrix for the nodal pair a, b and F^a is a force vector. The stiffness matrix and the force vector are represented by the following,

$$\begin{aligned} K^{ab} &= \int_{\Omega^e} \kappa_{ij} N_{a,i} N_{b,j} d\Omega \\ F^a &= \int_{\Gamma_\omega^e} \omega N_a. \end{aligned} \tag{3.16}$$

3.3.3 Mesh Generation

The domain to be meshed is shown in the highlighted region of figure 3.1. Due to symmetry conditions, only 1/8th of the substrate between two electrode line widths needs to be meshed.

The electrode creates a singularity along its edge. To remedy this, control of element size near the singularity is needed. To control element sizes, node generation was chosen such that along an edge, the ratio of successive element sizes is a constant growth factor. The 1D representation of this is defined with the sequence element lengths L_i as,

$$\frac{L_{i+1}}{L_i} = C = B^{1/(N-1)}, \tag{3.17}$$

where C is the element growth factor, N is the total number of elements, B is a growth factor denoted by $B = \frac{L_{\text{Max}}}{L_{\text{Min}}}$, L_{Max} is the maximum element length, and L_{Min} is the minimum element length. Figure 3.8 represents the visualization of this element growth method.

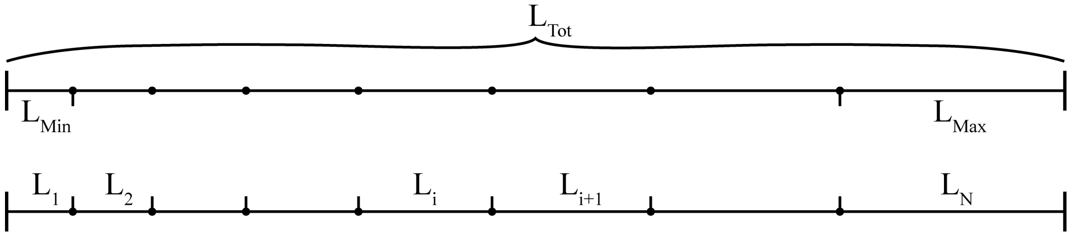

Figure 3.8: One dimensional representation of nodal spacing with constant element length growth factor

The meshing was defined by denoting number of elements N, the length of the edge L_{Tot} and the smallest element size needed L_{Min} to determine the growth factor C from them. To formulate, first consider L_{Tot} is just the sum of the individual element lengths,

$$\begin{aligned} L_{\text{Tot}} &= \sum_{k=1}^{N} L_k \\ &= \sum_{k=0}^{N-1} L_{\text{Min}} C^k. \end{aligned} \tag{3.18}$$

A series of the form 3.18 is a geometric series. Provided, $C \neq 1$ (no growth), the sum is given by

$$\sum_{k=0}^{N-1} L_{\text{Min}} C^k = L_{\text{Min}} \frac{C^N - 1}{C - 1} \tag{3.19}$$

Combining equations 3.18 and 3.19, yields the following polynomial.

$$C^N - \frac{L_{\text{Tot}}}{L_{\text{Min}}} C + \frac{L_{\text{Tot}}}{L_{\text{Min}}} - 1 = 0 \tag{3.20}$$

Using Descartes' Rule of Signs and considering $L_{\text{Tot}}/L_{\text{Min}} > 1$, there can only be 2 or 0 positive real roots. But, with 1 being a root of equation 3.20, there must be one other real root. This other real root is the growth factor needed and was found numerically.

The previous formulation was for 1D generation of elements across an edge. This formulation was extended into multi-dimensions by generating nodes across multiple edges and connecting neighboring nodes together. Figure 3.9 shows this process of generating nodes and tying the elements together into quadrilateral elements. A series of meshes were generated for various L_2, L and H values. The mesh was deemed dense enough by a series of successive denser meshes and monitoring average electric field along the positive x_3 face until there was only a 0.1% change.

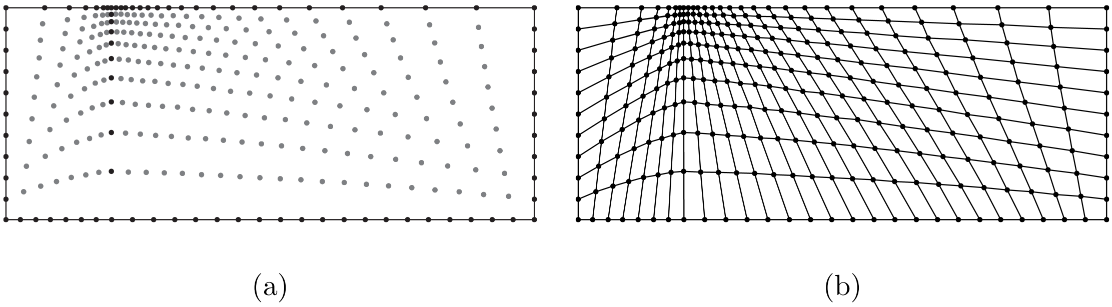
(a) (b)

Figure 3.9: Mesh generation using constant element length growth factor across multiple edges. (a) represents the nodal generation, and (b) represents the formed 2D elements

With the mesh generated, boundary conditions were applied such that a test electric potential was applied underneath the electrode and at the substrates midsection or positive x_3 face. Across the rest of the boundary, zero free charge was set. The average electric field along the positive x_3 face was found and compared to the nominal electric field defined earlier.

3.4 Results and Discussion

The results of dielectric model comparing the nominal electric field to the midplane electric field can be seen in figure 3.10. The electric field ratio $E^{\text{Mid}}/E^{\text{Nom}}$ equal to unity indicates the nominal and midplane electric field are in agreement. As the electrode gap to plate height ratio $(L - L_2)/H$ increases this electric field ratio tends towards unity. As the electrode line width ratio to plate height L_2/H decreases, there is no electric field ratio drop off until $L_2/H = 1$. If the electrode line width to plate height ratio dips below $L_2/H = 1$, the electric field ratio starts to sharply dip. This is in conjunction with the predictions from Gauss's law which showed polarization problems when L_2/H is less than one. In regions where the electric field ratio $E^{\mathrm{Mid}}/E^{\mathrm{Nom}}$ gradient is small, it would be permissible to use a nominal electric field.

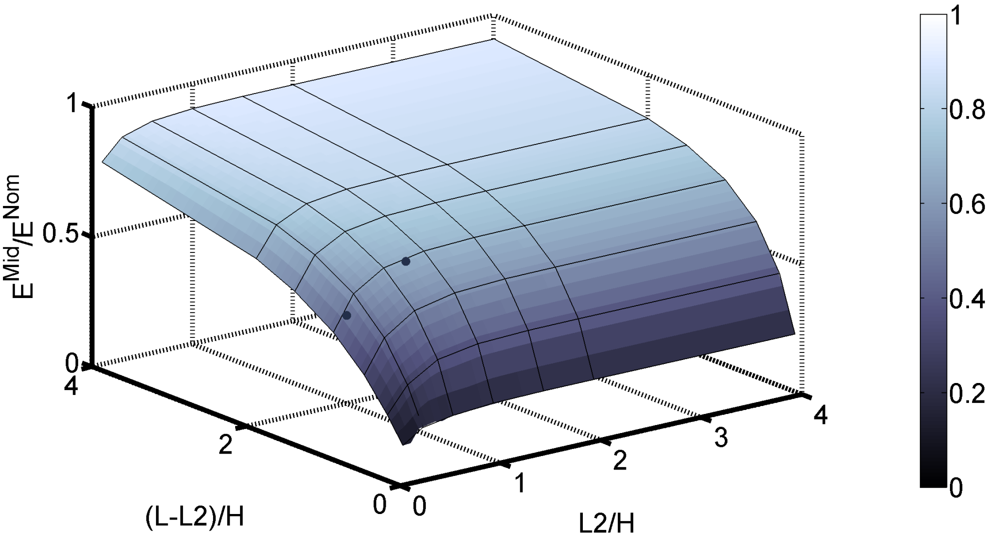

Figure 3.10: Surface plot comparing the midplane electric field from the dielectric model E^{Mid} to the nominal electric field E^{Nom} when both use the same electric potential. Black dots indicate the geometries of actuators 1 and 2 being analyzed

The geometries of actuators 1 and 2 are indicted in figure 3.10 by black dots. Actuator 1 had an electric field ratio $E^{\mathrm{Mid}}/E^{\mathrm{Nom}}$ of 0.6814 and actuator 2 had an electric field drop off of 0.5287. The nominal electric field and the dielectric midplane electric field are not in agreement in this electrode geometry space. Also, the electric field ratios differ between actuators which creates discrepancies in the actuator comparison. Ideally, one would just run the actuators until just before dielectric breakdown and compare their performance based on maximum operating voltage. Preliminary tests on these actuators and other electrode geometries have indicated that dielectric breakdown occurs around a midplane electric field from 3.5 MV/m to 4.0 MV/m.

While the midplane electric field is a logical choice of an electric field parameter, it was investigated when its use could break down. Figure 3.11 shows three separate dielectric midplane electric fields: maximum, average, and minimum. The maximum, average and minimum electric field correspond to the top, middle and bottom surfaces respectively. When the relative electrode gap is large the three surfaces coalesce and there is not much variance between the three. When the relative electrode gap is less than 2.0, the surfaces begin to diverge. The diverged surfaces indicate a region in which the electric field is varying within the midplane of the actuator and is no longer uniform. In this region, comparison using electric field becomes more arbitrary.

To better understand the reasoning behind the electric field discrepancies, a plot of the midplane electric field and electric potential distributions were made as shown in figure 3.12. The dielectric IDE model had a relative electrode line width L_2/H equal to one and a relative electrode gap $\left(L-L_2\right)/H$ equal to 0.5. Figure 3.12a shows the midplane electric field distribution. The x_3 component of electric field is plotted such that x_3 is perpendicular to the midplane. The x_3 component of electric field varies from a maximum of 0.664 MV/m to a minimum 0.444 MV/m. The minimum electric field corresponds to a 33% difference from the maximum electric field. The maximum electric field is at the top and bottom of the substrate, while the minimum electric field is in the center of the midplane.

The reasoning for this distribution can be seen in the electric potential contour plot in figure 3.12b. In this figure, the electrodes are the top and bottom white surfaces. The midplane is the surface on the right hand side of the figure. The distance from the electrode edges to the top/bottom of the midplane is a much shorter distance than to the middle of the midplane. This causes higher electric fields at the top and bottom. Also, the large electric field concentrations at the electrode edges do not have time to properly adjust and become uniform across the midplane. Equipotential lines were plotted to help show this phenomenon.

When the relative electrode gap is increased, the electric field has more space for a uniform electric field to develop. The distances from the electrode edges to the top/bottom and middle of the midplane assypmptote to the same value. Thus, the reasoning behind the discrepancies between maximum, average and minimum electric field explain their divergence as seen in figure 3.11.

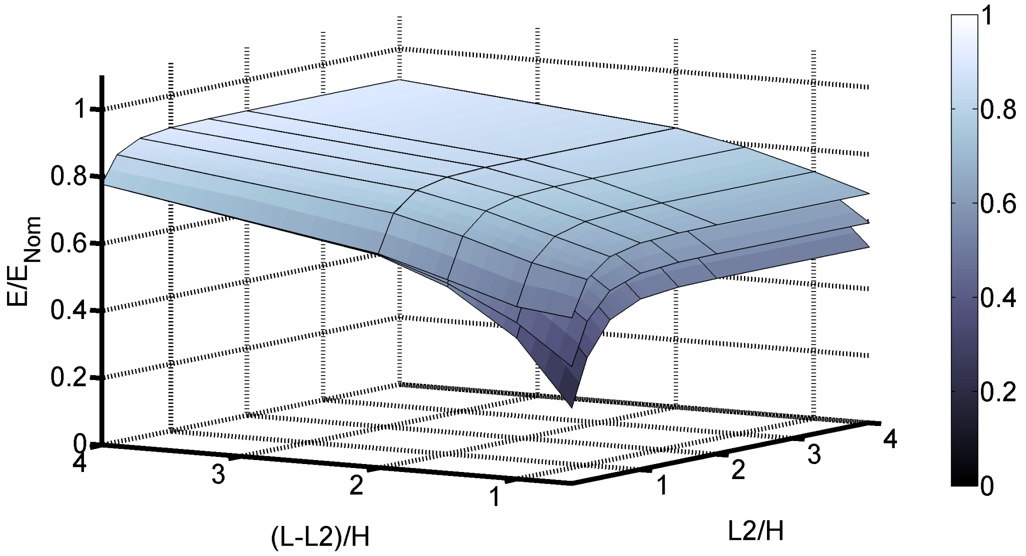

Figure 3.11: Surface plot comparing the average midplane electric field, maximum midplane electric field, and minimum midplane electric field from the dielectric model. The top, middle and bottom surface correspond to the maximum, average and minimum midplane electric field respectively.

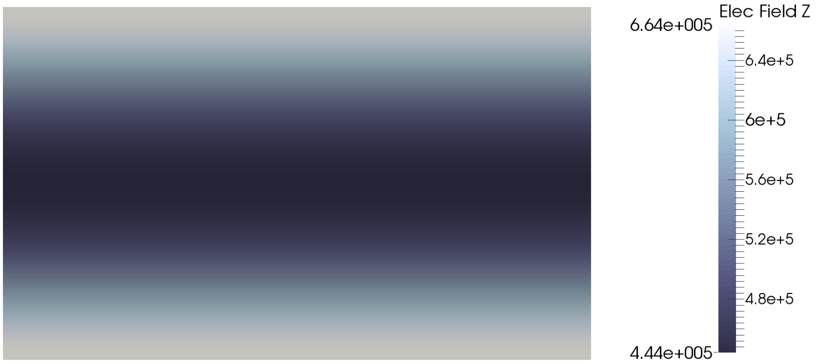

(a)

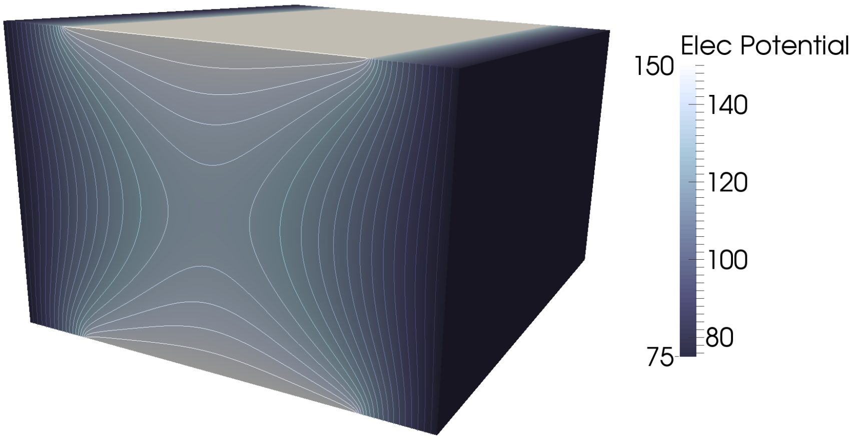

(b)

Figure 3.12: Electric field/potential distribution in IDE substrate (a) electric field in the x_3 direction and (b) electric potential distribution.

Unipolar cycling was run on the actuators again, but each actuator was run to the same maximum midplane electric field of 3.5 MV/m. The result is shown in figure 3.13. Figure 3.13a shows the longitudinal strain for both actuators during the unipolar polarization cycle. At a midplane electric field of 3.5 MV/m, actuator 1 achieved a peak longitudinal strain of 1098 $\mu\epsilon$. Upon removal of the field, the actuator initially held a remnant longitudinal strain of 173.3 $\mu\epsilon$ which then diminished to zero from creep. Applying a midplane electric field of 3.5 MV/m to actuator 2, the achieved peak longitudinal strain was 1352 $\mu\epsilon$ or 23% greater than actuator 1. Upon removal of the field, the actuator initially held a remnant longitudinal strain of 407 $\mu\epsilon$ which then diminished to zero from creep. Figure 3.13b shows the transverse strain for both actuators during the unipolar polarization cycle. Actuator 1 had a peak transverse strain of -760 $\mu\epsilon$ and a remnant transverse strain of -109.5 $\mu\epsilon$. Actuator 2 had a peak transverse strain of -810 $\mu\epsilon$ and a remnant transverse strain of -200 $\mu\epsilon$.

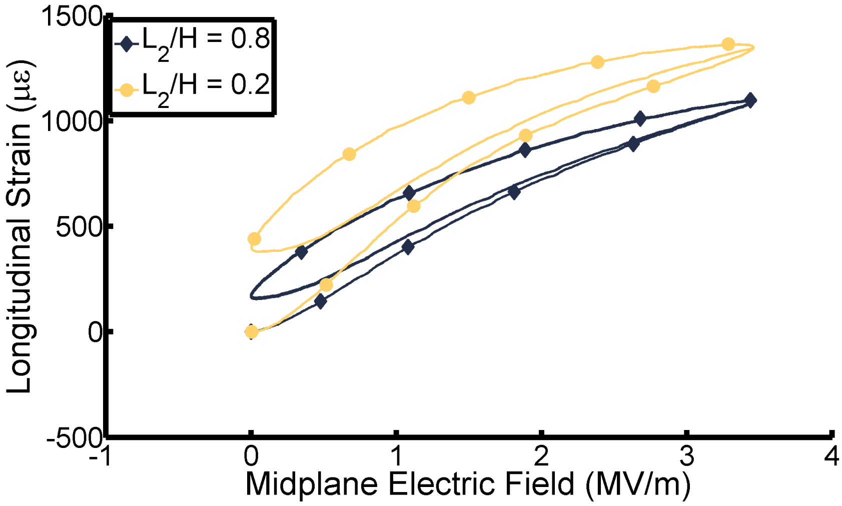

(a)

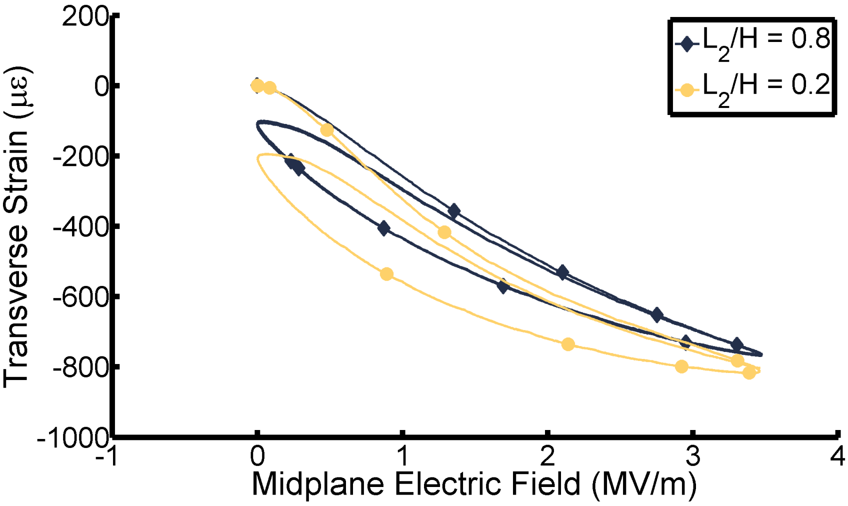

(b)

Figure 3.13: A comparison of actuators 1 and 2 with a unipolar sinusoidal midplane electric field of 3.5 MV/m at 0.1 Hz applied after DC polarization for (a) longitudinal strain and (b) transverse strain. Electric field was applied in same direction as actuator polarization.

Actuator 3 was an actuator with electrode geometries that produced large free strain outputs. Actuator 3 was compared to a commercial MFC in figure 3.14. Considering there was a negative electric field bias for both actuators, the strains were reported such that at the minimum electric field strain is zero. From the dielectric analysis, actuator 3 had an electric field ratio $E^{\mathrm{Mid}}/E^{\mathrm{Nom}}$ of 0.69 and the MFC had an electric field ratio of 0.72.

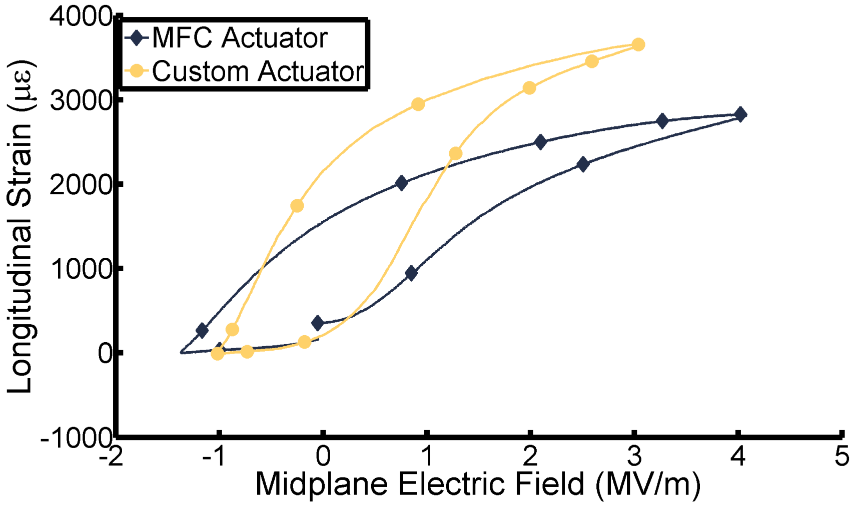

(a)

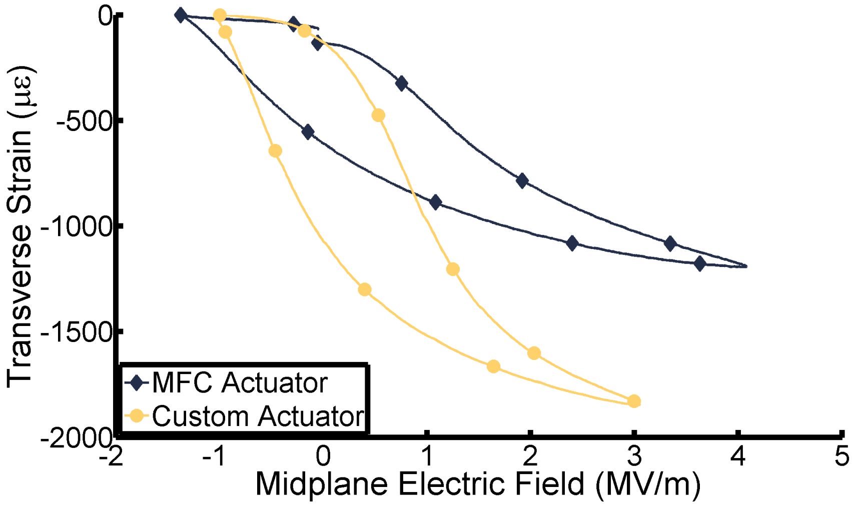

(b)

Figure 3.14: A comparison of actuator 3 and a commercial MFC with a unipolar sinusoidal midplane electric field at 0.1 Hz applied after DC polarization for (a) longitudinal strain and (b) transverse strain. Electric field was applied in same direction as actuator polarization.

Figure 3.14a shows the longitudinal strain for actuator 3 and the commercial MFC. At a midplane electric field of 3.0 MV/m, actuator 3 achieved a peak longitudinal strain of 3657 $\mu\epsilon$. Applying n midplane electric field of 4.0 MV/m to the commercial MFC, a peak longitudinal strain of 2828 $\mu\epsilon$ was achieved. Comparing the two peak strains, actuator 3 achieved a 29% increase in free strain actuation over the commercial MFC. Figure 3.14b shows the transverse strain for actuator 3 and the commercial MFC. Actuator 3 had a peak transverse strain of -1847 $\mu\epsilon$ and the custom actuator had a peak transverse strain of -1193.

3.5 Conclusions

A comparison of two ferroelectric plate actuators with interdigitated electrodes was made. Initially it was found that the smaller electrode line width to plate height actuator had significantly less polarization. Using Gauss's law it was found that actuators with electric line width to plate height ratios less than one would have polarization problems. A DC voltage was applied to both actuators for a length of time until the creep type strain saturated. Surprisingly the actuator which initially could not be polarized was found to have a higher strain output than the other actuator after the DC polarization cycle.

Applying a unipolar electric field opposite to the polarization direction in the actuators yielded differing results. Actuator 1 with the larger electrode line width to plate height ratio did not resist polarization reorientation and fully switched its polarization direction in one cycle. Actuator 2 with the smaller electrode line width to plate height ratio resisted polarization reorientation. The polarization direction in the actuator resisted change, and only after many cycles it was polarized opposite to the original polarization direction. Changing only electrode geometry, the material behavior can thus be changed.

The effect of the inhomogenous electric field that is present when interdigitated electrodes are used was assessed. It was found that comparing actuators using electric potential divided by electrode gap spacing had discrepancies with dielectric analysis. A dielectric computational analysis found significant differences between the nominal electric field and the midplane electric field when the electrode gap to plate height ratio $(L - L_2)$ was small and when the electrode line width to plate height ratio L_2/H was less than one. A comparison of the actuators was performed again using the midplane electric field. The initially poor performing actuator 2 was shown to outperform actuator 1 by having 23% greater peak strain.

Other electrode geometries were explored and compared after applying a DC polarization cycle. One such actuator, actuator 3, was found to have a large free strain output of 3657 $\mu\epsilon$. Actuator 3 was compared to a commercial MFC. Actuator 3 achieved 29% greater longitudinal free strain actuation than the commercial MFC.

CHAPTER 4

Ferroelectric IDE

4.1 Introduction

The motivation of this work is to improve device performance of IDE piezocomposites for use as sensor/actuator rosettes in chapter 2.1 and self-latching shape memory piezocomposite actuators [97]. Due to the anisotropic properties of IDE piezocomposites, a rosette can be oriented to enable resolving two principle strain components and the corresponding principle directions. This concept enables not only directional sensing, important for structural health monitoring, it also enables directional actuation, important for structural vibration and acoustic control [57–59]. The design of IDE piezocomposites is also critical for self-latching actuators for efficient actuation of aerodynamic control surfaces [53, 98]. By using a shape memory actuators, deflections of control surfaces can be adjusted in-flight and maintained without constant power.

In chapter 3 it was found that IDE devices with small relative electrode line widths would not polarize unless a DC poling field was applied for an extended amount of time. This allowed for some devices to have superior actuation performance than previously expected. In order to fully characterize the custom actuators and discover other unforseen phenomenon, a full parametric study on 20 custom plate actuator was performed to fully characterize the sensor/actuator behavior. The parametric study was also supplemented with a 3D ferroelectric finite element code to gain any other insight on the actuator behavior.

A construction with IDE on rectangular fibers as shown in figure 4.1. Several key features are shown on the inset. The electric field lines between the electrodes result in polarization along the length of the fibers, with d_{33} in this direction (along the fibers) and d_{31} perpendicular to this direction (perpendicular to the fibers). There is an electric field concentration at the electrode edges indicated in figure 4.1 where the electric potential lines converge. There is a region beneath the electrodes where the field lines are not along the length of the fiber, labeled the dead zone. In the dead zone, the longitudinal strain is actually of the opposite sign than in the uniform field region due to contraction from the d_{31} effect.

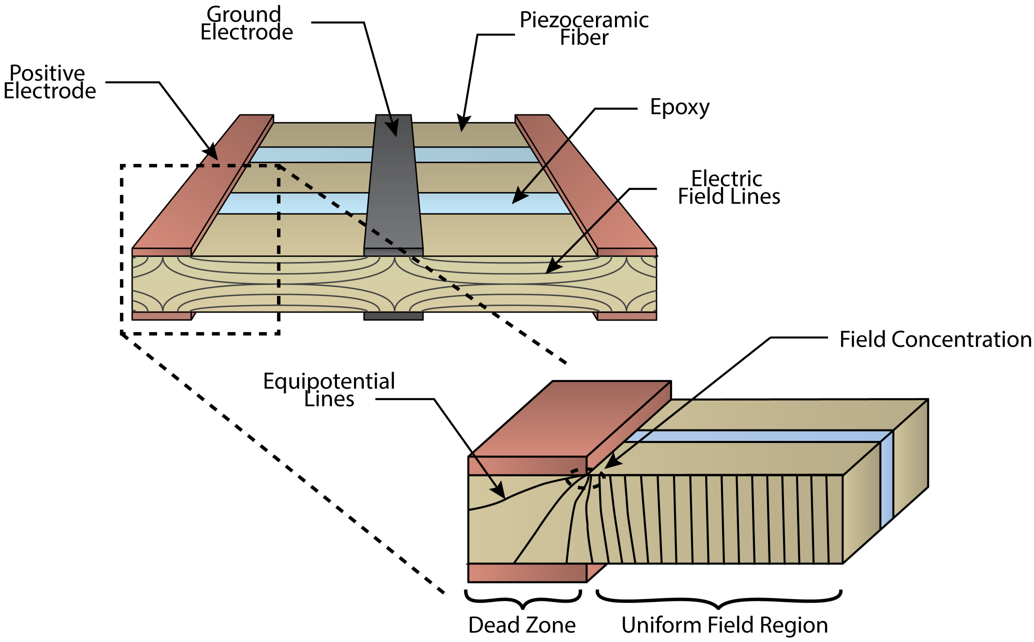

Figure 4.1: Interdigitated electrodes on a macro fiber composite and the resulting field gradient within the fibers.

4.2 Experimental Arrangement

4.2.1 Materials and Specimen Preparation

Three actuator types were initially tested. The first type of actuator tested was a commercially available macro fiber composite, model number M8528-P1. Overall active dimensions of the commercial actuators are 85 mm × 28 mm × 0.2 mm. The second type actuators tested were custom PZT-5A plate with copper cladded interdigitated electrodes on polymide film. Unlike the commercial MFC which has a piezoelectric substrate diced into fibers, the custom actuators substrate was kept as monolithic plate. Overall active dimensions of the custom actuators are 85 mm × 25 mm × 0.6 mm. The custom actuators were provided by Smart Material Corp. The third type of actuator was a monolithic plate actuator with uniform electrodes.

Actuator dimensions and coordinate directions used are defined in figure 4.2. The four geometric parameters of interest defined for IDE actuators are electrode spacing L, electrode line width L_2, plate/fiber height H, and fiber depth D for MFC. Twenty separate custom actuators were tested. Two key ratios for the custom actuators were identified as the electrode line width to plate height ratio L_2/H and the electrode gap to plate height ratio $\left(L - L_2\right)/H$. The custom actuators were designed such that in every set of five actuators, L_2/H was varied and $\left(L - L_2\right)/H$ was held constant. The table of values for the custom actuator and commercial MFC dimensions are given in table 4.1.

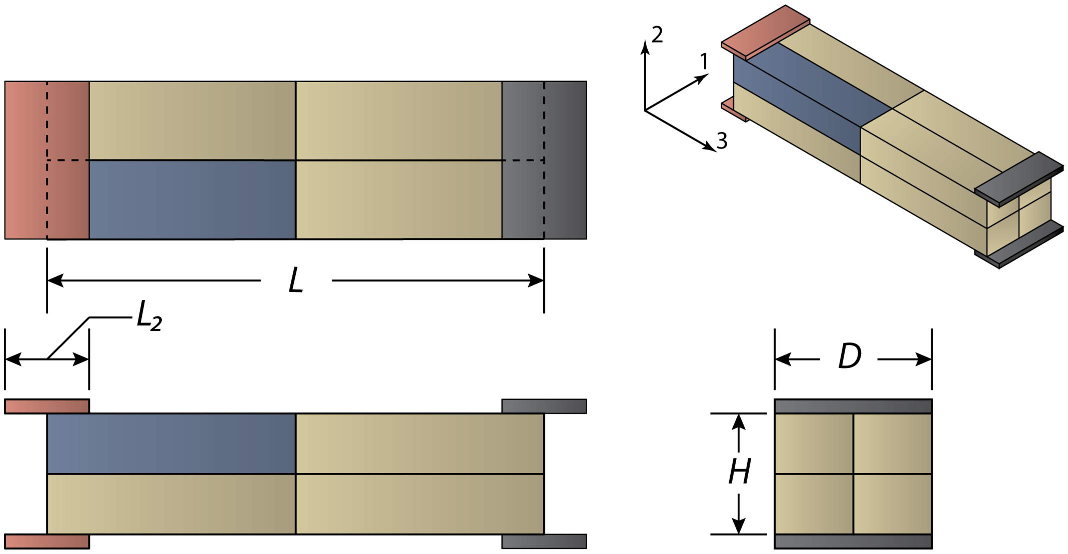

Figure 4.2: Layout of an interdigitated electrode on a ferroelectric substrate. Highlighted region indicates meshed region for computation.

The commercial actuators were instrumented with longitudinal (x_3) and transverse (x_1) oriented tee rosette strain gages; pattern number 250UT from Vishay Precision Group. The custom actuators were instrumented with separate linear strain gages oriented in the longitudinal (x_3) and transverse (x_1) direction. The custom actuators longitudinal gages were model number SGD-7/350-LY43 and the transverse gages were model number SGD-7/350-LY43 from Omega. The longitudinal gages were chosen such that they would span

Table 4.1: Actuator Geometry Values for Parametric Study

Actuator	L_2(mm)	L(mm)	L_2/H	$(L-L_2)/H$	$E^{\text{Mid}}/E^{\text{Nom}}$
MFC	0.09	0.45	0.40	1.60	0.725
1	0.94	1.51	1.56	0.95	0.70
2	0.48	1.06	0.79	0.97	0.68
3	0.30	0.89	0.51	0.97	0.65
4	0.18	0.75	0.30	0.95	0.58
5	0.12	0.68	0.19	0.94	0.53
6	0.92	2.10	1.54	1.97	0.83
7	0.48	1.65	0.80	1.96	0.81
8	0.33	1.50	0.55	1.96	0.79
9	0.18	1.36	0.30	1.97	0.74
10	0.11	1.29	0.18	1.97	0.69
11	0.92	2.40	1.52	2.47	0.86
12	0.49	1.96	0.81	2.46	0.85
13	0.35	1.81	0.58	2.44	0.83
14	0.18	1.66	0.30	2.47	0.78
15	0.12	1.60	0.21	2.46	0.75
16	0.92	3.00	1.53	3.48	0.89
17	0.49	2.55	0.81	3.44	0.88
18	0.33	2.41	0.55	3.47	0.87
19	0.18	2.26	0.30	3.47	0.84
20	0.12	2.20	0.21	3.45	0.81

at least 6 interdigitated electrode spacings L. The gages were mounted on top and bottom of both commercial and custom actuators to monitor for bending and extension. A strain gage amplifier and high voltage amplifier were fed to digital acquisition hardware. Applied voltage and strain were recorded.

4.2.2 Experimental Procedure

In order to investigate the self latching of piezoceramics, a test was performed on commercial macro fiber composites as a base point for feasibility. The voltage applied to the MFC follows the voltage profile as seen in figure 4.3. The test was composed of several cycles in which the actuator was fully poled to 2.5 kV and subjected to various back voltages. The back voltages ranged from 0 kV to -2.5 kV with -100V back voltage increments per cycle. Each cycle was a single period sinusoidal waveform performed at 0.25 Hz.

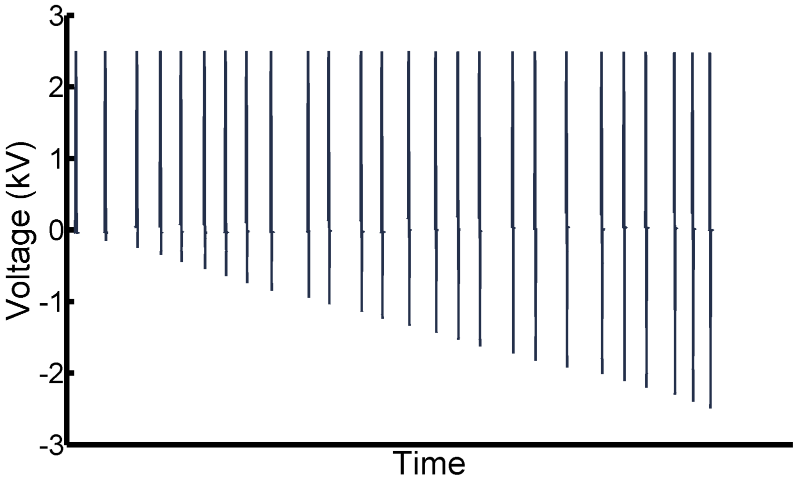

Figure 4.3: Voltage vs time for shape memory MFC actuator

The performance of the custom actuators was then investigated. In order to compare the twenty custom actuators, a dielectric finite element analysis was performed to determine the electric field within the actuators. A dielectric analysis was used to find the average electric field E^{Mid} at the midplane between interdigitated electrodes on a plane perpendicular to the (x_3) direction. Many authors choose to use a electric field defined as the applied voltage V divided by the electrode spacing L_2 as a basis for reporting values. Considering actuator geometries are being compared against one another, it was found using the electric field found in the dielectric analysis was more appropriate.

The electric field computation can be seen in a surface plot in figure 4.4. The dielectric electric field E^{Mid} was normalized by a nominal electric field $E_{\mathrm{Nom}} \equiv (V/\,(L - L_2))$ in which the applied voltage V is divided by the electrode gap distance $L - L_2$. Black dots on the surface plot indicate the twenty custom actuators geometries investigated. The dielectric electric field to nominal electric field ratios $E^{\mathrm{Mid}}/E^{\mathrm{Nom}}$ for actuators 1 through 20 can be found in table 4.1. The electric field found from the dielectric analysis will be referred to as a midplane electric, or just electric field unless otherwise stated, in the rest of the chapter.

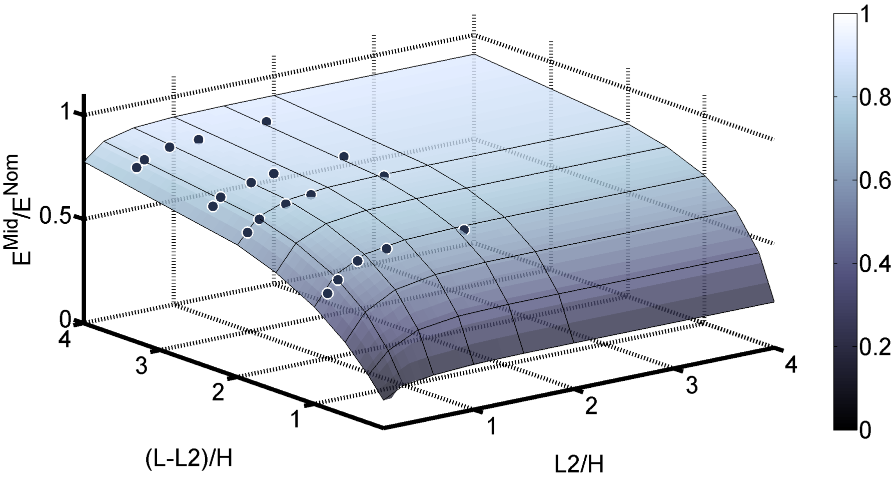

Figure 4.4: Surface plot comparing the average electric field in the midsection between electrodes using a dielectric model E^{Mid} to the nominal electric field E^{Nom}. Black dots indicate the twenty geometries of the actuators being analyzed.

Each custom actuator started in an unpoled state. A unipolar sinusoidal electric field of 2.5 MV/m at 0.1 Hz was applied to each actuator. After the initial polarization cycle, a DC electric field of 2.5 MV/m was applied to each actuator. The strain was monitored while the electric field was held. When the strain was saturated the DC electric field was removed. The actuators were again subjected to a unipolar sinusoidal electric field of 2.5 MV/m at 0.1 Hz. The actuators were then subjected to a bipolar sinusoidal electric field from -2.5 MV/m to 2.5 MV/m at 0.1 Hz. The custom actuator's bipolar sinusoidal electric field response were then compared to the monolithic actuator with uniform electrodes.

Actuator 10 with its small electrode line widths was found to have high strain outputs with minimum voltage inputs. Actuator number 10 was thus chosen to compare to the MFC self-latching shape memory tests. The test was composed of six cycles in which the actuator was poled to 2.5 MV/m and subjected to various back electric fields. The back electric fields ranged from 0 MV/m to -1.25 MV/m in -0.25 MV/m increments. Each cycle was performed at 0.1 Hz. Actuator number 10 was then subjected to various frequencies with a sinusoidal electric field cycle from 2.5 MV/m to -1.0 MV/m. The frequencies investigated were 0.025 Hz, 0.5 Hz, and 2 Hz.

4.3 Experimental Results

The first experiment investigated the feasibility of a MFC as a shape memory self latching actuator. The strain outputs for the voltage profile of figure 4.3 are indicated in figure 4.5. The longitudinal strains are indicated in the figure on the left and transverse strains are indicated in the figure on the right. It can be seen that upon applying negative bias voltages from 0 kV to -1 kV the remnant longitudinal strain decreases from its maximal value of 200 $\mu\epsilon$ to its minimal value of -1000 $\mu\epsilon$. Upon further increasing the backfield from -1 kV to -2.5 kV, the remnant strain begins to increase back again towards 200 $\mu\epsilon$. This increase is due to the polarization reorientation of the material as the back voltages go beyond the coercive field.

Electrode geometry was modified in an attempt to increase the remnant strain range or reduce remnant strain creep. Actuators 6 through 10 all have the same relative electrode gap but differing relative electrode line widths. Thus, actuators 6 through 10 are discussed first to illustrate the device performance of the custom actuators while varying relative electrode line widths. The discussion will then be supplemented by surface plots showing the results for all 20 actuators.

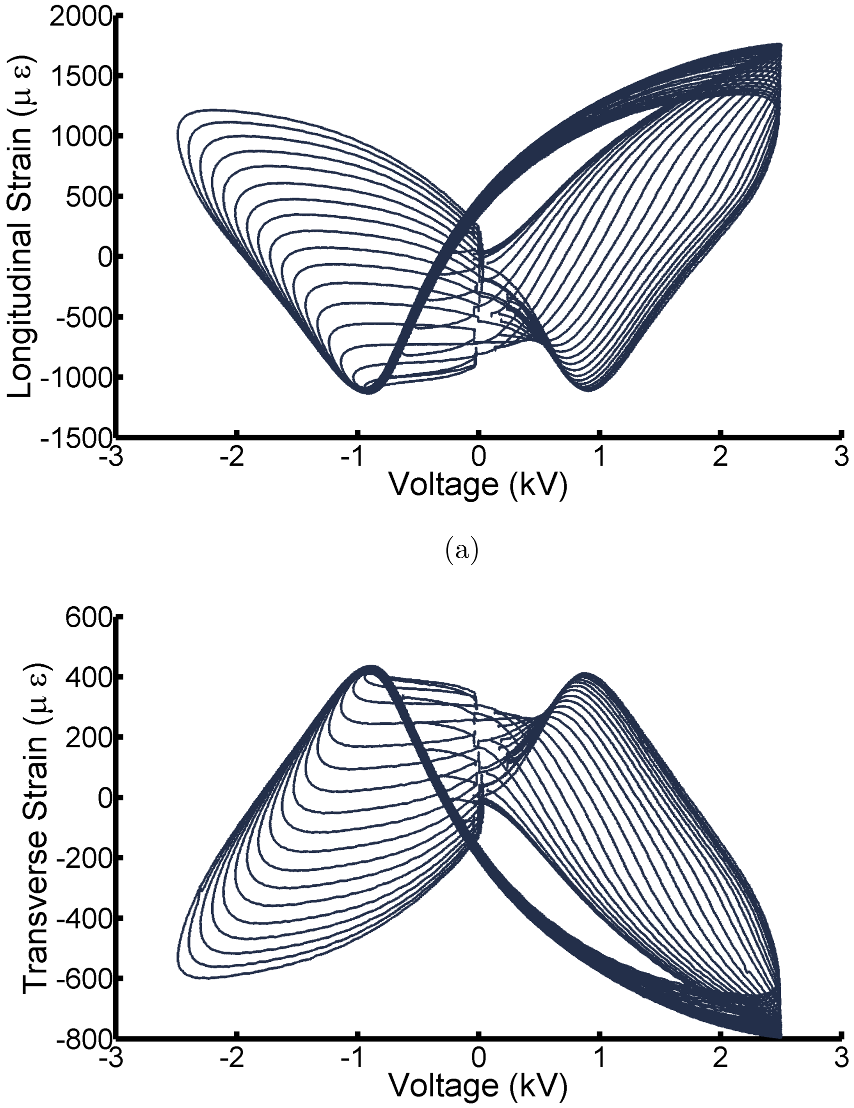

(a)

(b)

Figure 4.5: Strain versus voltage behavior on MFC actuator for strain locking tests. Subfigure (a) indicates longitudinal strain output while subfigure (b) indicates transverse strain output.

The results of the initial polarization cycle are shown in figure 4.6. It is shown that as the relative electrode line width L_2/H increases from 0.17 to 0.80, the remnant strain and peak strain increases. When L_2/H increases even further, the remnant strain and peak strain drop begin to decrease. Using the dielectric considerations of Gauss's law, it has been shown that the ideal relative electrode line width L_2/H should be unity. This corresponds with what is seen in the initial polarization plots.

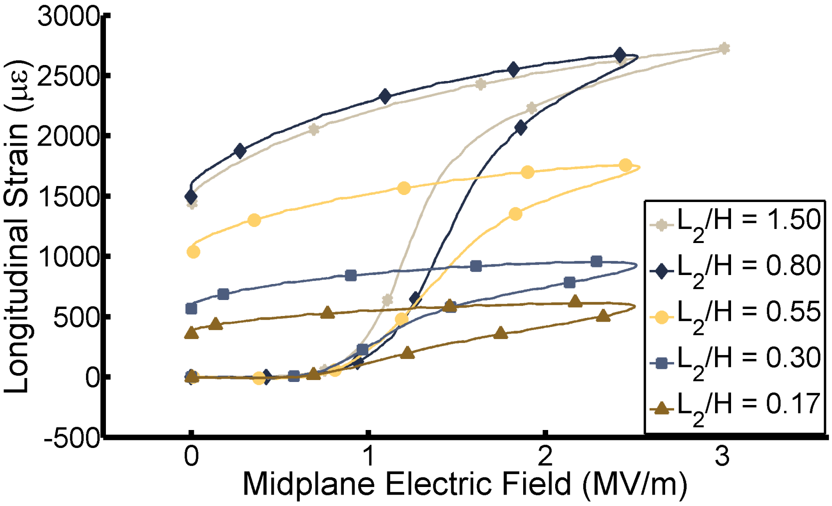

Figure 4.6: Initial polarization cycle of custom actuators

The initial polarization plots again correspond to the dielectric considerations of Gauss's law used in chapter 3. Again applying a DC voltage to the actuators caused the strain magnitudes to steadily increase in time. In actuator number 10, applying a DC voltage for 7 minutes caused the longitudinal strain to increase by 3670 $\mu\epsilon$ until it saturated. Actuator number 5 contrasts this by saturating in seconds, but only to 2700 $\mu\epsilon$. The time to saturate the strain induced by the poling process was found to be inversely proportionally to the relative electrode line width.

Unipolar cycling was run on the actuators after the strain had been saturated during the DC poling process. The results of the unipolar actuation cycles are shown in figure 4.7. Strains are reported relative to the poled state. It is shown that as the relative electrode line width L_2/H increases from 0.17 to 1.50, the peak strain decreases from 1916 $\mu\epsilon$ to 1290 $\mu\epsilon$. Similarly the remnant strain decreases from 500.2 $\mu\epsilon$ to 125.9 $\mu\epsilon$. The remnant strain for each actuator was fully recovered back to the zero over time in a creep like process. The time required for the strain to creep back to zero was found be inversely proportionally to the relative electrode line width. The DC polarization cycle caused any performance peaks at $L_2/H = 1.0$ to disappear.

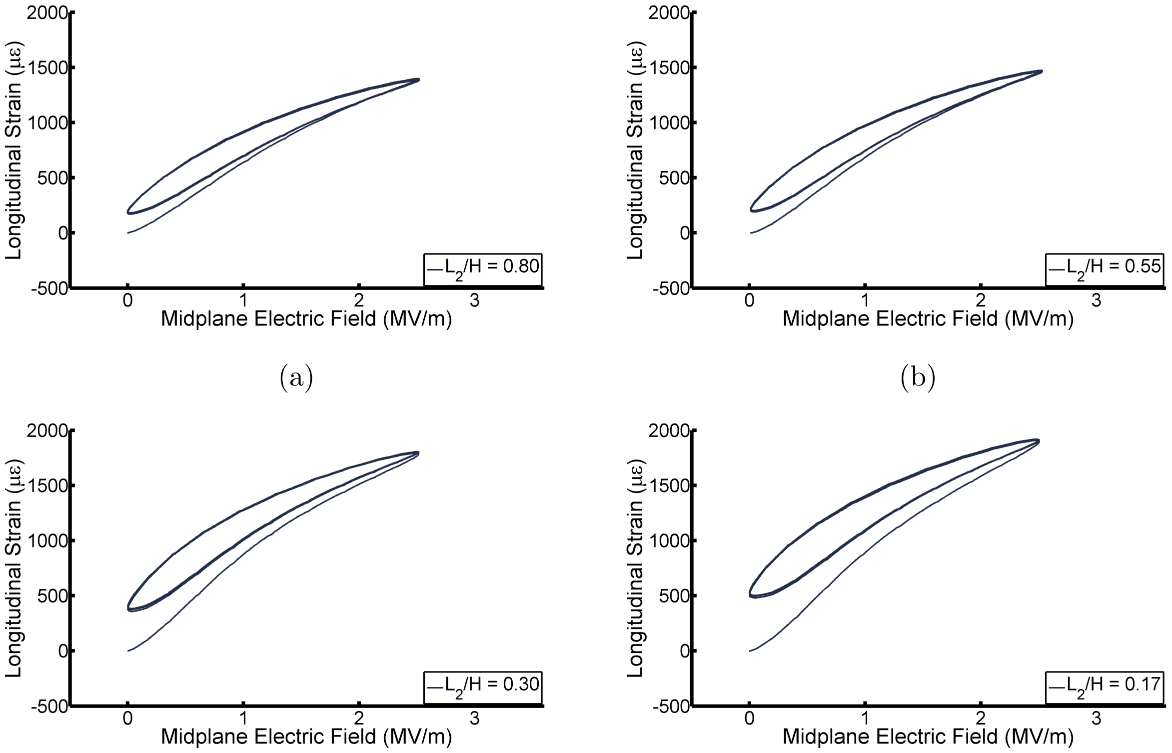

(a) (b)

(c) (d)

Figure 4.7: A comparison of custom actuators with unipolar sinusoidal electric field of 2.5 MV/m at 0.1 Hz applied after DC polarization.

Next a bipolar electric field cycle was run on the custom actuators. The results of the bipolar actuation cycle is shown in figure 4.8. The strains are reported relative to the unpoled actuator state. For actuators with larger relative electrode line widths L_2/H, the bipolar response resembles a strain-electric field butterfly loop. As the electrode line width begins to decrease, the symmetry of the butterfly loop degrades. When the electric field is positive (aligned with the polarization direction), the peak strain compared to unipolar peak strain degrades from a 3.2% difference to a 14.8% difference as relative electrode line widths decrease. When the electric field is negative (antiparallel with the polarization direction), the peak strain compared to unipolar peak strain degrades from a 23.9% difference to a 82.6% difference as relative electrode line widths decrease. There is less strain drop when the electric field is parallel to polarization rather than antiparallel.

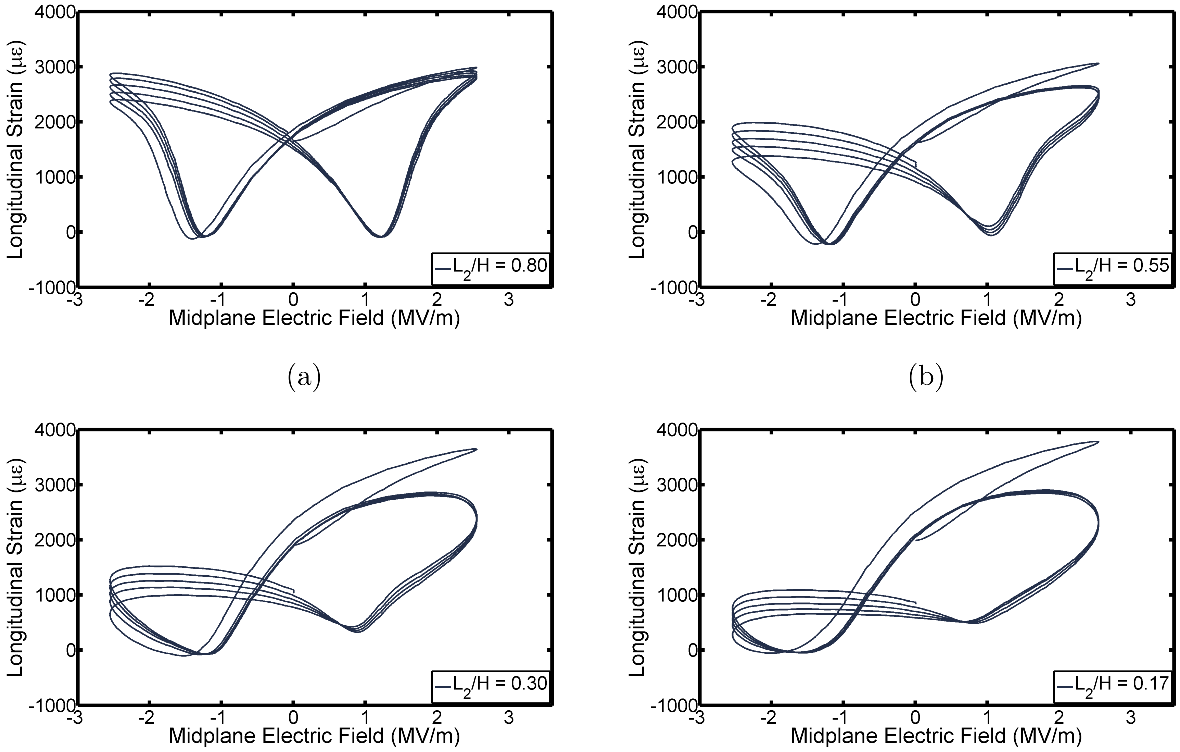

(a) (b)

(c) (d)

Figure 4.8: A comparison of custom actuators with bipolar sinusoidal electric field from -2.5 MV/m to 2.5 MV/m at 0.1 Hz applied after DC polarization.

Considering that the electrode geometry greatly affects the qualitative behavior of the actuator when run with a bipolar electric field cycle, a comparison was made to the bulk material. The results of the bipolar actuation cycle for the monolithic wafer with uniform electrodes is shown in figure 4.9. The bulk response showed very little dependence on electric field direction and had a near symmetric response. Also, the actuator needed very few cycles for its free strain output to train into a single closed loop curve.

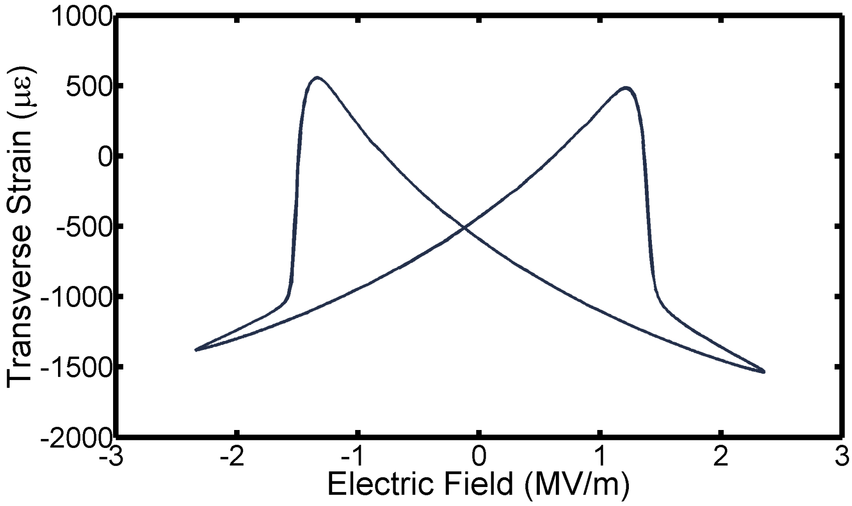

Figure 4.9: Monolithic wafer with uniform electrodes response to bipolar electric field from -2.5 MV/m to 2.5 MV/m.

Actuator 10 was used to test its abilities as a shape memory self-latching actuator. Figure 4.10 shows the results of the self-latching tests at various back electric fields. At zero back electric field the remnant longitudinal strain was 1392 $\mu\epsilon$ and the remnant transverse strain was -639 $\mu\epsilon$. As the back electric field increased to -1.25 MV/m the remnant longitudinal strain was -466.1 $\mu\epsilon$ and the remnant transverse strain was 290.4 $\mu\epsilon$. The remnant longitudinal strain range for custom actuator 10 was 1857 $\mu\epsilon$, while the remnant longitudinal strain range for the MFC actuator was 1290 $\mu\epsilon$.

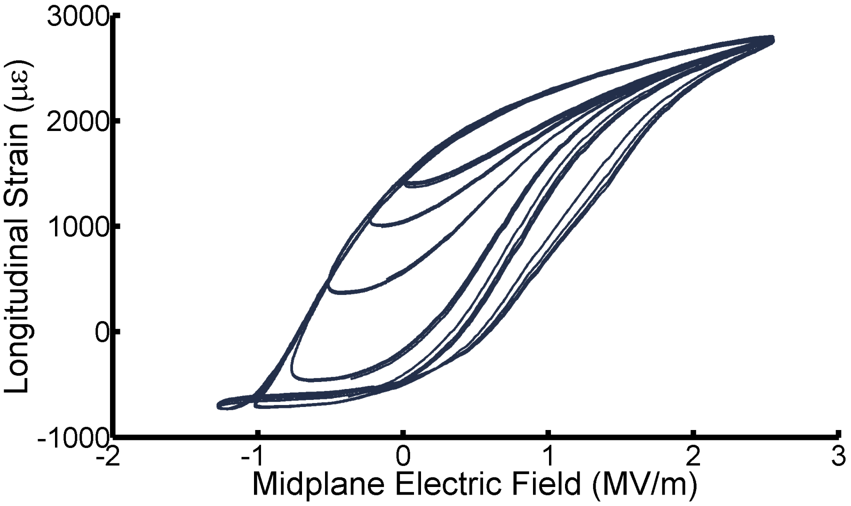

(a)

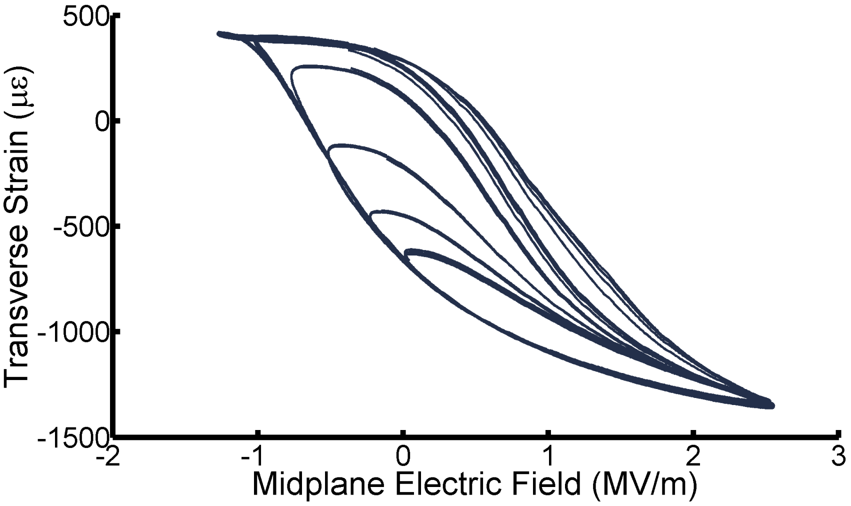

(b)

Figure 4.10: Strain versus voltage behavior on custom actuator 10 for strain locking tests. Subfigure (a) indicates longitudinal strain output while subfigure (b) indicates transverse strain output.

Considering the custom actuators with smaller relative electrode line widths L_2/H, reorient their polarization under larger time scales, the frequency response of actuator 10 was investigated. Figure 4.11 shows the results of the frequency tests. Strain differences are reported as the difference in strain from -1 MV/m to 2.5 MV/m At the lowest frequency, 0.025 Hz, the longitudinal strain difference was 3448 $\mu\epsilon$ and the transverse strain difference was 1710 $\mu\epsilon$. As the frequency increased, the strain differences dropped. At the highest frequency, 2.0 Hz, the longitudinal strain difference was 2554 $\mu\epsilon$ and the transverse strain difference was 1307 $\mu\epsilon$. The strain difference drops corresponds to a 25% decrease.

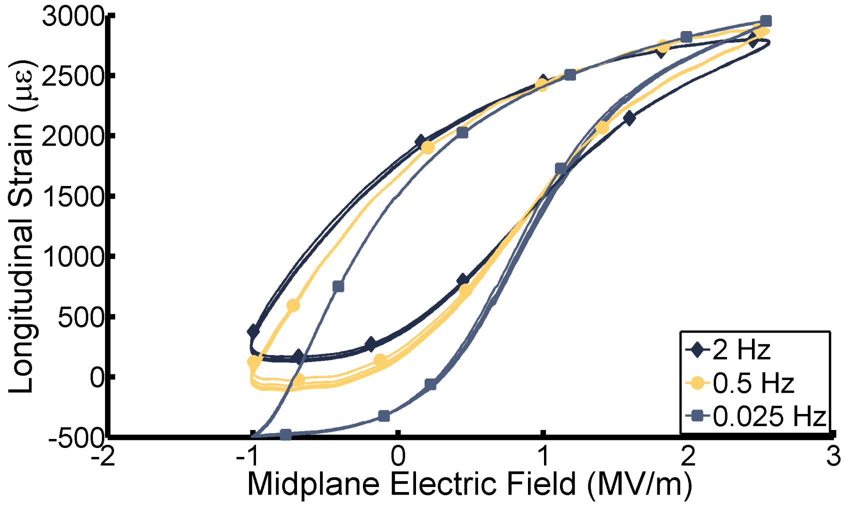

(a)

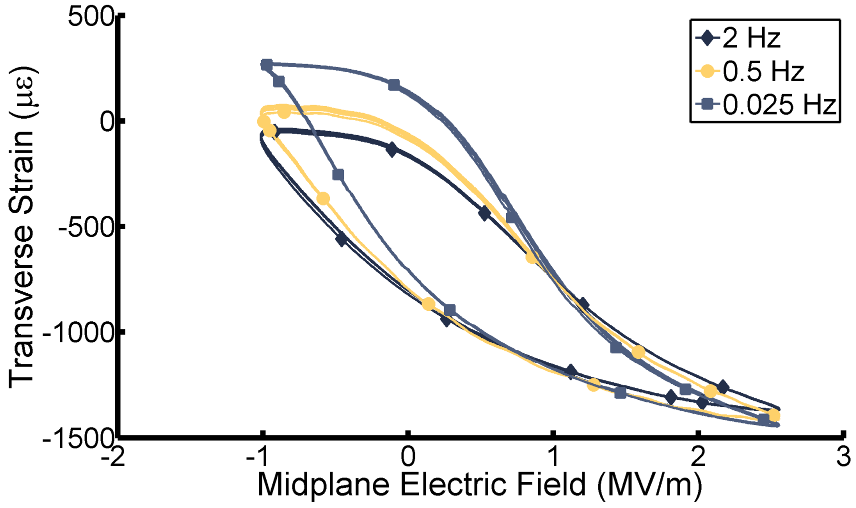

(b)

Figure 4.11: Strain versus voltage behavior on custom actuator 10 for frequency response tests. Subfigure (a) indicates longitudinal strain output while subfigure (b) indicates transverse strain output.

4.4 Computational Model

The analysis in this section addresses the interaction of IDE with the polarization process and the resulting effects on the piezoelectric properties of the device. Interactions between electrode geometry, ferroelectric plate geometry and the polarization process are addressed.

4.4.1 Linear FEM

The finite element approach initially developed by Chen and Lynch [17], outlined below, was extended to 3-D elements for this work. Equating the variation of the electric Gibbs energy density of the system to the virtual work of the external loads yields,

$$\int_{\Omega} (\sigma_{ij}\delta\varepsilon_{ij} - D_i\delta E_i) d\Omega = \int_{\Omega} (b_i\delta u_i - \rho\delta\phi)\, d\Omega + \int_{\Gamma_t} t_i\delta u_i\, d\Gamma_t - \int_{\Gamma_\omega} \omega\delta\phi\, d\Gamma_\omega, \tag{4.1}$$

where σ_{ij} is the Cauchy stress tensor, ϵ_{ij} is infinitesimal strain, D_i is electric displacement, E_i is electric field, b_i are body forces, u_i are displacements, t_i are surface tractions, ω is free surface charge density, ϕ is electric potential, δ denotes a virtual variable, Ω denotes the body volume, Γ_ω denotes the body surface in which ω is defined, and Γ_t denotes the body surface in which t is defined. Repeated subscripts imply a summation. Variables i, j, k, l are spatial indices. The constitutive laws given by:

$$\begin{aligned} \sigma_{ij} &= c^E_{ijkl}\left(\varepsilon_{kl} - \varepsilon^r_{kl}\right) - e_{kij}E_k \\ D_i - P^r_i &= e_{ikl}\left(\varepsilon_{kl} - \varepsilon^r_{kl}\right) + \kappa^{\varepsilon}_{ij}E_j, \end{aligned} \tag{4.2}$$

are used in this formulation, where c^E_{ijkl} are the elastic stiffness tensor coefficients, e_{kij} are the piezoelectric tensor coefficients, κ^{ϵ}_{ij} are the permittivity tensor coefficients, ϵ^r_{kl} are the remnant strain components, and P^r_i are the remnant polarization components. Substituting the constitutive relations, strain-displacement equations and electric field-potential equations into the energy functional of equation 4.1 simplifies the functional into terms in the independent variables. Interpolation of the independent variables using shape functions gives the fields within the elements in terms of nodal values.

Eight-noded linear isoparametric brick elements were used. Isoparametric functions were utilized for calculating global derivatives. While an eight-noded brick element has spurious energy modes, and higher order shape functions remedy this problem, it has the advantage of simplicity and speed of calculation when incorporating a micromechanical model. To address the problem of spurious modes, reduced quadrature was used in element integrations.

Using the symmetry of the constitutive tensors and noting that the virtual displacements and potentials are arbitrary gives,

$$\begin{aligned}\int_\Omega \left(c^E_{ijkl} N^u_{b,l} N^u_{a,j} \tilde{u}^b_k - c^E_{ijkl} \varepsilon^r_{kl} N^u_{a,j} + e_{kij} N^\phi_{b,k} N^u_{a,j} \tilde{\phi}^b\right) d\Omega &= \int_\Omega \left(b_i N^u_a\right) d\Omega + \int_\Gamma \left(t_i N^u_a\right) d\Gamma \\ \int_\Omega \left(e_{ikl} N^u_{b,l} N^\phi_{a,i} \tilde{u}^b_k - e_{ikl} \varepsilon^r_{kl} N^\phi_{a,i} - \kappa^\varepsilon_{ij} N^\phi_{a,i} N^\phi_{b,j} \tilde{\phi}^b + P^r_i N^\phi_{a,i}\right) d\Omega &= -\int_\Gamma \left(\omega N^\phi_a\right) d\Gamma,\end{aligned} \tag{4.3}$$

where, a, b are nodal indices, N_a is a shape function for a specific elements node a, and $\tilde{\Box}^a$ denotes a functions nodal value for an element's node a.

This is a system of linear equations that can be simplified by grouping terms into stiffness matrices as given by

$$\begin{aligned}\left[K_{uu}\right]^{ab}_{ik} \tilde{u}^b_k + \left[K_{u\phi}\right]^{ab}_{i} \tilde{\phi}^b &= \int_\Omega \left(c^e_{ijkl} \varepsilon^r_{kl} N^u_{a,j}\right) d\Omega + \int_\Omega \left(b_i N^u_a\right) d\Omega + \int_\Gamma \left(t_i N^u_a\right) d\Gamma \\ \left[K_{\phi u}\right]^{ab}_{k} \tilde{u}^b_k - \left[K_{\phi\phi}\right]^{ab} \tilde{\phi}^b &= \int_\Omega \left(\left(e_{ikl} \varepsilon^r_{kl} - P^r_i\right) N^\phi_{a,i}\right) d\Omega - \int_\Gamma \left(\omega N^\phi_a\right) d\Gamma,\end{aligned} \tag{4.4}$$

where K_{uu} is an elastic stiffness matrix, $K_{u\phi}$ and $K_{\phi u}$ are piezoelectric stiffness matrices, and $K_{\phi\phi}$ is a dielectric stiffness matrix. At each loading step the micromechanical model is used to update the constitutive tensors, remnant strain, and remnant polarizations.

4.4.2 Micromechanical Model

In the micromechanical material model, each element is represented as a set of randomly oriented single crystal grains using the approach of Hwang et al [29] and modified by Chen et al [17]. A work-energy criterion governs switching of the polarization between six equivalent crystal variants. The remnant polarization and remnant strain are found by volume averaging the spontaneous polarization and spontaneous strain of each grain. The remnant polarization, remnant strain, and constitutive tensors are returned to the finite element code and the applied loads are incremented. Each gauss point on an element is coupled with a number of grains with randomized crystallographic orientation and different polarization directions as shown in figure 4.12a. Applying stress or electric field above a work-energy threshold causes the polarization directions to switch into more favorable orientations as seen in the rest of the subfigures of figure 4.12.

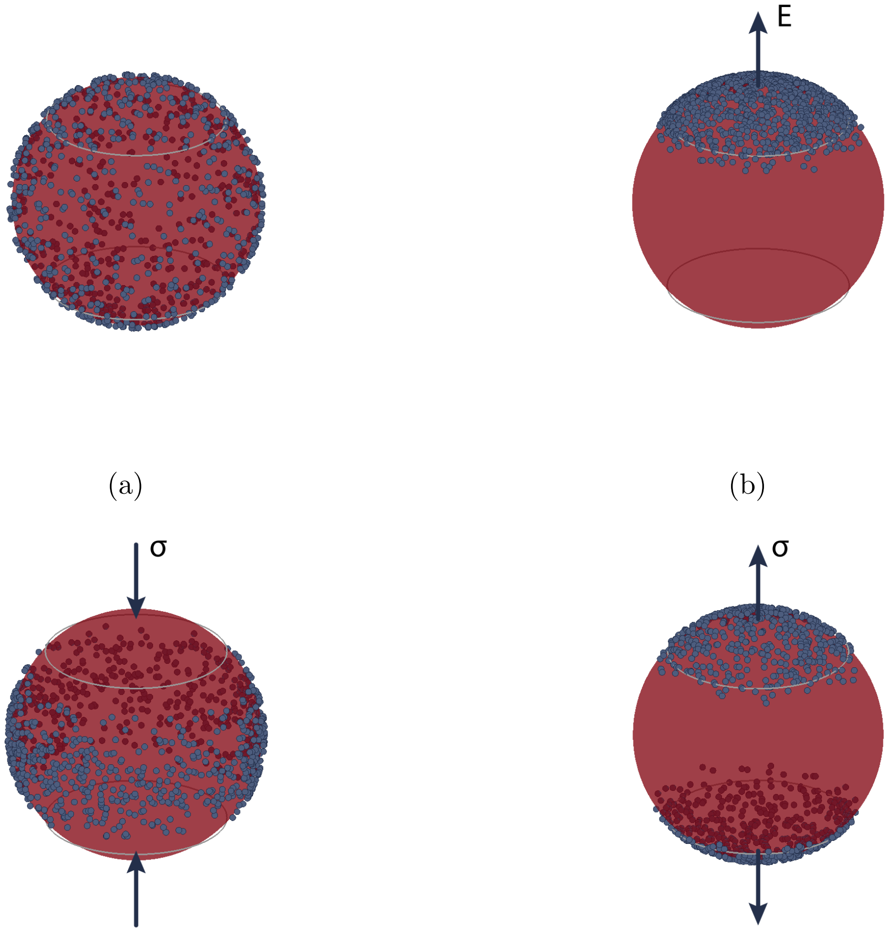

(a)

(b)

(c)

(d)

Figure 4.12: Representation of a set of grains with switchable polarization constrained by the orientation of the grains. The polarization direction of each grain is represented by a dot on the sphere. Subfigure (a) represents an initial random distribution of grains, (b) represents polarization orientation with applied electric field, (c) represents polarization orientation with applied compressive stress, (d) represents polarization orientation with applied tensile stress

Remnant strain, remnant polarization, and constitutive tensors are calculated for each gauss point by performing a volume average of the grain behavior. They are found using the following relations

$$\begin{aligned} \boldsymbol{P}^r &= \frac{1}{n}\sum_{g=1}^{n}\boldsymbol{P}_g^0 \\ \boldsymbol{\varepsilon}^r &= \frac{1}{n}\sum_{g=1}^{n}\boldsymbol{\varepsilon}_g^0 \\ \boldsymbol{c}^E &= \frac{1}{n}\sum_{g=1}^{n}\boldsymbol{c}_g^{E0} \end{aligned} \qquad \begin{aligned} \boldsymbol{e} &= \frac{1}{n}\sum_{g=1}^{n}\boldsymbol{e}_g^0 \\ \boldsymbol{\kappa}^{\varepsilon} &= \frac{1}{n}\sum_{g=1}^{n}\boldsymbol{\kappa}_g^{\varepsilon 0} \end{aligned}, \tag{4.5}$$

where the super script 0 denotes a spontaneous value and n is the number of grains per gauss point.

The switching criterion used in the micromechanical model is given by

$$E_i \Delta P_i^0 + \sigma_{kl}\Delta\varepsilon_{kl}^0 \geq W_s^{cd}, \tag{4.6}$$

where Δ represents a change in polarization/strain from one state to another, W_s^{cd} is the switching work required to change the polarization from orientation c to d. The energy barrier is defined by

$$W_s^{cd} = 2E^0 P^r, \tag{4.7}$$

where E^0 is the coercive field.

4.4.3 Geometry and Boundary Conditions

Interdigitated electrodes on a ferroelectric fiber were modeled as shown in figure 4.2. The model incorporated the ferroelectric substrate between two interdigitated electrodes. By symmetry, only one-eighth of the fiber was required to be meshed. The highlighted region in figure 4.2, indicates the meshed region required for computation. A series of relative electrode line widths,

$$L_2/H = \{0.25, 0.50, 1.00, 2.50, 5.00, 8.33, 9.17\}, \tag{4.8}$$

were varied. The relative electrode gap distance $(L - L_2)/H$ was kept constant at 2.0. The relative substrate depth D/H was kept constant at 1.5.

The mesh was generated with smaller element sizes biased along the electrode edge to account for large electric field gradients. Element sizes were chosen such that the ratio of successive element sizes away from the electrode edge grew at a constant growth factor. A convergence study was performed on each mesh such that the electric field on the positive x_3 face of the meshed region only varied by 0.1%.

The boundary conditions were applied to simulate a free straining actuator under applied voltage. An electric potential, ϕ, was applied on the electrode surface. Due to symmetry an electric potential $\phi/2$ was applied on the positive x_3 face. The electric potentials were linearly ramped until the average electric field on the x_3 face was 2.5 MV/m. Where electric potential was not applied, zero free charge was applied. Displacement symmetries were applied on the positive x_1 face, negative x_2 face and positive x_3 face. Where displacement boundary conditions were not applied, zero tractions were applied.

The material properties of PZT-5A were used for the constitutive tensors and remnant strains and polarizations. The micromechanical model for PZT-5A was tuned by comparing a modeled linear plate actuator with experimental results.

4.5 Discussion and FEM Analysis

4.5.1 Discussion

The commercial MFC underwent tests for feasibility as a shape memory piezocomposite. The controllability of remnant strain versus back voltage due to the self latching tests can be seen in figure 4.13. The longitudinal remnant strain decreased near linearly with the back voltage from 0 kV to -0.8 kV. Decreasing the back voltage further caused the longitudinal strain to increase again. It may prove advantageous to set the remnant strain of the actuator using the voltage range from -1 kV to -2.5 kV due to the decreased sensitivity of the remnant strain to back voltage (i.e. smaller remnant strain difference per change in back voltage).

While the test proved successful, there was some remnant strain creep when the back voltage was removed.

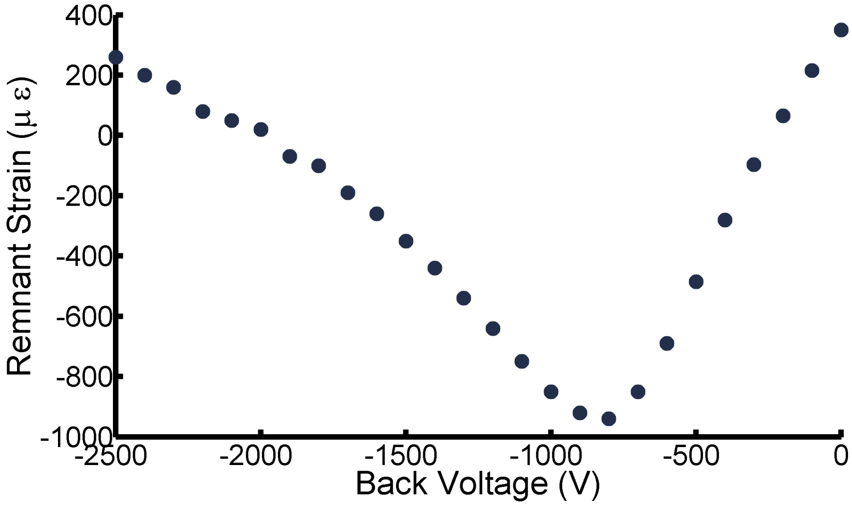

Figure 4.13: Remnant strain versus back voltage from self latching tests for MFC actuator.

The maximum free strain during the initial polarization cycle can be seen in figure 4.14. The same trends can be seen for each set of five actuators in which the relative electrode gap $(L - L_2)/H$ was held constant. As the relative electrode line width L_2/H increases towards 1.0, the maximum longitudinal strain increases. Increasing the relative electrode line width beyond 1.0, the maximum longitudinal strain slowly rolls off. While the trends are the same for each set of actuators with the same relative electrode gap, the peak strain values all increased with an increase of the relative electrode gap. Thus, during the initial polarization cycle, the actuator with the best performance was with a relative electrode line width of 1.0 and with the largest possible relative electrode line gap. The largest relative electrode line gap would be dictated by the desired amount of voltage to be applied to the actuator.

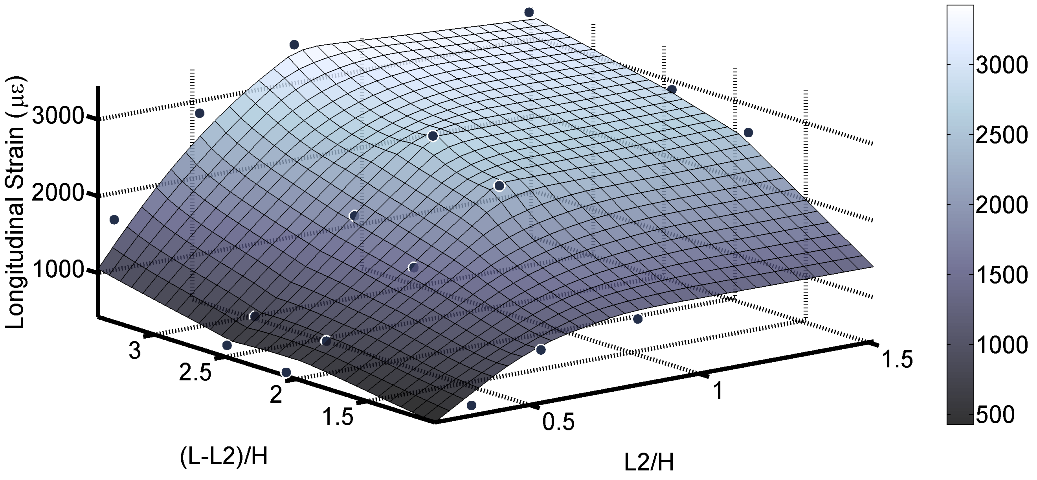

Figure 4.14: Surface plot comparing the maximum free strain during the initial polarization cycle. Black dots indicate experimentally found values. Surface plot generated through interpolation.

After DC polarization such that the free strain of each actuator had been saturated, the free strain response of the actuators to a unipolar electric field vastly changed. A DC polarization cycle changed the actuators strain response, and negated the boundary integral assumptions that were utilized with Gauss's Law. The actuators when monitoring for free charge on the electrodes, showed charge leakage when a voltage was applied. The charge leakage is indicative of conduction within the actuator. It is surmised that the charge leakage is breaking the boundary line integral assumptions used in equation 3.1 and causing the effective size of the electrodes to change. This is allowing for the polarization of actuators with small relative electrode line widths.

The maximum free strain response of the actuators due to a unipolar electric field after saturation can be seen in figure 4.15. Again the same trends can be seen for each set of five actuators in which the relative electrode gap $(L - L_2)/H$ was held constant. Instead of a peak free strain at a relative electrode line width L_2/H of 1.0, the peak free strain now occurs at the smallest relative electrode line width. Increasing the relative electrode line width causes the maximum free strain to decrease. While the trends are the same for each set of actuators with the same relative electrode gap, again the peak strain values all increased with an increase of the relative electrode gap. The actuator with the best performance had the smallest possible relative electrode line width with the largest possible relative electrode gap. The largest relative electrode line gap again would be dictated by the desired amount of voltage to be applied to the actuator.

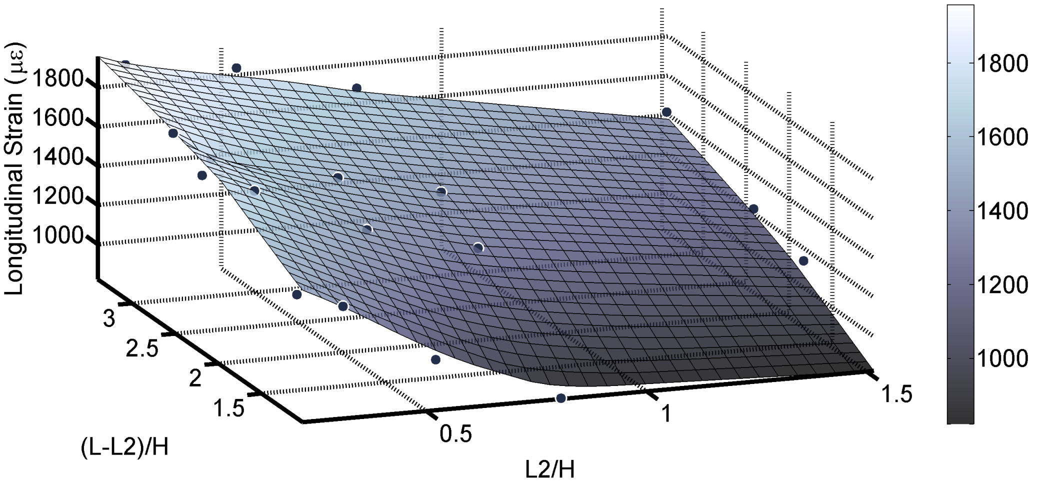

Figure 4.15: Surface plot comparing the maximum free strain response to a unipolar electric field after DC polarization saturation. Black dots indicate experimentally found values. Surface plot generated through interpolation.

While the peak performing actuator after DC polarization was determined to have the smallest relative electrode line width and the largest relative electrode gap, it is not without negative impact on other performance issues. As shown in figure 4.16, reducing the relative electrode line width has a significant impact on the amount of creep strain. Increasing the relative electrode gap cause a slight decrease in the creep, which does mitigate some of the issues. While not plotted, it was also found that the amount of time for the creep strain to relax and to DC polarize the actuators is proportional to the values on this figure. Thus the best performing actuator from figure 4.15 has significant creep strain and relaxation time issues. To mitigate these issues, the relative electrode line width can be increased, but at the sacrifice of free strain output. A piezoelectric strain rosette would benefit from using the actuators with less hysteresis and time dependence. When used for this application, actuators with larger relative electrode line widths would be best.

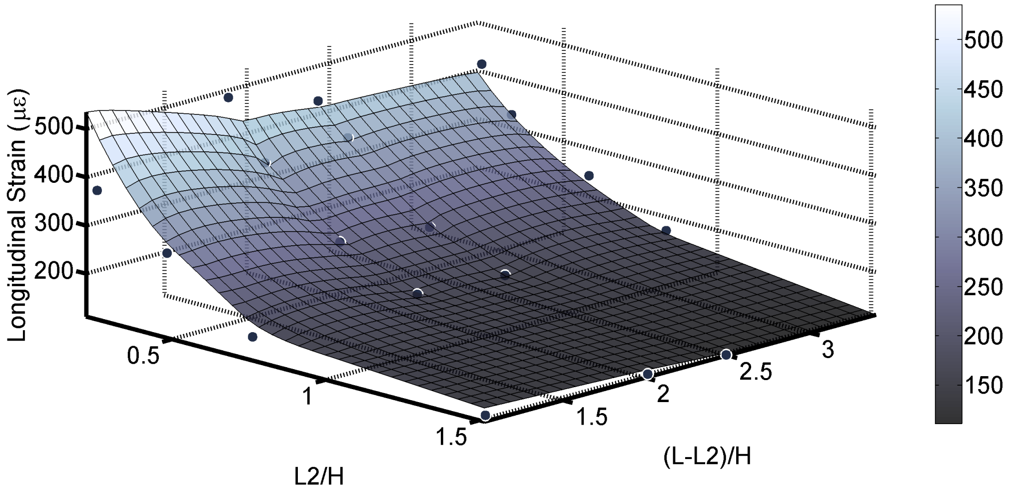

Figure 4.16: Surface plot comparing the creep strain response after an applied unipolar electric field and DC polarization saturation. Black dots indicate experimentally found values. Surface plot generated through interpolation.

The bipolar custom actuator response shown in 4.8 show responses that are both "soft" ferroelectric and "hard" ferroelectric like. A piezoelectric ceramic is characterized depending on its composition whereas "soft" ceramics contain donor dopants and hard ceramics contain acceptor dopants. One of the differing characteristics of these materials is "soft" ceramics are easier to polarization reorient while "hard" ceramics are harder to polarization reorient. With respect to this characteristic, actuators with small relative electrode line widths were shown to act more like a "hard" ferroelectric during bipolar actuation. This contrasts with the actuators with large relative electrode line widths that act like a "soft" ferroelectric. The PZT-5A material used in the actuators is a "soft" ferroelectric and was easily able to reorient its polarization as shown in figure 4.9. Using only geometry, the intrinsic material response was vastly affected.

Using the bipolar actuator response, a midplane coercive field $E_{\mathrm{C}}^{\mathrm{Mid}}$ was found for each custom actuator. The midplane coercive field values were compared to the coercive field of the bulk material $E_{\mathrm{C}}^{\mathrm{Bulk}}$ in figure 4.17. The coercive field ratio $E_{\mathrm{C}}^{\mathrm{Mid}}/E_{\mathrm{C}}^{\mathrm{Bulk}}$ equal to unity indicates that the midplane coercive field and the bulk coercive field are in agreement. When the relative electrode gap $\left(L - L_2\right)/H$ was greater than 2.0, the coercive field ratio did not vary with the relative electrode line width L_2/H. When the relative electrode gap was below 2.0, there were larger gradients on the surface indicating that the coercive field ratio was no longer uniform. This trend follows the observations of the average midplane, maximum midplane and minimum midplane electric fields from figure 3.11.

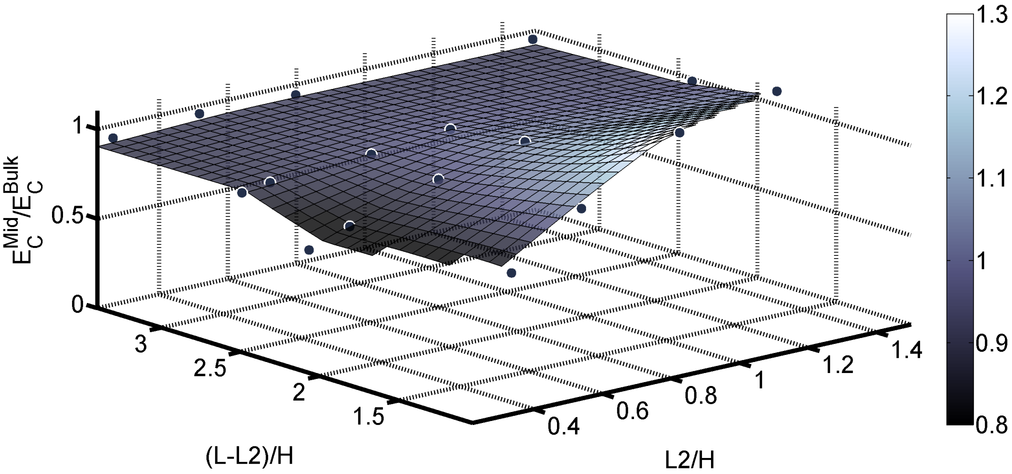

Figure 4.17: Surface plot comparing the midplane coercive field $E_{\mathrm{C}}^{\mathrm{Mid}}$ to the bulk material coercive field $E_{\mathrm{C}}^{\mathrm{Bulk}}$. Black dots indicate experimentally found values. Surface plot generated through interpolation.

For its large free strain response, actuator 10 was tested for its feasibility as a shape memory piezocomposite actuator. The remnant longitudinal strain versus back electric field for custom actuator 10 can be seen in figure 4.18. The figure shows that as the back electric field decreases from 0 MV/m to -0.8 MV/m the remnant longitudinal strain steadily decreases. Further decreasing the back electric field, the remnant longitudinal strain asymptotes to -466.1 $\mu\epsilon$. The "hard" ferroelectric behavior of actuator 10 prevents polarization reorientation contrasting the MFCs response to back field in figure 4.13.

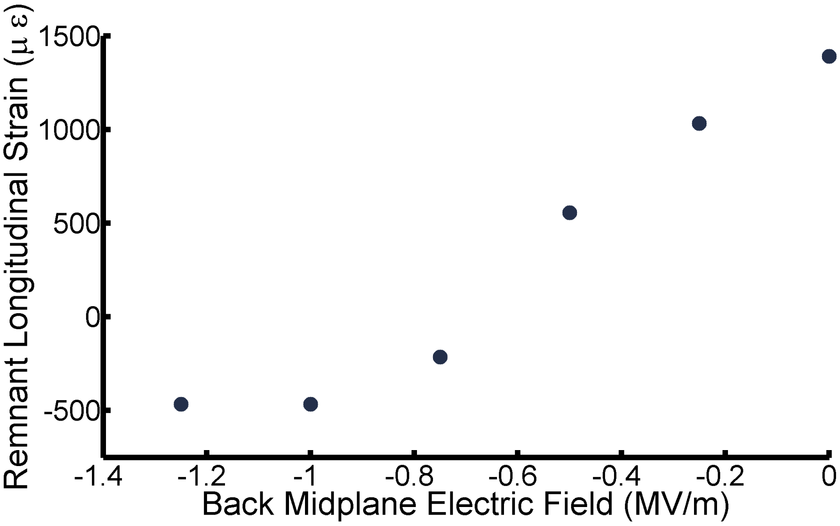

Figure 4.18: Remnant strain versus back electric field for custom actuator 10

4.5.2 FEM Analysis

The computed results of the polarization of the actuator with the relative electrode line width ratio L_2/H of 1.0 is shown in figure 4.19. The electric potential distribution within the actuator is shown in figure 4.19a. Electric potential is indicated in volts. The equipotential lines coalesce around the electrode edge. This indicates that the electric field is larger relative to the rest of the actuator in this area. In the areas to the right of the electrode the equipotential lines are uniformly spaced and vertical. This indicates that the electric field is uniform and pointed along the x_3 direction. Directly underneath the electrode the equipotential lines are more spaced out relative to the rest of the actuator and rotate from horizontal to vertical. This indicates that the electric field is lower in this region and rotates from being normal to the electrode (in the x_2 direction) to aligning in the x_3 direction. The computed results confirm and reiterate the designated regions of the dead zone, uniform field and field concentration region.

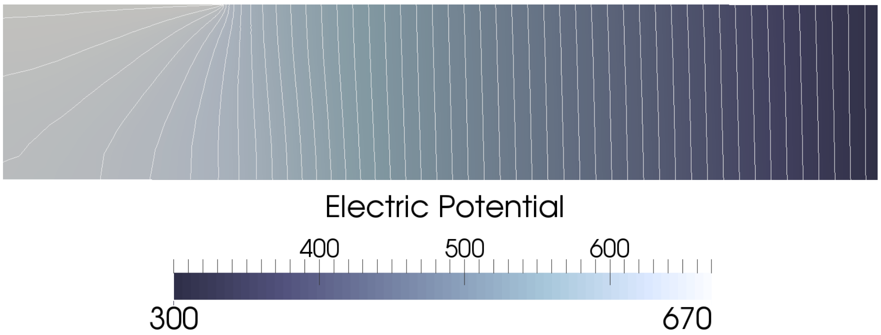

(a)

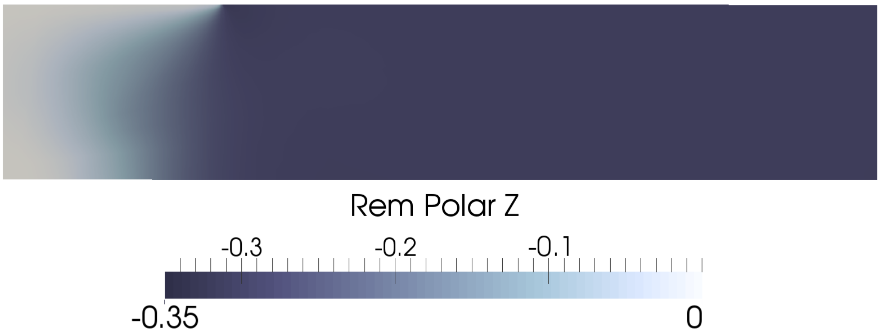

(b)

Figure 4.19: Computed results of actuator with maximum applied voltage. Subfigure (a) represents the electric potential distribution within the actuator. White lines indicate equipotential lines. Subfigure (b) represents the x_3 component of remnant polarization within the actuator. The electrode is located on the top left face.

The remnant polarization component in the x_3 direction is shown in figure 4.19b. Remnant polarization is indicated in C/m^2 The maximal remnant polarization magnitude was set for the material to be 0.33 C/m^2. To the right of the electrode the material is uniformly polarized to its maximal value in the $-x_3$ direction. Underneath the electrode, there is little polarization along the x_3 direction. The polarization rotates from pointing in the x_2 direction to the x_3 direction. The portion of polarization pointing in the x_2 direction actually can hinder the actuation in the uniform field region due to d_{31} mode actuation in the dead zone.

The computed relative remnant strain versus relative electrode line width is shown in figure 4.20. Relative remnant strain is defined by the normal remnant strain in the x_3 direction ϵ^r divided by the remnant strain in a bulk material in the polarization direction ϵ^r_{Bulk}. For the actuator with the smallest relative electrode line width, the relative strain was 31.43%. The relative strain then increases fairly linearly with the relative electrode line width. At a relative electrode line width of 1.0, the relative electrode line width is maximal at 77.4%. Continued increase in the relative electrode line width causes the relative strain to decrease. The trend matches with the initial polarization cycle of the custom actuators shown in figure 4.6.

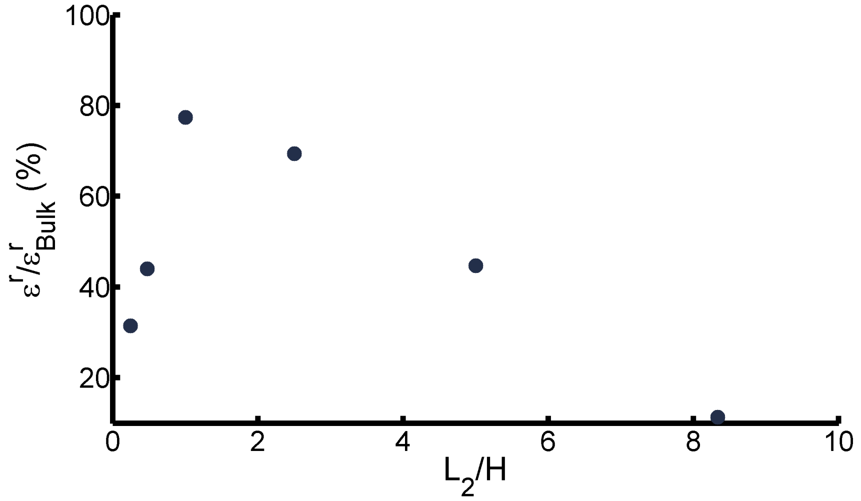

Figure 4.20: Computed results for normal remnant strain in the x_3 direction versus relative electrode length L_2/H. Strain values were normalized by the remnant strain of a linear plate actuator.

The computational model was able to predict the trends of the custom actuators only for the initial polarization cycle. There is a phenomenon from the geometry of interdigiated electrodes on a ferroelectric substrate that can not be captured by a micromechanical finite element model with a work-energy switching criterion. More sophisticated models are required that can capture the mechanism causing creep, frequency dependency, and time dependent polarization from a DC voltage.

For relative electrode line widths greater than or equal to one, there is very little strain creep and the time to creep is on much smaller time scales. Actuators with this configuration still have increased hysteresis compared to monolithic actuators with uniform electrodes. The finite element model can be used to explain this phenomenon.

Figure 4.21 shows the computed polarization state of a fiber. The longitudinal (horizontal) electric field away from the electrodes results in uniform polarization along the fiber axis. In this region the fiber extends along its length and shrinks in the vertical direction. The horizontal uniform field between alternating electrodes causes lateral extension along the fiber axes corresponding to d_{33} and transverse contraction corresponding to d_{31}. The longitudinal component of electric field is zero beneath the electrodes and the material is polarized vertically. This results in a shape mismatch between the electroded area and the region away from the electrodes. This shape mismatch results in stress. Larger stress occurs when the transition in polarization is more abrupt. The field concentration at the edges of the electrodes corresponds to a very large strain mismatch while diffuse regions have a lower strain mismatch.

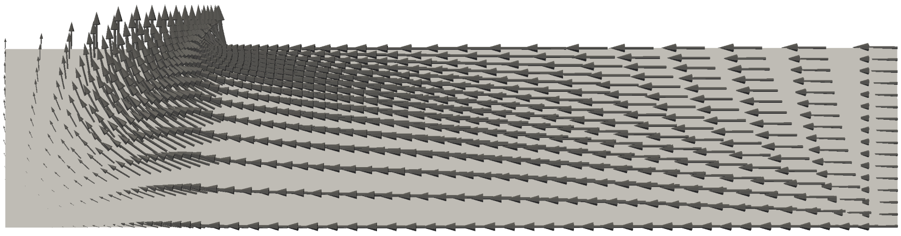

Figure 4.21: Polarization state at maximum applied voltage. The arrows are scaled with the polarization magnitude, where the maximum polarization was 0.31 C/m^2. The electrode edge is on the top left face.

These strain mismatches yield corresponding stresses in the material after poling as shown in figure 4.22. The largest stress occurs when the field gradient is greatest beneath the electrode. The uniform field region away from the electrode experiences no polarization induced stress. The stress state changes under application of electric field. When a large field is applied, the strain mismatch between the region under the electrode and the region away from the electrode increases. This results in ferroelastic polarization changes in the regions near the electrode. When the field is removed, the shape mismatch is reduced. This induces a reverse ferroelastic polarization change.

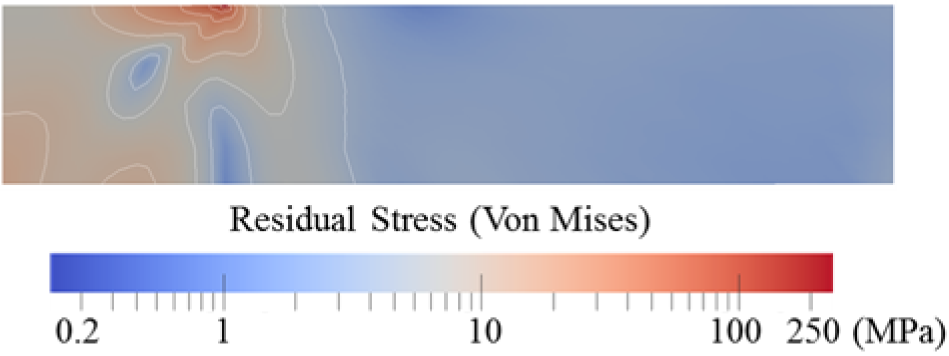

Figure 4.22: Model of the residual stress state when the voltage is removed from the fiber after poling. The electrode is located on the top left face.

The ferroelastic induced polarization changes can be seen in figure 4.23. Figure 4.23 shows the difference in remanant polarization states between the fully applied voltage and when the voltage is removed. When the voltage is applied the ferroelastic switching causes more remanant polarization to be pulled upwards towards the electrode. Upon release, the remanant polarization states return as reflected in figure 4.23. This results in the experimentally observed increased hysteresis in the MFC over that of the uniformly poled plate of the same material.

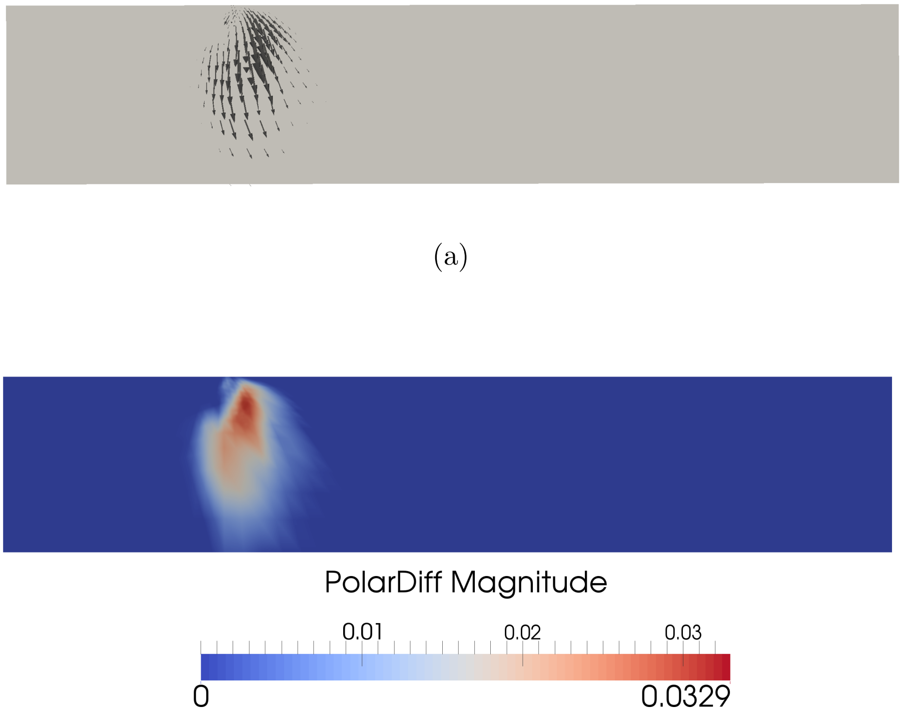

(a)

(b)

Figure 4.23: Difference in the remanant polarization when the voltage is removed and when the maximum voltage is applied. (a) Shows a a vector plot of the polarization difference. The arrows are scaled such that the maximum arrow size corresponds to $0.03\,\mathrm{C/m^2}$ (b) Shows a contour plot of the polarization difference.

4.6 Conclusions

A commercial MFC was tested for its abilities as a self-latching shape memory piezocomposite actuator. It was found that by applying various back voltages, the remnant strain of the actuator could be controlled. The remnant strain could be controlled over a range of 1290 $\mu\epsilon$.

Twenty custom actuators were made and tested to determine their actuation performance relative to the commercial MFC actuator. Every set of five actuators had had different relative electrode line widths and the same relative electrode gap distance. After an initial polarization cycle, the actuator with the highest peak strain had the largest relative electrode gap and a relative electrode line width equal to 1.0.

After a DC electric field was applied to each actuator until their strains saturated, the actuator responses changed. The actuator with the highest peak strain had the largest relative electrode gap and smallest relative electrode line width. For unipolar actuation, creep strain magnitude, creep strain time, and hysteresis were all found to be inversely proportional to the relative electrode line width and relative electrode gap. For bipolar actuation, the strain-electric field loop of the actuator with the largest relative electrode line width resembled a typical butterfly loop. As the relative electrode line width was decreased, the butterfly loop became more asymmetrical with little strain when the electric field was antiparallel to the polarization direction.

Actuator 10 was chosen to test as a self-latching shape memory actuator. While actuator 20 had the highest peak strain, actuator 10 was chosen such that it resisted polarization reorientation when the electric field was negative. Compared to a commercial MFC, it was found that the remnant strain could be controlled over a larger range of 1857 $\mu\epsilon$. The remnant strain asymptotes as the back electric field increased due to the resistance of the actuator to change polarization. While the larger strain range might be more favorable for a self-latching actuator, there is significantly increased strain creep. At the detriment of strain actuation, a large relative electrode line width could be used to mitigate strain creep. A large relative electrode line width would also be useful for a strain/actuator rosettes by reducing frequency dependency and other time dependent effects.

A micromechanical computational model was incorporated to consider its ability to predict actuator performance. While, the computational model could predict actuator performance for the initial polarization cycle, it could not compensate for the time dependent effects of the actuators. There is some mechanism due to the geometry of the interdigitated electrodes that increases time dependency of the actuators as the relative electrode line width shrinks. More sophisticated models must be developed in order to handle time dependent effects before they can be used to predict IDE sensor/actuator performance.

CHAPTER 5

Piezocomposite Actuator Frequency Dependency

5.1 Introduction

The motivation of this chapter is to address the frequency response of piezocomposite actuators. Piezocomposite actuators are commonly used in vibration control of aeroelastic structures. Knowledge of precise actuator output is thus important over a wide array of frequencies. The piezocomposite actuator explored in this manuscript was the macro fiber composite or MFC [9]. It was found that there was a sharp decrease in MFC performance as it was electrically driven from 0.1 Hz to 15 Hz. Specifically, there was nearly 50% degradation of the low-field, unbiased-operation d_{33} coefficient from published values when operating at 15 Hz.

The focus on this chapter is on the actuation performance of a MFC over a range of frequencies from 0.1 Hz to 15 Hz. A schematic of the MFC is shown in figure 5.1. The interdigitated electrode configuration allows a significant portion of the electric field to point along the direction of the fiber's longitudinal axis. The region of the fiber where this is true is denoted as the uniform field region. Electric field lines along the longitudinal fiber axis allow for d_{33} actuation in plane with the actuator. While this is preferential, the IDE configuration can lead to increased hysteresis and nonlinear responses [101]. In chapter 4, it was found that actuators with small relative electrode line widths and large relative electrode gaps had significantly less creep strain and relaxation times than other actuators.

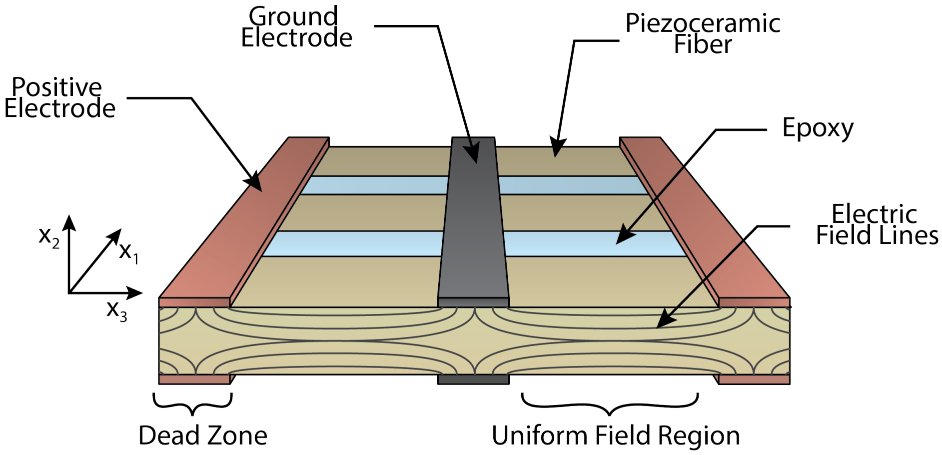

Figure 5.1: Layout of interdigitated electrodes on a macro fiber composite.

Experimentally and computationally, few have addressed the time dependent creep behavior inherent in interdigitated electrode devices. Schröck et al used MFC patches on a flexible beam to characterize hysteresis and strain creep [99, 100]. The creep behavior has a significant affect on the piezocomposite performance when actuating at low frequencies. The performance of the MFC in the frequency range of 0.1 Hz to 15 Hz was investigated. An alternative design using larger electrode line widths was shown to mitigate some strain creep/frequency dependence.

5.2 Experimental Arrangement

5.2.1 Materials and Specimen Preparation

Two actuator types are used in this study. The first actuator tested was a commercially available macro fiber composite from Smart Material Corp. The model number used was M8528-P1 with overall active dimensions of 85 mm × 28 mm × 0.23 mm. Smart Material Corp. reports a MFC thickness of 0.3 mm which includes the substrate and polymide film. The aforementioned thickness dimension of 0.23 mm is for the ferroelectric substrate only. The second actuator tested was custom ordered from Smart Material Corp. The custom actuator type tested was comprised of a PZT-5A plate laminated with copper cladded interdigitated electrodes on polymide film. The custom actuator's substrate was not diced into fibers like the commercial MFC. The active dimensions of the custom actuator were 85 mm × 25 mm × 0.6 mm.

The geometric definitions and actuator micrographs are shown in figure 5.2. Figure 5.2a is a micrograph of the MFC actuator and figure 5.2b is a micrograph of the custom actuator. The vertical dark lines are the electrode lines. The electrode geometry is characterized by the electrode line widths L_2 and electrode spacing L. Another important geometric parameter which is out of plane of the figure is the plate/fiber height, H. The plate/fiber height is defined as the length of the plate/fiber in the x_2 direction. The horizontal bright lines perpendicular to the electrodes in figure 5.2a are epoxy filled gaps between the MFC fibers. The epoxy filled gaps are absent in figure 5.2b due to being a plate actuator.

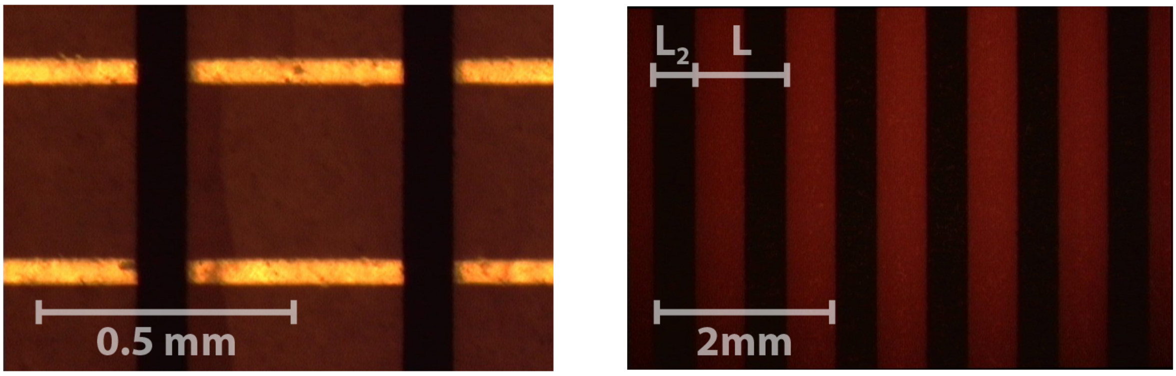

(a) (b)

Figure 5.2: Micrograph image of electrode geometries (a) MFC and (b) Custom actuator. Darker areas indicate electrode lines. Bright areas in subfigure (a) are epoxy filled gaps due to fiber structure.

The geometric parameter values for the actuators are indicated in table 5.1. The relative electrode line width of the custom actuators were designed to be greater than that of the commercial MFC in an attempt to reduce frequency dependency. The creep strain for the two custom actuators and the commercial MFC are shown in figure 5.3. The greater relative electrode gap and relative electrode line width of the custom actuators should alleviate the frequency dependency.

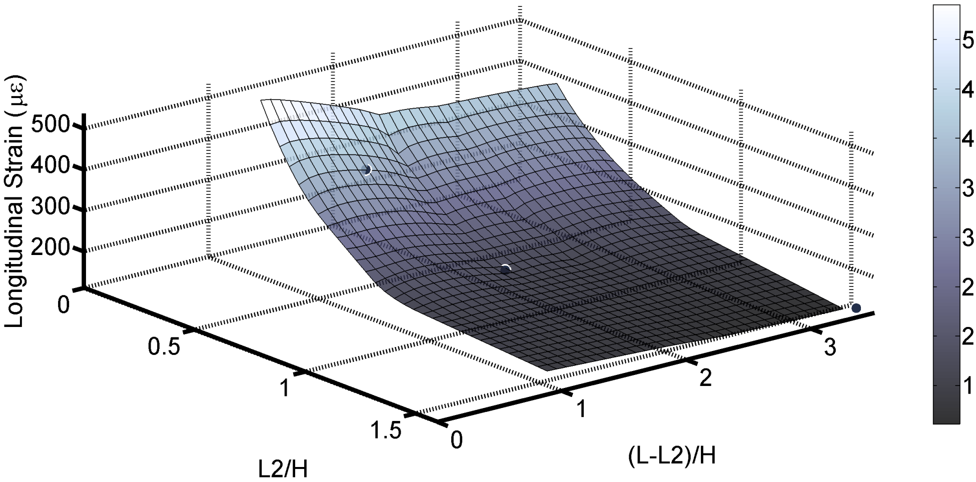

Figure 5.3: Surface plot comparing the creep strain response after an applied unipolar electric field and DC polarization saturation. Black dots indicate experimentally found values. Surface plot generated through interpolation.

Table 5.1: Actuator Geometry Values for Frequency Study

Actuator	L_2(mm)	L(mm)	H(mm)	L_2/H	$(L - L_2)/H$
MFC	0.09	0.45	0.23	0.40	1.60
1	0.48	1.65	0.60	0.80	1.96
2	0.92	3.00	0.60	1.52	3.48

The actuators were electrically driven using a 10 kV voltage amplifier. Both actuators were instrumented with four strain gages. Two strain gages were placed on the positive x_1 and two on the negative x_1 side of the actuator. On a given side the strain gages were oriented along the primary extension direction x_3 and the transverse direction x_2. These directions are denoted longitudinal and transverse respectively. The respective gages on the top and bottom were averaged to compensate for bending. Strain gages were chosen such that they span at least 6 electrodes. The strain gages were fed to a strain gage amplifier. The output of the voltage amplifier and strain gage amplifier were recorded by a digital acquisition system.

5.2.2 Experimental Procedure

The commercial and custom actuators were subjected to various electric loading voltages and frequencies to determine its response. Both actuator types started in a poled state. Each experiment consisted of a sinusoidal applied voltage ranging from a minimum voltage V_{min} to a maximum voltage V_{max}. The frequency of the sinusoidal voltage was swept from a starting frequency f_{start} to a end frequency f_{end}. The total time of the frequency sweep is denoted Δt.

Figure 5.4 shows an example frequency sweep applied to an actuator. In each experiment the frequency was swept from 0.1 Hz to 15 Hz over the course of 20 seconds. Figure 5.4a shows the voltage versus time of an example experiment. The voltage ranges were kept constant while the frequency was increased. Figure 5.4b shows the logarithmic frequency sweep with time. The frequency sweep was logarithmic such that the instantaneous frequency at a given time, t, is given by,

$$f\left(t\right) = f_{\text{start}} \times \beta^{t}, \tag{5.1}$$

where the coefficient β is defined as,

$$\beta \equiv \left(\frac{f_{\text{end}}}{f_{\text{start}}}\right)^{\frac{1}{\Delta t}}. \tag{5.2}$$

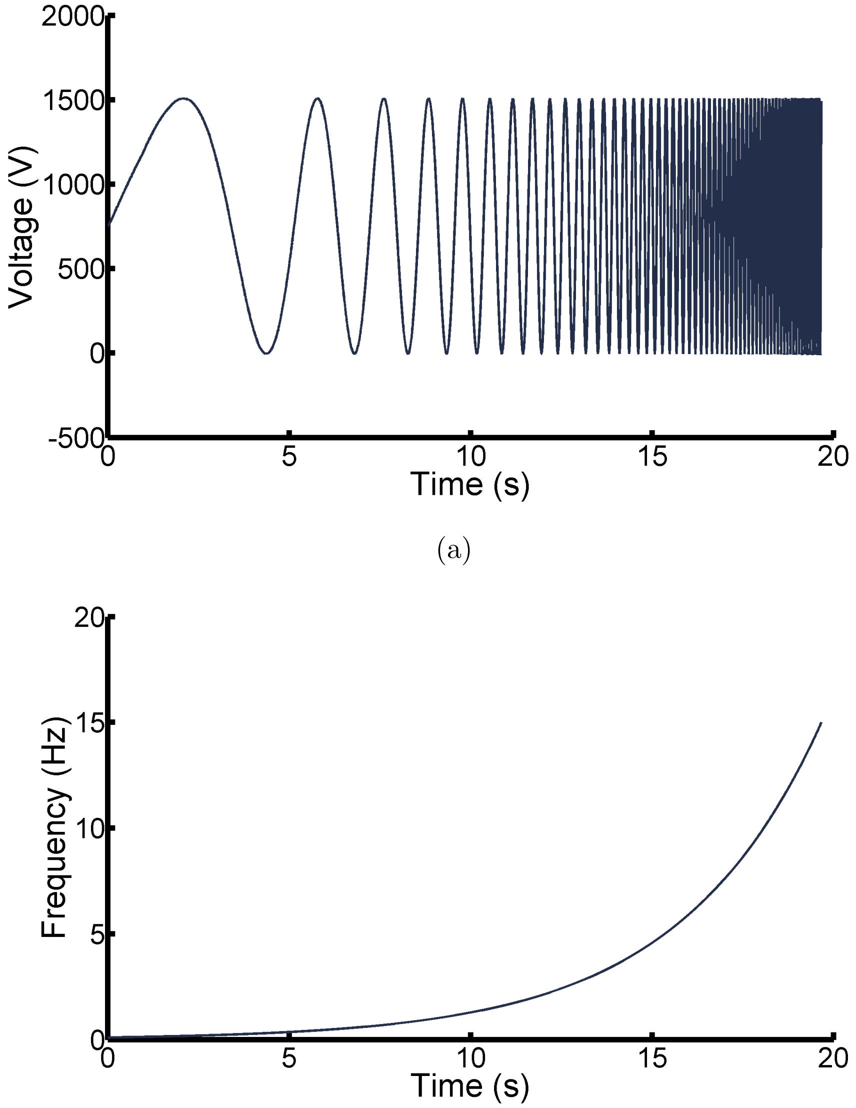

(a)

(b)

Figure 5.4: Example of frequency sweeping of sinusoidal signal. Subfigure (a) represents the applied voltage versus time. The voltage ranges are uniform while the frequency is increased. Subfigure (b) represents the electrically driven frequency applied to the actuator at a given time.

Table 5.2 shows the experimental procedure parameters for each experiment. While each experiment was performed under frequency ranges from 0.1 to 15 Hz, at higher frequencies some experiments hit the voltage amplifier's current limits. The maximum frequency $f_{\max}$ depicts the maximum frequency before the current limit was hit. Experiments 1-7 were performed on the commercial MFC actuator within given operating ranges. The minimum and maximum operating voltages of a MFC are -500 and 1500 volts respectively. The first three experiments were unipolar with V_{min} at 0 volts. The maximum voltages were applied up to 1500 volts in 500 volt increments from the minimum voltage. Experiments 4-7 were performed under biased operation such that V_{min} was -500 volts. The maximum voltages were applied up to 1500 volts in 500 volt increments from the minimum voltage.

Experiments 8 and 9 were performed on custom actuator 1 and experiments 10 and 11 were performed on custom actuator 2. The voltage ranges of experiment 8 and 10 were applied such that the longitudinal strains on the custom actuator at the initial frequencies matched that of the commercial actuator in experiment 2. The voltage ranges of experiment 9 and 11 were applied such that the longitudinal strains on the custom actuator at the initial frequencies matched that of the commercial actuator in experiment 5.

A frequency response measurement was also performed on a monolithic PZT-5A wafer with uniform electrodes. The bulk response of the PZT-5A plate were used to make comparisons of IDE actuators with the bulk material.

Table 5.2: Experimental Procedure for Actuators

Experiment	Actuator	V_{min} (kV)	V_{max} (kV)	f_{start} (Hz)	f_{max} (Hz)
1	MFC	0.00	0.50	0.10	15.0
2	MFC	0.00	1.00	0.10	15.0
3	MFC	0.00	1.50	0.10	15.0
4	MFC	-0.50	0.00	0.10	15.0
5	MFC	-0.50	0.50	0.10	15.0
6	MFC	-0.50	1.00	0.10	11.0
7	MFC	-0.50	1.50	0.10	8.50
8	1	0.00	2.57	0.10	11.1
9	1	-0.60	1.73	0.10	7.42
10	2	0.00	3.16	0.10	9.82
11	2	-0.78	2.23	0.10	9.82

5.3 Experimental Results

The results of experiment 1 is shown in figures 5.5 and 5.6. The figures for experiment 1 give similar qualitative trends for experiments 2 and 3 which also have $V_{\min} = 0\ V$. Figure 5.5 shows the strain versus voltage response during the frequency sweep. Time is depicted by the changing brightness value in the HSV color space. As time increases, the brightness value decreases.

Figure 5.5a shows the longitudinal strain versus voltage for the MFC in experiment 1. As the frequencies increased, the longitudinal strain difference from $V_{\min}$ to $V_{\max}$ of each cycle decreased. This is seen in the figure as the major axis of the elliptical-like cyclic curves rotating to a shallower angle as frequency/time increases. By defining a nominal electric field E as voltage applied divided by electrode spacing L, a piezoelectric coefficient can be defined. The d_{33} coefficient as a function of cycle was defined as,

$$d_{33}\left(N\right) = \frac{\epsilon^{\text{long}}\left(E_{\max}, N\right) - \epsilon^{\text{long}}\left(E_{\min}, N\right)}{E_{\max} - E_{\min}}, \tag{5.3}$$

where N is the current cycle number, $E_{\max}$ is the maximum applied nominal electric field, $E_{\min}$ is the minimum applied nominal electric field, and $\epsilon^{\text{long}}\left(E, N\right)$ is the longitudinal strain as a function of cycle number and electric field applied. The piezoelectric coefficient $d_{33}\left(N\right)$ is geometrically equivalent to the slope of the secant line combining the longitudinal strains from $E_{\min}$ to $E_{\max}$ for a given cycle. As the cycles/frequencies increased, the $d_{33}\left(N\right)$ coefficient for experiment 1 varied from an initial value of 386.1 pC/N to 198.2 pC/N.

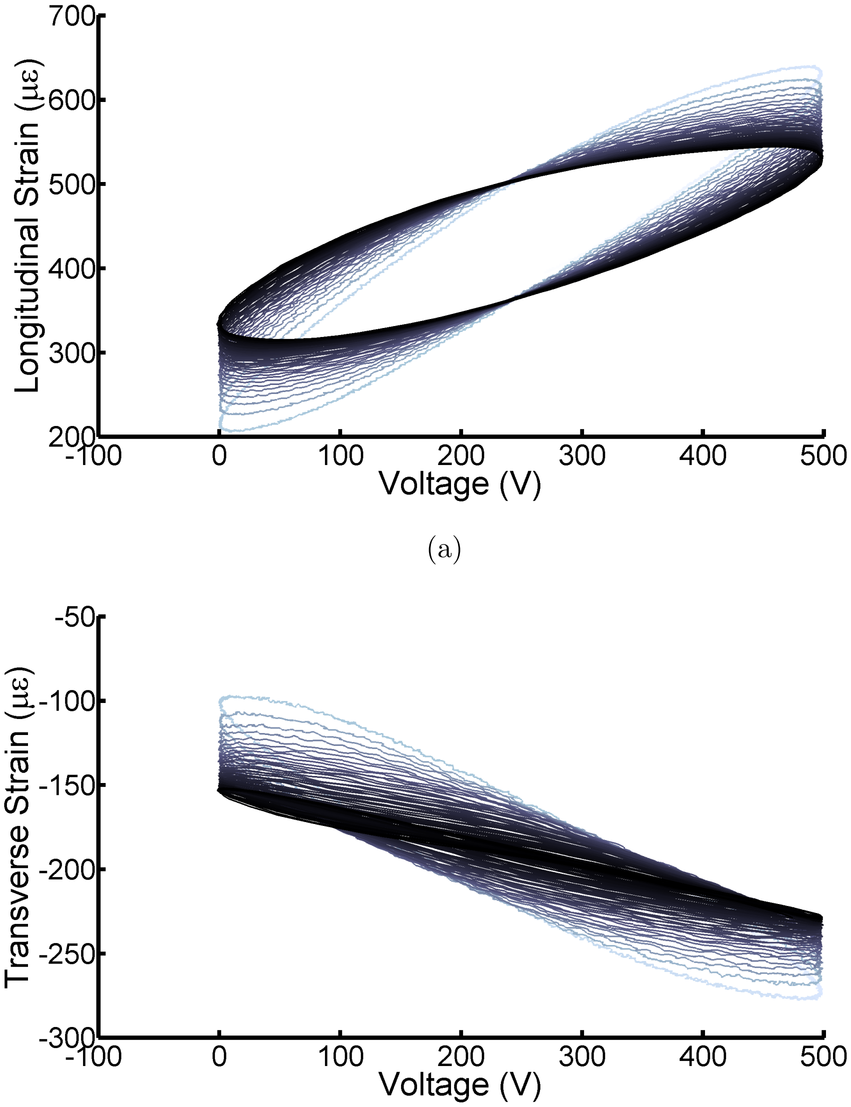

(a)

(b)

Figure 5.5: Strain versus voltage behavior of MFC actuator in experiment 1. Subfigure (a) indicates longitudinal strain output while subfigure (b) indicates transverse strain output. Time/Frequency is inversely proportional to color brightness.

Figure 5.5b shows the transverse strain versus voltage for the MFC in experiment 1. Similar to d_{33}, d_{31} per cycle was defined as,

$$d_{31}(N) = \frac{\epsilon^{\text{tran}}(E_{\max}, N) - \epsilon^{\text{tran}}(E_{\min}, N)}{E_{\max} - E_{\min}}, \tag{5.4}$$

where $\epsilon^{\text{tran}}(E, N)$ is the transverse strain as a function of cycle number and electric field applied. The d_{31} coefficient for experiment 1 varied from an initial value of -158.3 pC/N to -73.4 pC/N as cycles/frequencies increased.

The strain output versus instantaneous frequency of the MFC is shown in figure 5.6 to better demonstrate the behavior of the maximum and minimum strain per cycle. The instantaneous frequency was found from the time data using equation 5.1. In order to find a bounds on the strain output, each local maxima and minima were found such that a corresponding maximum and minimum strain bound could be plotted. The figures show a qualitative horizontal symmetry and asymptotic behavior of the bounds.

When finding the piezoelectric coefficients per cycle, $d\left(N\right)$, the slope of the secant line combining the strains from E_{min} to E_{max} was needed. This corresponds to needing the strain difference per cycle, $\epsilon\left(E_{\text{max}}, N\right) - \epsilon\left(E_{\text{min}}, N\right)$. While the strain difference per cycle was calculated, the instantaneous frequency varied per cycle. In order to find the strain difference and thus a piezoelectric coefficient as a function of instantaneous frequency, the upper and lower strain bounds of figure 5.6 were cubically interpolated. The piezoelectric coefficients as a function of frequency are defined as,

$$\begin{aligned} d_{33}\left(f\right) &= \frac{\epsilon_{\text{max}}^{\text{long}}\left(f\right) - \epsilon_{\text{min}}^{\text{long}}\left(f\right)}{E_{\text{max}} - E_{\text{min}}} \\ d_{31}\left(f\right) &= \frac{\epsilon_{\text{min}}^{\text{tran}}\left(f\right) - \epsilon_{\text{max}}^{\text{tran}}\left(f\right)}{E_{\text{max}} - E_{\text{min}}}, \end{aligned} \tag{5.5}$$

where $\epsilon_{\text{max}}^{\text{long}}\left(f\right)$ is the maximum longitudinal strain bound as a function of frequency, $\epsilon_{\text{min}}^{\text{long}}\left(f\right)$ is the minimum longitudinal strain bound as a function of frequency, $\epsilon_{\text{max}}^{\text{tran}}\left(f\right)$ is the maximum transverse strain bound as a function of frequency, and $\epsilon_{\text{min}}^{\text{tran}}\left(f\right)$ is the minimum transverse strain bound as a function of frequency. Note the order of the binary operation of the strain bounds in the numerator of $d_{31}\left(f\right)$ was chosen to correspond with the order of their values at E_{max} and E_{min}.

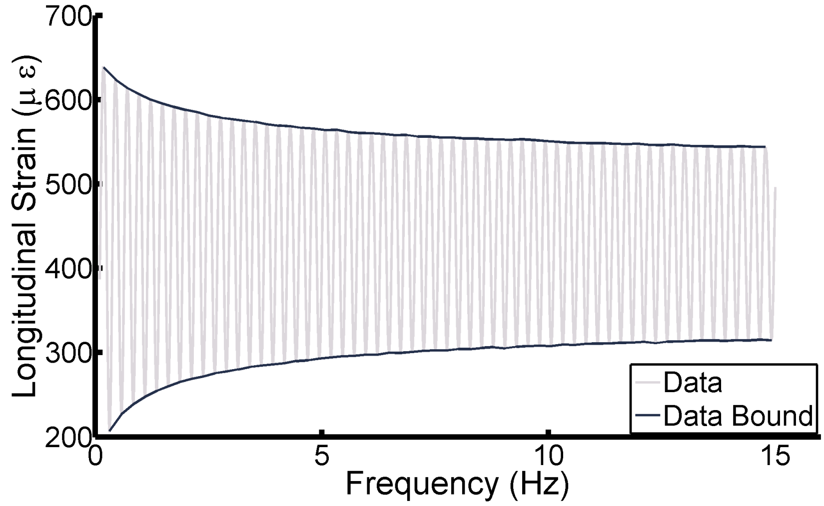

(a)

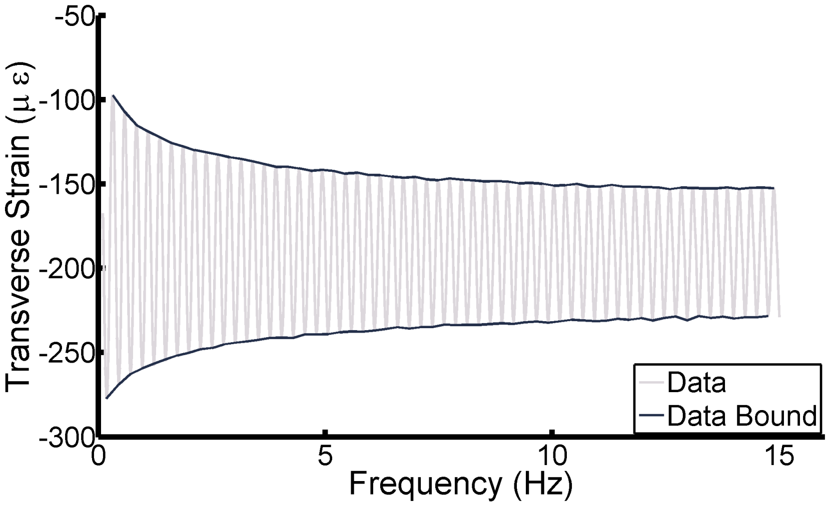

(b)

Figure 5.6: Strain versus frequency behavior of MFC actuator in experiment 1. Subfigure (a) indicates longitudinal strain output while subfigure (b) indicates transverse strain output. Data indicates the strain value at the instantaneous frequency. Data bound indicates the strain envelope which bounds the plot.

For the rest of the manuscript the longitudinal strain difference will be defined as,

$$\epsilon_{\delta}^{\text{long}}(f) \equiv \epsilon_{\max}^{\text{long}}(f) - \epsilon_{\min}^{\text{long}}(f), \tag{5.6}$$

and the transverse strain difference will be defined as,

$$\epsilon_{\delta}^{\text{tran}}(f) \equiv \epsilon_{\min}^{\text{tran}}(f) - \epsilon_{\max}^{\text{tran}}(f)\,. \tag{5.7}$$

Figure 5.6a shows the longitudinal strain versus instantaneous frequency for the MFC in experiment 1. At 0.3 Hz, the MFC had a maximum longitudinal strain of 638.1 $\mu\epsilon$ and a minimum longitudinal strain of 207.1 $\mu\epsilon$. This corresponds to a longitudinal strain difference of 431.0 $\mu\epsilon$. At 14.8 Hz, the MFC had a maximum longitudinal strain of 544.0 $\mu\epsilon$ and a minimum longitudinal strain of 314.6 $\mu\epsilon$. This corresponds to a longitudinal strain difference of 229.4 $\mu\epsilon$. The range of frequencies was reported from 0.3 to 14.8 Hz due to the frequencies in the domain of the strain bound functions being dependent on the instantaneous frequencies of the first and last maxima/minima. As the frequency increased from 0.3 to 14.8 Hz, the longitudinal strain difference decreased by 46.8%.

A similar trend occurred for the transverse strain in experiment 1. Figure 5.6b shows the transverse strain versus voltage for the MFC. At 0.3 Hz, the MFC had a maximum transverse strain of -97.52 $\mu\epsilon$ and a minimum transverse strain of -277.3 $\mu\epsilon$. This corresponds to a transverse strain difference of -179.8 $\mu\epsilon$. At 14.8 Hz, the MFC had a maximum transverse strain of -152.5 $\mu\epsilon$ and a minimum transverse strain of -228.4 $\mu\epsilon$. This corresponds to a transverse strain difference of -75.9 $\mu\epsilon$. As the frequency increased from 0.3 to 14.8 Hz, the transverse strain difference decreased by 57.8%. The output of the MFC actuator was nearly halved for the longitudinal and transverse strain difference.

Figure 5.7 shows the strain differences for experiments 1-3. The strain differences are proportional to the piezoelectric coefficients in equation 5.5. The strain differences seemed to decay and asymptote to a single value per experiment as frequencies increased. The longitudinal strain differences for experiments 1-3 are shown in figure 5.7a. As V_{max} was increased from 500 V to 1500 V the longitudinal strain difference at 0.3 Hz increased from 424.4 $\mu\epsilon$ to 1009 $\mu\epsilon$. As the frequencies increased the longitudinal strain differences decreased. At 14.8 Hz, when V_{max} was increased from 500 V to 1500 V, the longitudinal strain difference increased from 229.1 $\mu\epsilon$ to 706.9 $\mu\epsilon$. From 0.3 to 14.8 Hz the longitudinal strain difference drops at 500 V, 1000 V and 1500 V were 46.0%, 38.9% and 29.9% respectively.

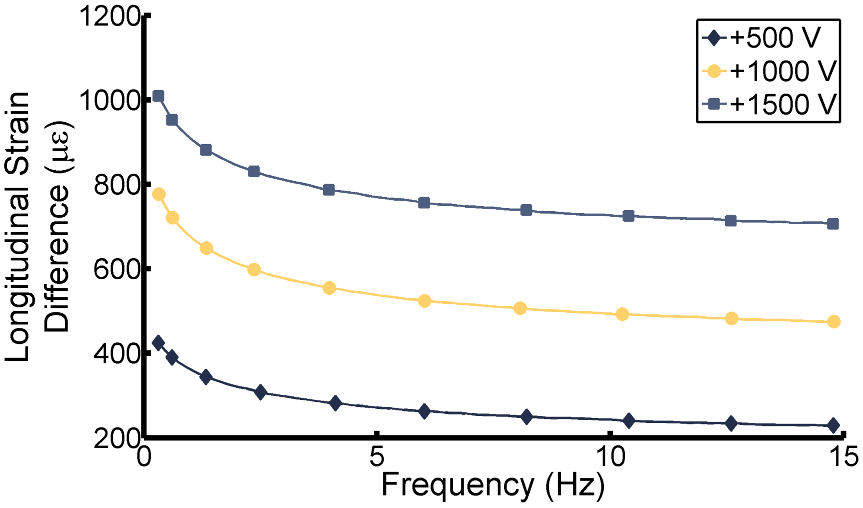

(a)

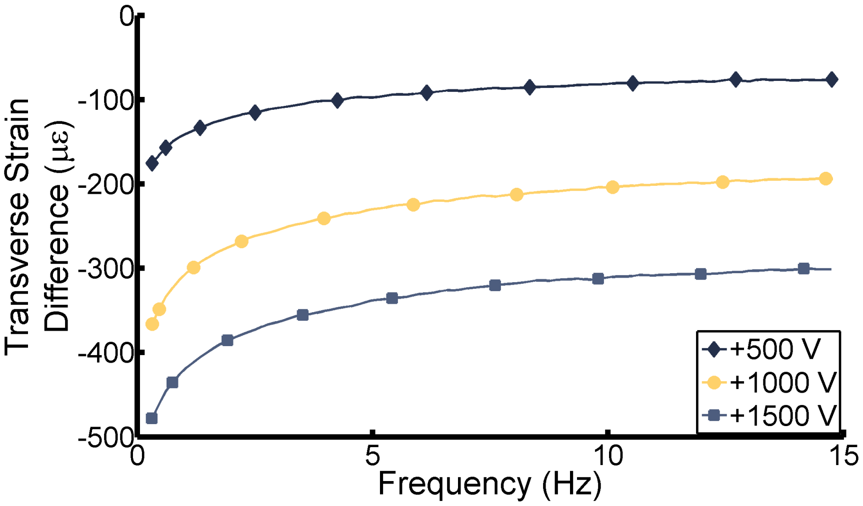

(b)

Figure 5.7: Strain difference versus frequency for experiments 1-3. Subfigure (a) indicates longitudinal strain difference while subfigure (b) indicates transverse strain difference.

The transverse strain differences for experiments 1-3 are shown in figure 5.7b. As V_{max} was increased from 500 V to 1500 V the transverse strain difference at 0.3 Hz decreased from -175.5 $\mu\epsilon$ to -478.0 $\mu\epsilon$. As the frequencies increased the absolute value of transverse strain differences decreased. At 14.8 Hz, when V_{max} was increased from 500 V to 1500 V, the transverse strain difference decreased from -76.0 $\mu\epsilon$ to -301.1 $\mu\epsilon$. From 0.3 to 14.8 Hz the longitudinal strain difference drops at 500 V, 1000 V and 1500 V were 56.7%, 47.0% and

37.0% respectively.

The results of experiment 4 is shown in figures 5.8 and 5.9. The figures for experiment 4 give similar qualitative trends for experiments 5, 6 and 7 which also have a biased back voltage, $V_{\text{min}} = -500\ V$. Figure 5.8 shows the strain versus voltage response during the frequency sweep. At low frequencies the curves are no longer elliptic-like as in figure 5.5. As frequencies increased the curves resembled more and more the elliptic like structure. The longitudinal and transverse strain at V_{min} varied little as frequencies increased compared to at V_{max}.

The longitudinal and transverse strain variations with frequency is more easily seen in figure 5.9. The minimum longitudinal strain bound varied from -768.2 $\mu\epsilon$ to -725.6 $\mu\epsilon$ as frequency increased from 0.3 to 14.8 Hz. The maximum longitudinal strain bound varied from -387.6 $\mu\epsilon$ to -607.2 $\mu\epsilon$ as frequency increased from 0.3 to 14.8 Hz. The minimum longitudinal strain bound only had a increase of 5.5% compared to the maximum longitudinal strain bound decrease of 56.6%. A similar trend occurred for the opposite bounds for the transverse strain. The minimum transverse strain bound only had a increase of 2.02% compared to the maximum longitudinal strain bound increase of 78.0%. These lopsided bound changes account for a lack of horizontal symmetry as opposed to the symmetry seen in figure 5.6.

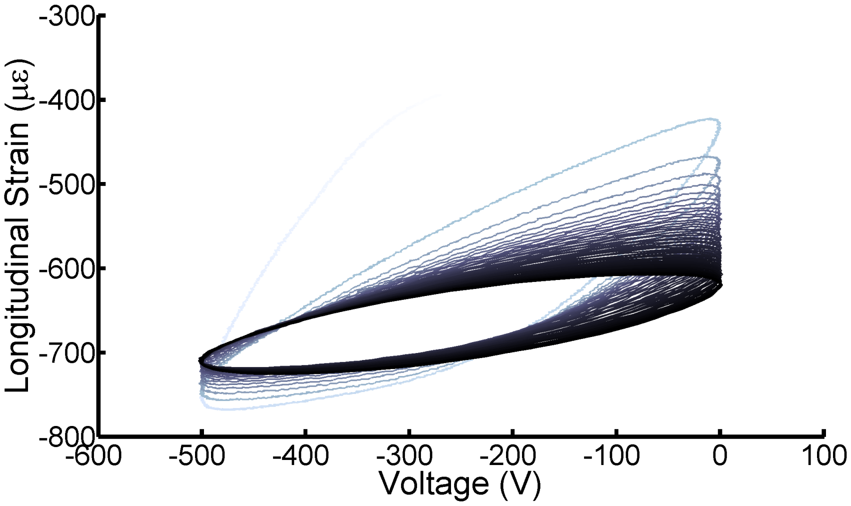

(a)

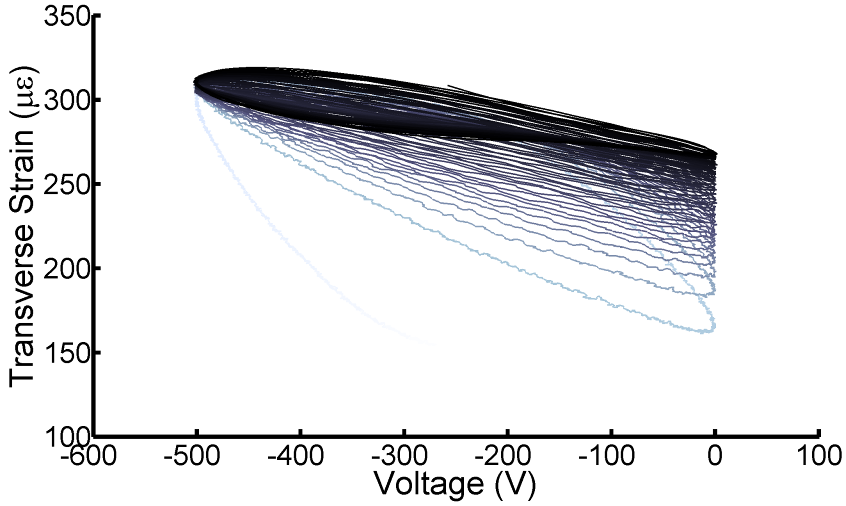

(b)

Figure 5.8: Strain versus voltage behavior of MFC actuator in experiment 4. Subfigure (a) indicates longitudinal strain output while subfigure (b) indicates transverse strain output. Time/Frequency is inversely proportional to color brightness.

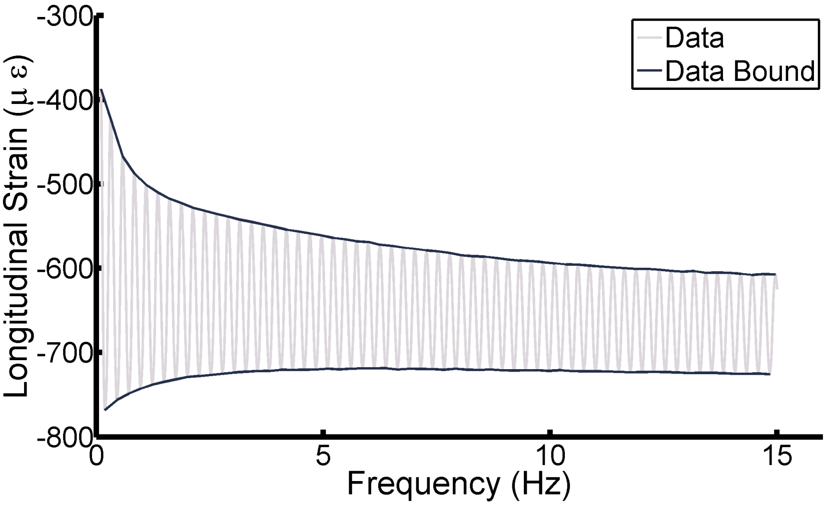

(a)

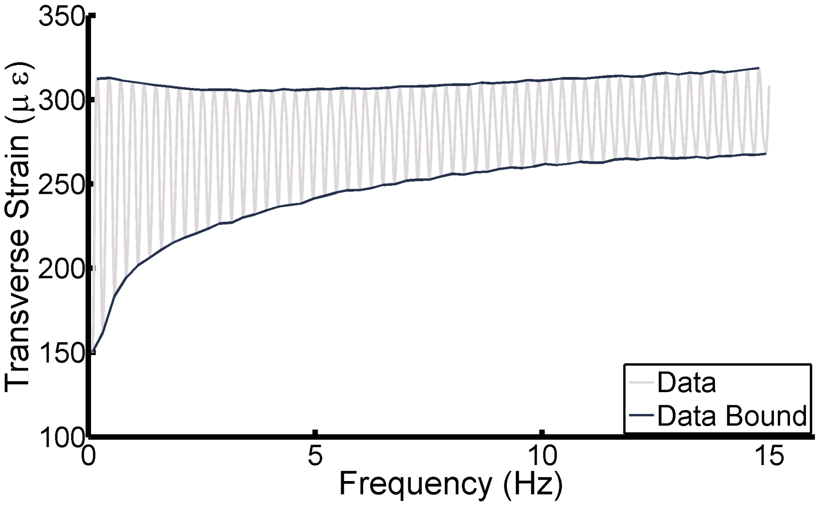

(b)

Figure 5.9: Strain versus frequency behavior of MFC actuator in experiment 4. Subfigure (a) indicates longitudinal strain output while subfigure (b) indicates transverse strain output. Data indicates the strain value at the instantaneous frequency. Data bound indicates the strain envelope which bounds the plot.

Figure 5.10 shows the strain differences for experiments 4-7. Again, the strain differences seemed to decay and asymptote to a single value per experiment as frequencies increased. The longitudinal strain differences for experiments 4-7 are shown in figure 5.10a. As $V_{\max}$ was increased from 0 V to 1500 V the longitudinal strain difference at 0.3 Hz increased from 366.4 $\mu\epsilon$ to 1975 $\mu\epsilon$. As the frequencies increased the longitudinal strain differences decreased. At 8.3 Hz, when $V_{\max}$ was increased from 0 V to 1500 V, the longitudinal strain difference increased from 134.7 $\mu\epsilon$ to 1402 $\mu\epsilon$. From 0.3 to 8.3 Hz the longitudinal strain difference drops at 0 V, 500 V, 1000 V and 1500 V were 63.2%, 46.9%, 34.5% and 29.0% respectively.

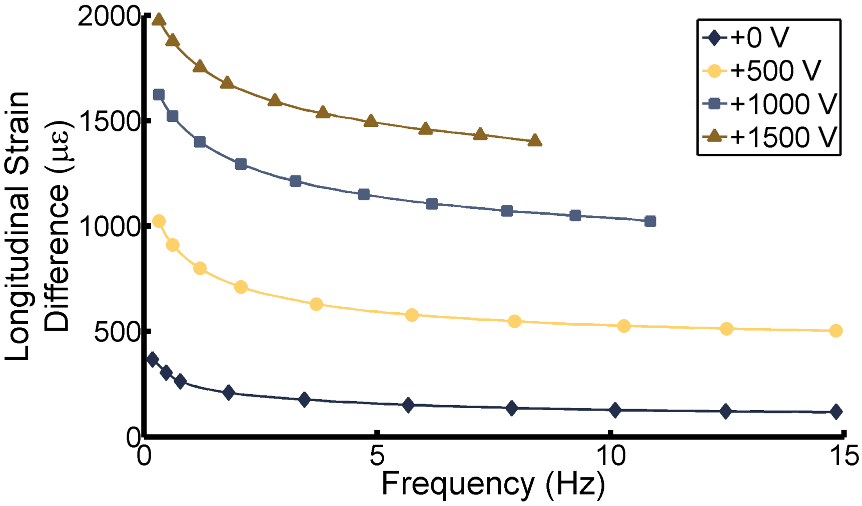

(a)

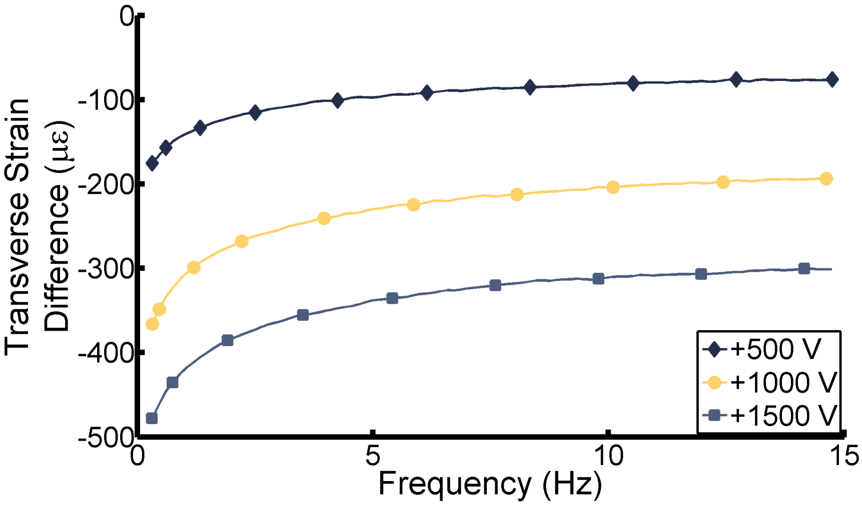

(b)

Figure 5.10: Strain difference versus frequency for experiments 4-7. Subfigure (a) indicates longitudinal strain difference while subfigure (b) indicates transverse strain difference.

The transverse strain differences for experiments 4-7 are shown in figure 5.10b. As $V_{\max}$

was increased from 0 V to 1500 V the transverse strain difference at 0.3 Hz decreased from -157.0 $\mu\epsilon$ to -889.2 $\mu\epsilon$. As the frequencies increased the absolute value of transverse strain differences decreased. At 8.3 Hz, when $V_{\max}$ was increased from 0 V to 1500 V, the transverse strain difference decreased from -53.5 $\mu\epsilon$ to -594.8 $\mu\epsilon$. From 0.3 to 8.3 Hz the longitudinal strain difference drops at 0 V, 500 V, 1000 V and 1500 V were 65.9%, 53.1%, 39.0% and 33.1% respectively.

A custom actuator was prepared to try to alleviate the drop in strain from the higher frequencies. Large relative electrode line width ratios L_2/H, yield less strain creep and relaxation times. The custom actuator was designed with a larger relative electrode line width than the commercial MFC.

The result of the custom actuator experiments is shown in figure 5.11. The custom actuators, with no negative voltage bias (experiments 8 and 10), shown in figure 5.11a, were electrically driven to near the same strain as the commercial actuator in experiment 2. The custom actuator's longitudinal strain difference tended to asymptote faster than the commercial MFC. From 0.3 Hz to 10 Hz, the longitudinal strain drop of custom actuators 1 and 2 were 17.4% and 7.68% respectively compared to the commercial actuator which had a 36.5% drop.

The custom actuators with a negative voltage bias (experiment 9 and 11), shown in figure 5.11b, were electrically driven to near the same strain as the commercial MFC in experiment 5. Again, the custom actuator's longitudinal strain difference tended to asymptote faster than the commercial MFC. From 0.3 Hz to 7.3 Hz, the longitudinal strain drop of custom actuators 1 and 2 were only 19.5% and 10.5% respectively compared to the commercial actuator which had a 45.0% drop. In both subfigures of figure 5.11, the commercial MFC's strain differences hadn't fully decayed at the comparable end frequencies. Accounting for this would yield even larger drops in strain differences for the commercial MFC.

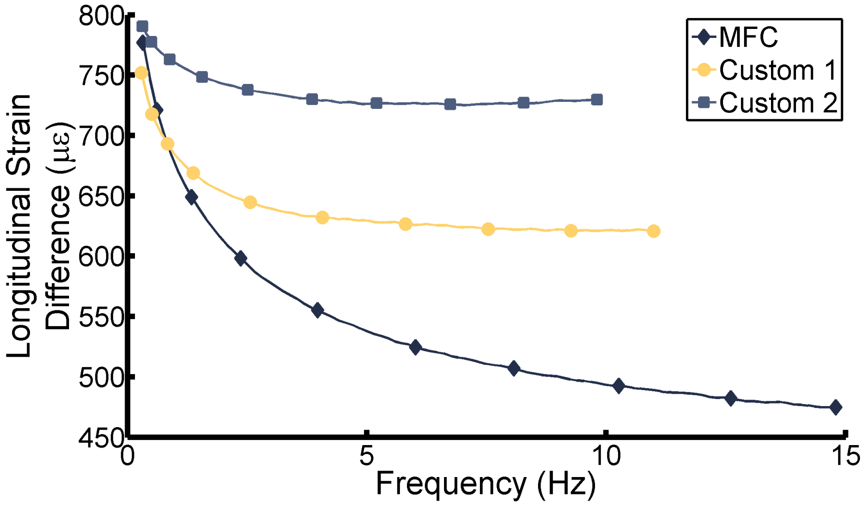

(a)

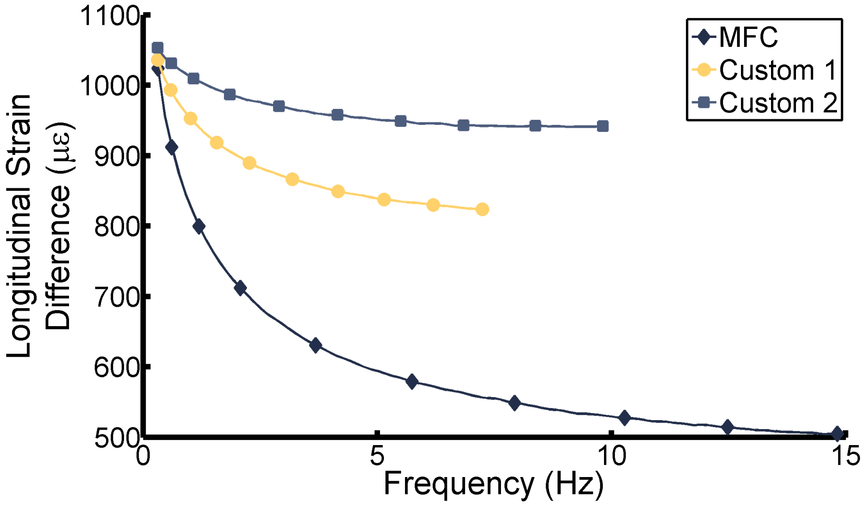

(b)

Figure 5.11: Comparison of longitudinal strain difference versus frequency between custom actuator and MFC. Subfigure (a) is a comparison of experiments 2 and 8 while subfigure (b) is a comparison of experiments 5 and 9.

Considering the electrode geometry greatly affects the qualitative behavior of the actuator when run a frequency sweep, a comparison was made to the bulk material. The results of the frequency sweep cycle for the monolithic wafer with uniform electrodes is shown in figure 5.12. The bulk response showed very little dependence on electric field frequency. Increasing the frequency from 0.1 Hz to 15 Hz caused the transverse strain difference to increase from

-327 $\mu\epsilon$ to -301 $\mu\epsilon$.

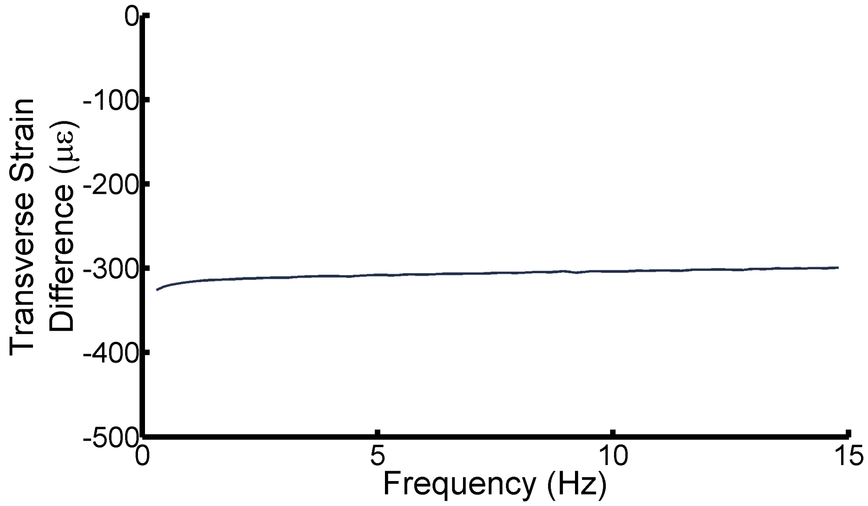

Figure 5.12: Frequency response of monolithic wafer with uniform electrodes.

5.4 Experimental Discussion

The longitudinal and transverse strain differences were sensitive to frequencies when varied from 0.1 Hz to 15 Hz. Thus the piezoelectric coefficients $d_{33}(f)$ and $d_{31}(f)$ are also sensitive to electrically driven frequencies due to being proportional to the longitudinal and transverse strain differences respectively. The commercial MFC properties are reported independently of applied electrically driven frequency.

The piezoelectric constants at low electric field, $E < 1$ MV/m, with unbiased operation, $V_{\mathrm{min}} = 0$ V, are reported to be $d_{33} = 400$ pC/N and $d_{31} = -170$ pC/N. The experiment performed corresponding to low electric field with unbiased operation is experiment 1. Figure 5.13 shows a comparison of the piezoelectric constants as a function of frequency versus published values. There is a slight discrepancy at the low frequencies with the published value. Extrapolating the experimental data to smaller frequencies would lower this discrepancy. From 0.3 Hz to 14.8 Hz the low field $d_{33}(f)$ varied from 381.7 pC/N to 206.2 pC/N. This represents a increase in the percent difference of the reported value of 400 pC/N from 4.58% to 48.5%. From 0.3 Hz to 14.8 Hz the low field $d_{31}(f)$ varied from -157.9 pC/N to

-68.44 pC/N. This represents a increase in the percent difference of the reported value of -170 pC/N from 7.12% to 59.7%. During unbiased operation at low electric field, the experimental piezoelectric coefficients were found to be around half of reported values when operating at 14.8 Hz.

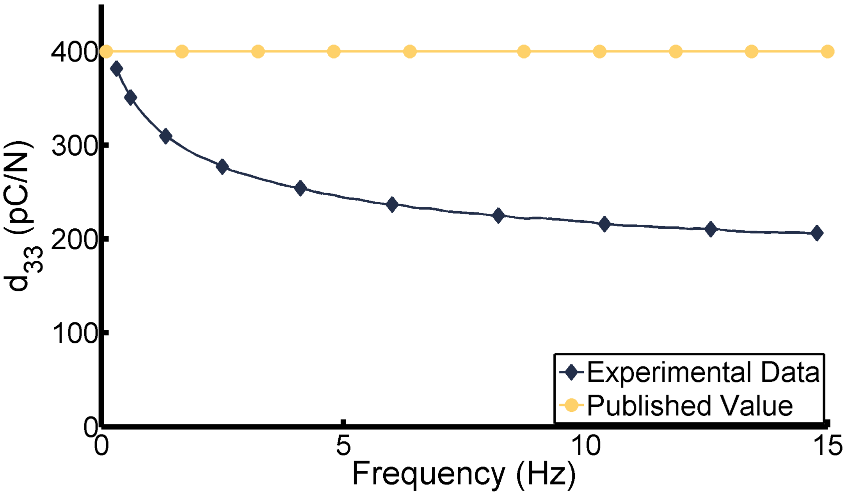

(a)

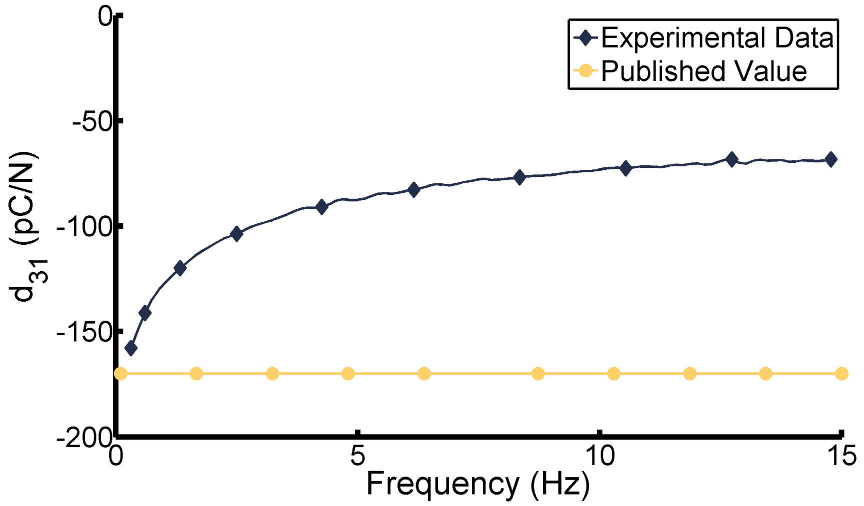

(b)

Figure 5.13: Low-field, unbiased-voltage piezoelectric coefficients versus frequency (Experiment 1). Subfigure (a) indicates the d_{33} piezoelectric coefficient while subfigure (b) indicates the d_{31}.

The piezoelectric constants at high electric field, $E > 1$ MV/m, with biased operation,

$V_{\min} = -500$ V, are reported to be $d_{33} = 460$ pC/N and $d_{31} = -210$ pC/N. The experiment performed corresponding to high electric field with biased operation is experiment 1. Figure 5.14 shows a comparison of the piezoelectric constants as a function of frequency versus published values. Again there is a slight discrepancy at low frequencies with the published value, the reasonings are the same as mentioned for the low field constant. From 0.3 Hz to 14.8 Hz the high field $d_{33}(f)$ varied from 444.4 pC/N to 315.3 pC/N. This represents a increase in the percent difference of the reported value of 460 pC/N from 3.39% to 31.5%. From 0.3 Hz to 14.8 Hz the high field $d_{31}(f)$ varied from -200.1 pC/N to -133.8 pC/N. This represents a increase in the percent difference of the reported value of -210.0 pC/N from 4.71% to 36.3%. During biased operation at high electric field, the experimental piezoelectric coefficients were found to be around 2/3rd of reported values when operating at 14.8 Hz.

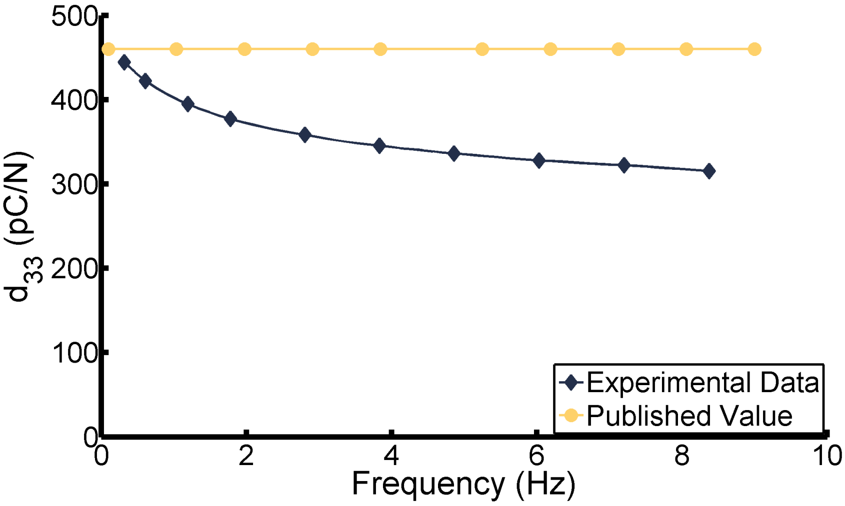

(a)

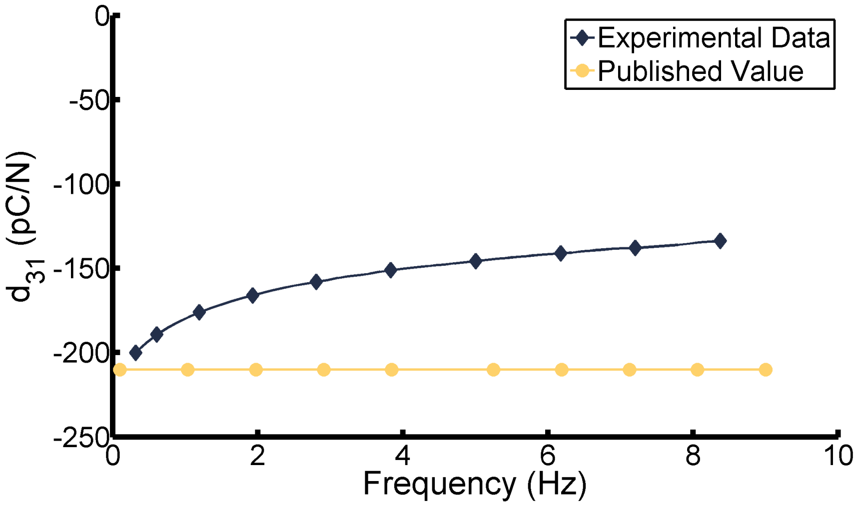

(b)

Figure 5.14: High-field, biased-voltage piezoelectric coefficients versus frequency (Experiment 7). Subfigure (a) indicates the d_{33} piezoelectric coefficient while subfigure (b) indicates the d_{31}.

To reproduce the data, the strain differences from experiments 1-11 were fit to,

$$\epsilon_\delta\left(f\right) = \epsilon_\Delta\, e^{-f/\tau} + \epsilon_\infty, \tag{5.8}$$

where $\epsilon_\delta\left(f\right)$ is the strain difference, either longitudinal or transverse, as a function of frequency, ϵ_∞ is a coefficient which represents a strain difference as the frequency approaches infinity, ϵ_Δ is the change in the strain difference from the 0 Hz to infinity, and τ is the mean lifetime constant of the exponential decay. The exponential decay equation with a shifted constant value was chosen due to the observation all the strain difference data seemed to decay to a constant strain difference as frequencies were increased.

The coefficients of equation 5.8 can not be found explicitly using linear least squares. To remedy this, the derivative of equation 5.8 was taken and then exponentiated yielding a linearized relation,

$$\ln\left(-\epsilon'_\delta\right) = \ln\left(\frac{\epsilon_\Delta}{\tau}\right) - \frac{f}{\tau}, \tag{5.9}$$

where ϵ'_δ, is a strain difference differentiated by frequency. Using a least squares algorithm via QR factorization on equation 5.9 the coefficients ϵ_Δ and τ were found. Plugging ϵ_Δ and τ back into equation 5.8 and using the least square algorithm via QR factorization, the coefficient ϵ_∞ was found.

The numerical differentiation of ϵ_δ amplifies the errors of the experimental data. This can cause the coefficients found to not minimize the residual of the system of equations. To alleviate this, the found coefficients were used as initial guesses for the Gauss-Newton nonlinear least squares algorithm. Without first finding the initial guesses, the Gauss-Newton method would converge to values giving a poor goodness of fit.

An example of fitting for experiment 8 is shown in figure 5.15. The figure shows good qualitative agreement between experimental data and the exponential fit. The curve fitting coefficients and goodness of fit values are found in tables 5.3 and 5.4. Table 5.3 represent the curve fitting parameters relating the longitudinal strain differences for experiments 1-9. Table 5.4 represent the curve fitting parameters relating the transverse strain differences for experiments 1-9. The goodness of fit parameters reported in both tables are, the coefficient of determination R^2 and the root mean square error RMSE. The coefficient of determination was never less than 96.6% and was on average 98.7%. The root mean square error was never greater than 14.0 $\mu\epsilon$ and was on average 6.54 $\mu\epsilon$.

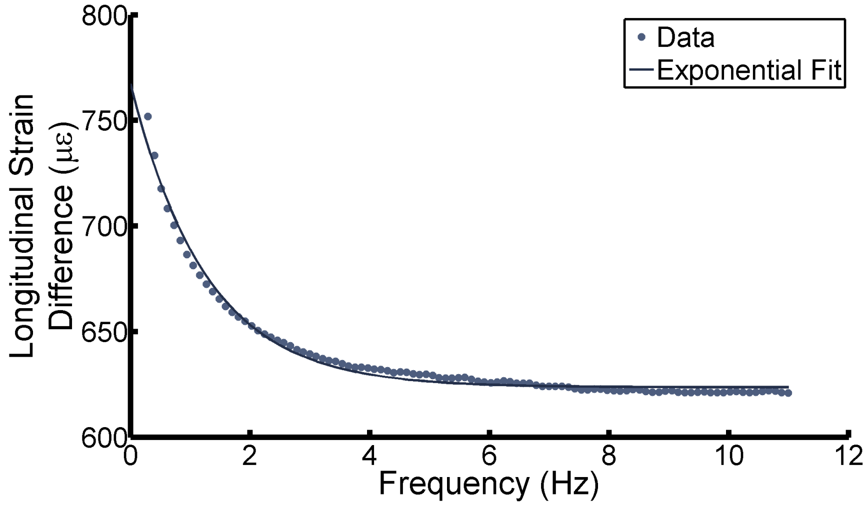

Figure 5.15: Curve fit of exponential decay plus a constant for experiment 8. Scatter points indicate data values while the solid line indicates the fitted curve.

Table 5.3: Exponential Fitting Values for Longitudinal Strain Difference

Experiment	Coefficients			Goodness of Fit	
#	ϵ_Δ ($\mu\epsilon$)	τ (Hz)	ϵ_∞ ($\mu\epsilon$)	R^2 (%)	RMSE ($\mu\epsilon$)
1	184.2	3.03	233.5	98.6	4.70
2	284.7	2.86	483.0	98.5	8.12
3	284.4	2.86	715.7	98.6	7.90
4	212.2	2.32	125.3	96.6	9.14
5	492.7	2.45	519.0	98.3	14.0
6	600.1	2.65	1036	99.1	13.7
7	604.3	2.36	1406	99.3	12.1
8	140.2	1.26	608.4	98.8	2.84
9	229.0	1.80	803.7	99.6	3.12
10	85.66	1.24	807.4	99.1	1.42
11	123.0	1.98	940.3	99.7	1.49

The mean lifetime constant, τ can be thought of as the frequency in which the addition of the ϵ_Δ term in equation 5.8 is reduced by $1/e$. In figure 5.11a, for unbiased operation,

Table 5.4: Exponential Fitting Values for Transverse Strain Difference

Experiment	Coefficients			Goodness of Fit	
#	ϵ_Δ ($\mu\epsilon$)	τ (Hz)	ϵ_∞ ($\mu\epsilon$)	R^2 (%)	RMSE ($\mu\epsilon$)
1	-93.95	2.88	-78.08	98.5	2.70
2	-161.6	2.99	-197.3	98.5	4.69
3	-168.5	3.02	-303.9	98.8	4.39
4	-103.4	2.29	-50.33	98.8	2.64
5	-243.4	2.86	-194.1	98.1	7.89
6	-302.1	3.10	-417.2	98.9	7.77
7	-309.2	2.77	-591.0	99.2	6.45
8	-110.7	2.27	-398.9	98.7	2.95
9	-176.5	2.37	-561.0	99.6	2.60

it was noted the longitudinal strain difference of the custom actuator decayed faster than the MFC. Using the fitted parameters of experiments 2, 8 and 10 in table 5.3 actual decay values can be conveyed. The MFC in experiment 2 had a mean lifetime of 2.86 Hz while in experiments 8 and 10 the custom actuator had a mean lifetime of 1.26 Hz and 1.24 Hz respectively. For unbiased operation, the mean lifetime coefficient of the custom actuator in experiment 10 was 56% less than the MFC. Also, the amount of strain difference that decays, ϵ_Δ, was less for the custom actuators then that of the MFC. The parameter ϵ_Δ was 140.2 $\mu\epsilon$ and 85.66 $\mu\epsilon$ for the custom actuators 1 and 2 respectively while it was 284.7 $\mu\epsilon$ for the MFC.

Biased operation comparison between the MFC and custom actuator yields similar results. In figure 5.11b, for biased operation, it was noted the longitudinal strain difference of the custom actuator decayed faster than the MFC. Using the fitted parameters of experiments 5, 9 and 11 in table 5.3 decay values are noted. The MFC in experiment 5 had a mean lifetime of 2.45 Hz while in experiments 9 and 11 the custom actuators had a mean lifetime of 1.80 Hz and 1.98 respectively. For biased operation, the mean lifetime coefficient of custom actuator 1 was 25% less than the MFC. Again, the amount of strain difference that decays ϵ_Δ was less for the custom actuator then that of the MFC. The parameter ϵ_Δ was 229.0 $\mu\epsilon$ and 123.0 $\mu\epsilon$ for the custom actuator while it was 492.7 $\mu\epsilon$ for the MFC.

In both the unbiased and biased operations of the commercial actuators the strain difference drop ϵ_Δ converged towards a single value as maximum applied voltages were increased. In table 5.3, the unbiased operation ϵ_Δ approached 285 $\mu\epsilon$, and in the biased operation ϵ_Δ approached 600 $\mu\epsilon$. While, the strain difference drop was shown to asymptote, the strain difference at high frequency ϵ_∞ continued to increase as maximum applied voltages were increased. These trends on ϵ_∞ and ϵ_Δ explain why the strain difference drop percentage decreased when increasing the maximum voltage V_{max}.

5.5 Conclusion

A commercial MFC was tested for its actuation abilities across a range of electrically driven frequencies form 0.1 Hz to 15 Hz. Seven separate experiments were performed on the MFC with applied voltages ranging within operating parameters from -500 V to 1500 V. The first three experiments performed were under unbiased actuation $V_{\text{min}} = 500$ V. The next four experiments were performed under biased actuation $V_{\text{min}} = -500$ V.

Under unbiased actuation it was found that the strain differences decayed rapidly as frequencies were increased from 0.1 Hz to 15 Hz. Eventually, the strain difference was shown to asymptote at high enough frequencies. At the lowest maximum applied voltage, V_{max}, the longitudinal strain difference drop from operating at 15 Hz was largest at 46%. Increasing the maximum applied voltage to 1500 V lessened the strain difference drop to 29.9%.

Similar trends were found under biased actuation of the commercial MFC actuators. A key difference was found that the biased operation lacked symmetry in the strain output compared to the unbiased operation. The strain differences again decayed rapidly as and converged as frequencies were increased. At the lowest maximum applied voltage, V_{max}, the longitudinal strain difference drop from operating at 15 Hz was largest at 63.2%. Increasing the maximum applied voltage to 1500 V lessened the strain difference drop to 29.0%.

Custom IDE actuators were manufactured with a smaller relative electrode line width and larger relative electrode gap than that of the commercial MFC. The smaller relative electrode line widths and larger relative electrode gaps tend to reduce strain creep and relaxation times in IDE actuators. It was found that the custom actuators had a reduced the strain drop as actuation frequencies increased. The mean lifetime coefficient also was less implying that the strain difference was quicker to asymptote than the commercial MFC.

It was noted that the high-field, biased-voltage piezoelectric coefficient and the low-field unbiased-voltage piezoelectric coefficients of the commercial MFC were reported independent of frequency. Increasing the actuation frequencies caused the high-field, biased-voltage d_{33} piezoelectric coefficient to drop below 31.5% of the reported value. Similarly, increasing actuation frequencies caused the low-field, unbiased-voltage d_{33} piezoelectric coefficient to drop below 48.5% of the reported value.

The strain difference versus frequency plots were curve fit to an exponential decay equation with a added constant. The fitted equation had an average coefficient of determination of 98.7% and an average root mean square error of 6.54 $\mu\epsilon$ across all experiments. The coefficients found helped quantify the decay properties of the experiments.

CHAPTER 6

IDE Composition Experiment

6.1 Introduction

While the effect of geometry is of interest for intedigitated electrode piezoceramic acutators, composition was also studied. Two compositions were explored, phase transforming 55/33/12 PLSnZT and quadratic electrostrictive 9.5/65/35 PLZT. The geometry of the exotic MFC was chosen to be that of commercial MFC so that direct comparisons are possible. By utilizing exotic materials in MFC, it was the hope that the use of piezocomposites could be expanded.

Antiferroelectric to ferroelectric phase transitions of PLSnZT was established by Berlincourt when he developed the materials ternary phase diagram [102]. He found that compressive hydrostatic stresses favored antiferroelectric states, while electric fields forced an antiferroelectric to ferroelectric phase transformation. Pan et al experimentally found that the volumetric strain change associated with phase transforming from antiferroelectric to ferroelectric could yield up to 0.85% strain [103, 104]. The high strain output has also been used for microactuator microelectric devices [27, 105].

PLZT phase diagrams [106, 107] show that compositions (x/65/35) with x ranging from 6 mol% to 12 mol% are along a morphotropic phase boundary in the slim loop ferroelectric phase region. In the 9% to 10% La range, the material possess zero coercive field and zero remnant polarization [107]. The phase transition in x/65/35 is sensitive to electric field, temperature and frequency [108, 109]. Materials in the slim loop phase region are useful for pyroelectric energy conversion [110] and for their quadratic electrostrictive behavior across a wide range of temperatures [111, 112]

The phase transforming behavior of PLSnZT is ideal for a binary actuator in which the strain has two states (on and off). The composition can be modified so that when the material phase transforms to ferroelectric upon removal of electric field it stays ferroelectric. This behavior may have use for the self-latching piezocomposite discussed in previous chapters. The binary actuation was explored for these actuators.

Quadratic electrostrictors possess very little creep compared to PZT and exhibit low strain hysteresis. Thus, the material properties of electrostrictors are ideal for use in high precision positioning devices. They are typically employed as monolithic plate actuators which make use of the d_{31} effect. By combining an electrostrictor with the anisotropic d_{33} mode actuation of a MFC, it was the hope that a large strain high-precision actuator could be devised.

6.2 Experimental Arrangement

6.2.1 Materials and Specimen Preparation

The ferroelectric ceramic material used in these experiments was synthesized by the typical mixed oxide method. Starting precursors included high purity(> 99.9 mol%) $2PbCO_3 \cdot Pb(OH)_2$ (Hammond Group Inc., IN, USA), La_2O_3 (Inframat Advanced Materials LLC, CT, USA), ZrO_2 (Magnesium Elektron Inc., NJ, USA), and SnO_2 (Triple-S Chemical Products Inc., CA, USA), and TiO_2 (Ishihara Sangyo Kaisha Ltd, Japan). Each precursor was weighted with respect to the nominal composition of $(Pb_{1-3x}/2La_x)(Zr_{1-y}Sn_yTi_z)O_3$ assuming A-site vacancy.

Each material was heated at 300 °C for 2 hours prior to mixing. This allowed any volatile impurities or moisture content to escape. This loss percent on ignition was measured. Deionized water with volume between 100% and 200% of volume of the powder, 1 wt.% NH_4OH solution, and 5wt.% Darvan dispersant (R.T. Vanderbilt Holding Company, Inc., CT, USA) were added to the mixture of powder to form a freely flowing hypersaturated slurry. Using zirconia balls with triple volume of powder as grinding media, the suspension was milled for 16 hours to improve the homogeneity. The slurry was dried, and the substance was calcined at 900 °C for 8 hours. The calcined powder was re-milled through the same steps as before and passed through a 100-mesh sieve to limit the size of particles and increase the packing efficiency. 3 wt.% polymer binder (Rohm and Haas Company, PA, USA) was added using acetone as the solvent, and the binderized powder was uniaxially compressed into a cylinder at 2500 psi. The compact disc was placed in an alumina crucible and sintered at 1250 °C for 2 hours in lead-rich environment provided by PbO and ZrO_2 powder to minimize the volatile Pb loss from the disc. A Pt foil was also laid between cylinder and crucible to avoid diffusion.

The resulting ferroelectric ceramic cylinder had a radius of around 23 mm and a height of 15 mm. The cylinder was sent to Smart Material Corp. to be cut and have the IDE applied. The process is outlined in figure 6.1. The ceramic cylinder was processed into a 14 mm cube. The 14 mm cube was then sliced into a number of 14 mm × 14 mm × 0.23 mm wafers. Two wafers were were placed end-to-end and diced in tandem for packaging in a standard MFC size actuator. Wafers from each composition were also polished and electroded using Au sputter deposition to measure bulk properties.

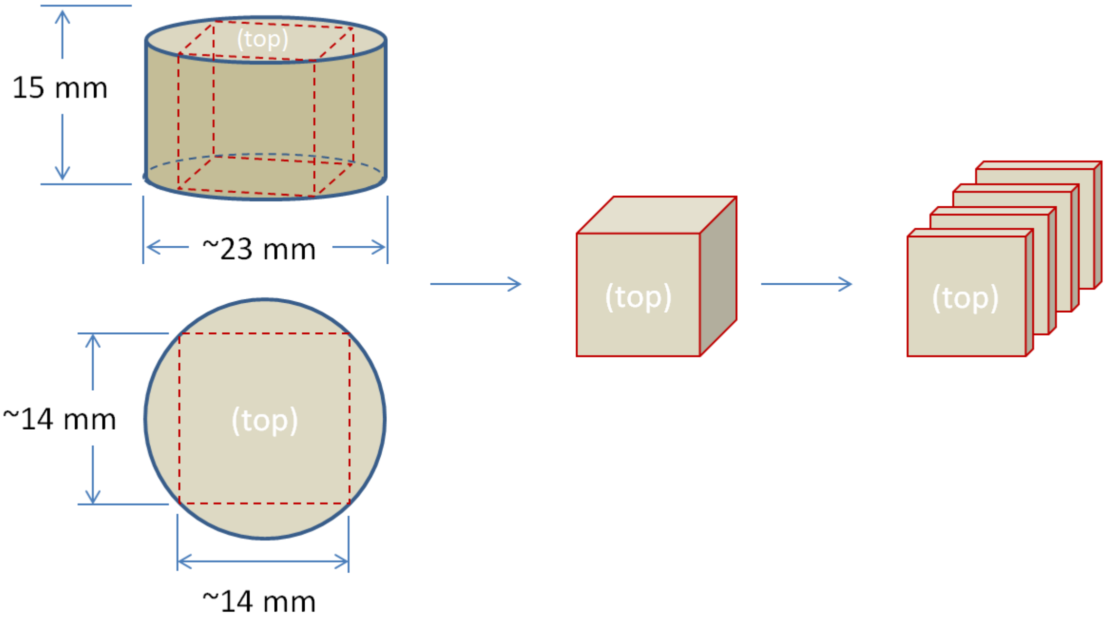

Figure 6.1: Custom ceramic material dicing scheme.

The PLSnZT, PLZT, and commercial MFC piezocomposite actuators were instrumented with tee rosette strain gages to measure longitudinal and transverse extensions. Two gages were mounted on the top and two on the bottom of the actuator to monitor the bending and extension of the specimen. The bulk wafers were instrumented with a single strain gage on the ground electrode. The strain gages were powered by a strain gage amplifier and fed into a digital acquisition system. The actuators were electrically driven with a 10 kV amplifier. Applied voltage and strain was recorded for both the piezocomposites and the bulk actuators. Charge output was additionally recorded for the bulk actuators using a Sawyer Tower circuit.

6.2.2 Experimental Procedure

Throughout this chapter the piezocomposite actuator performance is reported in terms of a nominal electric field. The nominal electric field $E_{\mathrm{Nom}} \equiv V/\left(L - L_2\right)$ is defined as the applied voltage V divided by the gap distance between electrodes $L - L_2$. Nominal electric field is appropriate for comparing these actuators due to having the same electrode geometry and plate dimensions. For the monolithic plate actuators, the electric field is reported as the voltage applied divided by plate thickness.

The free strain and electric displacement response of the monolithic PLSnZT and PLZT actuators was performed as a basis of comparison to the piezocomposite actuators. A bipolar sinusoidal electric field at 0.1 Hz was applied to each specimen. Similarly, the free strain response of the piezocomposite PLSnZT and PLZT and MFC actuators was performed. A bipolar sinusoidal electric field from -7.6 MV/m to 7.6 MV/m at 0.1 Hz was applied to each piezocomposite specimen.

The response of the PLZT piezocomposite actuator under different electrically driven sinusoidal frequencies was also compared. A bipolar sinusoidal electric field from -7.0 MV/m to 7.0 MV/m was applied to the PLZT piezocomposite specimen. The electric field was applied at 0.05 Hz, 0.025 Hz, and 0.0125 Hz actuation frequencies.

6.3 Experimental Results

The transverse strain output of the monolithic PLSnZt actuator is shown in 6.2. As electric field was initially increased, little strain output was recorded. When the coercive field of 2 MV/m was hit, there was a sudden strain jump. As the field increased to 3 MV/m a 290 $\mu\epsilon$ transverse strain was achieved in the plate actuator. As the field decreased, from 3 MV/m, the transverse strain stayed relatively constant. While decreasing the electric field at 1 MV/m, there was a sudden strain drop. When the electric field was completely removed, the actuator only had 20 $\mu\epsilon$ remnant transverse strain. This residual strain crept back to 0. Reversing the electric field polarity yields a similar trend.

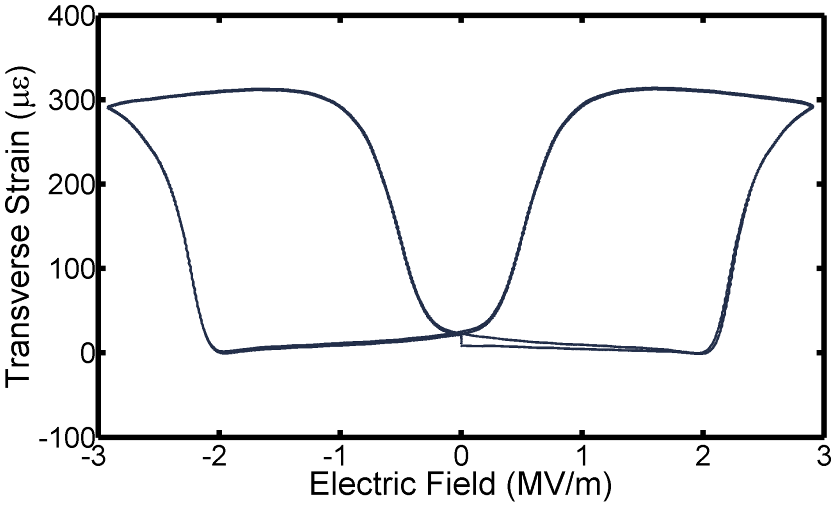

Figure 6.2: Transverse strain output of bulk 55/33/12 PLSnZT.

The polarization of the monolithic PLSnZT actuator is shown in figure 6.3. A double loop behavior is observed. As the electric field was initially increased, the polarization change increased linearly. When the coercive field of 2 MV/m was hit, there was a sudden jump in polarization. As the field increased to 3 MV/m a 0.3 C/m^2 polarization was achieved. As the electric field decreased from 3 MV/m, the polarization linearly dropped. While further decreasing the electric field at 1 MV/m there was a sudden drop in polarization. When the electric field was completely removed, only a polarization of 0.03 C/m^2 remained. Reversing the electric filed polarity yields an opposite trend in polarization.

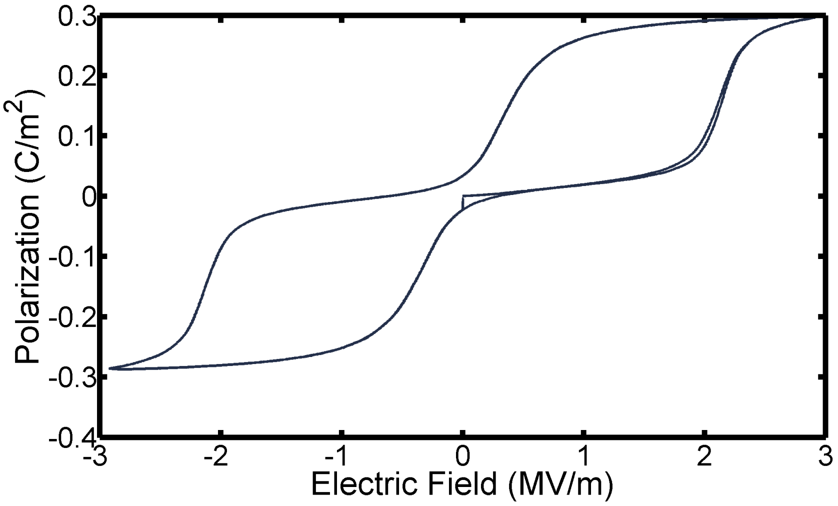

Figure 6.3: Polarization output of bulk 55/33/12 PLSnZT.

The longitudinal strain output of the PLSnZT piezocomposite actuator is shown in figure 6.4. As the electric field was initially increased, little strain output was recorded. When the nominal electric field hit 4.0 MV/m, there was a sudden strain jump. As the field increased to 7.6 MV/m a 1087 $\mu\epsilon$ longitudinal strain was achieved. As the field decreased from 7.6 MV/m, the longitudinal strain immediately began to drop. Further decreasing the nominal electric field, at around 2 MV/m the strain drop is more pronounced. When the electric field is completely removed, the actuator holds a 522 $\mu\epsilon$ remnant longitudinal strain. Over the course of 5 minutes the remnant longitudinal strain decays to 150 $\mu\epsilon$. Reversing the electric field polarity yields a similar trend.

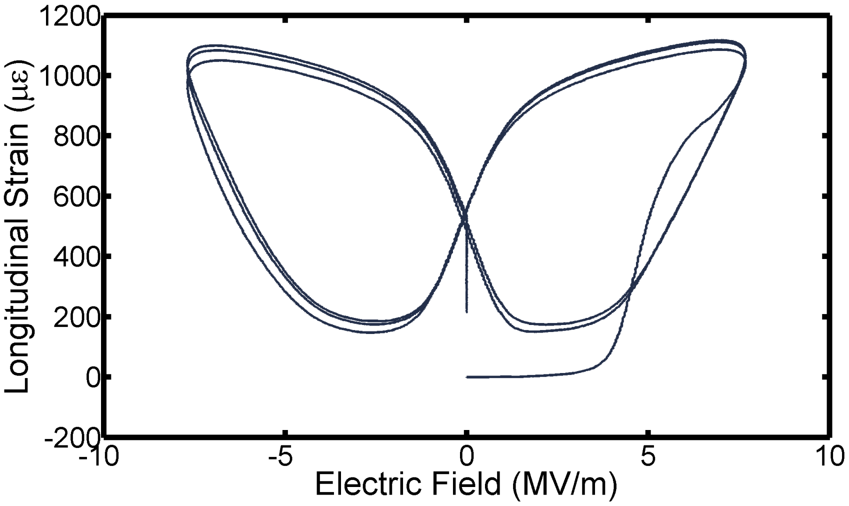

Figure 6.4: Longitudinal strain output of 55/33/12 PLSnZT piezocomposite.

The transverse strain output of the PLSnZT piezocomposite actuator is shown in figure 6.5. It took two cycles for the transverse strain to train and follow the same path. Following from 0 electric field at -215 $\mu\epsilon$ transverse strain, as the electric field was increased the transverse strain began to increase. At 2.3 MV/m, the transverse strain ceased increasing with any increase of electric field. Increasing the field to 5 MV/m, the transverse strain began to decrease. At a field of 7.6 MV/m a transverse strain of -250 $\mu\epsilon$ was achieved. While decreasing the electric field, the transverse strain slowly increased towards the starting point of -215 $\mu\epsilon$ at 0 MV/m. Reversing the electric field polarity yields a similar trend.

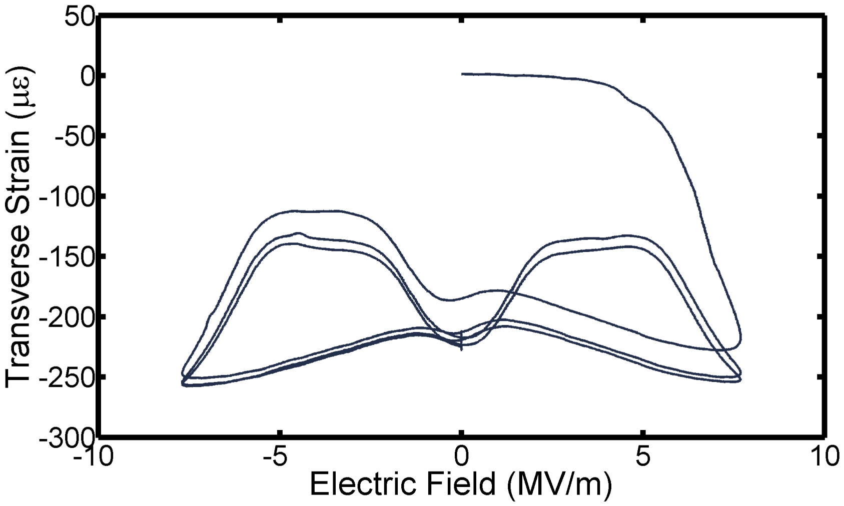

Figure 6.5: Transverse strain output of 55/33/12 PLSnZT piezocomposite.

The transverse strain output of the monolithic PLZT actuator is shown in figure 6.6. The transverse strain shows quadratic electrostrictive behavior. Increasing the electric field from 0 MV/m to 1.6 MV/m, the transverse strain begins to increase quadratically until it starts to saturate. At 1.6 MV/m a maximum transverse strain of -812 $\mu\epsilon$ was achieved. Decreasing the electric field, the transverse strain begins to quadratically decrease. When the electric field was removed, zero transverse strain remained.

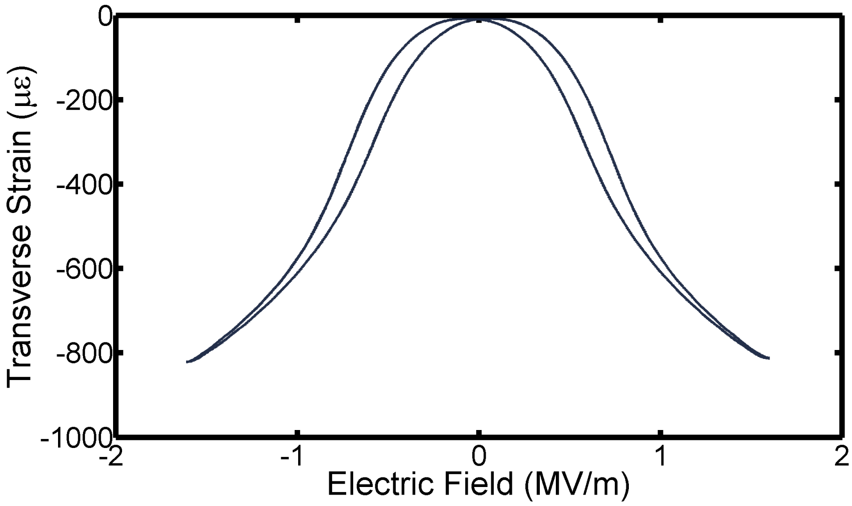

Figure 6.6: Transverse strain output of bulk 9.5/65/35 PLZT.

The polarization of the monolithic PLZT actuator is shown in figure 6.7. A slim loop ferroelectric behavior is observed. When the external electric field is applied, almost no coercive field is observed. Increasing the electric field to 1.6 MV/m causes the polarization to saturate at 0.23 C/m^2. Upon removal of the electric field little remnant polarization is observed. Reversal of the electric field yields the opposite trend in the polarization behavior.

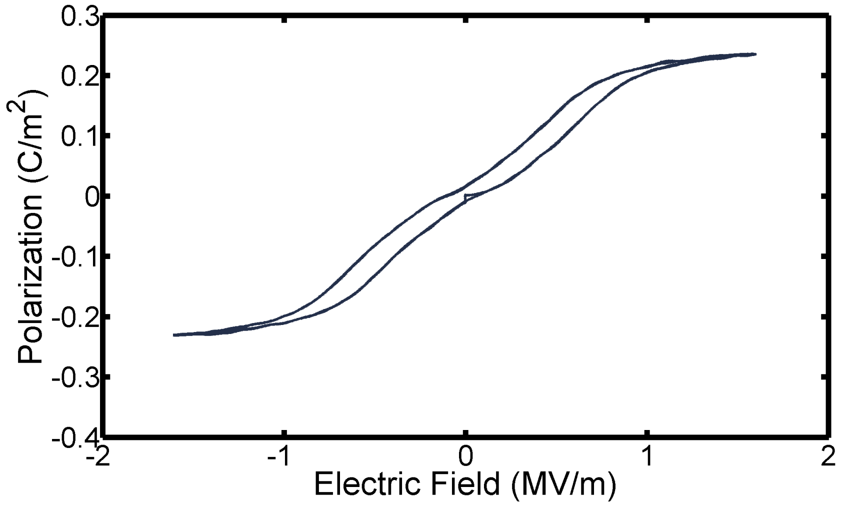

Figure 6.7: Polarization output of bulk 9.5/65/35 PLZT.

The longitudinal strain output of the PLZT piezocomposite actuator is shown in figure 6.8. When initially increasing the electric field from 0 MV/m to 7.6 MV/m, the strain follows a quadratic electrostrictive trend. At an electric field of 7.6 MV/m the actuator achieves a maximum longitudinal strain of 1555 $\mu\epsilon$. Decreasing the electric field, the longitudinal strain does not follow the same return path. When the electric field is removed, residual longitudinal strain of 300 $\mu\epsilon$ remains on the actuator. Over the course of one minute, the longitudinal strain relaxes to zero.

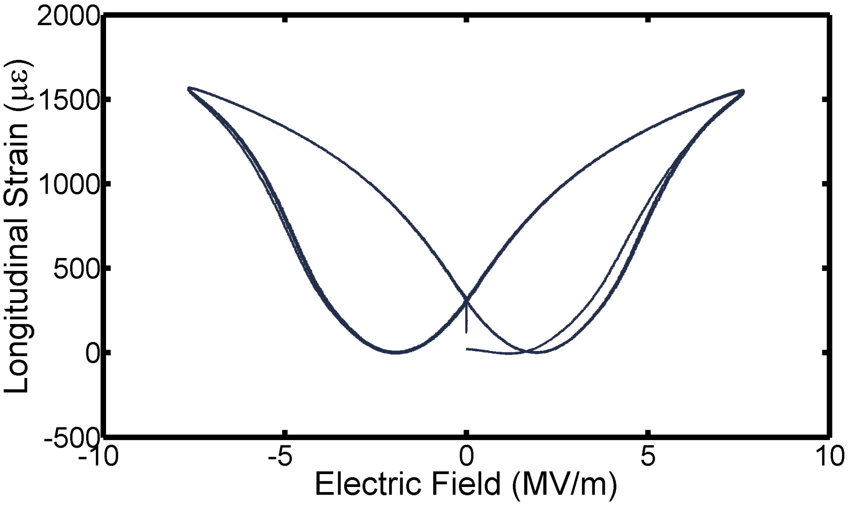

Figure 6.8: Longitudinal strain output of 9.5/65/35 PLZT piezocomposite.

The transverse strain output of the PLZT piezocomposite actuator is shown in figure 6.9. When initially increasing the electric field from 0 MV/m to 7.6 MV/m, the strain follows a quadratic electrostrictive trend. At an electric field of 7.6 MV/m the actuator achieves a minimum transverse strain of -850 $\mu\epsilon$. Decreasing the electric field, the transverse strain does not follow the same return path. When the electric field is removed, residual transverse strain of -175 $\mu\epsilon$ remains on the actuator. Over the course of one minute, the transverse strain relaxes to zero.

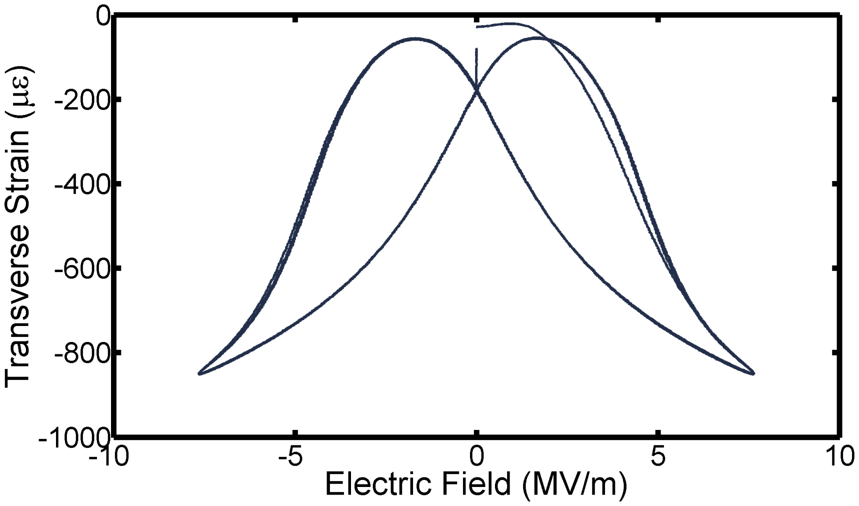

Figure 6.9: Transverse strain output of 9.5/65/35 PLZT piezocomposite.

The electric field driving frequency comparison of the PLZT piezocomposite actuator is shown in figure 6.10. The peak longitudinal strains decreased from 1489 $\mu\epsilon$ to 1390 $\mu\epsilon$ as frequencies were increased from 0.0125 Hz to 0.05 Hz. As the frequency of actuation increased, the longitudinal strain output was delayed causing a shift in the curves and increased hysteresis. Upon removal of electric field, the return path was independent of frequency of actuation.

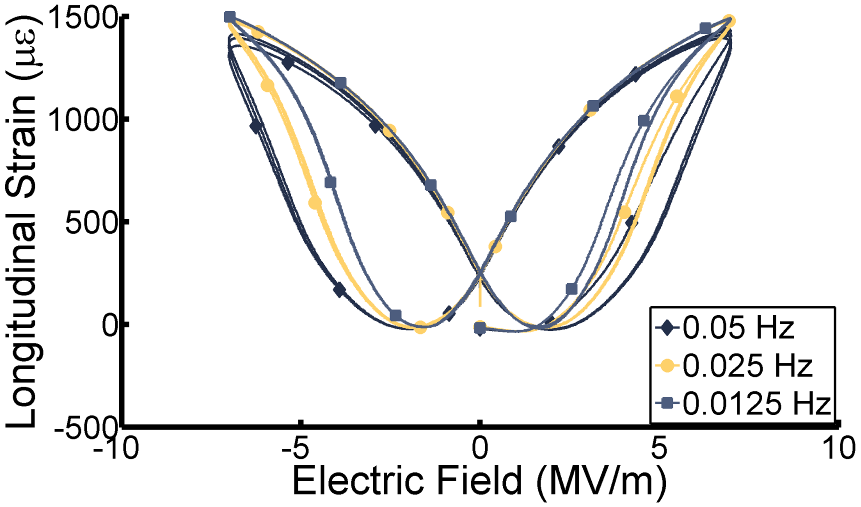

Figure 6.10: Frequency comparison of longitudinal strain output of 9.5/65/35 PLZT piezocomposite.

6.4 Experimental Discussion

A comparison is first made between the piezocomposite actuator performance and the bulk material. When discussing the results of the PLSnZT piezocomposite actuator, it must be noted that the bulk transverse strain was roughly half that of the published value for 55/33/12 PLSnZT. Thus, statements of maximal performance cannot be made, only the change in the performance from a bulk to a piezocomposite actuator.

The bulk actuator exhibits a response in which an application of electric field leads to a phase transformation from an antiferroelectric tetragonal phase to a ferroelectric rhombohedral phase. This is observed as the abrupt strain and polarization jump. Upon removal of the field, the crystal structure undergoes a reverse phase transformation from ferroelectric to antiferroelectric. In the bulk material, both longitudinal and transverse strain exhibit positive strain jumps due to the dilatation of the crystal structure.

The transverse strain output of the bulk PLSnZT actuator and the PLSnZT piezocomposite are very different. While the transverse strain of the bulk actuator performed qualitatively as expected, the piezocomposite actuator showed some oddities. Upon first polarizing the transverse strain of the piezocomposite actuator jumps negative. After the material had been polarized, starting from a state of zero electric field, the transverse strain exhibits a positive strain jump at low field levels. Increasing the electric field levels even further the strain again jumps negative. Upon removal of the field, no abrupt jumps were are observed. The negative transverse strain jump along with the, remnant transverse strain contrast with the bulk actuator performance. The remnant strain can be explained as stresses underneath the electrode stabilizing the ferroelectric phase of the material when the electric field is removed.

The longitudinal strain output of the PLSnZT piezocomposite actuator exhibits a response more expected. A positive longitudinal strain jump is observed with the application of electric field. Upon removal of the field the strain jumps down. What differs from the bulk response is the remnant longitudinal strain and creep behavior. The creep behavior was previously found to be inherent in interdigitated ferroelectric actuators. This causes the strain jumps of the PLSnZT piezocomposite to be more rounded.

The creep behavior of interdigitated piezocomposites also effected the PLZT actuator. The bulk response of the PLZT showed a quadratic electrictive transverse strain response with little hysteresis and no remnant strain. Conversely the PLZT piezocomposite actuator shows a significant increase in hysteresis and a remnant strain with removal of field. The remnant strain of the piezocomposite actuator does creep to zero after a period of one minute. Both the monolithic actuator and piezocomposite actuator achieved around the same transverse strain of 825 $\mu\epsilon$. The longitudinal strain output of the PLZT piezocomposite actuator also showed increased hysteresis, remnant strain, and creep. By slowing the frequency down, the hysteresis was decreased due by allowing for the strain to creep throughout the actuation process.

A comparison of the PLZT, PLSnZT and commercial MFC piezocomposite actuators is shown in figure 6.11. The quadratic electrostrictive PLZT actuator achieves peak strains similar to that of commercial MFC. The PLSnZT actuator though shows only 1000 $\mu\epsilon$ longitudinal strain compared to 1500 $\mu\epsilon$ longitudinal strain of the commercial MFC. Due to the poor bulk material response of PLSnZT compared to published values, it is believed that through better material manufacturing the strain output of the PLSnZT could be doubled.

Also to note is the very small transverse strain output of the PLSnZT actuator. With such a small transverse strain the volumetric strain ouput of the PLSnZT actuator bests both the PLZT and commercial MFC piezocomposite actuator.

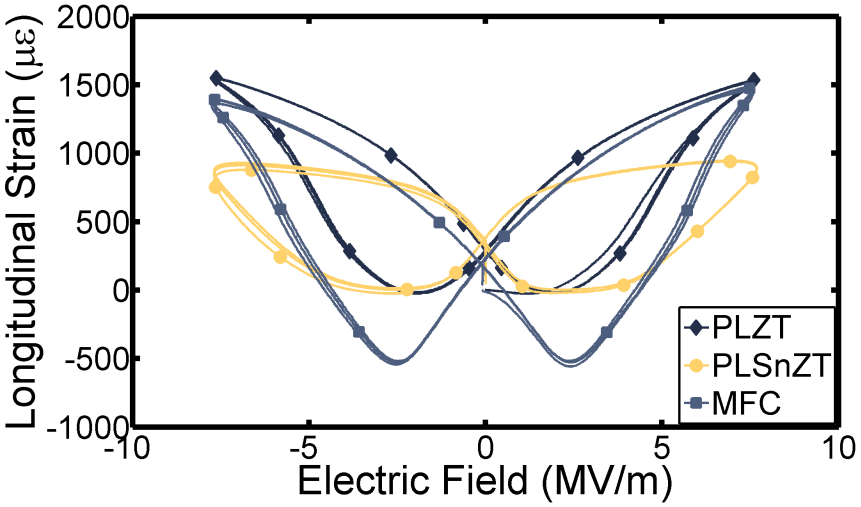

(a)

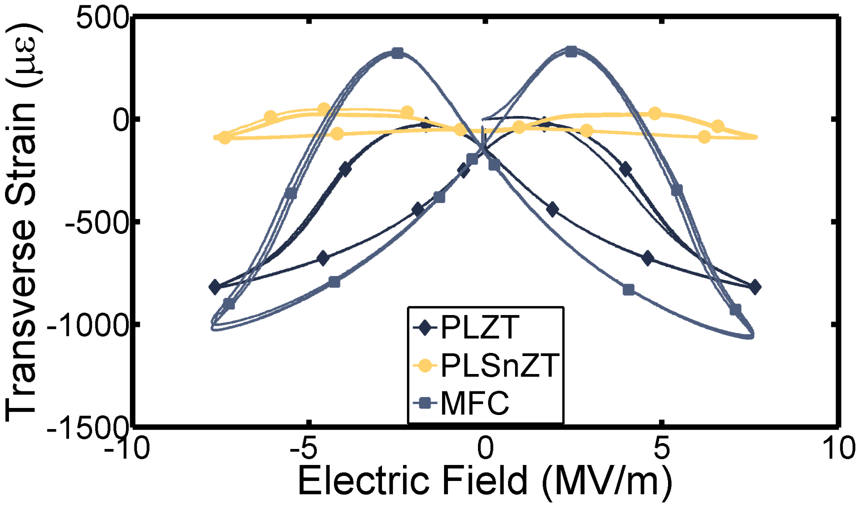

(b)

Figure 6.11: Piezocomposite actuator performance comparison of 55/33/12 PLSnZT 9.5/65/35 PLZT and MFC. Subfigure (a) indicates longitudinal strain output while subfigure (b) indicates transverse strain output.

6.5 Conclusion

Two new materials were explored for use as a piezocomposite actuator with interdigitated electrodes. The two explored compositions were phase transforming 55/33/12 PLSnZT and quadratic electrostrictive 9.5/65/35 PLZT. Both the compositions were manufactured using commercial actuator dimensions and electrode geometries.

The phase transforming PLSnZT piezocomposite actuator was able to phase transform from antiferroelectric tetragonal to ferroelectric rhombohedral. Upon removal of the electric field the actuator exhibited a permanent remnant strain. This was indicative of a partial reverse transformation from ferroelectric to antiferroelectric and retention of some of the ferroelectric phase. Also, while small, the actuator had a negative transverse strain which differs from the bulk material response in which both longitudinal and transverse strains are positive. The actuator also showed strain creep when the electric field on the actuator was removed.

The slim loop ferroelectric, quadratic electrostrictive PLZT piezocomposite actuator also showed creep and increased hysteresis. The increased hysteresis is troublesome, for the bulk material is used for its slim loop behavior. The PLZT piezocomposite actuator exhibited a small amount of remnant strain which crept back to zero when the electric field was removed. Slowing the frequency of actuation down decreased the hysteresis of the free strain response.

CHAPTER 7

Phase Field

7.1 Phase Field Framework

This chapter discusses an approach to modeling domain evolution in ferroelectric materials at the unit cell level. The approach combines a finite element code with a Landau-Devonshire ferroelectric polarization reorientation scheme. The finite element code uses linearly interpolated hexahedral elements to represent the unit cells of a ferroelectric material. Electrical and mechanical compatibility is governed by the finite element code and yields stress and electric fields in the material domain. The materials stress and electric field are then fed to the Laundau-Devonshire subroutine to determine polarization reorientation. A local gradient energy density is included for the material free energy density to approximate the atomic mismatch between neighboring unit cells. The polarization distribution is modeled as a discrete distribution of eigenstrains and eigenpolarizations. These discrete parameters are then subjected to compatibility conditions and boundary conditions from the finite element framework. The results show that the domain wall direction and width are dependent on a balance of atomic structure, electrostatic interactions, mechanical interactions, and atomic mismatches.

7.1.1 Introduction

Allik and Hughes laid the groundwork for ferroelectric finite element models by formulating a piezoelectric finite element routine utilizing an electric scalar potential and tetrahedral elements [14]. Since Allik and Hughes first modeled the piezoelectric effect using finite elements, it has been adapted for use with multiple element types and shape functions [15].

Chen and Lynch modeled ferroelectric materials using a linear piezoelectric finite element code with a micromechanical subroutine to determine polarization reorientation [17]. In this approach the finite element model used the electric scalar potential to model the electrical degree of freedom. Landis noted the scalar potential can yield non positive definite stiffnesses. He proposed using a vector potential formulation to account for the electrical degree of freedom [24]. Kamlah [19, 23, 113] and Fang et al [18, 114, 115] have also used finite element models to account for ferroelectric polarization reorientation.

Phase field theory is a model for solving interfacial problems. It is often employed using thermodynamic arguments to calculate driving forces that temporally evolve a material's microstructure. GJ Fix and Langer were one of the first to apply phase field theory. They used phase field theory to study crystal growth formations [116–118]. Nambu and Sagala applied phase field theory to model ferroelectric material behavior [119, 120]. They accomplished this by modeling the ferroelectric material analogously to Onuki's method for phase separating alloys. Onuki's method to model phase separating alloys used a time-dependent Ginzburg-Landau (TDGL) method. Onuki used elastic driving forces to drive the TDGL method in the seperation of alloys. Nambu and Sagala's approach used Landau-Devonshire theory to drive the TDGL method for ferroelectric microstructure evolution.

Devonshire first formulated Landau-Devonshire theory in the 1950s as a phenomenological technique to model the non linear behavior of ferroelectric materials [121]. Devonshire modeled the free energy surface such that energy wells captured the symmetry and spontaneous polarization behavior of ferroelectric materials. Landau, Rosetti, and other research groups have since extended Devonshire's work [122, 123]. Extending Devonshire theory, Caos and Cross added phenomenologically consistent elastic and polarization gradient energy density terms to the free energy density to account for domain wall widths of perovskite twinning structures [124]. Hu and Chen showed that global elastic and long range electrostatic interactions were required to achieve correct dipole-dipole arrangements [125, 126]. Li and Chen adapted the phase field model for ferroelectric thin films applications [127]. Wang et al utilized a phase field model to demonstrate macroscopic polarization-electric field and strain-electric field hysteresis loops [128].

Multiple solution schemes have been employed to numerically solve phase field problems. Shen and Chen used spectral methods for solving microstructure evolution. They showed that computations in Fourier space allowed for faster solution times and greater accuracy then Euler based finite-difference methods [129]. Su and Landis explored domain wall pinning utilizing a phase field model with a finite element formulation [130]. Wang and Kamlah developed a phase field model using a finite element code with Landau-Devonshire theory in order to investigate physical defects in single domain ferroelectric materials [131, 132].

This chapter uses a phase field model with a finite element based solution method to model unit cell length scale domain evolution problems. The element type used was a linearly interpolated hexahedral element to represent unit cells inside a ferroelectric crystal. The free energy density formulation used incorporates structural, electrostatic, electromechanical, and polarization gradient terms. This study attempts to model the physics of unit cell interactions.

A characteristic trait of ferroelectric materials is their spontaneous polarization. The spontaneous polarization induces an electrostrictive strain that elongates the unit cell along the polarzation axis and contracts transverse to the polarization axis. The possible spontaneous polarization orientations are dependent on crystal symmetries. Neighboring dipoles tend to orient themselves in the same direction forming domains. The interface between two different domains is referred to as a domain wall. Considering the spontaneous polarization is limited depending on the crystal symmetry, each phase can only accommodate domain walls of certain angles. The domain walls for tetragonal materials occur at 90 ° and 180 ° angles [133]. Experimental measurements on barium titanate have shown that the domain wall width of 180 ° domain walls are much smaller than 90 ° domain walls. Meyer and Vanderbilt [134] and Little [135, 136] found the domain wall thickness of a 90 ° wall to be around 4 nm and the domain wall thickness of a 180 ° wall to be the dimension of a unit cell.

7.1.2 Theory

Polarization evolution is governed by the TDGL method as shown in the following equation,

$$\frac{\Delta P_i^n}{\Delta t} = -\Gamma \frac{\delta F^n}{\delta P_i^n} + \eta_i^n, \tag{7.1}$$

where P is polarization, t is time, Γ is a kinetic coefficient, F is a free energy density and η is a noise term. Indicial notation is employed, the subscript i indicates spatial dimensions. For this formulation, there are three spatial dimensions, thus the index i runs from 1 to 3. The superscript n indicates an element number. The left-hand side of equation 7.1 is the temporal evolution of polarization, where ΔP_i^n is a change in polarization and Δt is the time step taken. The right-hand side shows that the polarization evolution is composed of a driving force term to minimize the free energy density F^n and a noise term η.

This approach discretizes the material domain into individual elements. Each element represents a perovskite unit cell that has its own eigenpolarization and eigenstrain. The finite element formulation to satisfy mechanical equilibrium and Gauss's law is shown in the following equation,

$$\sigma_{ij,j} + b_i = 0 \qquad\qquad D_{i,i} = \rho, \tag{7.2}$$

where σ, b, D, and ρ are stress, body forces, electric displacement and charge density respectively. As in Einstein summation convention, repeated indices indicate a summation of that term over all values of that index. Commas imply spatial differentiation with respect to the index to the right of the comma.

The finite element framework approximates each element as a unit cell. Figure 7.1 graphically depicts the ABO_3 perovskite structure represented by a linearly interpolated hexahedron element. The element nodes represent the A site atoms. Considering the element is linearly interpolated, both the eigenpolarization and eigenstrain are of constant value in each element. The eigenpolarizations are automatically induced in each unit cell by applying an appropriate unbalanced charge on each of the hexahedral element's eight nodes. Similarly, the eigenstrain of each element is automatically induced in each unit cell by applying an appropriate unbalanced force vector on each of the element's nodes. The finite element code is then used to find the electric potential and mechanical displacement fields and to make sure mechanical and electrical compatibility are maintained.

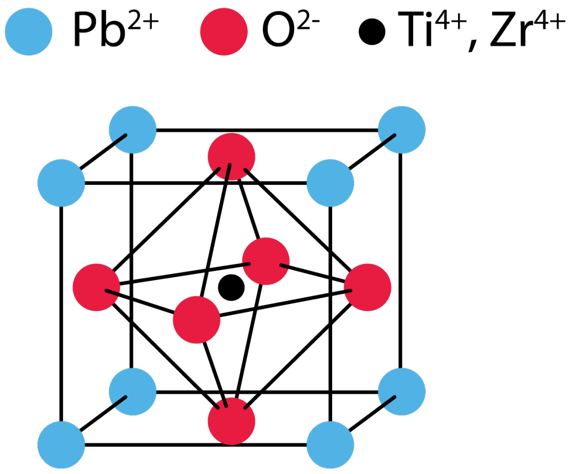

(a) (b)

Figure 7.1: (a) Perovskite unit cells. (b) Finite element representation of a poled perovskite unit cell using a hexahedron (brick) element showing the unbalanced charges at the nodes.

Spontaneous polarizations lead to eigenstrains that are not necessarily mechanical compatible with neighboring cells. Figure 7.2 demonstrates how the finite element code satisfies equlibrium to maintain mechanical compatibility between unit cells. Neighboring unit cells with incompatible strains that do not satisfy equilibrium are shown in figure 7.2a. When equilibrium is satisfied, the unit cells are forced into mechanical compatibility resulting in local stresses as shown in figure 7.2b. A similar technique is used to force electrical compatibility by using finite elements to satisfy Gauss's law.

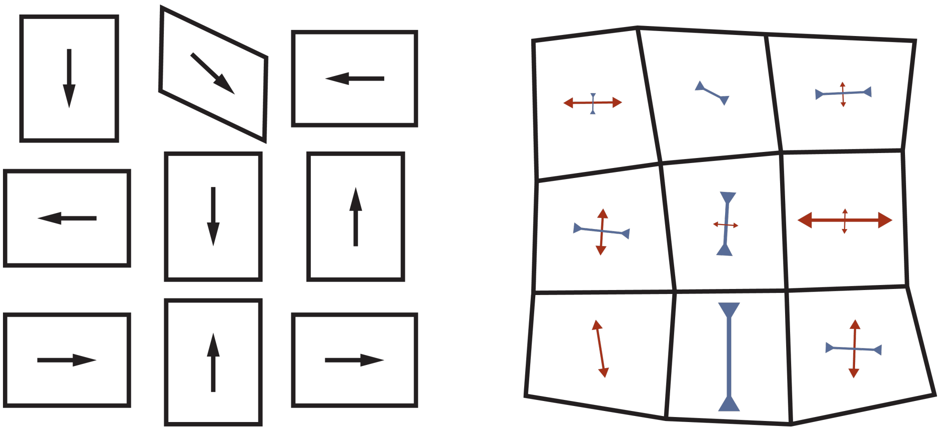

(a) (b)

Figure 7.2: (a) Polarizations, shown with arrows, give each unit cell an associated eigenstrain. (b) Displacments due to the total strain after compatibility are satisfied. Arrows indicate the principle stresses with compression in blue and tension in red.

The polarization evolution of the material is programmed into a material subroutine that uses the TDGL model from equation 7.1. Devonshire theory models the constitutive behavior of a ferroelectric material by taking a series expansion of the Gibbs elastic energy density, G_1. The series expansion of G_1 is,

$$\begin{aligned} G_1 = \underbrace{\frac{1}{2}a_{ij}P_iP_j + \frac{1}{4}a'_{ijkl}P_iP_jP_kP_l + \frac{1}{6}a''_{ijklmn}P_iP_jP_kP_lP_mP_n}_{\text{f structure}} \\ \underbrace{-Q_{abij}\sigma^{\text{local}}_{ab}P_iP_j}_{\text{f electrostrictive}} \underbrace{-E^{\text{local}}_{m}P_m}_{\text{f electrostatic}}, \end{aligned} \tag{7.3}$$

where G_1 is separated into three terms: the structure energy density, $f_{\text{structure}}$, also known as the Landau energy density, the electrostrictive energy density, $f_{\text{electrostrictive}}$, and the electrostatic energy density, $f_{\text{electrostatic}}$. In this formulation, polarization can be used to replace electric displacement in the constitutive law since $P \gg \epsilon_0 E$.

The $f_{\text{structure}}$ term creates energy wells along crystallographic families of directions to correspond to the material symmetry. The $f_{\text{electrostrictive}}$ term accounts for the effect on the free energy density when a local stress is applied. The tensor Q_{ijkl} is an isotropic electrostrictive tensor. The $f_{\text{electrostatic}}$ term accounts for the effect on the free energy density when a local electric field is applied. Both local stresses $\sigma^{\text{local}}_{ab}$ and local electric fields E^{local}_{m}

when applied to an element distort the surface of the total free energy density. The local stress and electric field are determined from the finite element frameworks solution of mechanical equilibrium and Gauss's law.

The Gibbs elastic energy from equation 7.3 can be rewritten in the form of a total free energy density, F. Heitmann and Rosetti proposed utilizing the total free energy density and separating the structural energy density into both isotropic and anisotropic components [137]. Using this technique, the free energy density is written as,

$$\begin{aligned} F &= f_{\text{structure}} + f_{\text{electrostrictive}} + f_{\text{electrostatic}} \\ f_{\text{structure}} &= \frac{1}{2}\alpha_2\left(P_1^2+P_2^2+P_3^2\right)+\frac{1}{4}\alpha_4\left(P_1^2+P_2^2+P_3^2\right)^2+\frac{1}{6}\alpha_6\left(P_1^2+P_2^2+P_3^2\right)^3 \\ &\quad +\frac{1}{4}\alpha_4'\left(P_1^4+P_2^4+P_3^4\right)+\frac{1}{6}\left[\alpha_6'\left(P_1^6+P_2^6+P_3^6\right)+\alpha_6''\left(P_1^2P_2^2P_3^2\right)\right] \\ f_{\text{electrostrictive}} &= -Q_{abij}\sigma_{ab}^{\text{local}}P_iP_j \\ f_{\text{electrostatic}} &= -E_m^{\text{local}}P_m. \end{aligned} \tag{7.4}$$

In order to visualize how the free energy density terms effect the energy surface landscape, different surface plots were created. Figure 7.3 shows a surface energy plot for a ferroelectric material with two-dimensional tetragonal symmetry. Figure 7.3a, is an example of the energy landscape with no local stress or electric field applied. Only the $f_{\text{structure}}$ term effects the energy surface. The structural energy creates four energy wells which represent the four possible in-plane spontaneous polarization directions. Each energy well has the same depth, thus each polarization direction is equally favorable. Figure 7.3b, is an example of the energy landscape with local stress and no electric field applied. In this figure, the effect of the $f_{\text{electrostrictive}}$ term on the energy landscape is observed. The electostrictive energy term causes the energy wells to deepen along the axis perpendicular to where the compressive stresses are applied. Similarly the energy wells become more shallow along the axis parallel to where the compressive stresses are applied. By changing the energy landscape, ferroelastic switching can occur as different energy wells become more favorable. Figure 7.3c, is an example of the energy landscape with no local stress and an applied electric field. In this figure, the effect of the $f_{\text{electrostatic}}$ term on the energy landscape is observed. The electrostatic energy term causes the energy density surface to tilt such that the energy lowers in the direction of the applied electric field. As the energy well along the electric field direction becomes more favorable, ferroelectric switching can occur.

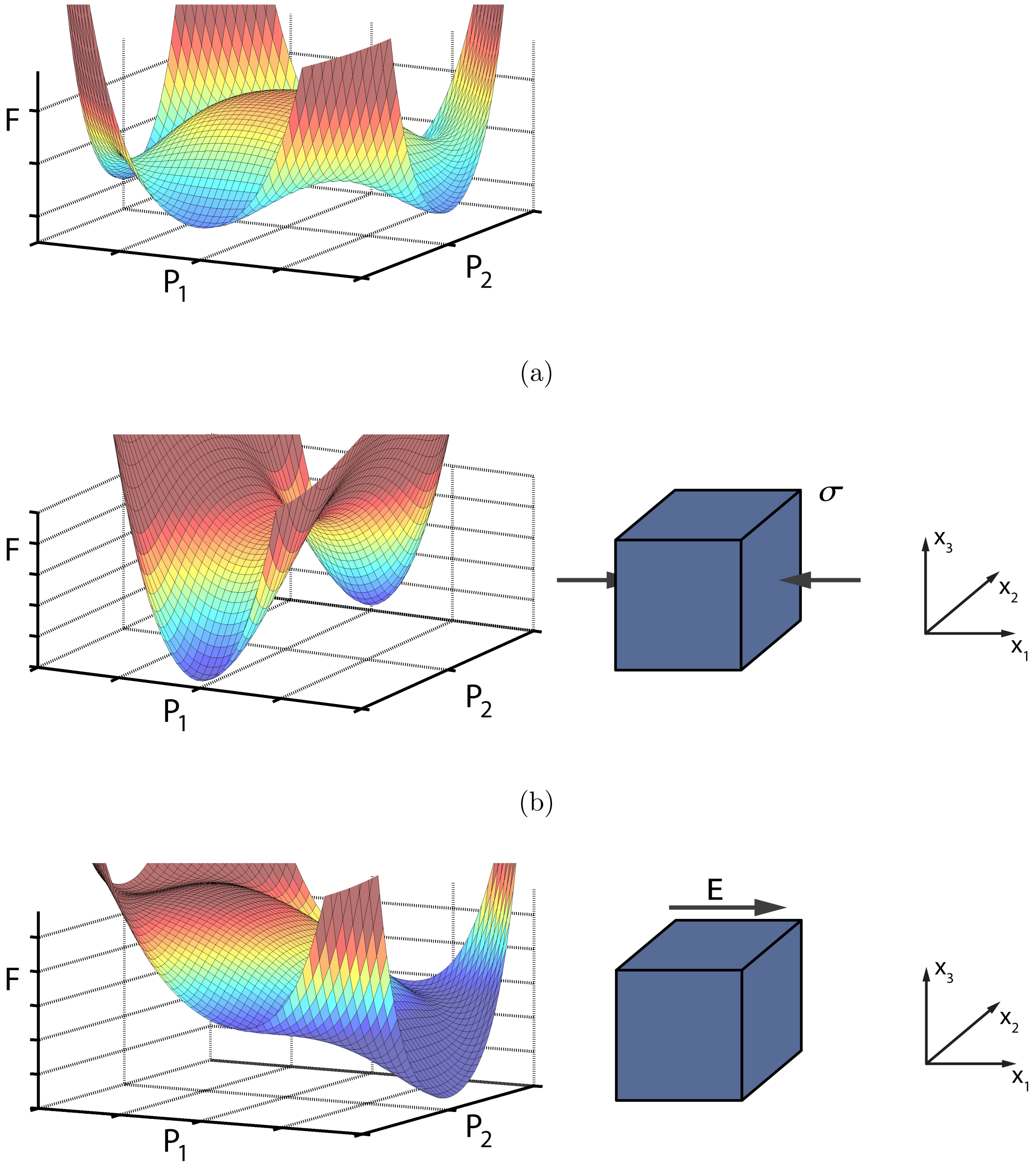

(a)

(b)

(c)

Figure 7.3: Gibbs elastic free energy density for a tetragonal material under: (a) no load, (b) externally applied stress, (c) externally applied electric field

The model for the free energy density takes into account structural, electrostatic, and electrostrictive terms. These terms determine spontaneous polarization directions and magnitudes and domain wall angles and thickness. Depending on the energy penalties for forming a domain wall, the driving forces can either favor a narrow or thick domain wall. By constructing simple domain formations, it can be determined whether the current model correctly forms domains such that the domain wall width of 180 ° domain walls are much smaller than 90 ° domain walls.

Figure 7.4 visualizes the energy penalties for forming both 90 ° and 180 ° domain walls in a material with tetrangonal symmetry. Electric compatibility for a 90 ° domain wall is shown in figure 7.4a. The eigenpolarizations are represented as charges on the nodes. The charges remain neutral for a 90 ° domain wall, and thus electric compatibility does not penalize a narrow domain wall width. Mechanical compatibility for a 90 ° domain wall is shown in figure 7.4b. The eigenstrains cause elongation of the unit cell along the spontaneous polarization direction. In order to be mechanically compatible internal stresses will develop, this leads to an energy penalty. Thus, a larger domain wall width will occur in order to reduce the energy penalty from the internal stresses. The third term dictating domain formation is the structural term. The structural term has symmetry such that the energy wells equally favor each of the spontaneous polarization directions and thus does not dictate domain wall width.

Similarly, the energy penalties for 180 ° can be seen in figures 7.4c and 7.4d. The electric compatibility for a 180 ° domain wall is shown in figure 7.4c. The charges again remain neutral and do not penalize a narrow domain wall width. Mechanical compatibility for a 180 ° domain wall is shown in figure 7.4c. For the 180 ° domain wall, the unit cells are mechanically compatible and thus do not cause internal stresses. Thus, there is no mechanical energy penalty for a 180 ° domain wall and narrow wall widths are not penalized.

From the visualization of the domain walls using our model, it is determined that the domain wall widths correspond to experiment. The mechanical incompatibility of 90 ° domain walls yield larger domain wall widths. The 180 ° domain wall has neither mechanical or electrical incompatibility which favors a narrow width.

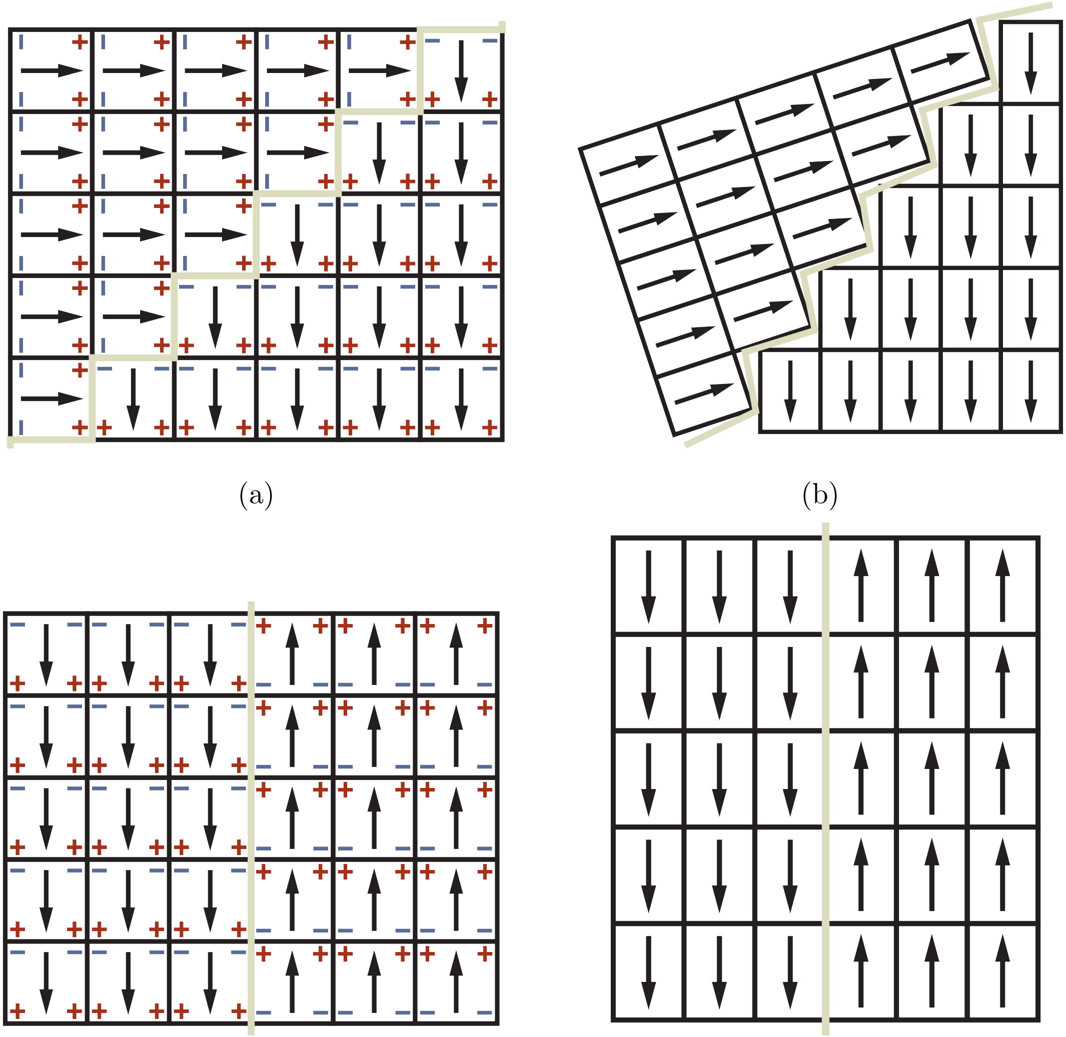

(a) (b)

(c) (d)

Figure 7.4: (a) Electrical compatibility along a 90° domain wall in tetragonal material. (b) Mechanical compatibility along a 90° domain wall in tetragonal material. (c) Electrical compatibility along a 180° domain wall in tetragonal material. (d) Mechanical compatibility along a 180° domain wall in tetragonal material.

With the structural, electrostrictive, and electrostatic free energy terms derived from devonshire theory it is seen that it qualitatively yields the correct domain wall line widths. A problem still arises in 180° domain formation. By enforcing only mechanical and electrical compatibility, both ferroelectric and antiferroelectric domain configurations are equally favorable. Figure 7.5 visualizes the ferroelectric (single domain) and antiferroelectric (anti-parallel head-to-tail) domain configurations. The single domain configuration shown in figure 7.5a is just as energetically favorable as the anti-parallel head-to-tail configuration shown in figure 7.5b. In both cases mechanical and electric compatibilities are satisfied causing domains of both types to likely form. In ferroelectric materials, the single domain configuration is more favored. In antiferroelectric materials, the anti-parallel head-to-tail domain configuration is more favored. Thus, there must be another energy term that allows for favoring of one of the domain types over the other.

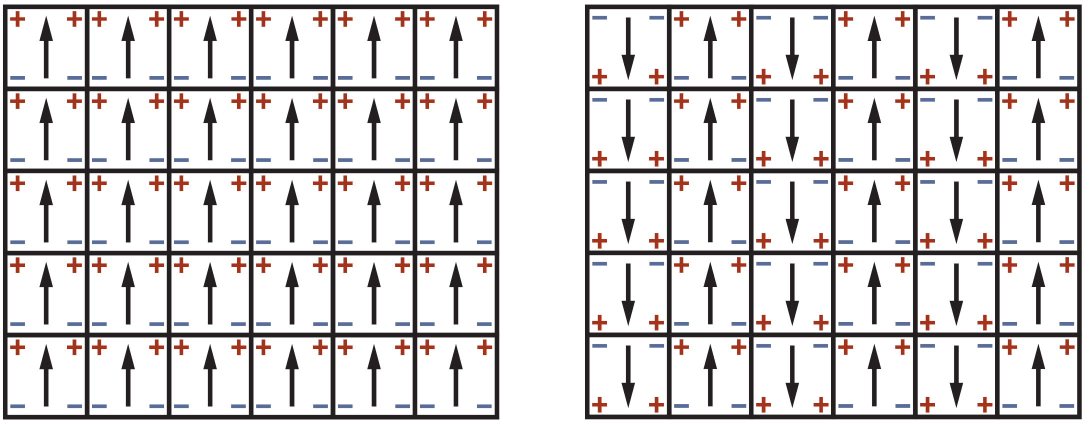

(a) (b)

Figure 7.5: Mechanical and electrical compatibility for the (a) single domain and (b) anti-parallel head-to-tail configurations

The finite element formulation was used to enforce mechanical compatibility. The eigenstrains resulting from a unit cell's spontaneous polarization only account for shift of the A site ions in an ABO_3 perovskite crystal structure. The eigenstrains do not account for the B site ions or the oxygen atoms. The distortion of the B site ions and the oxygen atoms do not necessarily distort in a similar fashion to the A site ions. Shirane et al [138] found that for lead titanate, the oxygen octahedra shifts off center from the unit cell formed by the lead atoms. This is represented in figure 7.6a

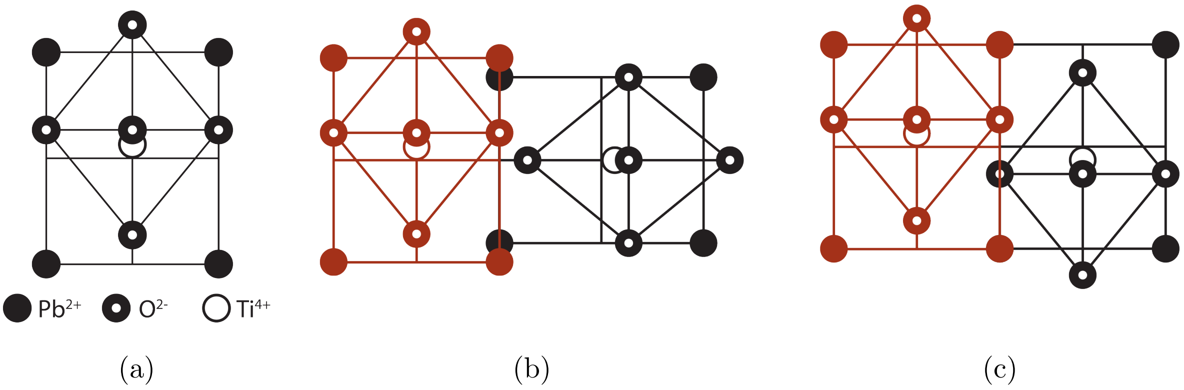

(a) (b) (c)

Figure 7.6: (a) The atomic distortions for a poled $PbTiO_3$ unit cell modified from Shirate [138]. (b) Neighboring $PbTiO_3$ unit cells with a 90 ° change in polarization direction. (c) Neighboring $PbTiO_3$ unit cells with a 180 ° change in polarization.

The distortion of the oxygen octahedra in an ABO_3 perovskite structure with spontaneous polarization also effects domain formation. The mechanical compatibility taking into account the oxygen octahedra for both 90 ° and 180 ° domain walls is shown in figures 7.6b and 7.6c. Figure 7.6b shows the atomic mismatch associated with 90 ° domain walls. There is a mechanical incompatibility for the A site lead atoms as previously predicted. The oxygen octahedra also yields further mechanical incompatibility. Figure 7.6c shows the atomic mismatch associated with 180 ° domain walls. There is no mechanical incompatibility for the A site lead atoms as previously predicted. The off center shift of the oxygen octahedra yields a mechanical incompatibility. This incompatibility is not inherent in the model presented in equation 7.4. An energy penalty for the mechanical incompatibility of the oxygen octahedra must be accounted for to control the formation of single domain versus anti-parallel head-to-tail domain configurations.

A simple technique is incorporated from other phase field models in order to account for the mechanical incompatibility of the oxygen octahedra. The oxygen octahedra mechanical incompatibility is incorporated by penalizing the square of polarization gradients. This energy penalty is as follows,

$$f_{\text{gradient}} = g_{ijkl} P_{i,j} P_{k,l}, \tag{7.5}$$

where f_{gradient} is variable denoting the definition of a local gradient energy density term, g_{ijkl} is a tensor that is used penalize atomic mismatches according to material symmetry. The tensor g_{ijkl} can be simplified down to four different constants for cubic symmetry [124–126, 128]. The four separate constants are denoted as g_{11}, g_{12}, g_{44} and g'_{44}. The gradient free energy term can thus be represented as,

$$\begin{aligned} f_{\text{gradient}} = \frac{1}{2}g_{11}\left(P_{1,1}^2 + P_{2,2}^2 + P_{3,3}^2\right) + g_{12}\left(P_{1,1}P_{2,2} + P_{1,1}P_{3,3} + P_{2,2}P_{3,3}\right) \\ +\frac{1}{2}g_{44}\left[\left(P_{1,2} + P_{2,1}\right)^2 + \left(P_{1,3} + P_{3,1}\right)^2 + \left(P_{2,3} + P_{3,2}\right)^2\right] \\ +\frac{1}{2}g'_{44}\left[\left(P_{1,2} - P_{2,1}\right)^2 + \left(P_{1,3} - P_{3,1}\right)^2 + \left(P_{2,3} - P_{3,2}\right)^2\right]. \end{aligned} \tag{7.6}$$

7.1.3 Results

Simulations were conducted to test the energy formulation with the structure, electrostrictive, electrostatic and gradient terms. The coefficients used for the simulations are shown in table 7.1. The TDGL method was modified such that the maximum change in polarization could not deviate more than 10% of the spontaneous polarization magnitude. This limited any oscillatory behavior of the solution and prevented instabilities. In calculating each of the free energy terms, the structure, electrostrictive, and electrostatic terms were independent of the element dimensions. The free energy term for gradient energy is dependent on element dimensions as it depends on spatial derivatives of the polarization terms. The gradient free energy term was scaled such that the g coefficients can be represented as $g_{ij} = \gamma_{ij}a^2$ where $a \times a \times a$ is the dimension of an undistorted element. The electrostrictive tensors are given in a coordinate system such that the x_1 axis is parallel to the polarization of the element. The simulations were run in effectively two-dimensions such that one of the dimensions was only five elements thick. The polarization was restricted to only be in-plane with the two-dimensional structure. The ferroelectric material was simulated with a five element thick vacuum around it's border. The vacuum was formulated such that it had zero stiffness, the permittivity was of free space, and it had zero polarization. The vacuum permitted the simulation of open circuit unclamped boundary conditions. This boundary condition was necessary to prevent the formation of single domains, considering any polarization normal to the ferroelectric material surface would incur an energy penalty due to Gauss's law.

$f_{\text{structure}}$					
$\alpha_2\,(\mathrm{Jm^{-3}})$	$\alpha_4\,(\mathrm{Jm^{-3}})$	$\alpha_6\,(\mathrm{Jm^{-3}})$	$\alpha'_4\,(\mathrm{Jm^{-3}})$	$\alpha'_6\,(\mathrm{Jm^{-3}})$	$\alpha''_6\,(\mathrm{Jm^{-3}})$
-0.31×10^6	-1.05×10^6	2.67×10^6	-1.30×10^6	0	0
f_{gradient}					
$\gamma_{11}\left(\mathrm{mVC^{-1}}\right)$	$\gamma_{12}\left(\mathrm{mVC^{-1}}\right)$	$\gamma_{44}\left(\mathrm{mVC^{-1}}\right)$	$\gamma'_{44}\left(\mathrm{mVC^{-1}}\right)$		
282	0	138.4	138.4		
$f_{\text{electrostrictive}}$ and FEM coefficients					
$Q^0_{11}\left(\mathrm{m^4 \cdot C^{-2}}\right)$	$Q^0_{22}\left(\mathrm{m^4 \cdot C^{-2}}\right)$	c_{11} (MPa)	c_{12} (MPa)	c_{44} (MPa)	$\epsilon\,(\epsilon_0)$
0.015	-0.0075	120	80	20	200

Table 7.1: Simulation coefficients for tetragonal ferroelectric material

Two simulations were conducted to show the effect of a ferroelectric material's aspect ration on domain formation. The first simulation was that of a ferroelectric material with an aspect ratio of unity. Figure 7.7 shows the formation of domains for this material. The open circuit boundary conditions promote polarizations parallel to the material boundary. The aspect ratio of unity promotes the development of four 90 ° domain walls that span from the corners of the material. The domains form in that of a vortex pattern. The influence of the separate free energy terms can be seen. The electrostrictive energy term creates an energy penalty for the 90 ° domain walls. Wide 90 ° domain walls can be seen. The gradient energy term prevents any anti-parallel head-to-tail domains to form. The preference for the material polarizations to lie in vertical or horizontal directions is from influence in the structure term.

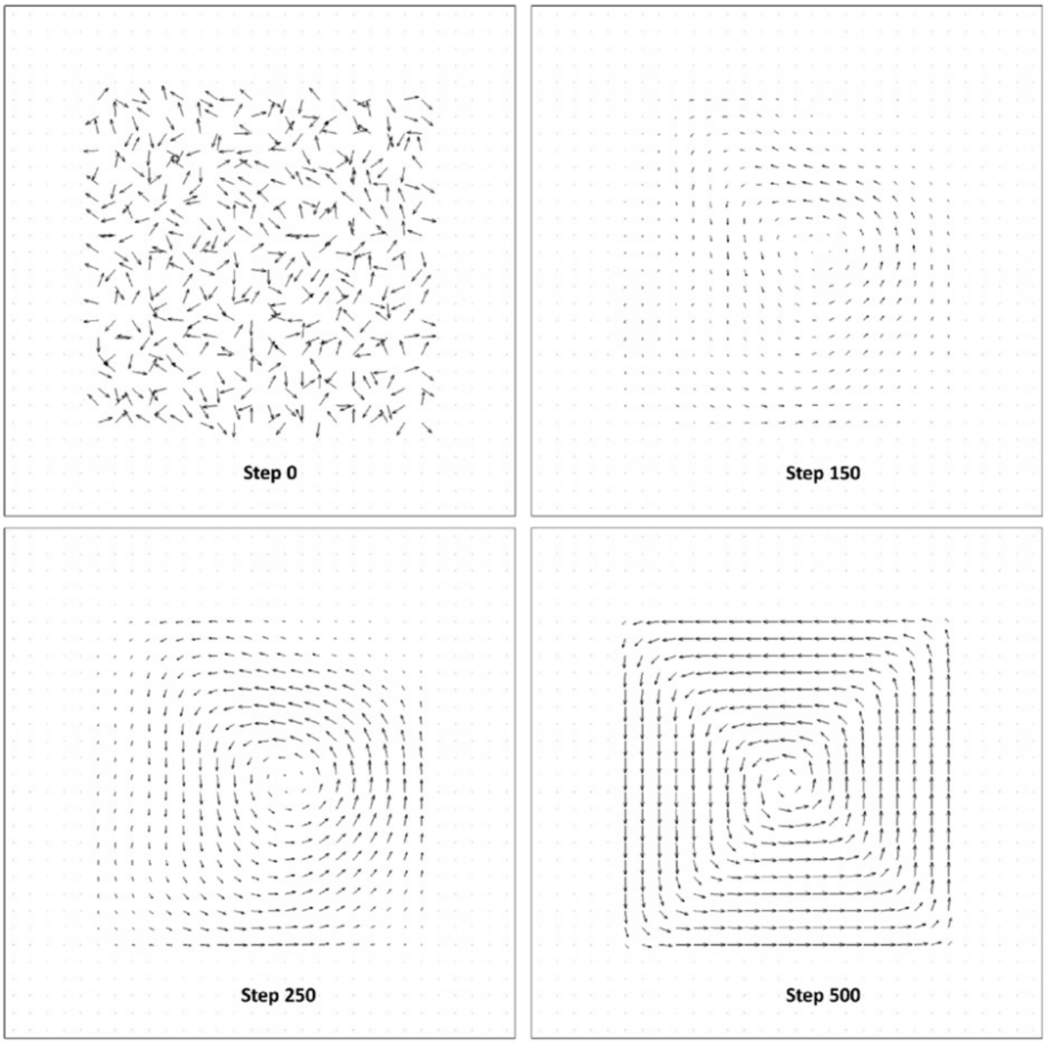

Figure 7.7: 20 × 20 element simulation of tetragonal ferroelectric material with unconstrained open circuit boundary conditions.

A simulation of a ferroelectric material with a higher aspect ratio of 2.5 was performed. Figure 7.8a shows the formation of domains for this material. The same boundary conditions as the material with an aspect ratio of unity were used for this simulation. The simulation with an aspect ratio of unity had only 90 ° domain walls. By increasing the aspect ratio to 2.5, 180 ° domain walls were also formed. Figure 7.8b investigates the domain wall widths formed. Both 90 ° and 180 ° domain wall widths were compared. It was found that the 180 ° domain wall width was around $3a$ whereas the 90 ° domain wall had a width of $5.4a$. This corresponds to the findings of Meyer and Vanderbilt [134] and the model implementation.

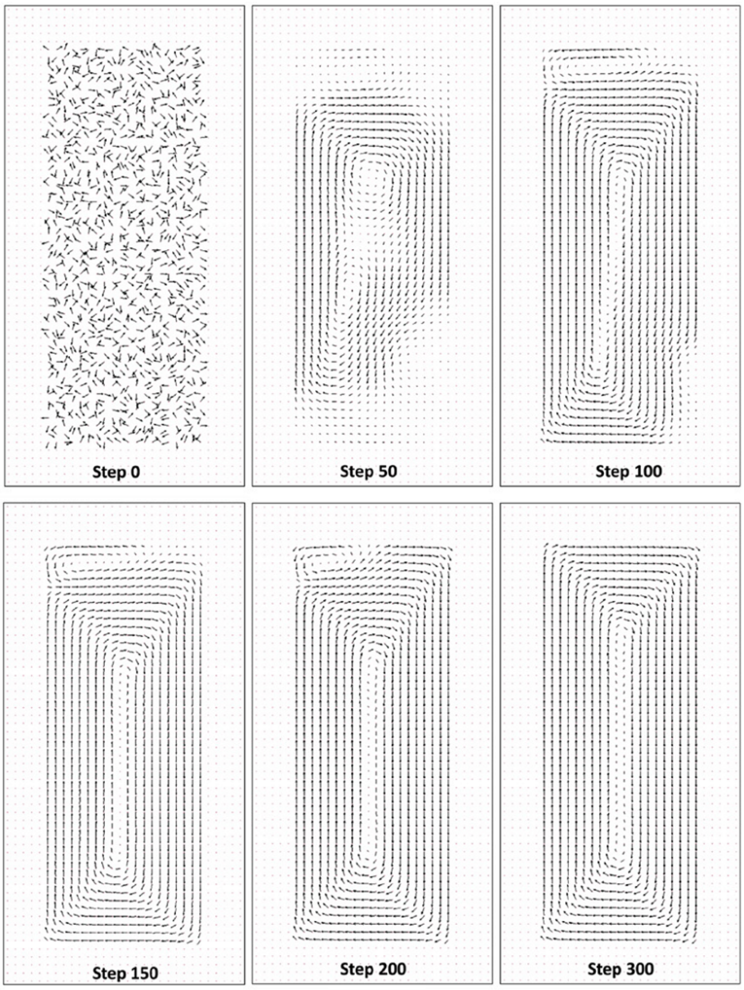

(a)

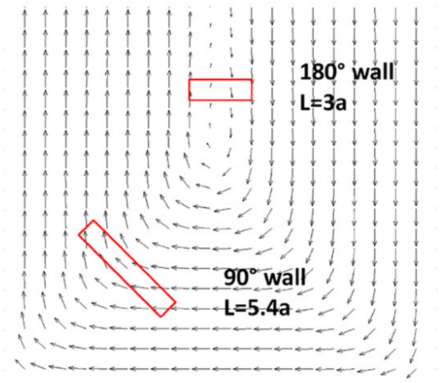

(b)

Figure 7.8: (a) 50 × 20 element simulation of tetragonal ferroelectric material with unconstrained open circuit boundary conditions. (b) Enlarged portion of the simulation shown in (a) that highlights the difference in width between the 90 ° and 180 ° domain walls.

CHAPTER 8

Conclusions

Piezoceramic composite actuators have offered many advantages over conventional monolithic piezoceramic devices. The use of piezoceramic fibers embedded in an epoxy matrix allows for the device to be conformable to surfaces with larger curvatures. The conformability of the device also leads to durability. Dubbed an active fiber composite, Bent combined the interdigitated electrode design with a piezoceramic fiber composite. The AFC is composed of cylindrical fibers embedded in a soft epoxy matrix. The IDE design allowed the AFC to polarize along the longitudinal axis of the fibers. This led to larger strains in the device due to d_{33} mode actuation and for anisotropic sensing/actuation.

Researchers at NASA Langley extended the AFC design by using square fibers instead of round fibers. This device was coined the macro fiber composite. The MFC improved upon the AFC by having a larger contact area with the electrodes to the fibers. This mitigated some of the electric field drop in the fibers due to dielectric mismatch between the epoxy and the piezoceramic fibers. The manufacturing of the device was streamlined by dicing fibers out of a piezoceramic wafer on top of a polymer carrier film. The polymer carrier film allowed for handling whole sheets of fibers rather than individual fibers. When handling individual fibers, manufacturing time/cost was increased and the sharp corners tended to sever the device's electrodes.

While piezocomposites with IDE have enabled practical applications for piezoelectric devices ranging from aircraft control surface morphing, sensor/actuator rosettes and helicopter rotor blade vibration control, they also introduced new device problems. The devices have increased creep and strain relaxation times leading to frequency and time dependent behavior. Studies that have attempted to model these piezocomposites largely ignore this problem.

The focus of this dissertation has been to address some of these deficiencies and find designs that could diminish them.

8.1 Summary of Results

Equations for a $0^\circ, 45^\circ, 90^\circ$ strains sensing rosette was developed for piezoceramic devices with anisotropic in-plane properties. The piezoceramic crystals were bonded to an aluminum plate that was instrumented with strain gages. The plate was bent about various axes relative to the strain sensing rosette. The strain components in the plate were calculated using both the strain gages and the piezoceramic rosette. The strain sensing rosette equations for the piezoceramic device demonstrated the possibility to sense principal strain components and actuate principle strains.

The feasibility of the MFC for use as a strain sensing rosette was explored. A single MFC was bonded to an aluminum plate that was instrumented with strain gages. The MFC was subjected to various strain conditions by bending the plate using a four point bend system. The strain conditions read on the strain gages were used to predict the charge output of the MFC. It was found that the MFC had increased error when used as a strain sensor over single crystal rosettes.

A parametric study of 20 distinct piezoceramic actuators with IDE was compared. It was found that when the electrode line width L_2 was less than the piezoceramic substrate height H, the actuator was difficult to pole. The reasoning for the poling difficulties was identified by using Gauss's law. The polarization of the substrate's midplane was limited by how much free charge was on the electrodes. By applying a high DC voltage to the actuator, the net polarization and strain output increased. Over time the strain output would saturate and the polarization process was completed. In some cases the polarization process could take 50 minutes.

In order for the this unforeseen polarization to occur, the symmetry arguments used for Gauss's law must have been broken. It is surmised that charge conduction in the epoxy, or charge conduction in cracks along the electrode edges must have allowed for some of the actuators to polarize. The charge conduction causes a larger effective electrode size then its actual size. The larger effective electrode size would then cause the material to polarize.

Typically comparisons between actuator geometries are made by defining a nominal electric field as the applied voltage V divided by the electrode separation L or electrode gap $L - L_2$. A dielectric model of the custom actuators was made that compared na average dielectric midplane electric field to the nominal electric field. It was found that the dielectric electric field in the fiber was only proportional to the nominal electric field in regions where the relative electrode gap $(L - L_2)$ was larger than 2.0. Thus, when comparing actuators, the nominal electric field may not be appropriate when the relative electrode gap is less than 2.0. It was also found that care must be made when using the midplane electric field, for the distribution of the electric field at the midplane ceases to be uniform when the relative electrode gap is less than 2.0.

A commercial MFC was used as a shape memory piezoelectric actuator. It was found that its use as a shape memory piezoelectric actuator was feasible, but attempts were made to improve upon its performance. A custom actuator with a small relative electrode line width was polarized using the DC polarization technique. It was found that the commercial MFC had a shape memory strain range of around 1400 $\mu\epsilon$, while the custom actuator had a shape memory strain range of 2000 $\mu\epsilon$.

The twenty custom actuators were compared for initial polarization strain, unipolar strain after DC polarization, and creep strain. During the initial polarization cycle, it was found that when the relative electrode gap was held constant, actuators with a relative electrode line width of 1.0 had peak performance. When the relative electrode line width was held constant, actuator performance increased as the relative electrode gap was increased. Thus, during the initial polarization cycle the best performing actuator had the largest relative electrode gap and a relative electrode line width of 1.0.

After DC polarization, the free strain performance was again compared. The free strain performance was vastly different from the initial polarization performance. The actuators still showed that when the relative electrode line width was held constant, actuator performance increased as the relative electrode gap was increased. There was no longer a peak performance at a relative electrode line width of 1.0. When the relative electrode gap was held constant, actuator performance increased as the relative electrode line width was decreased. Thus, after the DC polarization cycle the best performing actuator had the largest relative electrode gap and the smallest electrode line width.

After a unipolar actuation cycle, each actuator would exhibit relaxation creep strain. The creep response of each actuator was compared. It was found that when the relative electrode line width was held constant, the creep strain decreased as the relative electrode gap was increased. Also, when the relative electrode gap was held constant, the creep strain increased as the relative electrode line width decreased. Thus, actuators with the most creep had the smallest relative electrode gap and the smallest relative electrode line width. Actuators with the least amount of creep had the largest relative electrode gap and the largest relative electrode line width. It was found that relaxation time and DC polarization time was also proportional to the creep strain and showed the same trends.

The material used in the custom actuators was PZT-5A. PZT-5A is a “soft” ferroelectric which does not show any polarization direction preference in actuation performance. It was found that custom actuators with large relative electrode line widths also showed the soft ferroelectric behavior. As the relative electrode line width shrunk the custom actuators showed more and more of a directional preference for their initial polarization direction. This is more indicative of a “hard” ferroelectric. By changing the electrode geometry it was shown that the material response changed from a “soft” ferroelectric to be like a “hard” ferroelectric.

Most computational analysis of piezocomposite actuators has been performed with linear piezoelectric finite element codes. A ferroelectric finite element code was developed to extend the linear piezoelectric models typically employed. While it was found experimentally that certain geometries exhibit creep and time dependency, with a large enough relative electrode line width the quasistatic code could still be used. It was found that along the electrode edge there are large stress concentrations due to polarization gradients in the material. During unipolar actuation, the stress gradients cause ferroelastic switching and domain wall motion.

This domain wall motion leads to increased hysteresis in the actuator response.

With the increased creep and relaxation times of certain actuators, it was surmised that certain actuators would have significant frequency dependency. A commercial MFC was first used to test its free strain frequency response from 0.1 Hz to 15 Hz. Typically the commercial MFC has values that are reported independent of actuation frequency. It was found that increasing the frequency from 0.1 Hz to 15 Hz caused the piezoelectric coefficient of the MFC to decrease to 51% of the reported value. Custom actuators with large relative electrode line widths were found to have less creep strain and relaxation times. Two custom actuators with larger relative electrode line widths than the MFC were investigated. It was found that the custom actuators were able to prevent some of the decay of the piezoelectric coefficient. The bulk response of PZT-5A was also investigated. It found that there was very little frequency dependency of free strain response for the bulk material from 0.1 Hz to 15 Hz.

Two exotic ferroelectric ceramic material compositions were considered for use in a MFC configuration. The compositions were synthesized using a mixed oxide method. The two compositions explored were phase transforming 55/33/12 PLSnZT and quadratic electrostrictive 9.6/65/35 PLZT. Monolithic plates of the exotic material were formed. The plates were diced into fibers and packaged using the same geometric configuration as a commercial MFC.

It was found that the increased hysteresis in the MFC configuration greatly effected the exotic materials. The bulk electrostrictive PLZT exhibited a quadratic free strain response with little hysteresis and no remnant strain. The PLZT MFC actuator showed a significant increase in hysteresis and remnant strain. The material response of the PLZT MFC actuator no longer had any advantages of the bulk material. The peak unipolar strain was comparable to a commercial MFC.

A similar problem was found for the phase transforming PLSnZT in the MFC configuration. The bulk response PLSnZT is such that it has a strain jump when phase transforming from anti-ferroelectric to ferroelectric. The PLSnZT MFC actuator resisted the phase transformation. This caused the phase transformation to occur over a wider range of electric field values. The actuator no longer had a sharp strain jump. The peak unipolar strain of the PLSnZT MFC actuator was roughly 2/3 of the commercial MFC actuator. But, the bulk composition synthesized showed smaller than expected free strain response. Thus, it is still possible that the PLSnZT actuator could outperform the commercial MFC.

The domain configuration around the electrode edge is of interest when designing actuators with IDE. A finite element based phase field model was created by applying a Landau-Devonshire type multi-well potential as a material subroutine to a finite element framework. The formed domain walls are created by a balance of mechanical, structure, electrostatic, and local gradients. The effect of the free energy density balance was explored on the 180° and 90° domain walls.

8.2 Contributions

Prior to this research very little work had gone into characterizing piezocomposite actuators with IDE beyond using linear piezoelectric finite element analysis. The work of this dissertation has found several nonlinear effects which can significantly effect actuator performance. It is the hopes of the author that this research can help improve device design of piezocomposite actuators with IDE. A list of contributions is shown below.

- A method to create strain sensor/actuator rosettes using anisotropic piezoceramic devices was made. It was found that when using a MFC for use as a strain sensor/actuator rosette the hysteresis inherent in the device made it difficult to accurately sense strain. By increasing the relative electrode line width of the actuator, it could be possible to reduce the hysteresis and make a more accurate rosette.

- A DC polarization process was created to fully polarize piezoceramic actuators with IDE. By applying large enough DC polarizing fields, actuators with small relative electrode line widths were able to perform better than previously considered. This process has allowed for the discovery of actuator geometries whose free strain outperform commercial MFC.

- A process for comparing IDE geometries was explored. A dielectric finite element code was created to automatically mesh a range of IDE geometries and report average midplane electric fields. This could prove useful when comparing actuators over using a nominal electric field.

- A ferroelectric finite element code was created to explore the polarization process of an actuator with IDE. It proved useful in its exploration of stress concentrations along an electrode edge and any induced ferroelectric/ferroelastic switching inherent when electrically driving the actuator. The ferroelectric code also proved useful in showing the initial polarization response of the actuators.

- A 20 actuator parametric study was performed to experimentally determine actuator performance trends. It was found that after DC polarization actuators with large relative electrode gaps and small relative electrode line widths had the most free strain actuation. Actuators with large relative electrode gaps and large relative electrode line widths exhibited the least creep and smallest relaxation times.

- The frequency response of commercial MFC was explored. It was found that the free strain response of commercial MFC was sensitive to frequency from a range of 0.1 Hz to 15 Hz. The frequency sensitivity caused the free strain response to drop by over 50%. This frequency dependency was mitigated through the use of a custom actuators with larger relative electrode line widths.

- Phase transforming PLSnZT and quadratic electrostrictive PLZT was synthesized using a mixed oxide method. The materials were packaged with the same geometries as a commercial MFC actuator. It was found that the MFC actuator with exotic materials had significantly increased hysteresis and frequency dependency over a bulk actuator.

8.3 Future Work

The findings of the research in this dissertation have opened up many more interesting problems. Some of nonlinearities found were not expected to occur or not expected to have a significant contribution to material response. While this work has addressed some of these characterization issues, more can be done to accurately model the piezoceramic actuators with IDE.

While it is surmised that a conduction mechanism has allowed for actuators with small relative electrode line widths to polarize, the actual mechanism hasn't been proved or explored. Sensing the free charge on a Sawyer Tower Circuit has shown that both the custom actuators and MFC had appreciable conduction compared to the bulk material. It is hypothesized that the charge conduction in the epoxy or in cracks along the electrode edge is causing the effective electrode line width to increase. Experiments should be performed with metal deposited IDE to determine whether it is the epoxy or cracking that is causing the conduction issue. Also, the metal deposited IDE could be used to explore whether the DC polarization technique could still be used to polarize actuators with small relative electrode line widths.

When exploring the free strain frequency response of the MFC and custom actuators, an exponential decay plus a linear constant coefficient fit was used to describe to actuator response. While the goodness of fit parameters showed significant agreement, the fit has no physical significance besides experimental observation. It is surmised that the frequency response is due to the creep strain and relaxation times of the actuators. These creep strain and relaxation effects can be captured using rheological models. The rheological model could then be used to predict the frequency response of the MFC or other custom actuators.

Initial tests were performed using exotic phase transforming PLSnZT and quadratic electrostrictive PLZT. The exotic materials were packaged using the geometries of a MFC. It was found that the exotic materials deviated significantly from the bulk material due to increased creep and relaxation times. By packaging the exotic materials in a custom actuator with larger relative electrode line widths, the actuators should exhibit a response more comparable to the bulk material. Doing so should allow a better estimate whether these materials can be used in an IDE actuator configuration.

Finally, a domain evolution phase field model was developed. The phase field model was used as a proof of concept for determining domain patterns within a ferroelectric material. Along the electrode edge of the actuator there are large electric field gradients. These electric field gradients cause cracks to grow along the electrode edge. By using the phase field model, it could be possible design an electrode that mitigates some of the electric field concentrations discussed.

APPENDIX A

Rosette Equations

If the crystals are thin relative to their width and length and ideally bonded to the substrate such that shear lag effects can be neglected, the crystals will each be in a state of plane stress with in-plane strain components matching those of the substrate. This leads to a state of strain in which there are three in-plane components ε_{11}, ε_{22}, ε_{12} and one out-of-plane strain ε_{33}. The strains $\boldsymbol{\varepsilon}$ of each crystal in their local coordinates are expressed as ε^0_{11}, ε^0_{22}, ε^0_{12}, ε^0_{33};ε^{45}_{11}, ε^{45}_{22}, ε^{45}_{12}, ε^{45}_{33}; ε^{90}_{11}, ε^{90}_{22}, ε^{90}_{12}, ε^{90}_{33}. The three in-plane strain components in the substrate ε_{11}, ε_{22} and ε_{12} are to be found in terms of the three measured electric displacement components. In the coordinate system shown in figure 2.3, the crystals's local strains are defined in terms of the global coordinate system,

$$\begin{aligned}
\varepsilon^0_{11} &= \varepsilon_{22} & \varepsilon^{45}_{11} &= \frac{1}{2}\left(\varepsilon_{11}+\varepsilon_{22}\right)-\varepsilon_{12} & \varepsilon^{90}_{11} &= \varepsilon_{11} \\
\varepsilon^0_{12} &= -\varepsilon_{12} & \varepsilon^{45}_{12} &= \frac{1}{2}\left(\varepsilon_{11}-\varepsilon_{22}\right) & \varepsilon^{90}_{12} &= -\varepsilon_{12} \\
\varepsilon^0_{22} &= \varepsilon_{11} & \varepsilon^{45}_{22} &= \frac{1}{2}\left(\varepsilon_{11}+\varepsilon_{22}\right)+\varepsilon_{12} & \varepsilon^{90}_{22} &= \varepsilon_{22}
\end{aligned} \tag{A.1}$$

The piezoelectric constitutive law in indicial notation is given by,

$$\begin{aligned}
\sigma_{ij} &= C^E_{ijkl}\varepsilon_{kl} - e_{nij}E_n \\
D_m &= e_{mkl}\varepsilon_{kl} + \kappa^{\varepsilon}_{mn}E_n
\end{aligned} \tag{A.2}$$

where σ_{ij} and ε_{kl} are stress and strain, E_n and D_m are electric field and electric displacement, C^E_{ijkl}, e_{nij} and $\kappa^{\varepsilon}_{mn}$ are elastic, piezoelectric and dielectric tensors. Considering only the x_3 axis directions, the electric displacement constitutive law is,

$$D_3 = e_{3kl}\varepsilon_{kl} + \kappa^{\varepsilon}_{3n}E_n. \tag{A.3}$$

With electric fields E applied to each crystal along the x_3 directions, $(E_3^0; E_3^{45}; E_3^{90})$, equation A.3 is expanded as,

$$D_3^i = e_{311}\varepsilon_{11}^i + e_{322}^i + e_{333}^i\varepsilon_{33}^i + \kappa_{33}^{\varepsilon}E_3^i, \tag{A.4}$$

where $i = 0\,°, 45\,°, 90\,°$.

From equation A.2, since there is no traction in the ε_3 direction the stress constitutive law can be written as,

$$\sigma_{33}^i = C_{33kl}^E\varepsilon_{kl}^i - e_{n33}E_n^i = 0, \tag{A.5}$$

or by expanding,

$$C_{3311}^E\varepsilon_{11}^i + C_{3322}\varepsilon_{22}^i + C_{3333}^E\varepsilon_{33}^i - e_{333}E_3^i = 0, \tag{A.6}$$

which implies,

$$\varepsilon_{33}^i = -\frac{C_{3311}^E}{C_{3333}^E}\varepsilon_{11}^i - \frac{C_{3322}^E}{C_{3333}^E}\varepsilon_{22}^i + \frac{e_{333}}{C_{3333}^E}E_3^i. \tag{A.7}$$

Substituting equations A.7 and A.1 into equation A.3, electric displacements along the x_3 axis direction are obtained as,

$$\begin{aligned}
D_3^0 &= \left(e_{322} - e_{333}\frac{C_{3322}^E}{C_{3333}^E}\right)\varepsilon_{11} + \left(e_{311} - e_{333}\frac{C_{3311}^E}{C_{3333}^E}\right)\varepsilon_{22} + \left(k_{33}^{\varepsilon} + \frac{e_{333}^2}{C_{3333}^E}\right)E_3^0 \\
D_3^{45} &= \frac{1}{2}\left(e_{311} + e_{322} - \left(\frac{C_{3322}^E + C_{3311}^E}{C_{3333}^E}\right)e_{333}\right)\varepsilon_{11} \\
&\quad + \left(e_{322} - e_{311} + \left(\frac{C_{3311}^E - C_{3322}^E}{C_{3333}^E}\right)e_{333}\right)\varepsilon_{12} \\
&\quad + \frac{1}{2}\left(e_{311} + e_{322} - \left(\frac{C_{3322}^E + C_{3311}^E}{C_{3333}^E}\right)e_{333}\right)\varepsilon_{22} + \left(k_{33}^{\varepsilon} + \frac{e_{333}^2}{C_{3333}^E}\right)E_3^{45} \\
D_3^{90} &= \left(e_{311} - e_{333}\frac{C_{3311}^E}{C_{3333}^E}\right)\varepsilon_{11} + \left(e_{322} - e_{333}\frac{C_{3322}^E}{C_{3333}^E}\right)\varepsilon_{22} + \left(k_{33}^{\varepsilon} + \frac{e_{333}^2}{C_{3333}^E}\right)E_3^{90}
\end{aligned} \tag{A.8}$$

These are written in matrix form as,

$$\boldsymbol{D} = \boldsymbol{M}\boldsymbol{\varepsilon} + \left(\kappa_{33}^{\varepsilon} + \frac{e_{333}^2}{C_{3333}^E}\right)\boldsymbol{E} \tag{A.9}$$

where,

$$\boldsymbol{D} = \begin{Bmatrix} D_3^{0} \\ D_3^{45} \\ D_3^{90} \end{Bmatrix} \qquad \boldsymbol{\varepsilon} = \begin{Bmatrix} \varepsilon_{11} \\ \varepsilon_{12} \\ \varepsilon_{22} \end{Bmatrix} \qquad \boldsymbol{E} = \begin{Bmatrix} E_3^{0} \\ E_3^{45} \\ E_3^{90} \end{Bmatrix},$$

and

$$\boldsymbol{M} = \begin{bmatrix} e_{32} - e_{33}\dfrac{C_{32}^E}{C_{33}^E} & 0 & e_{31} - e_{33}\dfrac{C_{31}^E}{C_{33}^E} \\ \dfrac{1}{2}\left(e_{31} + e_{32} - \left(\dfrac{C_{32}^E + C_{31}^E}{C_{33}^E}\right) e_{33}\right) & e_{32} - e_{31} - \left(\dfrac{C_{31}^E - C_{32}^E}{C_{33}^E}\right) e_{33} & e_{31} + e_{32} - \left(\dfrac{C_{32}^E + C_{31}^E}{C_{33}^E}\right) e_{33} \\ e_{31} - e_{33}\dfrac{C_{31}^E}{C_{33}^E} & 0 & e_{32} - e_{33}\dfrac{C_{32}^E}{C_{33}^E} \end{bmatrix}.$$

This is solved for the strain component of the substrate in equation A.10

$$\boldsymbol{\varepsilon} = \boldsymbol{M}^{-1}\boldsymbol{D} - \left(\kappa_{33}^{\varepsilon} + \frac{e_{33}^2}{C_{33}^E}\right)\boldsymbol{M}^{-1}\boldsymbol{E} \tag{A.10}$$

APPENDIX B

Finite Element Approximation

The finite element models used throughout this thesis approximate displacements and electric potentials using finite element shape function expressions. The unknown displacement components u_i can be approximated by,

$$u_i \approx \hat{u}_i = N_a \tilde{u}_i^a \quad i = 1, 2, 3;\ a = 1, 2, \ldots, n\ , \tag{B.1}$$

where $\hat{\Box}$ denotes an approximation of a function, N_a is a shape function for a specific elements node a, $\tilde{\Box}^a$ denotes a functions nodal value for an element's node a, and n is the number of nodes the element has. In equation B.1 and all following, the shape function with its nodal value counterpart $N_a \tilde{\Box}^a$ denotes a summation across all the nodes of the element,

$$N_a \tilde{\Box}^a = \sum_a N_a \tilde{\Box}^a. \tag{B.2}$$

The vector representation of the the displacement field approximation is shown in the following equation,

$$\boldsymbol{u} \approx \hat{\boldsymbol{u}} = \begin{Bmatrix} \hat{u} \\ \hat{v} \\ \hat{w} \end{Bmatrix} = \sum_a N_a \begin{Bmatrix} \tilde{u}_a \\ \tilde{v}_a \\ \tilde{w}_a \end{Bmatrix} = \sum_a N_a \tilde{\boldsymbol{u}}_a. \tag{B.3}$$

Differential operations on the displacement field are required in the finite element models used. The differential operations are used to find a small deformation strain field ϵ_{ij} which is approximated by,

$$\hat{\varepsilon}_{ij} = \frac{1}{2}\left[N_{a,j}\tilde{u}_i^a + N_{a,i}\tilde{u}_j^a\right] \quad i, j = 1, 2, 3;\ a = 1, 2, \ldots, n\ , \tag{B.4}$$

where $N_{a,j}$ denotes partial differentiation of the shape function N_a with respect to x_j, and x_j is a spatial component. While the small deformation strain is a tensor, it can be approximated as a vector using voigt notation as,

$$\boldsymbol{\varepsilon} = \begin{Bmatrix} \varepsilon_{xx} \\ \varepsilon_{yy} \\ \varepsilon_{zz} \\ \gamma_{yz} \\ \gamma_{xz} \\ \gamma_{xy} \end{Bmatrix} \approx \hat{\boldsymbol{\varepsilon}} = \sum_a \begin{bmatrix} \dfrac{\partial N_a}{\partial x} & 0 & 0 \\ 0 & \dfrac{\partial N_a}{\partial y} & 0 \\ 0 & 0 & \dfrac{\partial N_a}{\partial z} \\ 0 & \dfrac{\partial N_a}{\partial z} & \dfrac{\partial N_a}{\partial y} \\ \dfrac{\partial N_a}{\partial z} & 0 & \dfrac{\partial N_a}{\partial x} \\ \dfrac{\partial N_a}{\partial y} & \dfrac{\partial N_a}{\partial x} & 0 \end{bmatrix} \begin{Bmatrix} \tilde{u}_a \\ \tilde{v}_a \\ \tilde{w}_a \end{Bmatrix} = \sum_a \boldsymbol{B}_a \tilde{\boldsymbol{u}}_a, \tag{B.5}$$

where $\boldsymbol{B}_a^u$ is a displacement differential operator operating on shape function N_a.

Another independent variable that comes up in the mathematical models used in this thesis is the electric potential ϕ. The electric potential can be approximated by a shape function in the following way,

$$\phi \approx \hat{\phi} = N_a^{\phi} \tilde{\phi}^a. \tag{B.6}$$

Differential operations on the electric potential are also required for the finite element models used. The differential operations on the scalar potential are used to find the electric field E_i which is approximated by,

$$\hat{E}_i = -N_{a,i}^{\phi} \tilde{\phi}^a. \tag{B.7}$$

The electric field can also be representing using vector notation as,

$$\boldsymbol{E} = \begin{Bmatrix} E_x \\ E_y \\ E_z \end{Bmatrix} \approx \hat{\boldsymbol{E}} = \sum_a \begin{Bmatrix} -\dfrac{\partial N_a}{\partial x} \\ -\dfrac{\partial N_a}{\partial y} \\ -\dfrac{\partial N_a}{\partial z} \end{Bmatrix} \tilde{\phi}_a = \sum_a \boldsymbol{B}_a^{\phi} \tilde{\phi}_a, \tag{B.8}$$

where $\boldsymbol{B}_a^{\phi}$ is a electric potential differential operator operating on shape function N_a.

B.1 Global Derivatives

When performing a finite element analysis, the stiffness matrix depends on differential operators which depend on derivatives of the shape functions with respect to global coordinates x, y, z. For the models used in this thesis the differential operators are shown in equations B.5 and B.8. While the differential operators depend on global derivatives, the shape functions spatial variables are in natural coordinates ξ, η, ζ. Using the chain rule of partial differential equations, the natrual derivatives on a shape function can be written in matrix form as,

$$\begin{Bmatrix} \dfrac{\partial N_a}{\partial \xi} \\ \dfrac{\partial N_a}{\partial \eta} \\ \dfrac{\partial N_a}{\partial \zeta} \end{Bmatrix} = \begin{bmatrix} \dfrac{\partial x}{\partial \xi} & \dfrac{\partial y}{\partial \xi} & \dfrac{\partial z}{\partial \xi} \\ \dfrac{\partial x}{\partial \eta} & \dfrac{\partial y}{\partial \eta} & \dfrac{\partial z}{\partial \eta} \\ \dfrac{\partial x}{\partial \zeta} & \dfrac{\partial y}{\partial \zeta} & \dfrac{\partial z}{\partial \zeta} \end{bmatrix} \begin{Bmatrix} \dfrac{\partial N_a}{\partial x} \\ \dfrac{\partial N_a}{\partial y} \\ \dfrac{\partial N_a}{\partial z} \end{Bmatrix} = \boldsymbol{J} \begin{Bmatrix} \dfrac{\partial N_a}{\partial x} \\ \dfrac{\partial N_a}{\partial y} \\ \dfrac{\partial N_a}{\partial z} \end{Bmatrix}, \tag{B.9}$$

where the matrix $\boldsymbol{J}$ is the Jacobian matrix. When using an isoparametric formulation the Jacobian matrix can be defined as,

$$\boldsymbol{J} = \sum_a \begin{bmatrix} \dfrac{\partial N_a}{\partial \xi} x_a & \dfrac{\partial N_a}{\partial \xi} y_a & \dfrac{\partial N_a}{\partial \xi} z_a \\ \dfrac{\partial N_a}{\partial \eta} x_a & \dfrac{\partial N_a}{\partial \eta} y_a & \dfrac{\partial N_a}{\partial \eta} z_a \\ \dfrac{\partial N_a}{\partial \zeta} x_a & \dfrac{\partial N_a}{\partial \zeta} y_a & \dfrac{\partial N_a}{\partial \zeta} z_a \end{bmatrix}, \tag{B.10}$$

where x_a, y_a, z_a denotes the global coordinates of an element at node a. To then find the global derivatives on N, the linear system of equation B.9 can be inverted in the following fashion,

$$\begin{Bmatrix} \dfrac{\partial N_a}{\partial x} \\ \dfrac{\partial N_a}{\partial y} \\ \dfrac{\partial N_a}{\partial z} \end{Bmatrix} = \boldsymbol{J}^{-1} \begin{Bmatrix} \dfrac{\partial N_a}{\partial \xi} \\ \dfrac{\partial N_a}{\partial \eta} \\ \dfrac{\partial N_a}{\partial \zeta} \end{Bmatrix}. \tag{B.11}$$

Both linear and quadratic isoparametric shape functions were developed for tetrahedron and brick elements. An example linear 8-node brick shape function is shown in as,

$$N_a = \frac{1}{8}\left(1+\xi_a\xi\right)\left(1+\eta_a\eta\right)\left(1+\zeta_a\zeta\right), \tag{B.12}$$

where ξ_a, η_a, ζ_a denotes the natural coordinates of an element at node a. The isoparametric map from global to natural coordinates is shown in figure B.1. The coordinate values and the node ordering of the 8-node brick implemented is showni n table B.1. The extents of the nodes of the 8-node brick element extend from +/- 1 in the natural coordinate system.

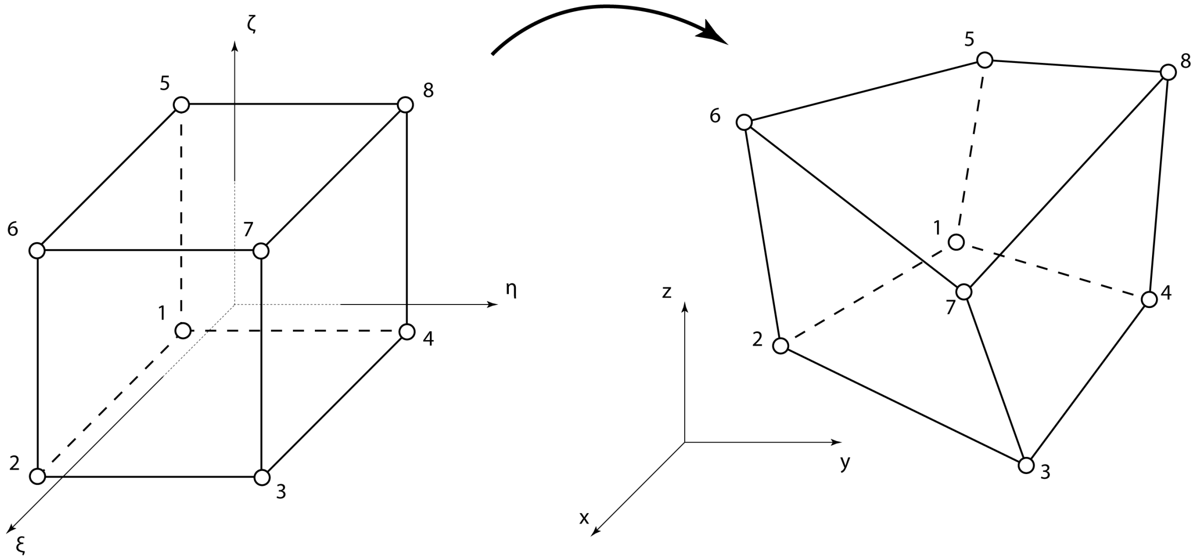

Figure B.1: Isoparametric mapping from natural to global coordinates

Node(a)	ξ	η	ζ
1	-1	-1	-1
2	1	-1	-1
3	1	1	-1
4	-1	1	-1
5	-1	-1	1
6	1	-1	1
7	1	1	1
8	-1	1	1

Table B.1: Local Node Locations of 8-Node Brick Element

To find the global derivatives as seen in equation B.11, the shape function of the 8-node brick are first differentiated by the natural coordinate system variables,

$$\begin{aligned}\frac{\partial N_a}{\partial \xi} &= \frac{1}{8}\xi_a \left(1+\eta_a\eta\right)\left(1+\zeta_a\zeta\right)\\ \frac{\partial N_a}{\partial \eta} &= \frac{1}{8}\eta_a \left(1+\zeta_a\zeta\right)\left(1+\xi_a\xi\right)\\ \frac{\partial N_a}{\partial \zeta} &= \frac{1}{8}\zeta_a \left(1+\xi_a\xi\right)\left(1+\eta_a\eta\right).\end{aligned} \tag{B.13}$$

The Jacobian matrix is also found using equation B.10 and is expressed for the 8-node brick as,

$$\boldsymbol{J} = \frac{1}{8}\sum_{a=1}^{8}\begin{Bmatrix}\xi_a \left(1+\eta_a\eta\right)\left(1+\zeta_a\zeta\right)\\ \eta_a \left(1+\zeta_a\zeta\right)\left(1+\xi_a\xi\right)\\ \zeta_a \left(1+\xi_a\xi\right)\left(1+\eta_a\eta\right)\end{Bmatrix}\begin{bmatrix}x_a & y_a & z_a\end{bmatrix}. \tag{B.14}$$

Using the expression for the Jacobian matrix and natural coordinate derivatives for the 8-node brick, the global shape function derivatives are obtained from equation B.11 as

$$\begin{Bmatrix}\dfrac{\partial N_a}{\partial x}\\ \dfrac{\partial N_a}{\partial y}\\ \dfrac{\partial N_a}{\partial z}\end{Bmatrix} = \frac{1}{8}\boldsymbol{J}^{-1}\begin{Bmatrix}\xi_a \left(1+\eta_a\eta\right)\left(1+\zeta_a\zeta\right)\\ \eta_a \left(1+\zeta_a\zeta\right)\left(1+\xi_a\xi\right)\\ \zeta_a \left(1+\xi_a\xi\right)\left(1+\eta_a\eta\right)\end{Bmatrix}. \tag{B.15}$$

While the global derivatives on a 8-node brick element was derived, similar derivations were required for the quadratic shape functions and tetrahedral elements developed. The tetrahedron global derivatives were fined using volumetric coordinates.

B.2 Volume Integrals

Not only are global derivatives on shape functions required when performing finite element analysis, integration across an element with respect to global coordinates is also required. Global integration across the 8-node brick element is represented in terms of natural coordinates using a coordinate transformation as,

$$\int\limits_{\Omega^E} f\left(x,y,z\right)d\Omega = \int\limits_{-1}^{1}\int\limits_{-1}^{1}\int\limits_{-1}^{1} f\left(x\left(\xi,\eta,\zeta\right),y\left(\xi,\eta,\zeta\right),z\left(\xi,\eta,\zeta\right)\right)J\left(\xi,\eta,\zeta\right)d\xi d\eta d\zeta, \tag{B.16}$$

where $J\left(\xi,\eta,\zeta\right) = \det\left(\boldsymbol{J}\right)$ and is known as the Jacobian.

The integration across an element using functions in global variables can thus be represented in terms of integration limits from +/- 1. Integration in this form is prime for numerically integrating equation B.16 using Gauss quadrature. Gauss quadrature on the 8-node brick can be represented as,

$$\int\limits_{-1}^{1}\int\limits_{-1}^{1}\int\limits_{-1}^{1} g\left(\xi,\eta,\zeta\right)d\xi d\eta d\zeta = \sum_{i=1}^{n}\sum_{j=1}^{n}\sum_{k=1}^{n} g\left(\xi_i,\eta_j,\zeta_k\right)w_i w_k w_k, \tag{B.17}$$

where ξ_i, η_j, ζ_k are quadrature points on quadrature index i, j, k and w_i, w_j, w_k are quadrature weights corresponding to quadrature index i, j, k. Again similar derivations can be employed for finding integrals across other elements.

REFERENCES

[1] G. Gautschi, *Piezoelectric sensorics: force, strain, pressure, acceleration and acoustic emission sensors, materials and amplifiers.* Springer, 2002.

[2] J. J. Dosch, D. J. Inman, and E. Garcia, "A self-sensing piezoelectric actuator for collocated control," *Journal of Intelligent Material Systems and Structures*, vol. 3, no. 1, pp. 166–185, 1992.

[3] J. T. Cutchen, "Plzt thermal/flash protective goggles: device concepts and constraints," *Ferroelectrics*, vol. 27, no. 1, pp. 173–178, 1980.

[4] N. W. Hagood and A. Pizzochero, "Residual stiffness and actuation properties of piezoelectric composites: theory and experiment," *Journal of intelligent material systems and structures*, vol. 8, no. 9, pp. 724–737, 1997.

[5] N. W. Hagood, R. Kindel, K. Ghandi, and P. Gaudenzi, "Improving transverse actuation of piezoceramics using interdigitated surface electrodes," in *1993 North American Conference on Smart Structures and Materials*, pp. 341–352, International Society for Optics and Photonics, 1993.

[6] A. A. Bent and N. W. Hagood, "Piezoelectric fiber composites with interdigitated electrodes," *Journal of Intelligent Material Systems and Structures*, vol. 8, no. 11, pp. 903–919, 1997.

[7] A. A. Bent, *Active fiber composites for structural actuation.* PhD thesis, Massachusetts Institute of Technology, 1997.

[8] A. A. Bent and A. E. Pizzochero, "Recent advances in active fiber composites for structural control," in *SPIE's 7th Annual International Symposium on Smart Structures and Materials*, pp. 244–254, International Society for Optics and Photonics, 2000.

[9] W. K. Wilkie, R. G. Bryant, J. W. High, R. L. Fox, R. F. Hellbaum, A. Jalink Jr, B. D. Little, and P. H. Mirick, "Low-cost piezocomposite actuator for structural control applications," in *SPIE's 7th Annual International Symposium on Smart Structures and Materials*, pp. 323–334, International Society for Optics and Photonics, 2000.

[10] J. W. High and W. K. Wilkie, *Method of fabricating NASA-standard macro-fiber composite piezoelectric actuators.* National Aeronautics and Space Administration, Langley Research Center, 2003.

[11] R. B. Williams, D. J. Inman, M. R. Schultz, M. W. Hyer, and W. K. Wilkie, "Nonlinear tensile and shear behavior of macro fiber composite actuators," *Journal of composite materials*, vol. 38, no. 10, pp. 855–869, 2004.

[12] R. B. Williams, D. J. Inman, and W. K. Wilkie, "Temperature-dependent thermoelastic properties for macro fiber composite actuators," *Journal of Thermal Stresses*, vol. 27, no. 10, pp. 903–915, 2004.

[13] R. B. Williams, B. W. Grimsley, D. J. Inman, and W. K. Wilkie, “Manufacturing and cure kinetics modeling for macro fiber composite actuators,” *Journal of reinforced plastics and composites*, vol. 23, no. 16, pp. 1741–1754, 2004.

[14] H. Allik and T. J. Hughes, “Finite element method for piezoelectric vibration,” *International journal for numerical methods in engineering*, vol. 2, no. 2, pp. 151–157, 1970.

[15] A. Benjeddou, “Advances in piezoelectric finite element modeling of adaptive structural elements: a survey,” *Computers & Structures*, vol. 76, no. 1, pp. 347–363, 2000.

[16] C. L. Hom and N. Shankar, “A finite element method for electrostrictive ceramic devices,” *International journal of solids and structures*, vol. 33, no. 12, pp. 1757–1779, 1996.

[17] W. Chen and C. Lynch, “Finite element analysis of cracks in ferroelectric ceramic materials,” *Engineering Fracture Mechanics*, vol. 64, no. 5, pp. 539–562, 1999.

[18] D. Fang and A. K. Soh, “Finite element modeling of electro-mechanically coupled analysis for ferroelectric ceramic materials with defects,” *Computer methods in applied mechanics and engineering*, vol. 190, no. 22, pp. 2771–2787, 2001.

[19] M. Kamlah and U. Böhle, “Finite element analysis of piezoceramic components taking into account ferroelectric hysteresis behavior,” *International Journal of Solids and Structures*, vol. 38, no. 4, pp. 605–633, 2001.

[20] C. M. Landis, “Fully coupled, multi-axial, symmetric constitutive laws for polycrystalline ferroelectric ceramics,” *Journal of the Mechanics and Physics of Solids*, vol. 50, no. 1, pp. 127–152, 2002.

[21] P. J. Chen, “Three dimensional dynamic electromechanical constitutive relations for ferroelectric materials,” *International Journal of Solids and Structures*, vol. 16, no. 12, pp. 1059–1067, 1980.

[22] C. S. Lynch, “On the development of multiaxial phenomenological constitutive laws for ferroelectric ceramics,” *Journal of intelligent material systems and structures*, vol. 9, no. 7, pp. 555–563, 1998.

[23] M. Kamlah and C. Tsakmakis, “Phenomenological modeling of the non-linear electro-mechanical coupling in ferroelectrics,” *International Journal of Solids and Structures*, vol. 36, no. 5, pp. 669–695, 1999.

[24] C. M. Landis, “A new finite-element formulation for electromechanical boundary value problems,” *International Journal for Numerical Methods in Engineering*, vol. 55, no. 5, pp. 613–628, 2002.

[25] R. M. McMeeking and C. M. Landis, “A phenomenological multi-axial constitutive law for switching in polycrystalline ferroelectric ceramics,” *International Journal of Engineering Science*, vol. 40, no. 14, pp. 1553–1577, 2002.

[26] M. Elhadrouz, T. B. Zineb, and E. Patoor, "Constitutive law for ferroelastic and ferroelectric piezoceramics," *Journal of intelligent material systems and structures*, vol. 16, no. 3, pp. 221–236, 2005.

[27] Y. Akiyama, S. Kimura, and I. Fujimura, "Development of (pb, nb)(zr, sn, ti) o3 film using a sol-gel process and resulting antiferroelectric properties," *Japanese journal of applied physics*, vol. 32, no. 9S, p. 4154, 1993.

[28] B. Laskewitz and M. Kamlah, "Finite element implementation of nonlinear constitutive models for piezoceramic materials," *Journal of Mechanics of Materials and Structures*, vol. 5, no. 1, pp. 19–45, 2010.

[29] S. Hwang, C. Lynch, and R. McMeeking, "Ferroelectric/ferroelastic interactions and a polarization switching model," *Acta metallurgica et materialia*, vol. 43, no. 5, pp. 2073–2084, 1995.

[30] X. Chen, D. Fang, and K.-C. Hwang, "Micromechanics simulation of ferroelectric polarization switching," *Acta materialia*, vol. 45, no. 8, pp. 3181–3189, 1997.

[31] W. Chen and C. Lynch, "A micro-electro-mechanical model for polarization switching of ferroelectric materials," *Acta Materialia*, vol. 46, no. 15, pp. 5303–5311, 1998.

[32] M. Elhadrouz, T. B. Zineb, and E. Patoor, "Constitutive law for ferroelectric and ferroelastic single crystals: a micromechanical approach," *Computational materials science*, vol. 32, no. 3, pp. 355–359, 2005.

[33] S. C. Hwang, J. E. Huber, R. M. McMeeking, and N. A. Fleck, "The simulation of switching in polycrystalline ferroelectric ceramics," *Journal of Applied Physics*, vol. 84, no. 3, pp. 1530–1540, 1998.

[34] S. C. Hwang and R. M. McMeeking, "A finite element model of ferroelastic polycrystals," *International Journal of Solids and Structures*, vol. 36, no. 10, pp. 1541–1556, 1999.

[35] J. Huber and N. Fleck, "Ferroelectric switching: a micromechanics model versus measured behaviour," *European Journal of Mechanics-A/Solids*, vol. 23, no. 2, pp. 203–217, 2004.

[36] J. Huber, "Micromechanical modelling of ferroelectrics," *Current Opinion in Solid State and Materials Science*, vol. 9, no. 3, pp. 100–106, 2005.

[37] M. Kamlah, A. C. Liskowsky, R. M. McMeeking, and H. Balke, "Finite element simulation of a polycrystalline ferroelectric based on a multidomain single crystal switching model," *International journal of solids and structures*, vol. 42, no. 9, pp. 2949–2964, 2005.

[38] A. Arockiarajan, A. Menzel, B. Delibas, and W. Seemann, "Micromechanical modeling of switching effects in piezoelectric materialsa robust coupled finite element approach," *Journal of Intelligent Material Systems and Structures*, vol. 18, no. 9, pp. 983–999, 2007.

[39] F. Li and R. Rajapakse, "Nonlinear finite element modeling of polycrystalline ferroelectrics based on constrained domain switching," *Computational Materials Science*, vol. 44, no. 2, pp. 322–329, 2008.

[40] M. S. Azzouz, C. Mei, J. S. Bevan, and J. J. Ro, "Finite element modeling of mfc/afc actuators and performance of mfc," *Journal of Intelligent Material Systems and Structures*, vol. 12, no. 9, pp. 601–612, 2001.

[41] A. Deraemaeker, H. Nasser, A. Benjeddou, and A. Preumont, "Mixing rules for the piezoelectric properties of macro fiber composites," *Journal of intelligent material systems and structures*, vol. 20, no. 12, pp. 1475–1482, 2009.

[42] S. C. Galea, T. G. Ryall, D. A. Henderson, R. W. Moses, E. V. White, and D. G. Zimcik, "Next generation active buffet suppression system," *AIAA paper*, vol. 2905, p. 2003, 2003.

[43] M. L. Wilbur, W. T. Yeager Jr, M. K. Sekula, *et al.*, "Further examination of the vibratory loads reduction results from the nasa/army/mit active twist rotor test," in *ANNUAL FORUM PROCEEDINGS-AMERICAN HELICOPTER SOCIETY*, vol. 58, pp. 1200–1214, AMERICAN HELICOPTER SOCIETY, INC, 2002.

[44] D. McDowell Jr, S. Plunkett, G. Goddu, and A. Bent, "Active fiber composite actuators for reducing acoustic radiation from cylindrical shells," *The Journal of the Acoustical Society of America*, vol. 105, no. 2, pp. 1240–1240, 1999.

[45] W. K. Wilkie, W. K. Belvin, and K. Park, "Aeroelastic analysis of helicopter rotor blades incorporating anisotropic piezoelectric twist actuation," *ASME-PUBLICATIONS-AD*, vol. 52, pp. 423–434, 1996.

[46] A. A. Bent, N. W. Hagood, and J. P. Rodgers, "Anisotropic actuation with piezoelectric fiber composites," *Journal of Intelligent Material Systems and Structures*, vol. 6, no. 3, pp. 338–349, 1995.

[47] J. P. Rodgers, *Development of an integral twist-actuated rotor blade for individual blade control.* PhD thesis, Massachusetts Institute of Technology, 1999.

[48] M. L. Wilbur, P. H. Mirick, W. T. Yeager, C. W. Langston, C. E. Cesnik, and S. Shin, "Vibratory loads reduction testing of the nasa/army/mit active twist rotor," *Journal of the American Helicopter Society*, vol. 47, no. 2, pp. 123–133, 2002.

[49] E. R. Booth and M. L. Wilbur, "Acoustic aspects of active-twist rotor control," *Journal of the American Helicopter Society*, vol. 49, no. 1, pp. 3–10, 2004.

[50] J.-S. Park and J.-H. Kim, "Design and aeroelastic analysis of active twist rotor blades incorporating single crystal macro fiber composite actuators," *Composites Part B: Engineering*, vol. 39, no. 6, pp. 1011–1025, 2008.

[51] J.-S. Park and J.-H. Kim, "Analytical development of single crystal macro fiber composite actuators for active twist rotor blades," *Smart materials and structures*, vol. 14, no. 4, p. 745, 2005.

[52] V. Mudupu, M. Trabia, W. Yim, and P. Weinacht, "Design and validation of a fuzzy logic controller for a smart projectile fin with a piezoelectric macro-fiber composite bimorph actuator," *Smart Materials and Structures*, vol. 17, no. 3, p. 035034, 2008.

[53] R. Paradies and P. Ciresa, "Active wing design with integrated flight control using piezoelectric macro fiber composites," *Smart Materials and Structures*, vol. 18, no. 3, p. 035010, 2009.

[54] O. Bilgen, C. De Marqui, K. B. Kochersberger, and D. J. Inman, "Macro-fiber composite actuators for flow control of a variable camber airfoil," *Journal of Intelligent Material Systems and Structures*, vol. 22, no. 1, pp. 81–91, 2011.

[55] O. Bilgen, K. Kochersberger, and D. Inman, "Macro-fiber composite actuators for a swept wing unmanned aircraft," *Aeronautical Journal*, vol. 113, no. 1144, pp. 385–395, 2009.

[56] P. Zhao, D. Pisani, and C. S. Lynch, "Piezoelectric strain sensor/actuator rosettes," *Smart Materials and Structures*, vol. 20, no. 10, p. 102002, 2011.

[57] G. Kawiecki and S. Jesse, "Rosette piezotransducers for damage detection," *Smart Materials and Structures*, vol. 11, no. 2, p. 196, 2002.

[58] H. Matt and F. L. di Scalea, "Macro-fiber composite piezoelectric rosettes for acoustic source location in complex structures," in *The 14th International Symposium on: Smart Structures and Materials & Nondestructive Evaluation and Health Monitoring*, pp. 65290Q–65290Q, International Society for Optics and Photonics, 2007.

[59] S. Salamone, I. Bartoli, P. Di Leo, F. L. Di Scala, A. Ajovalasit, L. D'Acquisto, J. Rhymer, and H. Kim, "High-velocity impact location on aircraft panels using macro-fiber composite piezoelectric rosettes," *Journal of Intelligent Material Systems and Structures*, vol. 21, no. 9, pp. 887–896, 2010.

[60] M. Collet, M. Ruzzene, and K. Cunefare, "Generation of lamb waves through surface mounted macro-fiber composite transducers," *Smart Materials and Structures*, vol. 20, no. 2, p. 025020, 2011.

[61] H. A. Sodano, G. Park, and D. J. Inman, "An investigation into the performance of macro-fiber composites for sensing and structural vibration applications," *Mechanical Systems and Signal Processing*, vol. 18, no. 3, pp. 683–697, 2004.

[62] A. J. Brunner, M. Birchmeier, M. M. Melnykowycz, and M. Barbezat, "Piezoelectric fiber composites as sensor elements for structural health monitoring and adaptive material systems," *Journal of Intelligent Material Systems and Structures*, vol. 20, no. 9, pp. 1045–1055, 2009.

[63] M. R. Schultz, M. W. Hyer, R. Brett Williams, W. Keats Wilkie, and D. J. Inman, "Snap-through of unsymmetric laminates using piezocomposite actuators," *Composites science and technology*, vol. 66, no. 14, pp. 2442–2448, 2006.

[64] T. Liu and C. Lynch, “Ferroelectric properties of [110],[001] and [111] poled relaxor single crystals: measurements and modeling,” *Acta materialia*, vol. 51, no. 2, pp. 407–416, 2003.

[65] T. Liu and C. Lynch, “Domain engineered relaxor ferroelectric single crystals,” *Continuum Mechanics and Thermodynamics*, vol. 18, no. 1-2, pp. 119–135, 2006.

[66] T. Wu, A. Bur, P. Zhao, K. P. Mohanchandra, K. Wong, K. L. Wang, C. S. Lynch, and G. P. Carman, “Giant electric-field-induced reversible and permanent magnetization reorientation on magnetoelectric ni/(011)[pb (mg 1/3 nb 2/3) o 3](1-x)–[pbtio 3] x heterostructure,” *Applied Physics Letters*, vol. 98, no. 1, pp. 012504–012504, 2011.

[67] T. Wu, P. Zhao, M. Bao, A. Bur, J. L. Hockel, K. Wong, K. P. Mohanchandra, C. S. Lynch, and G. P. Carman, “Domain engineered switchable strain states in ferroelectric (011)[pb (mg 1/3 nb 2/3) o 3](1-x)-[pbtio 3] x (pmn-pt, x= 0.32) single crystals,” *Journal of Applied Physics*, vol. 109, no. 12, pp. 124101–124101, 2011.

[68] Z.-G. Ye, “Crystal chemistry and domain structure of relaxor piezocrystals,” *Current Opinion in Solid State and Materials Science*, vol. 6, no. 1, pp. 35–44, 2002.

[69] Y. Lu, D.-Y. Jeong, Z.-Y. Cheng, Q. Zhang, H.-S. Luo, Z.-W. Yin, and D. Viehland, “Phase transitional behavior and piezoelectric properties of the orthorhombic phase of pb (mg 1/3 nb 2/3) o 3–pbtio 3 single crystals,” *Applied Physics Letters*, vol. 78, no. 20, pp. 3109–3111, 2001.

[70] D. La-Orauttapong, B. Noheda, Z.-G. Ye, P. Gehring, J. Toulouse, D. Cox, and G. Shirane, “Phase diagram of the relaxor ferroelectric (1-x) pb (zn_ {1/3} nb_ {2/3}) o_ {3}-xpbtio_ {3},” *Physical Review B*, vol. 65, no. 14, p. 144101, 2002.

[71] K. Fujishiro, R. Vlokh, Y. Uesu, Y. Yamada, J.-M. Kiat, B. Dkhil, and Y. Yamashita, “Optical observation of heterophase and domain structures in relaxor ferroelectrics pb (zn˜ 1˜/˜ 3nb˜ 2˜/˜ 3) o˜ 3/9% pbtio˜ 3,” *Japanese journal of applied physics*, vol. 37, no. part 1, pp. 5246–5248, 1998.

[72] Y. Uesu, Y. Yamada, K. Fujishiro, H. Tazawa, S. Enokido, J.-M. Kiat, and B. Dkhil, “Structural and optical studies of development of the long-range order in ferroelectric relaxor pb (zn1/3nb2/3) o3/9% pbtio3,” *Ferroelectrics*, vol. 217, no. 1, pp. 319–325, 1998.

[73] B. Noheda, D. Cox, G. Shirane, J. Gao, and Z.-G. Ye, “Phase diagram of the ferroelectric relaxor (1-x) pbmg_ {1/3} nb_ {2/3} o_ {3}-xpbtio_ {3},” *Physical Review B*, vol. 66, no. 5, p. 054104, 2002.

[74] Z.-G. Ye and M. Dong, “Morphotropic domain structures and phase transitions in relaxor-based piezo-/ferroelectric (1- x) pb (mgnb) o- xpbtio single crystals,” *Journal of Applied Physics*, vol. 87, p. 2312, 2000.

[75] R. Bertram, G. Reck, and R. Uecker, "Growth and correlation between composition and structure of (1-x) pb (zn1/3nb2/3) o3-xpbtio3 crystals near the morphotropic phase boundary," *Journal of crystal growth*, vol. 253, no. 1-4, pp. 212–220, 2003.

[76] A. K. Singh and D. Pandey, "Evidence for m_ {B} and m_ {C} phases in the morphotropic phase boundary region of (1-x)[pb (mg_ {1/3} nb_ {2/3}) o_ {3}]-xpbtio_ {3}: A rietveld study," *Physical Review B*, vol. 67, no. 6, p. 064102, 2003.

[77] S. Zhang, J. Luo, W. Hackenberger, and T. R. Shrout, "Characterization of pb (in 1/2 nb 1/2) o 3–pb (mg 1/3 nb 2/3) o 3–pbtio 3 ferroelectric crystal with enhanced phase transition temperatures," *Journal of applied physics*, vol. 104, no. 6, pp. 064106–064106, 2008.

[78] S. Zhang, J. Luo, W. Hackenberger, N. P. Sherlock, R. J. Meyer, and T. R. Shrout, "Electromechanical characterization of pb (in 0.5 nb 0.5) o 3–pb (mg 1/3 nb 2/3) o 3–pbtio 3 crystals as a function of crystallographic orientation and temperature," *Journal of Applied Physics*, vol. 105, no. 10, pp. 104506–104506, 2009.

[79] X. Liu, S. Zhang, J. Luo, T. R. Shrout, and W. Cao, "Complete set of material constants of," *JOURNAL OF APPLIED PHYSICS*, vol. 106, p. 074112, 2009.

[80] X. Liu, S. Zhang, J. Luo, T. Shrout, and W. Cao, "A complete set of material properties of single domain 0.26 pb (in [sub 1/2] nb [sub 1/2]) o [sub 3]–0.46 pb (mg [sub 1/3] nb [sub 2/3]) o [sub 3]–0.28 pbtio [sub 3] single crystals," *Appl. Phys. Lett*, vol. 96, p. 012907, 2010.

[81] S.-E. Park and T. R. Shrout, "Ultrahigh strain and piezoelectric behavior in relaxor based ferroelectric single crystals," *Journal of Applied Physics*, vol. 82, p. 1804, 1997.

[82] T. Liu and C. S. Lynch, "Orientation dependence of nonlinearity and hysteresis in pzn-4.5% pt single crystals i: Unipolar response," *Journal of intelligent material systems and structures*, vol. 17, no. 11, pp. 953–957, 2006.

[83] E. A. McLaughlin, T. Liu, and C. S. Lynch, "Relaxor ferroelectric pmn-32% pt crystals under stress and electric field loading: I-32 mode measurements," *Acta materialia*, vol. 52, no. 13, pp. 3849–3857, 2004.

[84] E. A. McLaughlin, T. Liu, and C. S. Lynch, "Relaxor ferroelectric pmn-32% pt crystals under stress, electric field and temperature loading: Ii-33-mode measurements," *Acta materialia*, vol. 53, no. 14, pp. 4001–4008, 2005.

[85] T. Liu, C. S. Lynch, and E. A. Mclaughlin, "Thermodynamics of stress and electric field induced phase transition in relaxor ferroelectric crystals," *Journal of intelligent material systems and structures*, vol. 18, no. 4, pp. 409–415, 2007.

[86] S.-F. Liu, S.-E. Park, T. R. Shrout, and L. Eric Cross, "Electric field dependence of piezoelectric properties for rhombohedral 0.955pb (zn 1/3 nb 2/3) o 3–0.045pbtio 3 single crystals," *Journal of applied physics*, vol. 85, no. 5, pp. 2810–2814, 1999.

[87] S.-E. Park and T. R. Shrout, "Characteristics of relaxor-based piezoelectric single crystals for ultrasonic transducers," *Ultrasonics, Ferroelectrics and Frequency Control, IEEE Transactions on*, vol. 44, no. 5, pp. 1140–1147, 1997.

[88] S. Zhang, S.-M. Lee, D.-H. Kim, H.-Y. Lee, and T. R. Shrout, "Temperature dependence of the dielectric, piezoelectric, and elastic constants for pb (mg 1/3 nb 2/3) o 3–pbzro 3–pbtio 3 piezocrystals," *Journal of Applied Physics*, vol. 102, no. 11, pp. 114103–114103, 2007.

[89] F. Wang, L. Luo, D. Zhou, X. Zhao, and H. Luo, "Complete set of elastic, dielectric, and piezoelectric constants of orthorhombic 0.71Pb(Mg1/3Nb2/3)O-3-0.29PbTiO(3) single crystal," *APPLIED PHYSICS LETTERS*, vol. 90, MAY 21 2007.

[90] T. Liu and C. Lynch, "Optimization of relaxor single crystals for bending mode applications," ASME, 2002.

[91] M. Haun, P. Moses, T. Gururaja, W. Schulze, and R. Newnham, "Transversely reinforced 1-3 and 1-3-0 piezoelectric composites," *Ferroelectrics*, vol. 49, no. 1, pp. 259–264, 1983.

[92] R. Newnham, J. Fernandez, K. Markowski, J. Fielding, A. Dogan, and J. Wallis, "Composite piezoelectric sensors and actuators," in *MATERIALS RESEARCH SOCIETY SYMPOSIUM PROCEEDINGS*, vol. 360, pp. 33–33, Cambridge Univ Press, 1995.

[93] R. Newnham, D. Skinner, and L. Cross, "Connectivity and piezoelectric-pyroelectric composites," *Materials Research Bulletin*, vol. 13, no. 5, pp. 525–536, 1978.

[94] S. Pilgrim and R. Newnham, "3: 0: A new composite connectivity," *Materials research bulletin*, vol. 21, no. 12, pp. 1447–1454, 1986.

[95] A. Safari, T. Gururaja, C. Hakun, A. Halliyal, and R. Newnham, "0-3 pieoelectric ceramic-polymer composites prepared by a new method: Fired composites," in *Applications of Ferroelectrics. 1986 Sixth IEEE International Symposium on*, pp. 305–308, IEEE, 1986.

[96] J. Tressler, S. Alkoy, A. Dogan, and R. Newnham, "Functional composites for sensors, actuators and transducers," *Composites Part A: Applied Science and Manufacturing*, vol. 30, no. 4, pp. 477–482, 1999.

[97] A. Furuta, K. Oh, and K. Uchino, "Shape memory ceramics and their application to latching relays," *Sensors and Materials*, vol. 3, no. 4, pp. 205–215, 1992.

[98] O. Bilgen, K. B. Kochersberger, D. J. Inman, and O. J. Ohanian, "Novel, bidirectional, variable-camber airfoil via macro-fiber composite actuators," *Journal of Aircraft*, vol. 47, no. 1, pp. 303–314, 2010.

[99] J. Schröck, T. Meurer, and A. Kugi, "Control of a flexible beam actuated by macro-fiber composite patches: I. modeling and feedforward trajectory control," *Smart Materials and Structures*, vol. 20, no. 1, p. 015015, 2011.

[100] J. Schröck, T. Meurer, and A. Kugi, "Control of a flexible beam actuated by macro-fiber composite patches: Ii. hysteresis and creep compensation, experimental results," *Smart Materials and Structures*, vol. 20, no. 1, p. 015016, 2011.

[101] J. A. Gallagher, D. M. Pisani, B. Smith-Stewart, and C. S. Lynch, "Stress and electric field gradient contributions to dielectric loss in ferroelectrics with interdigitated electrodes," *Journal of Intelligent Material Systems and Structures*, p. 1045389X14533433, 2014.

[102] D. A. Berlincourt, "Transducers using forced transitions between ferroelectric and antiferroelectric states," tech. rep., DTIC Document, 1965.

[103] W. Pan, Q. Zhang, A. Bhalla, and L. E. Cross, "Field-forced antiferroelectric-to-ferroelectric switching in modified lead zirconate titanate stannate ceramics," *Journal of the American Ceramic Society*, vol. 72, no. 4, pp. 571–578, 1989.

[104] W. Pan, C. Dam, Q. Zhang, and L. Cross, "Large displacement transducers based on electric field forced phase transitions in the tetragonal (pb0. 97la0. 02)(ti, zr, sn) o3 family of ceramics," *Journal of applied physics*, vol. 66, no. 12, pp. 6014–6023, 1989.

[105] K. G. Brooks, J. Chen, K. Udayakumar, and L. Cross, "Electric field forced phase switching in la-modified lead zirconate titanate stannate thin films," *Journal of applied physics*, vol. 75, no. 3, pp. 1699–1704, 1994.

[106] G. H. Haertling and C. E. LAND, "Hot-pressed (pb, la)(zr, ti) o3 ferroelectric ceramics for electrooptic applications," *Journal of the American Ceramic Society*, vol. 54, no. 1, pp. 1–11, 1971.

[107] D. Dausch and G. Haertling, "The domain switching and structural characteristics of plzt bulk ceramics and thin films chemically prepared from the same acetate precursor solutions," *Journal of materials science*, vol. 31, no. 13, pp. 3409–3417, 1996.

[108] M. W. Hooker, *Properties of pzt-based piezoelectric ceramics between-150 and 250c.* Citeseer, 1998.

[109] V. Bobnar, Z. Kutnjak, R. Pirc, and A. Levstik, "Electric-field–temperature phase diagram of the relaxor ferroelectric lanthanum-modified lead zirconate titanate," *Physical Review B*, vol. 60, no. 9, p. 6420, 1999.

[110] F. Y. Lee, H. R. Jo, C. S. Lynch, and L. Pilon, "Pyroelectric energy conversion using plzt ceramics and the ferroelectric–ergodic relaxor phase transition," *Smart Materials and Structures*, vol. 22, no. 2, p. 025038, 2013.

[111] Z. Meng, U. Kumar, and L. Cross, "Electrostriction in lead lanthanum zirconate-titanate ceramics," *Journal of the American Ceramic Society*, vol. 68, no. 8, pp. 459–462, 1985.

[112] Q. Zhang, W. Pan, A. Bhalla, and L. E. Cross, "Electrostrictive and dielectric response in lead magnesium niobate–lead titanate (0.9 pmn· 0.1 pt) and lead lanthanum zirconate titanate (plzt 9.5/65/35) under variation of temperature and electric field," *journal of the American Ceramic Society*, vol. 72, no. 4, pp. 599–604, 1989.

[113] H. Kessler, M. Kamlah, and H. Balke, "Constitutive and finite element modeling of ferroelectric repolarization," in *SPIE's 9th Annual International Symposium on Smart Structures and Materials*, pp. 21–30, International Society for Optics and Photonics, 2002.

[114] F. Li and D. Fang, "Simulations of domain switching in ferroelectrics by a three-dimensional finite element model," *Mechanics of Materials*, vol. 36, no. 10, pp. 959–973, 2004.

[115] D. Fang, F. Li, A. Soh, and T. Liu, "Analysis of the electromechanical behavior of ferroelectric ceramics based on a nonlinear finite element model," *Acta Mechanica Sinica*, vol. 21, no. 3, pp. 294–304, 2005.

[116] A. Fasano and M. Primicerio, *Free boundary problems: theory and applications*, vol. 2. Pitman Advanced Pub. Program, 1983.

[117] J. Langer, "Instabilities and pattern formation in crystal growth," *Reviews of Modern Physics*, vol. 52, no. 1, p. 1, 1980.

[118] S.-K. Ma, G. Grinstein, and G. Mazenko, *Directions in Condensed Matter Physics: Memorial Volume in Honor of Prof. Shang-keng Ma*, vol. 1. World Scientific, 1986.

[119] S. Nambu and D. A. Sagala, "Domain formation and elastic long-range interaction in ferroelectric perovskites," *Physical Review B*, vol. 50, no. 9, p. 5838, 1994.

[120] A. Onuki, "Ginzburg-landau approach to elastic effects in the phase separation of solids," *J. Phys. Soc. Jpn*, vol. 58, pp. 3065–3068, 1989.

[121] A. Devonshire, "Theory of ferroelectrics," *Advances in physics*, vol. 3, no. 10, pp. 85–130, 1954.

[122] G. Barsch, B. Achar, and L. Gross, "Landau-devonshire theory with rotationally invariant expansion coefficients," *Ferroelectrics*, vol. 35, no. 1, pp. 187–190, 1981.

[123] G. A. Rossetti Jr and N. Maffei, "Specific heat study and landau analysis of the phase transition in pbtio3 single crystals," *Journal of Physics: Condensed Matter*, vol. 17, no. 25, p. 3953, 2005.

[124] W. Cao and L. Cross, "Theory of tetragonal twin structures in ferroelectric perovskites with a first-order phase transition," *Physical Review B*, vol. 44, no. 1, p. 5, 1991.

[125] H.-L. Hu and L.-Q. Chen, "Computer simulation of 90 ferroelectric domain formation in two-dimensions," *Materials Science and Engineering: A*, vol. 238, no. 1, pp. 182–191, 1997.

[126] H.-L. Hu and L.-Q. Chen, "Three-dimensional computer simulation of ferroelectric domain formation," *Journal of the American Ceramic Society*, vol. 81, no. 3, pp. 492–500, 1998.

[127] Y. Li, S. Hu, Z. Liu, and L. Chen, "Effect of substrate constraint on the stability and evolution of ferroelectric domain structures in thin films," *Acta materialia*, vol. 50, no. 2, pp. 395–411, 2002.

[128] J. Wang, S.-Q. Shi, L.-Q. Chen, Y. Li, and T.-Y. Zhang, "Phase-field simulations of ferroelectric/ferroelastic polarization switching," *Acta Materialia*, vol. 52, no. 3, pp. 749–764, 2004.

[129] L. Chen and J. Shen, "Applications of semi-implicit fourier-spectral method to phase field equations," *Computer Physics Communications*, vol. 108, no. 2, pp. 147–158, 1998.

[130] Y. Su and C. M. Landis, "Continuum thermodynamics of ferroelectric domain evolution: Theory, finite element implementation, and application to domain wall pinning," *Journal of the Mechanics and Physics of Solids*, vol. 55, no. 2, pp. 280–305, 2007.

[131] J. Wang and M. Kamlah, "Three-dimensional finite element modeling of polarization switching in a ferroelectric single domain with an impermeable notch," *Smart Materials and Structures*, vol. 18, no. 10, p. 104008, 2009.

[132] J. Wang and M. Kamlah, "Effect of electrical boundary conditions on the polarization distribution around a crack embedded in a ferroelectric single domain," *Engineering Fracture Mechanics*, vol. 77, no. 18, pp. 3658–3669, 2010.

[133] P. Marton, I. Rychetsky, and J. Hlinka, "Domain walls of ferroelectric batio_ {3} within the ginzburg-landau-devonshire phenomenological model," *Physical Review B*, vol. 81, no. 14, p. 144125, 2010.

[134] B. Meyer and D. Vanderbilt, "Ab initio study of ferroelectric domain walls in pbtio_ {3}," *Physical Review B*, vol. 65, no. 10, p. 104111, 2002.

[135] E. A. Little, "Dynamic behavior of domain walls in barium titanate," *Physical Review*, vol. 98, no. 4, p. 978, 1955.

[136] C. Kittel, "Thickness of domain walls in ferroelectric and ferroelastic crystals," *Solid State Communications*, vol. 10, no. 1, pp. 119–121, 1972.

[137] A. Heitmann and G. Rossetti Jr, "Thermodynamics of polar anisotropy in morphotropic ferroelectric solid solutions," *Philosophical Magazine*, vol. 90, no. 1-4, pp. 71–87, 2010.

[138] G. Shirane, R. Pepinsky, and B. Frazer, "X-ray and neutron diffraction study of ferroelectric pbtio2," *Acta Crystallographica*, vol. 9, no. 2, pp. 131–140, 1956.

[139] W. D. Dong, D. M. Pisani, and C. S. Lynch, "A finite element based phase field model for ferroelectric domain evolution," *SMART MATERIALS AND STRUCTURES*, vol. 21, SEP 2012.